AEOLIAN SYSTEM DYNAMICS DERIVED FROM THERMAL INFRARED DATA

by

STEPHEN PAUL SCHEIDT

BS Environmental Sciences, University of Toledo, 1999

MS Geology, University of South Carolina, 2002

Submitted to the Graduate Faculty of

Arts and Sciences in partial fulfillment

of the requirements for the degree of

Doctor of Philosophy

University of Pittsburgh

2009

UNIVERSITY OF PITTSBURGH

FACULTY OF ARTS AND SCIENCES

This dissertation was presented

by

STEPHEN PAUL SCHEIDT

It was defended on

November 20, 2009

and approved by

Dissertation Advisor: Michael S. Ramsey, Associate Professor, University of Pittsburgh

Mark B. Abbott, Associate Professor, University of Pittsburgh

Rosemary C. Capo, Associate Professor, University of Pittsburgh

Michael F. Rosenmeier, Assistant Professor, University of Pittsburgh

Nicholas Lancaster, Research Professor, Desert Research Institute, Reno, Nevada

(External Examiner)

AEOLIAN SYSTEM DYNAMICS DERIVED FROM THERMAL INFRARED DATA

Stephen Paul Scheidt, Ph.D.

University of Pittsburgh, 2009

Thermal infrared (TIR) remote-sensing and field-based observations were used to study aeolian systems, specifically sand transport pathways, dust emission sources and Saharan atmospheric dust. A method was developed for generating seamless and radiometrically accurate mosaics of thermal infrared data from the Advanced Spaceborne Thermal Emission and Reflection Radiometer (ASTER) instrument. Using a combination of high resolution thermal emission spectroscopy results of sand samples and mosaic satellite data, surface emissivity was derived to map surface composition, which led to improvement in the understanding of sand accumulation in the Gran Desierto of northern Sonora, Mexico. These methods were also used to map sand transport pathways in the Sahara Desert, where the interaction between sand saltation and dust emission sources was explored. The characteristics and dynamics of dust sources were studied at White Sands, NM and in the Sahara Desert. At White Sands, an application was developed for studying the response of dust sources to surface soil moisture based on the relationship between soil moisture, apparent thermal inertia and the erosion potential of dust sources. The dynamics of dust sources and the interaction with sand transport pathways were also studied, focusing on the Bodele Depression of Chad and large dust sources in Mali and Mauritania. A dust detection algorithm was developed using ASTER data, and the spectral emissivity of observed atmospheric dust was related to the dust source area in the Sahara. At the Atmospheric Observatory (IZO) in Tenerife, Spain where direct measurement of the Saharan Air Layer could be made, the cycle of dust events occurring in July 2009 were examined. From the observation tower at the IZO, measurements of emitted longwave atmospheric radiance in the TIR wavelength region were made using a Forward Looking Infrared Radiometer (FLIR) handheld camera. The use of the FLIR to study atmospheric dust from the Saharan is a new application. Supporting data from AERONET and other orbital data enabled study of net radiative forcing.

TABLE OF CONTENTS

LIST OF TABLES

LIST OF FIGURES

ACKNOWLEDGEMENTS

Funding for this work was provided through the NASA Solid Earth and Natural Hazards Program (NAG5-13730), the Earth and Space Science Fellowship (NESSF) Program (NNX06-AF92H) and the ASTER science team (NNG04-GO69G). I am grateful for being able to present my research at the following conferences: the Planetary Dunes Workshop-A Record of Climate Change in 2008 in Alamogordo, NM; the 2007 American Geophysical Union Fall Meeting in San Francisco, CA; several ASTER Science Team Meeting, but especially the opportunity to attend on December 7, 2006 in Pasadena, CA; and the Sixth International Conference on Aeolian Research Meeting in Guelph, Ontario, Canada in July 2006. Some of the analyses and visualizations used in this dissertation were produced with the Giovanni online data system, developed and maintained by the NASA GES DISC. I would like to acknowledge the mission scientists and Principal Investigators who provided the data used in this research effort. I also acknowledge the numerous NASA affiliated organizations that make remote-sensing data available, as well as the PI investigators and their staff for establishing and maintaining the Izaña AERONET site used in this investigation.

The quality and accuracy of this dissertation and the manuscripts submitted for publication that came out of this work were both greatly improved by the detailed reviews of anonymous reviewers and the members of my Ph.D. committee. I would like to express my gratitude to them and the other outside reviewers and other consultants for their helpful comments on this work.

For their assistance of my fieldwork in the Gran Deiserto and providing me with a wonderful place to stay in Puerto Penasco, I thank the Intercultural Center for the Study of Deserts and Oceans (CEDO). For assistance at the White Sands National Monument, thanks go to David Bustos from the U.S. National Park Service. My field work at Tenerife, Spain would

not have been possible without Johanne Engelbrecht for his assistance in putting me in touch with another person I owe my gratitude, Dr. Sergio Rodríguez from the Centro de Investigación Atmosférica de Izaña. I thank Sergio for his assistance and helpful discussion on Saharan dust events occurring at the Izaña Atmospheric Observatory (IZO). My deepest appreciation goes to the science staff, maintenance and security personelle that made my work and stay in the month of July 2009 at IZO as easy, productive and pleasant as could ever be possible.

I would like to give special thanks to Michael Ramsey and Nicholas Lancaster for their guidance and financial support, assistance in the field and their expert contributions as co-authors. Special thanks also go to Itzhak Katra for the opportunity to co-author with him as well. I also thank the Department of Geology and Planetary Science, University of Pittsburgh, for the opportunity to conduct my graduate research teach, and be financial supported for two semesters as a teaching assistant, as well as their technical and administrative support. Specifically in Geology's main office, thanks to Matt Romick, Deanna Hitchcock, Dolly Chavez, Lorraine Robbins and Shannon Granahan for all their logistical support.

Thanks to all of my fellow Geology and IVIS lab mates for their collaboration and friendship, including Veronica Peet, Shellie Rose, and especially Topher Hughes for his lab support and sharing of ideas, Jeff Byrnes for his advice in my early days as a Ph.D. student, Kelly Larotonda for her assistance with my research and lab work, and Nathan Stansell for being an excellent professional role model. Thanks to Byron Steinman and Benjamin Cavallari for being fantastic roommates at the "Geo-Compound", as well as Broxton Bird and Neil for being the best Squirrel Hill neighbors. Our time was legendary. Thanks go to Adam Carter for being the absolute best sport and being a formidable opponent on the racquetball courts, of which is only one of many great things I could say about him. Thanks for your true friendship, helping me to keep a healthy work-life balance as a graduate student and being an excellent lab and office mate. For all the years of my rambling about science and remote-sensing, a special award (if one could be given) should go to Amy Wolfe. Your friendship, good humor, sound analytical advice, companionship, encouragement and Southern charm will always be remembered.

For your love, support, understanding, advice and unfailing encouragement – Mom, Dad, Omi, Opi, Melissa, Frank and Lauren – I could not have made the journey without you. Thanks for seeing me through.

1.0 INTRODUCTION

1.1 REMOTE-SENSING OF AEOLIAN SYSTEMS

There have been significant advances in orbital remote-sensing of the Earth over the past decade as the constellation of satellites that image and monitor the land surface, oceans and atmosphere continues to grow. This trend has led to the unprecedented availability of data to scientists, student researchers and the public. Visualization tools, such as the Google Earth™ mapping service, provide quick analysis and synergy of datasets with very high spatial resolution data (i.e., IKONOS, Quickbird, etc.). Anyone can quickly expand and deepen their knowledge of any territory. For geologists, interpretations of land cover, identification of landforms and discrimination of surface composition can begin to materialize long before going into the field. Even though the necessity will always exist to acquire ground truth for remote-sensing data and collect in-situ measurements, the ability to study a site remotely is an advantage, specifically for those studying aeolian systems in arid regions. Sand seas and dune fields are commonly difficult to access, field conditions can be problematic (i.e., extreme climate, safety, etc.) and locations are generally remote. Aeolian systems, such as sand seas and dune fields, are particularly attractive study sites for the application of multispectral and hyperspectral satellite sensors. These areas are good targets for analyzing surface composition, such as the mineralogy, because vegetation does not obscure the surface, particle size is usually uniform in sand seas and the areas are well exposed over large areas. Likewise, sand surfaces of varied composition make unique terrestrial analogues for Martian studies.

Arid land processes are associated with natural hazards such as desertification, sand encroachment, dust storms and climate change. These areas also may support a unique ecological niche, or they may be sensitive to changes in climate. As new remote-sensing data become available, so does the opportunity and a need to advance our understanding of aeolian systems.

We have the ability to extract land surface parameters using remote-sensing to study aeolian surface dynamics, where this dissertation focuses on the development and application of analytical tools that utilize the Advanced Spaceborne Thermal Emission and Reflection Radiometer (ASTER). This instrument provides good coverage and high spatial resolution, where the focus of this research utilizes the sensor's imaging capabilities in the thermal infrared (TIR) wavelength region.

A great deal of information can be learned about the Earth and its atmosphere using applications of multispectral thermal infrared imagery. According to the Wien Displacement Law, the peak wavelength (λ_{max}) of radiant energy emitted from a material at temperature (T) in degrees Kelvin is:

$$\lambda_{max} \times T = 2898 \quad (1).$$

Therefore, for the average temperature of the Earth surface, the emitted radiance peaks within the 8-14 μm infrared wavelength region. In order to study the Earth surface, a remote-sensing instrument must have an unobstructed view whereby the atmosphere allows transmission of radiant energy to propogate from the Earth surface to the lens of the instrument. Figure 1 shows the atmospheric windows (or areas of higher transmission) that can be used for TIR remote-sensing of the land surface, where water vapor, ozone and carbon dioxide absorption are the important atmospheric constituents responsible for signal interference.

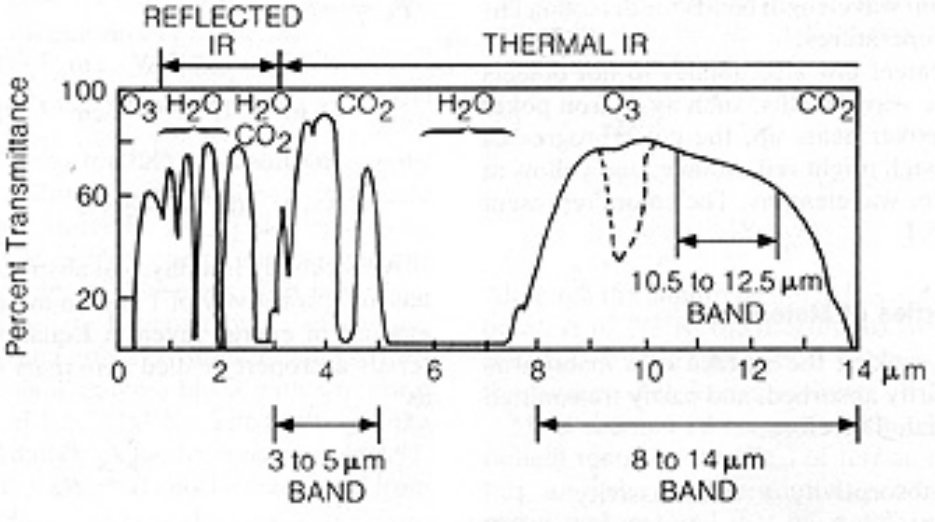

Figure 1. Atmospheric transmission as a function of wavelength [*Sabins* 1997].

For a perfect blackbody (an object that completely absorbs and reemits 100% of incident radiant energy), the flux of radiant energy (F_R) is related to the object's kinetic temperature (T_k) through the simplified Stefan-Boltzmann Law:

$$F_R = \varepsilon\sigma T_k^4 \quad (2)$$

where sigma (σ) is the Stefan-Boltzmann constant (W m^{-2} K^{-4}) and emissivity (ε) is a dimensionless quantity that can be expresses as a ratio of the radiant flux of an object to the radiant flux of a blackbody at the same temperature. Earth surface temperatures are important for global-change studies and determining radiation budgets, and measuring temperature globally by remote-sensing instruments is extremely important to validate climate models. Emissivity varies with the wavelength of radiant energy and is highly related to surface composition [*Salisbury and D'Aria* 1992; T*homson and Salisbury* 1993; *Ramsey and Christiansen* 1998], especially silicate minerals that make up much of the land surface in aeolian systems [*Ramsey et al.* 1999]. Emissivity can be used to study changes in vegetation cover, mapping of exposed rock, mineral resource exploration, soil development and erosion. Both temperature and emissivity vary, but these quantities can be separated from remote-sensing measurements of Earth's TIR radiant energy [*Kahl* et al. 1976]. The simple expression for thermal radiance (L_λ) at the aperture of a remote-sensing instrument is a function of both emissivity and radiant temperature, but also includes a number of terms to correct for atmophseric interference:

$$L_\lambda \approx \tau_\lambda [(\varepsilon_\lambda B_\lambda(T) + (1-\varepsilon_\lambda) (L_\lambda\downarrow)/\pi] + L_\lambda\uparrow \quad (3)$$

where,

τ_λ = atmospheric transmissivity (dimensionless)

ε_λ = spectral emissivity (dimensionless)

$B_\lambda(T)$ = blackbody radiance (Wm^{-2} μm^{-1} sr^{-1})

T = brightness temperature (K)

$L_\lambda\downarrow$ = downwelling atmospheric irradiance, (Wm^{-2} μm^{-1} sr^{-1})

$L_\lambda\uparrow$ = upwelling atmospheric path radiance (Wm^{-2} μm^{-1} sr^{-1})

$1-\varepsilon_\lambda$ = reflectivity, according to Kirchhoff's Law ($\rho_\lambda = 1- \varepsilon_\lambda$, dimensionless)

where,

ρ_λ = reflectance.

The blackbody radiance $B_\lambda(T)$ of an object can be described by Planck's Law as a function of wavelength:

$$B_\lambda(T) = \frac{2hc^2}{\lambda^5} \frac{1}{e^{hc/\lambda kT} - 1} \quad (4)$$

where,

h = Plank constant (J·s)

c = speed of light (m/s)

λ = wavelength (m)

T = temperature (K)

k = Boltzman constant (J/K)

In summary, the research presented in this dissertation is driven by our ability to measure the emitted radiance from the Earth's surface using remote-sensing and to derive temperature and emissivity using the relationships described above. Thermal infrared remote-sensing may be used by research scientists and those in academia for "high level" study of the the Earth surface and climate, but the application of this technology is used by everyone everyday (i.e., weather forecasting, hazard prediction, etc). Although these data are also readily available to almost everyone (for example, through U.S. entities such as NOAA, USGS and NASA), a specific skill set or software package is generally required to make use of those remote-sensing data sets. However, as mentioned above, visualization of these data has become more readily accessible, especially in the past six years.

1.2 SUMMARY OF RESEARCH OBJECTIVES

This dissertation describes a series of applications developed for thermal infrared remote-sensing of aeolian systems, focusing mainly on ASTER data, to understand Earth system problems at a variety of field sites. In an aeolian system, the atmosphere and the Earth surface interact to mutually affect each other. On one hand, the wind shapes the Earth surface, redistributing materials (sediments) and creating unique landforms. On the other, dust entrained by wind and lofted into the atmosphere alters the propagation of incoming solar and emitted

terrestrial radiation, which affects Earth's climate. This dissertation addresses both aspects of the Earth-atmosphere interaction.

First the effects of wind on the distribution of surface materials that create dunes were examined. The study site and the main focus of Chapters 2 and 3 is the Gran Desierto, Sonora, MX, where the goal of the research was to map the distribution of aeolian sediments. Several scales of measurement were conducted to support remote-sensing analysis through campaigns in the field (i.e., ground truth), where for this location, included high spectral resolution thermal infrared spectroscopy of dune sand samples in the lab. The secondary objective arose from the need to study sediment composition over very large geographic areas. A radiometric balancing and mosaicking algorithm was developed [*Scheidt et al*. 2008], and the geographic limits imposed by a single high spatial resolution ASTER image were expanded. Without the mosaicking technique, image data would otherwise be discontinuous. With a complete mosaic of ASTER TIR data of the Gran Desierto, a linear deconvolution algorithm [Ramsey et al. 1999] was utilized to derive surface composition of sands in the Gran Desierto. The remote-sensing data analysis was combined with a thorough study of laboratory TIR spectral data, which allowed for characterization of sand sources, transport pathways and sinks. This improved the previous understanding of sand accumulation in the Gran Desierto.

The second objective was to study the dynamics of dust and sand transport in response to other land surface variables, such as soil moisture content, the extent and timing of playa inundation, vegetation cover and mineral composition. In Chapter 4, the White Sands Dune field in New Meixco is the focus of study, where soil moisture is importance to controlling the erosion potential of sand and dust by wind (or sediment availability). This was accomplished by building upon an algorithm that derives wind threshold ratio (WTR) from ASTER image data. The WTR is the relative threshold of wind velocity of wet to dry sediment that must be exceeded for sediment to become entrained by wind. By combining the relationships among apparent thermal inertia (ATI), soil moisture [*Xu and Cracknell* 1995; *Ma and Xu* 1990] and the WTR [*Fecan et al.* 1990], the new algorithm that was developed determines WTR directly from ATI. The TIR data enabled the derivation of day and night surface temperatures, which were needed to derive ATI data. With data from multiple dates through time, changes in the availability of sediment (for erosion) were examined.

Uncertainty exists as to the relative impact of dust on the Earth's energy balance [*Trenberth et al*. 2008], both on regional and global scales. The effect of Saharan dust on the Earth's radiation budget and weather variability is an important component of climate studies. The Sahara Desert contributes a significant amount of dust to the atmosphere, and the interaction of dust with the Earth's radiant energy budget is inherently complex. Chapter 5 examines the cycle of atmospheric dust as a result of the Saharan Air Layer (SAL). Both remote-sensing data and field observations were used to characterize the radiative properties of dust emissions from the Sahara, and methods of dust source mapping (used in Chapter 2 and 3) were utilized to map the dust sources in parts of the Sahara Desert. These dust sources were linked to atmospheric dust observed at the Izana Atmospheric Observatory (IZO) in Tenerife, Spain, where field work was conducted in July 2009. Tenerife is part of the Canary Islands off the coast of West Africa and is directly impacted by the SAL at high elevations. TIR remote-sensing data, including field measurements using a Forward-Looking Infrared Radiometer (FLIR) instrument, were utilized to quantitatively measure the dust source composition and the radiative impacts. AERONET and orbital data from ASTER, AIRS and MODIS were combined to examine the changes in aerosol optical depth (AOD) and relative radiative forcing through time. A dust emission source from the Sahara was related to dust emissions at the IZO, utilizing 15 minute, temporally resolved dust detection products from the Spinning Enhanced Visible and Infrared Imager (SEVIRI) instrument to trace dust back to a dust source in Mali. All of these datasets were collected simultaneously; therefore these data can be directly compared and combined for analysis. For example, to understand the broader impact of dust composition variability on radiative forcing, radiant flux and aerosol data can be used to determine radiative efficiency of aerosols (W/m^2/AOD) [*Christopher and Jones* 2008].

Finally in Chapter 5, as part of the field work in July 2009 at the IZO, a field method, specifically utilizing side-looking FLIR data, was developed in order to quantify the direct longwave radiative forcing of aerosols. This enables mapping of the spatial and temporal distribution of dust emissions in the atmosphere. In this dissertation, FLIR measurements over the Atlantic Ocean of dusty and clear atmospheric conditions are compared. The location of the IZO allowed for direct measurement of emitted longwave infrared in the atmospheric window (8-12 μm) using a FLIR imaging camera. The analysis was based upon field work completed during one month of the potential dusty season (July 11 – August 4, 2009). These measurements

can be used for comparison to modeled longwave radiance using the Santa Barbara DISORT Atmospheric Radiative Transfer (SBDART) model, which is a software tool that computes plane-parallel radiative transfer in clear and cloudy conditions within the Earth's atmosphere and at the surface [*Ricchiazzi et al.* 1998].

2.0 RADIOMETRIC NORMALIZATION AND IMAGE MOSAIC GENERATION OF ASTER THERMAL INFRARED DATA: AN APPLICATION TO EXTENSIVE SAND SHEETS AND DUNE FIELDS

2.1 CHAPTER SUMMARY

Data from the Advanced Spaceborne Thermal Emission and Reflection Radiometer (ASTER) have a significant advantage over previous datasets because of the combination of high spatial resolution (15-90 m) and enhanced multispectral capabilities, particularly in the Earth's thermal infrared (TIR) atmospheric window (8-12 μm) where common silicate minerals are more easily identified. However, the 60 km swath width of ASTER can limit the effectiveness of accurately tracing large-scale features, such as eolian sediment transport pathways, over long distances. The primary goal of this work is to describe a method for generating a seamless and radiometrically accurate ASTER TIR mosaic of atmospherically-corrected radiance and from that, extract surface emissivity for arid lands, specifically, sand seas. The Gran Desierto in northern Sonora, Mexico was used as a test location for the radiometric normalization technique because of past remote-sensing studies of the region, its compositional diversity, and its size. A linear approach was taken to transform adjacent image swaths into a direct linear relationship between image acquisition dates. Pseudo-invariant features (PIFs) were selected using a threshold of correlation between radiance values, and change-pixels were excluded from the linear regression used to determine correction factors. The degree of spectral correlation between overlapping pixels is directly related to the amount of surface change over time; therefore, the gain and offsets between scenes were based only on regions of high spectral correlation. The result was a series of radiometrically normalized radiance-at-surface images that were combined with only a minimum of image edge seams present. These edges were subsequently blended to create the final mosaic. The advantages of this approach for TIR radiance (as opposed to

emissivity) data include the ability to: (1) analyze data acquired on different dates (with potentially very different surface temperatures) as one seamless compositional data set; (2) perform decorrelation stretches (DCS) on the entire dataset in order to identify and discriminate compositional units; and (3) separate brightness temperature from surface emissivity for quantitative compositional analysis of the surface, reducing seam-line error in the emissivity mosaic. The approach presented here is valid for any ASTER-related study of large geographic regions where numerous images spanning different temporal and atmospheric conditions are encountered.

2.2 INTRODUCTION

2.2.1 Thermal-infrared remote-sensing of aeolian systems

Data from the Advanced Spaceborne Thermal Emission and Reflection Radiometer (ASTER) have a significant advantage over previous datasets because of the combination of high spatial resolution (15-90 m) and enhanced multispectral capabilities, particularly in the Earth's thermal infrared (TIR) atmospheric window (8-12 μm) where common silicate minerals are more easily identified. However, the 60 km swath width of ASTER can limit the effectiveness of accurately tracing large-scale features, such as eolian sediment transport pathways, over long distances. The primary goal of this work is to describe a method for generating a seamless and radiometrically accurate ASTER TIR mosaic of atmospherically-corrected radiance and from that, extract surface emissivity for arid lands, specifically, sand seas. The Gran Desierto in northern Sonora, Mexico was used as a test location for the radiometric normalization technique because of past remote-sensing studies of the region, its compositional diversity, and its size. A linear approach was taken to transform adjacent image swaths into a direct linear relationship between image acquisition dates. Pseudo-invariant features (PIFs) were selected using a threshold of correlation between radiance values, and change-pixels were excluded from the linear regression used to determine correction factors. The degree of spectral correlation between overlapping pixels is directly related to the amount of surface change over time; therefore, the gain and offsets between scenes were based only on regions of high spectral correlation. The

result was a series of radiometrically normalized radiance-at-surface images that were combined with only a minimum of image edge seams present. These edges were subsequently blended to create the final mosaic. The advantages of this approach for TIR radiance (as opposed to emissivity) data include the ability to: (1) analyze data acquired on different dates (with potentially very different surface temperatures) as one seamless compositional data set; (2) perform decorrelation stretches (DCS) on the entire dataset in order to identify and discriminate compositional units; and (3) separate brightness temperature from surface emissivity for quantitative compositional analysis of the surface, reducing seam-line error in the emissivity mosaic. The approach presented here is valid for any ASTER-related study of large geographic regions where numerous images spanning different temporal and atmospheric conditions are encountered.

2.2.2 Previous image mosaicking methods

Satellite remote sensing data provide the synoptic view necessary to study large and inaccessible aeolian systems. Without a mosaicking procedure, the geographical extent imposes practical limits on the choice of the data used. The Terra satellite carries two primary instruments for observing the Earth surface in the TIR: The Moderate Resolution Imaging Spectroradiometer (MODIS) and ASTER. MODIS is advantageous for global coverage utilizing eight bands in the TIR wavelength region at a spatial resolution of 1 km/pixel and a swath width of 2,330 km. Spectral unmixing and classification of a mosaic of MODIS data was used for landform mapping in the Sahara [*Ballantine et al*. 2005], although it did not include multispectral TIR data. Even though sediment transport pathways are discernible over distances of hundreds of kilometers from MODIS data, a significantly higher spatial resolution is needed to quantify the composition and degree of mixing of small contributing areas of sand along paths of transport or the extent of dust source areas less than 1 km^2.

ASTER has a significant advantage in the remote sensing of geologic materials because of its higher spatial resolution than MODIS and enhanced spectral range [*Fujisada et al.* 1998; *Yamaguchi et al*. 1998]. ASTER has proven useful for mapping key mineral groups, especially for discriminating silicates [*Hewson et al*. 2001; *Rowan and Mars* 2003; *Rowan et al.* 2005]. However, because the ASTER footprint is only 60 km x 60 km, it is necessary to combine

multiple scenes into a mosaic for complete coverage of a large study region such as the Gran Desierto or Sahara Desert. Few published studies of ASTER data have been used in a multi-scene capacity. *Ogawa et al*. [2002] mosaicked the standard atmospherically-corrected ASTER surface emissivity data product [*Gillespie et al.* 1998] for a 750,000-km^2 portion of the Sahara Desert to estimate broadband emissivity at 90 m/pixel spatial resolution. *Hewson et al.* [2005] described the generation of a seamless mosaic of normalized SWIR band-ratio data, but this emissivity data, generated from TIR radiance, were not normalized because spectra compared well with field observations and the emissivity product was found to mosaic well despite scan line noise and a relatively low signal to noise ratio (SNR). Seamlessness of a mosaic is a most obvious advantageous for display purposes, but the combination of radiometrically non-normalized scenes hinders spectral analysis and geologic interpretation (e.g., such as the delineation of surface composition). The thermal radiance received by the ASTER sensor is affected by the emissivity (composition) and the temperature of the emitting surface. Atmospheric correction and the separation of temperature from the desired surface composition information (emissivity) may not be adequate alone to achieve radiometric normalization. There has been no detailed description or evaluation of the pre-processing issues and mosaicking strategy for TIR radiance data.

The need to combine multispectral remote sensing data using a relative radiometric normalization approximated by linear functions is not a new concept, and a number of techniques have had varied success for Earth [*Hall et al*. 1991; *Moranet al*. 1992; *Schott et al.* 1998; *Furby and Campbell* 2001; *Du et al.* 2001; *Du et al.* 2002; *Canty et al.* 2004; *Paolini et al.* 2006] and Mars [*Martínez-Alonso et al*. 2005] For these techniques, it is assumed that an approximately linear relationship can be determined between the at-sensor radiance measurements within the area of the overlapping scenes that contain PIFs, as the models for the atmospheric and viewing-geometry effects on the recorded data are far more complex. Changes in the land surface through time may not have the same linear relation as the whole image scene and are problematic for image mosaicking. *Canty et al.* [2004] demonstrated a successful example of mosaicking by automatically selecting PIFs between bitemporal images using the multivariate alteration detection (MAD) technique [*Nielsen et al.* 2002; 1998], and they emphasize a number of unique characteristics that are important to their mosaicking technique:

- Selection of PIFs was not manual or subjective except for one decision threshold, based on scale-invariant criteria, and corresponded to physical characteristics of the land surface.
- Their results compared favorably with other manual methods, but their technique was fast and automatic.
- After testing, orthogonal linear regression of PIFs was preferred to ordinary least squares regression (OLS).

2.2.3 Geographic Location and Primary Objectives

An ideal location for creating an ASTER TIR mosaic and testing its science applications is a large sand sea of diverse surface composition with few complicating factors (e.g., humid atmosphere, large amounts of vegetation, or poor access to the area for field validation). The Gran Desierto (Figure 2), a 5,700-km^2 area located along the northern coast of the Gulf of California in the state of Sonora, Mexico, was chosen as a focus and testing area because of the unique assemblages of dunes of variable composition and morphology [*Lancaster et al*. 1987; *Blount et al.* 1988, 1992; *Lancaster* 1992; *Muhs et al.* 2003; *Beveridge et al*. 2006]. The sand sea itself is a dynamic land surface feature over geologic time scales, but the mineralogy of its surface in the Gran Desierto is assumed to be in equilibrium or generally stable with respect to sediment flux over the range of ASTER acquisition dates (2000 – 2003). Therefore, a minimal amount change is expected for the composition of sand surfaces over the three year time scale of this study.

The main objective here was to present a straightforward method for creating seamless ASTER multispectral TIR radiance-at-surface mosaic from standard data products (Figure 3), and to then evaluate the effectiveness of a relative radiometric normalization technique in both radiance and emissivity space in an arid land environment. The method developed here using 26 ASTER scenes will guide production of a much larger (~4,000+ ASTER scenes), high resolution mosaic of the Sahara Desert. The desired final result must have reduced seam-line error and balanced images and it must be suitable for emissivity extraction, spectral analysis algorithms such as linear deconvolution [*Ramsey et al.* 1999], and final geologic interpretation. The application of the final mosaic data, beyond the scope of the work here, is to derive the bulk mineralogy of the surface of sand seas and dust sources in arid lands from emissivity derived from TIR data.

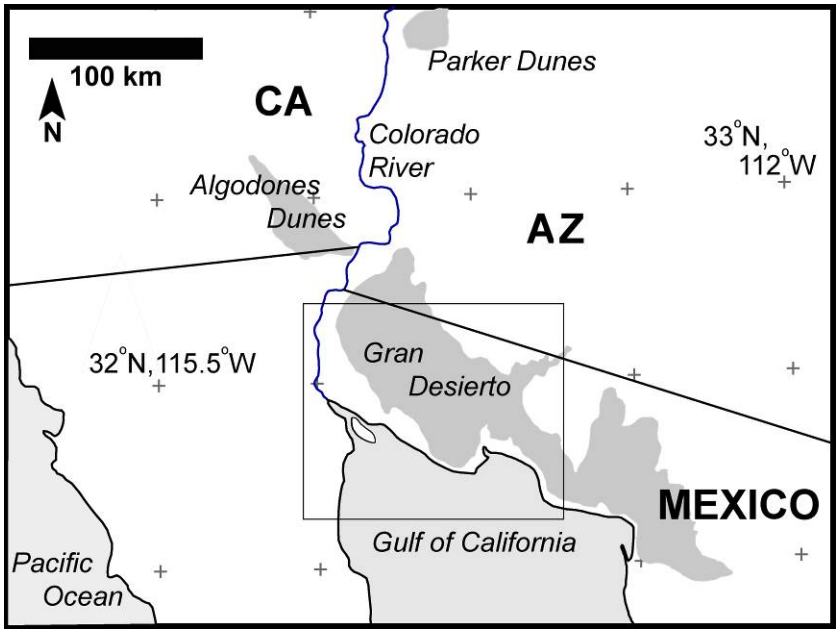

Figure 2. The location map shows the geographic location of the Gran Desierto sand sea [modified after *Muhs et al.* 2003].

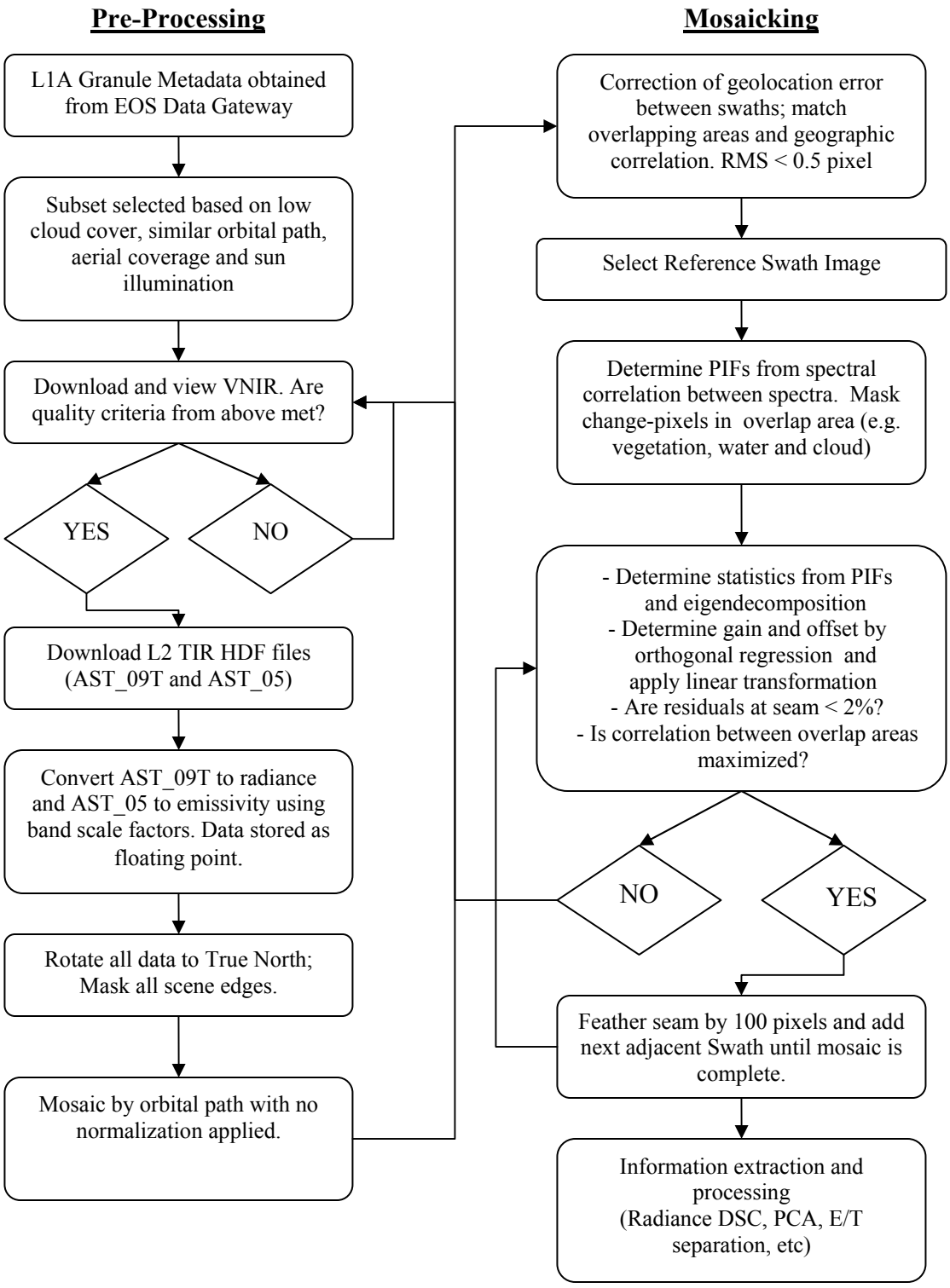

Figure 3. Flow chart of preprocessing, normalization and mosaicking of ASTER TIR radiance and emissivity.

2.3 MOSAIC GENERATION METHODS

2.3.1 TIR ASTER image datasets

ASTER measures spectral radiance in five TIR bands between 8.13 and 11.65 μm, has a spatial resolution of 90 m/pixel and the NEΔT < 0.3 K. The data used for this study include the Level-2 (L2) surface-leaving radiance (AST_09T) and the emissivity (AST_05) products. Calibration is applied to Level-1A (L1A) data, which is based on the sensor stability over time in order to create the geolocated and radiometrically-accurate L1B data, resulting in an absolute accuracy of 2% and a relative accuracy of 1% [*Yamaguchi et al.* 1998]. The AST_09T product, created from the L1B, has been radiometrically, geometrically, and atmospherically corrected *Thome et al.* [1998]. The AST_05 product is derived from the AST_09T data using the Temperature Emissivity Separation (TES) algorithm described by *Gillespie et al*. [1998], which accounts for both the spectral contrast and downwelling atmospheric irradiance. These data are distributed by the Land Processes Distributed Active Archive Center (LP DAAC), located at the U.S. Geological Survey (USGS) Center for Earth Resources Observation and Science (EROS) (http://LPDAAC.usgs.gov).

Consecutive scenes acquired along the same orbital path should combine seamlessly because these were acquired as one observation by ASTER. However, caution must be taken if combining imagery from different versions of calibration to ensure seamlessness in a final mosaic. L1B data used to generate the L2 on-demand TIR radiance products were previously archived at the LP DAAC. Depending on when L2 data were ordered, they may have been produced from slightly different versions of the L1B archived data and lead to inconsistencies. As a result, L1B images occasionally were found to have subtle seam boundaries in the same orbital path if these scenes had different versions of a radiometric calibration. This problem has now been eliminated for new data users, as all L1B data are processed on-demand and therefore always have the latest radiometric calibration. On-demand processing also ensures that subsequent L2 products have the same atmospheric correction.

To create an accurate mosaic of the Gran Desierto test local from the data available, 26 daytime scenes spanning 8 different dates (Table 1) were selected using metadata from The Terra ASTER Metadata Inventory (TAMI) and browse images previewed through the USGS Global

Table 1. Summary of ASTER scene metadata.

Date	Granule IDs	Time	Solar Azimuth Angle	Solar Elevation Angle	Pointing Angle
2-May-02	(SC:AST_L1A.003:2006812474)	18:29:16	134.092	67.019	-4.205
	(SC:AST_L1A.003:2006812482)	18:29:25	133.081	67.422	
28-Mar-01	(SC:AST_L1A.003:2006036884)	18:38:14	150.068	56.551	0.005
	(SC:AST_L1A.003:2006036886)	18:38:23	149.487	57.084	
	(SC:AST_L1A.003:2006036889)	18:38:31	148.896	57.371	
	(SC:AST_L1A.003:2006036890)	18:38:40	148.293	57.897	
9-Mar-03	(SC:AST_L1A.003:2014313094)	18:34:25	151.083	48.639	8.567
	(SC:AST_L1A.003:2014313092)	18:34:33	150.586	49.156	
	(SC:AST_L1A.003:2014313124)	18:34:42	150.341	49.561	
	(SC:AST_L1A.003:2014313115)	18:34:51	149.990	49.729	
13-Jan-03	(SC:AST_L1A.003:2010661057)	18:28:51	158.572	33.577	0.005
	(SC:AST_L1A.003:2010661063)	18:29:00	158.236	34.164	
16-Nov-01	(SC:AST_L1A.003:2004978686)	18:25:37	164.178	36.471	-8.557
	(SC:AST_L1A.003:2004978687)	18:25:46	164.123	36.828	
	(SC:AST_L1A.003:2004978691)	18:25:55	163.841	37.162	
	(SC:AST_L1A.003:2004978696)	18:26:04	163.553	37.677	
	(SC:AST_L1A.003:2004978697)	18:26:12	163.257	38.280	
5-May-03	(SC:AST_L1A.003:2013401786)	18:27:59	134.897	68.439	5.709
	(SC:AST_L1A.003:2013401708)	18:28:08	133.250	68.802	
	(SC:AST_L1A.003:2013402014)	18:28:16	132.137	69.029	
12-May-00	**(SC:AST_L1A.003:2006428564)**	**18:43:17**	**141.470**	**72.527**	**8.556**
	(SC:AST_L1A.003:2006428575)	**18:43:25**	**139.790**	**72.916**	
	(SC:AST_L1A.003:2006428582)	**18:43:34**	**137.789**	**73.345**	
21-May-00	(SC:AST_L1A.003:2006582977)	18:37:00	132.450	73.788	0.005
	(SC:AST_L1A.003:2006582981)	18:37:09	131.025	74.018	
	(SC:AST_L1A.003:2006582986)	18:37:18	129.558	74.240	

Visualization Viewer (GloVis) website. A custom set of software tools were designed to process and combine these data into a geographical information system (GIS). In the absence of these tools, scene selection was time-consuming and not easily streamlined for a large study area. An attempt was made to choose scenes based on similar acquisition date and time, low cloud cover, season, solar illumination, and sun angle. Using the VNIR browse images, data were screened based on overall quality and the presence of obvious change that would either mask or alter the spectral information of the geologic surface composition. Some scenes that passed initial screening were later rejected because of poor balance that was produced in the TIR mosaic process and final product.

2.3.2 Strategy for mosaic generation and radiometric balancing

All data were converted from digital number (DN), originally recorded as 16-bit integers, to calibrated thermal radiance (W/m^{-2} sr^{-1} μm^{-1}), and stored as floating-point data. No data loss is expected at the limit of the data's dynamic range and the accuracy level of the TIR instrument. The ASTER scenes were combined into swaths collected during the same orbital path and for which no radiometric normalization was needed. It was necessary to remove two to three pixels at the scene edges because these values were found to be inaccurate. This edge effect was produced during data cubic-convolution resampling during the L1B data production at the LP DAAC. ASTER data are stored in the WGS84 UTM projection and are rotated in the direction of the satellite's orbital path. All data were reprojected to geographic North using a rigorous pixel-by-pixel rotation and resampled using the cubic convolution method. Nearest-neighbor resampling results in less pixel to pixel averaging, but it was not chosen for the rotation step because it caused geometric distortions within the scene at the 90m spatial resolution. This could

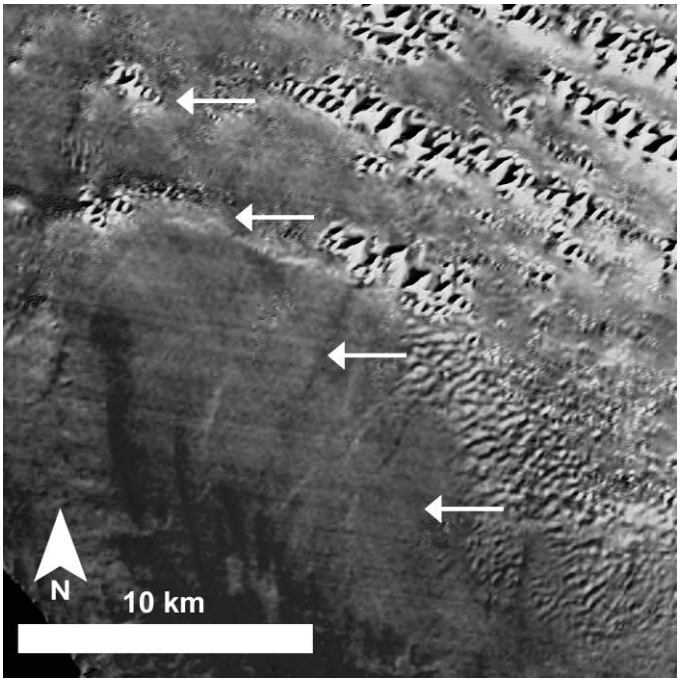

Figure 4. Subtle thermal temperature anomalies which are thermal wind streaks emanating from these star dunes (arrows). Temperature range of 1-2 K is stretched to 0-255 brightness values.

be most easily seen in the shapes of linear features such as coastlines and dune crests, which had discontinuous "saw tooth" patterns following a nearest-neighbor resampling. Small-scale features and dune patterns are not lost with the cubic convolution resampling. For example, subtle ~25 km-long wind streaks emanating from the crests of star dunes in the south-central sand sea are still visible after resampling (Figure 4). The streaks shown are most evident in the radiance mosaic and in the derived temperature image as anomalies of 1 – 2 K, and do not appear in the emissivity product. Because no rotation of data take place, the along track scenes were seamlessly mosaicked using nearest-neighbor resampling because this avoided averaging adjacent image and zero-edge pixel values.

Data from adjacent and overlapping scenes acquired at different times are expected to have different scene conditions with respect to surface temperature, atmospheric conditions, solar illumination and geometry, and instrument noise (Figure 5a). If the differences that occur between pixels that have constant emissivity spectra through time can be approximated by linear functions, the correlation between these areas may be considered to be scale-invariant under a linear transformation (Canty et al. 2004). After some minor georeferencing was applied to correct minor coregistration errors of 1 – 7 pixels of unorthorectified data (RMS > 0.5 pixel), each of the along-track orbital swath images were mosaicked in the cross-track direction to create the seamless product (Figure 5b) using the relative radiometric balancing technique described here.

For two bi-temporal multispectral images with n bands, an image acquired at time t_1 is determined to be of high quality and established as a reference $X_A(i)$. An adjacent image $X_B(i)$ acquired at time t_2 is added to the mosaic after a linear transformation is applied, where $X^*_B(i)$ is the radiometrically normalized image. The gain β and offset α are determined from the linear regression of PIFs for each thermal radiance band i separately. The linear transformation of the first image (B) to the reference image (A) is expressed as:

$$X^*_B(i) = X_B(i) \times \beta(i) + \alpha(i), \quad i = 1 \ldots n. \tag{5}$$

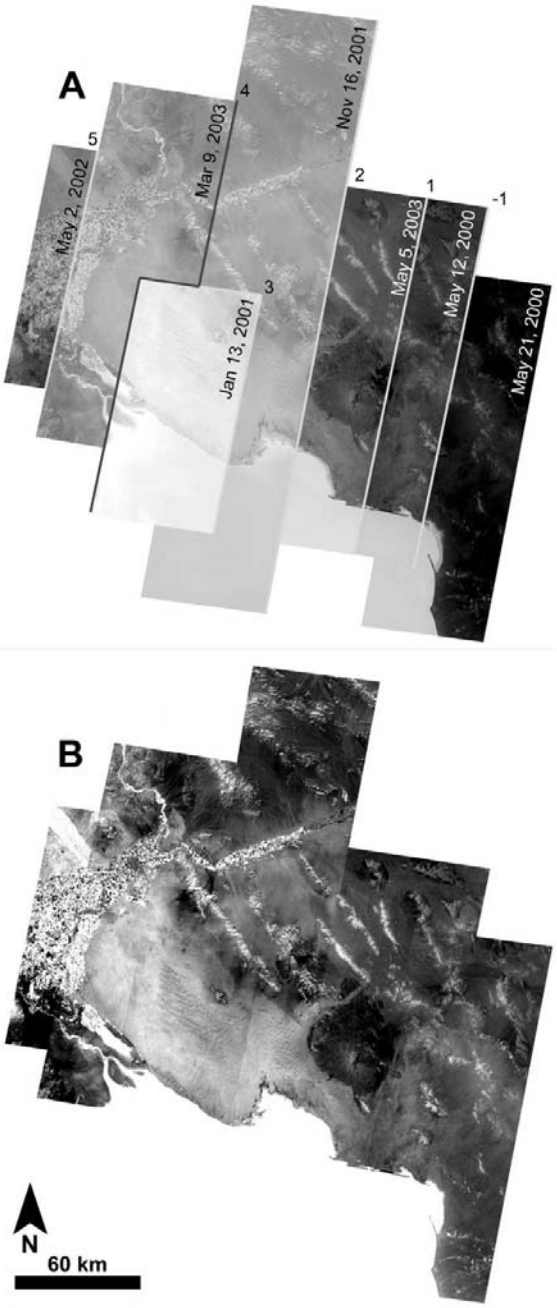

Figure 5. (a) The non-normalized mosaic example of ASTER band 10 (8.29µm) radiance shows the delineations of the mosaicked images. Date of image acquisition and mosaic order are indicated with numbering increasing west (+) or decreasing east (-) with distance from the reference swath. (b) Here the radiometrically normalized mosaic is shown without the final step of blending seam-lines.

In order to effectively determine the correct gain and offset for each band, PIFs were identified by the change in the spectral shape of the land surface between the multispectral images acquired at t_2 and t_1. This is approximated by the correlation ρ_{AB} calculated in radiance space between each overlapping, co-located pixel spectra where n is the number of bands in the multispectral image given by:

$$\rho_{\mathrm{AB}} = \frac{n\sum_{i=1}^{n} X_A(i)X_B(i) - \sum_{i=1}^{n} X_A(i)\sum_{i=1}^{n} X_B(i)}{\sqrt{\left[n\sum_{i=1}^{n} X_A^2(i) - \left(\sum_{i=1}^{n} X_A(i)\right)^2\right]\left[n\sum_{i=1}^{n} X_B^2(i) - \left(\sum_{i=1}^{n} X_B(i)\right)^2\right]}}. \quad (6)$$

The result ranges from -1.0 to 1.0, where 1.0 indicates the greatest possible positive correlation for the pixel and is scale-invariant to a linear transformation in radiance space. The correlation is used to manually set a decision threshold, where in this case $\rho_{AB} < 0.8$ yields pixels assumed not to be PIFs. *Canty et al*. [2004] similarly used scale-invariant MAD components to determine PIFs. If this reasonably excludes change-pixels, the approximate linear relationship between the radiance values of the two images can be determined from the remaining PIFs. Liking to orthogonal linear regression [*Kendal and Stewart* 1979; *Shapiro and Brady* 1995; *Canty et al*. 2004] or principle component analysis (PCA) operating in a multitemporal mode if applied to the same bands on two different dates [*Du et al*. 2002], the major PCA component or the first major eigenvector is determined to describe the positive linear correlation between PIFs of the two images. The gain β and offset α are approximated directly from the projection or slope (s) of the first major eigenvector, where $\mu(i)$ is the mean of the respective thermal radiance band i and $\beta = s^{-1}$:

$$\alpha = \mu_A(i) - \beta(i) \times \mu_B(i). \quad (7)$$

The absolute radiometric accuracy of the normalized images is sacrificed for radiometric coherency of the entire mosaic, but the relative normalization technique should estimate reasonable radiance values with respect to the reference image, especially if the PIFs are selected carefully with a reasonable decision threshold. The choice of the reference image influences the final statistics, but the quality of the final mosaic can be increased with the following assumptions: (1) the reference image is atmospherically corrected and radiometrically accurate, and (2) the mosaic procedure propagates in a direction that does not reduce the variance of the data. The seamless characteristic of the mosaic is an important goal, but may not be possible in

all locations. Reduced, faint seam edges between scenes may still be visible in the mosaic using the method described here because change-pixels, excluded from balancing statistics, are still included in the mosaic. Likewise, any pixel for which non-linear changes have occurred and could not be approximated by the linear transformation will not be normalized and show as residuals. *Du et al.* [2001] addressed remaining seam-lines between images through pixel compositing. Similarly, ASTER data were blended together at seam boundaries across a linear gradient at a specified distance from the seam boundary. At the midpoint of this distance, pixel values represent a mean between each of the overlapping pixels. Seam edge errors that averaged 1.5% at the overlapping edges were blended by 50 – 100 pixels (4.5 – 9 km) to reduce visible discontinuities in the mosaic. A significant seam edge in the northwest portion of the mosaic of the study area was expected between the March 9, 2003 and November 16, 2001 image swaths because sufficient overlap did not exist. Other minor seams of up to 15% radiance were observed in localized areas of the mosaic and will be discussed further.

2.3.3 Emissivity Separation and Extraction

Emissivity was extracted from thermal radiance using the emissivity normalization method (Realmuto, 1990) and an assumed maximum emissivity value of 0.960. Because these data are dominated by silicate minerals, the greatest amount of variance in emissivity spectra for the study area is contained within bands 10, 11, and 12, where the dominate absorption bands are contained [*Vincent and Thomson* 1972; *Clark et al*. 1990; *Salisbury and D'Aria* 1992; T*homson and Salisbury* 1993; *Ramsey and Christiansen* 1998]. The data in this region ranges between 0.7 and 0.96, whereas bands 13 and 14 have a significantly more narrow range (0.9 – 0.96). The emissivity of the land surface is a much smaller fraction of the total emitted radiance than is the temperature in the TIR. However, it is the emissivity that allows for a quantitative interpretation of the surface composition. The emissivity spectra extracted from ASTER TIR compared well with field- and laboratory-based spectra [*Hewson et al.* 2005, *Rowan and Mars* 2003, *Scheidt et al.* 2006], and it is important to preserve the spectral shape of each pixel in order to accurately analyze its composition. However, each band in the image was radiometrically normalized independently, therefore allowing the relative radiometric normalization to change, possibly correct, the emissivity spectra. This is a desired effect because true PIFs acquired at times t_2 and

t_1 should have no difference between emissivity spectra, especially if calculated from similar temperatures determined from normalized radiance values.

2.4 MOSAIC RESULTS

The previous attempts at radiometric normalization of ASTER TIR data using OLS regression analysis, estimation of gain and offsets from image mean μ and standard deviation σ statistics, and PCA to produce a seamless mosaic were similar, but all were less effective than the technique described here. Various approaches resulted in linearly transformed TIR images that had whole-scene differences, seam-lines, and low spectral correlation between cross-track images. The use of a commercial color-balancing tool (a proprietary code) did not work well because non-PIFs could not be masked from the estimation of gain and offsets. The end products generated by this technique described here was both visually compared and quantitatively evaluated with respect to the spatial coherency of data, the correlation between resulting emissivity spectra of co-located pixels, degree of seam boundaries and the quality of the DCS.

2.4.1 Radiometrically-balanced radiance

The complete radiance mosaic showed a good balance between most of the cross-track images as seen by the pre-normalized (Figure 5a) and post-normalized (Figure 5b) example mosaics of band 10. Prior to normalization, the mosaic is unbalanced. Each image swath had a different overall brightness and contrast dominated by temperature with winter month acquisitions having the lowest overall radiance. The mosaic was constructed using different starting reference images to compare how that choice affected the final mosaic by allowing the linear transformations to propagate in different directions. If the January 13, 2003 image with the lowest mean and standard deviation was used as the reference, the result was a similarly lower-brightness, lower-contrast mosaic. Use of the May 21, 2001 with the highest radiance mean and standard deviation resulted in a higher-brightness, higher-contrast mosaic. Even though each

reference image produced these differences, the radiance images had the same correlation between overlapping pixels in radiance space, where the average value of correlation of the radiance image overlap areas are reported in Table 2. The order of image normalization and mosaic construction for the final analysis presented here is specified by the sequential number at the seam boundaries (Figure 5a and Figure 6).

Table 2. The average correlation coefficients, as well as the standard deviation of those values, are reported for each overlap area between radiance images, emissivity before radiometric normalization and emissivity images after normalization. The amount of area affected by the normalization technique is summarized as (a) decreased, (b) slightly decreased or (c) the same and improved.

Overlap Area	Radiance Correlation (ρ_{AB})	Emissivity Correlation		Percent Change in Spatial Area of Correlation		
		Before(ρ_{AB})	After (ρ_{AB})	(a) $\Delta\rho_{AB} < -0.05$	(b) $-0.05 < \Delta\rho_{AB} < 0$	(c) $\Delta\rho_{AB} > 0$
-1	0.955 ± 0.072	0.986 ± 0.027	0.990 ± 0.024	< 1 %	29 %	71 %
1	0.813 ± 0.183	0.816 ± 0.242	0.988 ± 0.029	< 1 %	< 1 %	99 %
2	0.725 ± 0.290	0.989 ± 0.027	0.885 ± 0.313	24 %	59 %	17 %
3	0.982 ± 0.031	0.999 ± 0.002	0.995 ± 0.042	20 %	63 %	17 %
4	0.959 ± 0.111	0.996 ± 0.018	0.944 ± 0.270	6 %	43 %	51 %
5	0.766 ± 0.248	0.901 ± 0.174	0.724 ± 0.478	27 %	19 %	54 %

The spatial distribution of low correlation values ($\boldsymbol{\rho_{AB}}$) are mapped and easily seen in the color-classed image of overlapping image areas (Figure 6a). The Gran Desierto sand sea area is represented by an overall high correlation ($\boldsymbol{\rho_{AB}} > 0.97$) in the overlap areas 2, 3 and 4. Areas of low correlation correspond to areas of frequent land-cover change, such as the Colorado River Valley and delta (bottom of overlap area 5), the vegetated coastal plain south of the Sierra Pinacates volcanic field (bottom of area 1), coastal marsh and estuaries of the Bahia Adair (bottom of area 2), and parts of the Basin and Range mountains and alluvial drainages (top of area 2). Where correlation was greater between overlapping areas, a higher quality of seamlessness was expected. On the eastern side of the mosaic, the May 5, 2003, May 12, 2000 and May 21, 2000 balanced well. On the western side of the mosaic, March 9, 2003, January 13, 2003 and November 16, 2001 also balanced well. An attempt was made to add data from March 28, 2001, but poor balancing with adjacent images resulted, therefore it was excluded. The May 2, 2002 image on the farthest western edge of the mosaic (overlap area 5) also did not mosaic well because of the spatial extent of frequent land cover change, primarily due to agriculture. Only a small area could be specified as an overlap region for May 2, 2002 after masking, which

likely resulted in too few pixel values to accurately estimate the proper gain and offset. Likewise, most of these areas could be considered areas of change. May 2, 2002 was included to show the degree of error, as well as to include the dunes beyond the Colorado River. Inspection of the VNIR shows a higher amount of ephemeral vegetation in areas of poor balance between images, and is a result of diffuse areas of lower correlation in overlapping areas between vegetated and non-vegetated surfaces. This may also the case between the November 16, 2001 and March 5, 2003 (upper portion of overlap areas 2). Other plausible reasons for errors in balancing will be discussed below.

Emissivity contains most of the information on the composition of the land surface, and it is these values that are chosen for more quantitative comparison of before and after results of the radiance normalization technique. The spatial distribution of correlation between co-located emissivity spectra extracted from non-normalized (Figure 6b) and normalized (Figure 6c) radiance is recalculated using equation (2), where band ***i*** is the extracted emissivity. The change in correlation is shown as the difference image Figure 6d). Emissivity without prior radiometric normalization produces a map of emissivity that has obvious seam boundaries with values clearly varying with each whole image acquisition (Figure 7a). Emissivity extracted from normalized radiance is much more balanced and comparable between ASTER data acquisitions of different dates for the land surface area of interest, where water showed extreme differences (Figure 7b). The average correlation before and after normalization for the areas of overlap in the resulting emissivity images show that values increased and decreased depending on the image overlap area (Table 2). Correlation of emissivity did not decrease significantly or improved for much of the area of interest, especially for overlap area 1 and 2 (71% and 99% area, respectively). Correlation decreased in other areas after normalization, but most of these changes in the area of interest were small. A decrease in the average correlation occurred below 0.90 after normalization in overlap areas 2 and 5. This was made obvious by the visible seam-line error. In the upper portion of overlap area 2 where correlation was decreased after normalization, the difference can likely be attributed to the high vegetation noted in the November 16, 2001 VNIR data. The reason for lack of correlation in the upper portion of overlap area 5 is not known, even though this area can easily be classified as exposed sediments and the lower portion of that area is agricultural and frequently changing. Some mountain ranges also show differences at the seam boundaries between November 16, 2001 and May 5, 2003 and are

assumed to be due to differences in primarily sun illumination as well as instrument pointing angle between the two dates. The radiometric normalization does not guarantee correlation of all pixels because some areas will represent true land-cover change, but the lack of correlation may be due to the presence of scan line noise even in correlated areas.

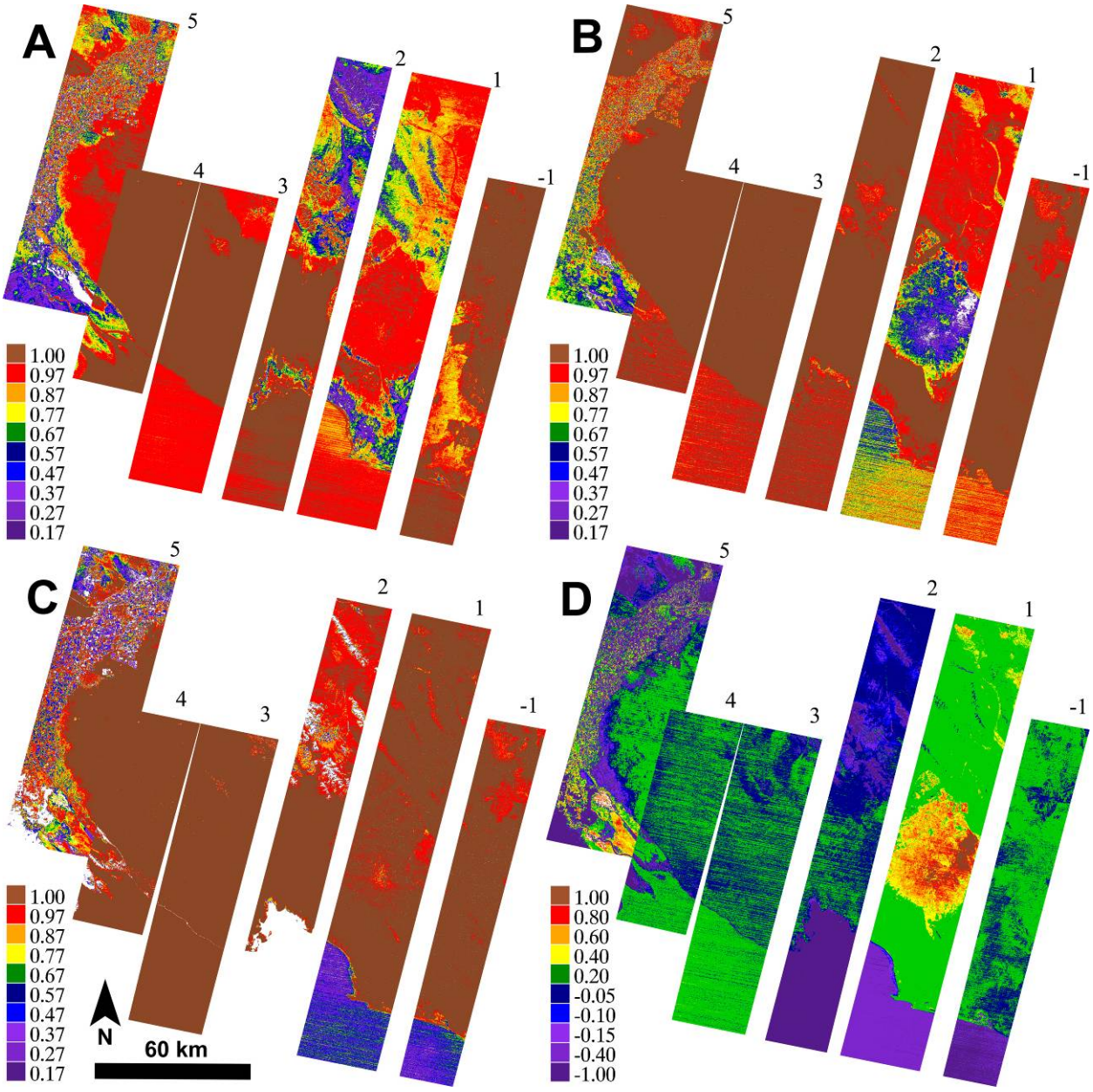

Figure 6. The spatial distribution of correlation coefficients (ρ_{AB}) is shown for areas of overlapping scenes for comparison at different steps of the mosaicking process for (a) non-normalized radiance, (b) emissivity extracted from non-normalized radiance (c) emissivity extracted from the normalized radiance mosaic, and (d) the difference in correlation between a and b.

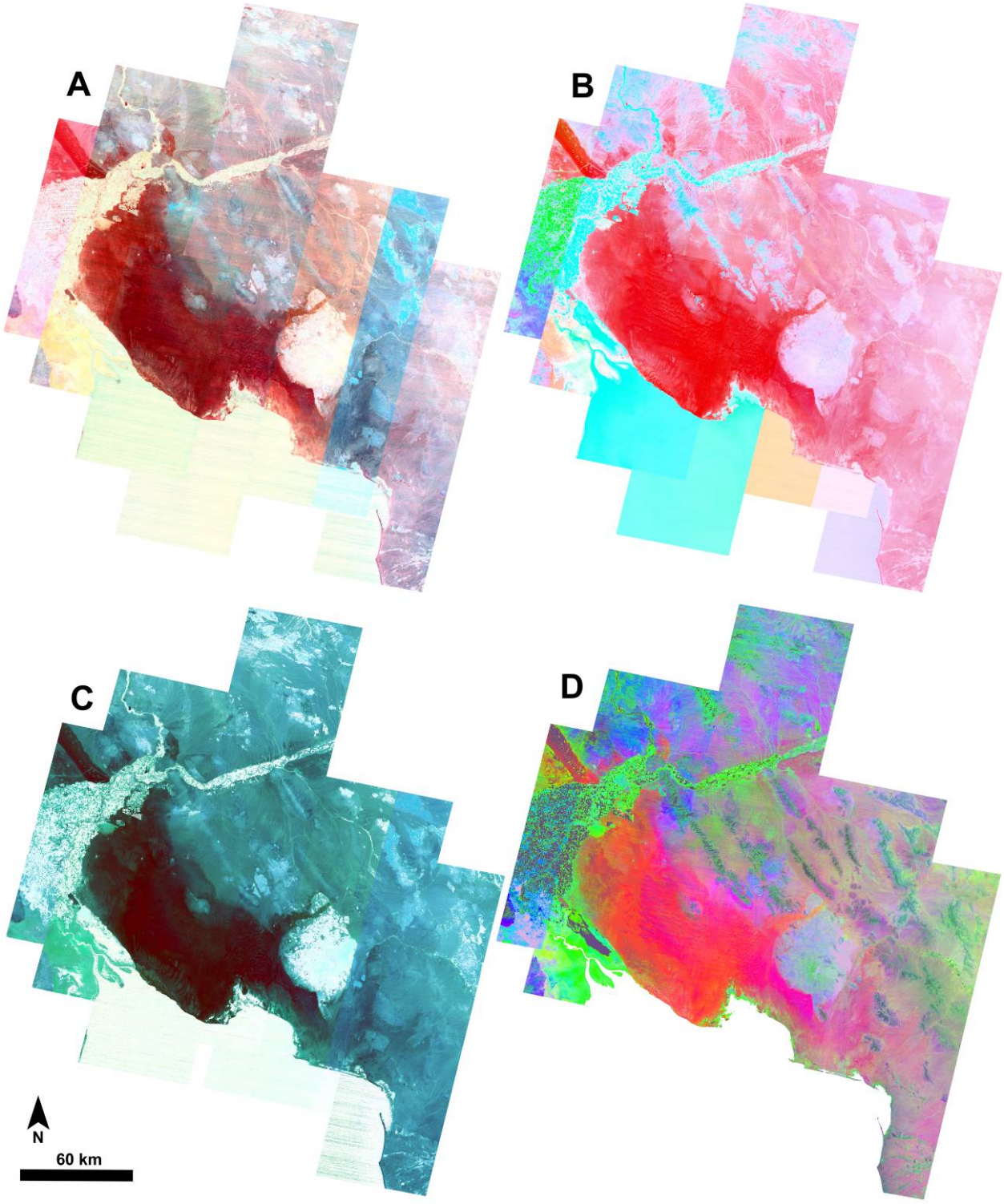

Figure 7. The mosaics of emissivity for ASTER bands 13, 12 and 10 (R,G,B respectively) are shown here for (a) emissivity extracted from the non-normalized mosaic, (b) emissivity extracted from the normalized mosaic, and (c) the non-normalized AST_05 emissivity product. Band 13 is used in the false color composition to show the seam-line errors most prominent in this band. (d) A DCS performed on the mosaic of normalized radiance from the traditionally used ASTER bands 14, 12 and 10 (R,G,B respectively).

2.4.2 Balancing in emissivity space

The linear transformation (equation 1), as well as the other balancing methods mentioned, were also applied to the emissivity data in order to determine if this was an equally effective method. Success was varied, but in general it was found that emissivity data did not mosaic well and seam-line error and poor balance was obvious without first normalizing in radiance space. Jan 13, 2003 and March 9, 2003 images were expected to blend seamlessly, but a seam-line error was present with an average difference of 4%. The linear transformation completely failed in bands 13 and 14, probably because of the low variance in the data for this region, where seam-line error and image-wide differences in average emissivity were apparent between the resulting images. Correlations between values are lower for bands 13 and 14 regardless of the approach, but an improvement in correlation is seen between some overlapping areas in these bands if radiance was normalized before emissivity extraction. Seams were also made evident from persistent scan line noise that has an average difference of less than 1% between adjacent pixels in the image.

The quality of the emissivity mosaic from normalized radiance is comparable to the non-normalized AST_05 emissivity mosaic (Figure 7c). Normalization of the AST_05 was also tested but was not successful. Because this product was generated using a different method of temperature-emissivity separation, the TES algorithm, a direct quantitative comparison is not easily made with emissivity values extracted using emissivity normalization of AST_09T. This is clearly evident by comparing the color contrast of the two mosaics in Figure 7b and Figure 7c. Seam-line error was most apparent again in band 13 for the AST_05 mosaic. Improvement was made at the seam boundary between May 2, 2002 and March 9, 2003 images in the AST_05 mosaic compared to the emissivity extracted from normalized AST_09T radiance. Feathering of most seam edges produced areas with little perceptible error in the sand sea region, but image swaths in the east (acquisition dates May 12 and 21, 2000) had consistent, image-wide average emissivity error of 2 – 3%, and caused undesirable effects on preliminary spectral analysis.

2.4.3 Results of the decorrelation stretch transformation

The DCS [*Gillespie* 1992] is a useful and common spectral analysis technique for TIR data of both Earth and Mars [*Kahle* 1987; *Rowan and Mars* 2003; *Rogers et al*. 2003]. The DCS enhances the color separation of three highly correlated bands chosen from the multispectral data. Emissivity (compositional) variations are shown as color differences, whereas the intensity of those colors relates to the surface brightness temperature. The ideal frequency distribution of input data for a DCS is close to Gaussian, and color separability is reduced with an increasingly multimodal data distribution [*Alley* 1996]. This has significant implications for a DCS of a mosaic that has not been radiometrically normalized. Consistent variations of surface composition in radiance or a DCS of a radiometrically non-normalized mosaic cannot be visualized because large inter-scene color differences result and are much greater than intra-scene color contrast. A DCS was performed on the radiometrically normalized, seam-blended, radiance-at-surface mosaic to examine the large-scale surface compositional diversity, and the results have good potential to aid in the selection of spectral end–members, not limited to a single scene (Figure 7d). For a DCS of these bands and typical interpretation: Red areas correspond to quartz rich material, green to granitic composition, vegetation (locally demarking arroyos in this area) and some volcanic features, and blue to volcanic and mafic outcrops. The DCS resulted in good discrimination of compositional units in the Gran Desierto region and can be compared to those described in *Blount et al.* [1990]. As the spatial extent of a mosaic increases, so does the likelihood of including a number of spectrally distinct materials, which will increase the modal frequency of the data. The usefulness of this visualization method is spatially limited even for a perfectly balanced mosaic of radiance because it enhanced the larger scale spectral differences between major compositional groups. In the case of the Gran Desierto and surrounding region, areas of agriculture, waters of the Gulf of California and the delta of the Colorado River reduced the contrast of the DCS. If these areas were not masked from the stretch statistics, even large-scale differences in surface composition become less evident. The subtle but spectrally distinct variations of small-scale surface units can be further enhanced by creating a DSC stretch for a smaller subset of the mosaic, no longer limited to single scenes or scenes combined in the along-track direction.

2.5 DISCUSSION AND ALGORITHM PERFORMANCE

In all attempts at normalizing and mosaicking radiance and emissivity data, some degree of seam-line error between images resulted. This is ultimately inevitable because rarely do land surfaces remain unchanged, even under short time scales. The sources of potential error in the generation of a radiometrically normalized mosaic of ASTER TIR deserve further discussion. The factors affecting the quality of the resulting mosaic include the spatial extent of overlap between images and sensor coverage and the change in spectral characteristics of the land surface. The technique used for radiometric normalization is also important, especially the selection of PIFs, the masking of change-pixels and the user input on a decision threshold.

Ideally, a radiometric normalization technique would rely on atmospheric correction and the conversion of radiance to standard reflection or emissivity units, and there would be no need for relative normalization using image statistics. The spectral emissivity represents a small fraction of the variance in the emitted thermal radiance collected by the sensor, where the signal is largely a function of brightness temperature. Normalization of emissivity did not work well because variance is generally small in bands 13 and 14 for the observed target materials, and the noise level becomes a greater portion of the calculated emissivity. The linear transformation in radiance space is estimated from data that has a higher SNR and greater variance compared to emissivity. *Kahle and Alley* [1992] found that a change of one degree in temperature was synonymous with an error of 1% emissivity where doing a temperature-emissivity separation [*Kahle and Alley* 1992]. Because temperature is also normalized if normalizing radiance prior to the calculation of emissivity, it is not surprising to find these magnitudes of improvement in the emissivity mosaic. Normalization in radiance space improved the inter-scene balance between most of the images in both radiance and emissivity mosaics, and it did not unreasonably alter emissivity spectra. Preliminary comparisons of emissivity spectra from normalized radiance matched well with laboratory spectra of samples at these locations. The absolute accuracy of the emissivity mosaic may be increased after more rigorous comparisons with ground truth, and a vicarious calibration is applied to the entire mosaic.

Some of the techniques of relative radiometric normalization referenced earlier (simple linear regression, scene statistics, and PCA) produced similar results but with varying degrees of successful balancing. The results described here compared well, although improved, even if

compared to the AST_05 emissivity product mosaic. This relative normalization technique described here shares characteristics emphasized in the MAD technique by Canty et al. (2004), but a comparison of results from this and the MAD technique is needed. This technique relies directly on a threshold of correlation between the raw radiance values of pixels to identify PIFs, whereas *Canty et al.* [2004] rely on a chi-square percentile limit for MAD components. MAD enhances change pixels as much as possible prior to selection of PIFs [*Canty et al.* 2004]. Both techniques rely on a scale-invariant statistic based on physical (spectral) characteristics to determine PIFs. Similarly, the orthogonal components are found by eigendecomposition of the data, but the technique is computationally fast even though each individual, bitemporal band pair at times t_2 and t_1 are handled separately.

The most important part of the relative normalization is the selection of PIFs, but several complicating factors exist due to the variety of scene components and the spectral changes that occur in time. The selection of PIFs by a spectral correlation threshold attempted to remove these complicating factors, which are:

- The amount of ephemeral desert vegetation is time-variant, commonly dry and sparse, but can be a dominating scene component for arid lands even at the 90 m/pixel TIR spatial resolution.
- Seasonal weather patterns (rain and wind) can spatially redistribute soil moisture, resulting in temporally variable thermal inertia for each soil type. (e.g., the coastal zone has a significant tidal range in the Gulf of California, periodically inundating and saturating the ground surface.)
- Where changes in sediment distribution occur, the variable thermal inertia of these materials of different grain size (i.e., fine sand, alluvium and rock) cause variations of emitted thermal radiance in time.
- The illumination in areas of high relief, including mountains and dune topography cause variable brightness temperature through differential heating and shading [*McAtee et al*. 2003]. For example, at the low solar elevation (34º) on January 13, 2003, illumination, perpendicular to the crests of large star dunes, caused heating and shadowing, and resulted in an average brightness temperature difference of 20 °C between opposite dune surfaces. This temperature effect propagated into the radiance mosaic as an intensity difference unrelated to compositional variation.
- The atmosphere, commonly unstable in arid lands, may have local temporal and spatial changes in temperature of the land surface and atmospheric column due to variable winds (i.e.,

wind streaks). These effects are not as apparent after the DCS and emissivity extraction, but may have an effect on radiometric normalization.

The distribution of radiance values would be normally distributed as a single mode for a single land-cover type, but the overlapping area usually contains several spectrally distinct surface compositions, which results in a data distribution that are multimodal. Each mode may also experience a different linear (or non-linear) change in temperature and its spectral characteristics through time. By comparing the radiance values in a scatter plot between two dates (November 16, 2001 and May 5, 2003) for a small image subset of the coastal area (inset), different linear relationships and degrees of correlation can be linked to different spatial areas (Figure 8). The sand sea area in the upper half of the inset, shown by the elliptical cloud of black points and the linear regression line, has a different relationship than data points that correspond to surface water (red) and the inundated coastal marsh sediments and vegetation (green and yellow, respectively). The blue areas on the map correspond to noise surrounding the main data cloud and linear regression of land pixels. A different linear transformation would be needed for each mode (i.e., classification groups) in order to match all pixels, but these modes are rarely distinct and not easily separated. It was found that masking contiguous areas of vegetation and water was not solely accomplished by the radiance decision threshold of ρ_{AB} because water is spectrally similar through time. Including water pixels would negatively affect the linear regression of PIFs because the change in radiance was characterized by a different linear temperature relationship than land pixels. Rock and sand (geologic land-cover) may also have slightly different linear relationships in time due to local surface composition and vegetation changes, and these complicating factors are mixed with other scene components at the ASTER TIR resolution.

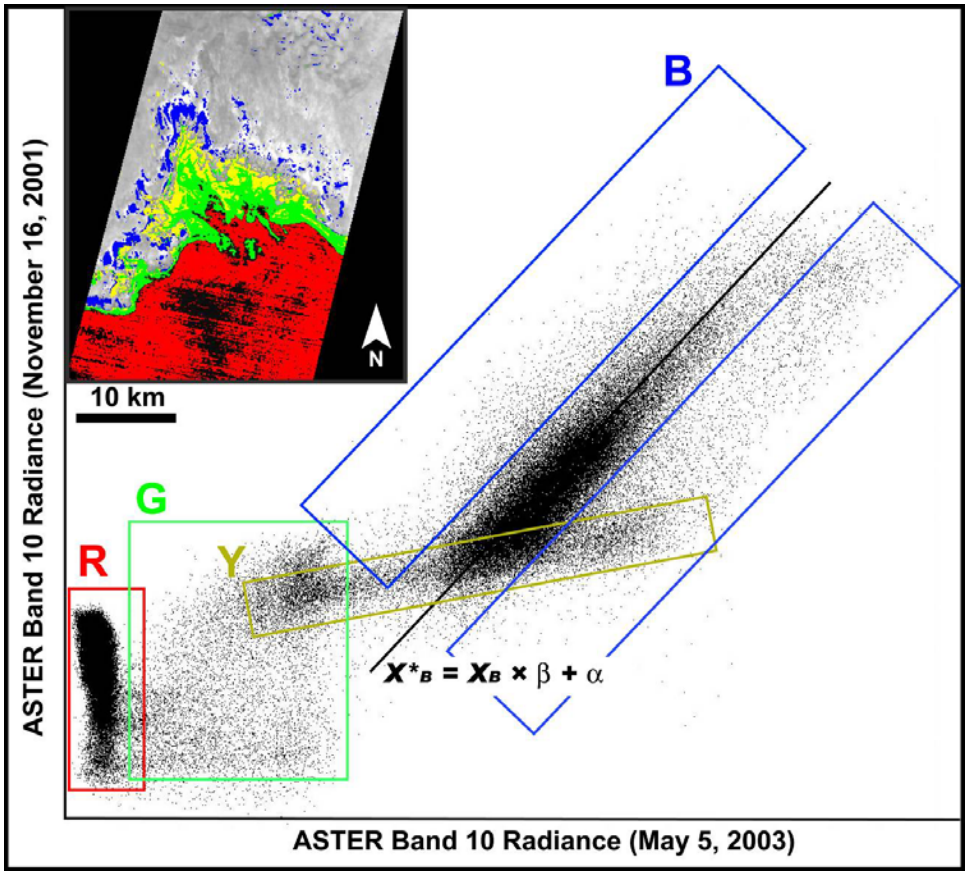

Figure 8. Radiance values are presented in a scatter plot between two dates (November 16, 2001 and May 5, 2003) for a small image subset of the Bahia Adair coastal area (inset). Colored boxes mark data points that correspond to the colored areas of the inset map. The majority of the desert land area in the inset is not colored, and corresponds to the data points that more closely fit the linear regression model.

2.6 CONCLUSIONS

Radiometric balancing of ASTER data in the cross-track direction using the linear transformation methods described above produces acceptable results that can be used to examine the spectral variability and surface composition across a region. The method addresses an over-arching need to compare data that are collected from acquisitions that are not temporally continuous. Although there are limitations to the effectiveness of linear transformations across large distances (e.g., areas of land cover and surface composition change), the method appears to work well within the processing limitations, specifically for this sandy desert. The DCS can be

applied to the normalized cross-track mosaic of radiance as a first order discriminator, even though its effectiveness seems to decrease with increasing spatial area and the diversity of surface materials. However, use of the DCS on the mosaic allows for the identification of possible compositional end-members that exist beyond the boundaries of just one ASTER scene. In addition, the use of the spectral correlation equation used here is a tool that can assess land cover change, such as vegetation, sediment composition and possibly other surface characteristics. Identification of change pixels will help eliminate these areas from normalization, but it will also help to remove these areas from a mosaic where other data in time may be used to fill gaps.

The technique of balancing radiance prior to emissivity extraction produced a more consistent TIR data set on which to perform a regional study of aeolian sediments. The seamless characteristic is a requirement for an effective analysis of possibly narrow, subtle sediment transport pathways that would be masked by non-normalized data and seam-lines between scenes acquired on different dates. This technique should easily be transferable to other regional studies of deserts and sand seas, and will in fact be less cumbersome in regions where water, vegetation, and other temporally/spectrally variable materials are lacking (i.e., the central Sahara). Limitation will be imposed on areas where land surface conditions are highly variable with season, for example, dominant vegetation communities, high relief areas affected by sun illumination geometry, or areas of significant erosion and deposition (fluvial or aeolian). A more thorough interpretation of the patterns of dune sand composition and how they relate to the geologic evolution of the Gran Desierto is beyond the scope of this work. It will be the focus of future work incorporating field and laboratory-based analysis to identify the sand sea's mineralogy using a linear deconvolution algorithm on the final mosaic. The addition of multispectral TIR to previous remote-sensing studies should be highly useful for interpretations of sediment transport and dune dynamics in the Gran Desierto [*Blount et al.* 1990; *Beveridge et al.* 2006) and elsewhere for studies of aeolian history [*Ewing et al*. 2006] and the response of sand seas to climate and sea level change.

3.0 AEOLIAN DYNAMICS AND SEDIMENT MIXING IN THE GRAN DESIERTO, NORTHWESTERN SONORA, MX: AN ANALYSIS OF THERMAL INFRARED SPECTROSCOPY AND MOSAICKED ASTER DATA

3.1 CHAPTER SUMMARY

This work combined the analyses of high resolution thermal infrared emission spectroscopy and mosaicked ASTER TIR remote-sensing data to determine the spatial distribution of sand composition of the Gran Desierto in Sonora, Mexico. These results were compared to the previous models of sand accumulation and sediment distribution, whereby modifications were proposed by replacing the delineations of sand populations with a spatial contiguous mineral map based on the remote-sensing results. Laboratory spectra were grouped into nine spectrally distinct, compositionally variable regions. The most likely end-members as a result of laboratory analysis (depending on region) in decreasing order of average areal abundance were: mono/cryptocrystalline quartz > albite > oligoclase > microcline >> carbonate >> ferrohornblende >> anorthite. The lab spectroscopy drew upon a large line of sand samples collected over several decades from various locations that provided almost complete coverage of the entire sand sea. Additional sand samples were collected in December 2004 and March 2005 that filled some gaps in coverage. Spatial interpolation of laboratory spectra essentially generated a moderate spatial resolution, hyperspectral TIR data cube. This study derived accurate maps of surface composition from interpolated lab results that were directly compared to ASTER retrievals of sand composition. The results agree with the potential sources of sediment described by previous researchers and indicate that the method works well. The limits of precision in these techniques have been thoroughly examined with respect to mosaicked ASTER data and are integrated with laboratory spectroscopy results over a large geographic area for these interpretations. Proper treatment of ASTER data, specifically the correction of

reflected downwelling radiance in areas of quartz-rich dunes that reflect higher radiance in the thermal infrared wavelength region, was shown to improve linear deconvolution results and accuracy of composition retrieval. The analysis results suggest that local sources exert a much greater influence on sand composition as opposed to a model of sand accumulation dominated by quartz-rich, ancestral fluvial-deltaic deposits of the Colorado River. Variation in feldspar content led to a previously uncharacterized source of sand, unique in its higher potassium feldspar content of local source rocks east of the Sierra Pinacate. The significant spatial extent and high average feldspar abundance (21-60%) in aeolian sediments estimated here supports a sand accumulation model that accounts for local feldspathic-rich sand input to most of the dunes at the perimeter of the dune field, especially those of the Sierra del Rosario. In the central portion of the dune field, the gradual compositional transition in the star dunes area is unnoticeable in the field where distinct differences are seen in several remote-sensing datasets and were not previously quantified. The ASTER and laboratory results explained this transition as a gradational 30% change in areal abundance from feldspar with respect to quartz over a distance of 10 km from northeast to southwest across the star dune field. The highest quartz content was found in the western crescentic dunes that transition to star dunes. The southwestern dune field had some samples as high as 90%, and the eastern crescentic dunes averaged ≈ 70% quartz.

3.2 INTRODUCTION

3.2.1 Background

The model of sand accumulation in the El Desierto de Altar (Gran Desierto) in Sonora, Mexico (Figure 9), a large sand sea (>5700 km^2), is described as a system of diverse groups of dunes superimposed on an abandoned channel of the Colorado River, juxtaposed on volcanic and plutonic rocks [*Lancaster* 1992; *Blount et al.* 1990]. This is an important aeolian depositional system wherein a number of possible regional-scale sand transport pathways exist for sources of sediment of varied composition. The sands of the Gran Desierto have been commonly attributed only to the ancestral bed loads of the Colorado River. In general, the hypotheses for the

depositional history of the Gran Desierto range between: 1) continuous accumulation, 2) episodic construction of different groups of dune forms in response to tectonic, climatic and eustatic forcing, and 3) reworking of previously deposited sediment, mostly from the Colorado River. Much work has been completed in the aeolian systems in and near the Gran Desierto region to explain the history of dune emplacement by examining dune morphology [*Lancaster et al.* 1987; *Lancaster* 1992, 1993, 1995; *Ewing* 2007], regional patterns of dune forms and ages [*Beveridge et al.* 2006], ground penetrating radar of bed forms in the nearby Algodones Dunes [*Derickson et al.* 2007] and geochemical and grain-size analysis of sand sources [*Kasper-Zubillaga et al.* 2005; 2007; 2008]. An early interpretation of the Quaternary history of the Gran Desierto was proposed by *Blount and Lancaster* [1990] drawing upon remote-sensing analysis, field work, laboratory reflectance spectroscopy of sand samples and detailed sedimentological analysis of grain composition, size, sorting and surface alteration.

The remote-sensing analysis of Landsat 5 Thematic Mapper (TM) reflectance data [*Blount et al.* 1990] was used to support the current model of sand accumulation, delineations of sand populations and source-to-deposition relationships; however the remote-sensing data are not fully capable or accurate enough to completely support this model. Granite, carbonate and basalt were fractional, spectral end-members that resulted in mineralogical distributions, where other spectral end-members were non-compositional, and included shade, vegetation, active and inactive sand [*Blount et al.* 1990]. These fractional end-members clearly do not mix linearly with mineralogical end-members; therefore the linear unmixing techniques had some complicating factors in the analysis and were not overcome. The basalt end-member was difficult to separate from shade, requiring second order modeling. Carbonate composition was not separated from granite in the mixing model. These are common problems for linear unmixing of data with moderate spectral resolution.

The interpretation of surface mineral composition of dunes from this and other previous studies of dune areas using reflectance data [*Shipman and Adams* 1987; *Paisley et al*. 1991; *Pease et al.* 1999] is limited due to the spectral complications of VNIR remote-sensing and the inability to accurately distinguish many silicate minerals because of their generally featureless spectra in the visible to shortwave-infrared wavelength region (0.45 - 2.35 μm). Nonlinear mixing of reflected energy and particle size effects alter spectral features in this wavelength region [*Hapke* 1981; *Mustard and Pieters* 1988]. Because of these uncertainties, the current

understanding of the Gran Desierto sand populations via reflectance remote-sensing data [*Blount* 1988; *Blount et al.* 1990; *Blount and Lancaster* 1990] remain ambiguous and the need exists to more accurately determine the spatial distribution of mineral composition. This paper describes a more robust quantitative analysis utilizing the advantages of multispectral TIR remote-sensing and spectroscopy.

Figure 9. Location map of the Gran Desierto, Sonora, Mexico (upper map). Patterns of dune types in the Gran Desierto modified after *Lancaster* [1995] using recent, mosaicked ASTER data, expanded in geographic extent (lower map).

The key for the different types of dunes in this figure are:

A- Star dunes superimposed on relict linear dunes [*Beveridge et al.* 2006].
B- Crescentic dunes
- **1,2** Active simple crescentic dunes
- **3** Large relict crescentic dunes, stabilized by vegetation
- **4** Coalescing multiple generations of largely relict crescentic dunes
- **5** Compound/complex crescentic dunes

C- Reversing dunes; active crescentic dunes on margins; stabilized/relict dunes in topographic lows.
D- Linear and parabolic dunes, largely vegetated
E- Sand sheets
- **1** Sparse vegetation, low relief
- **2** Moderate vegetation, 2-3m local relief
- **3** Undifferentiated

(See figure on following page)

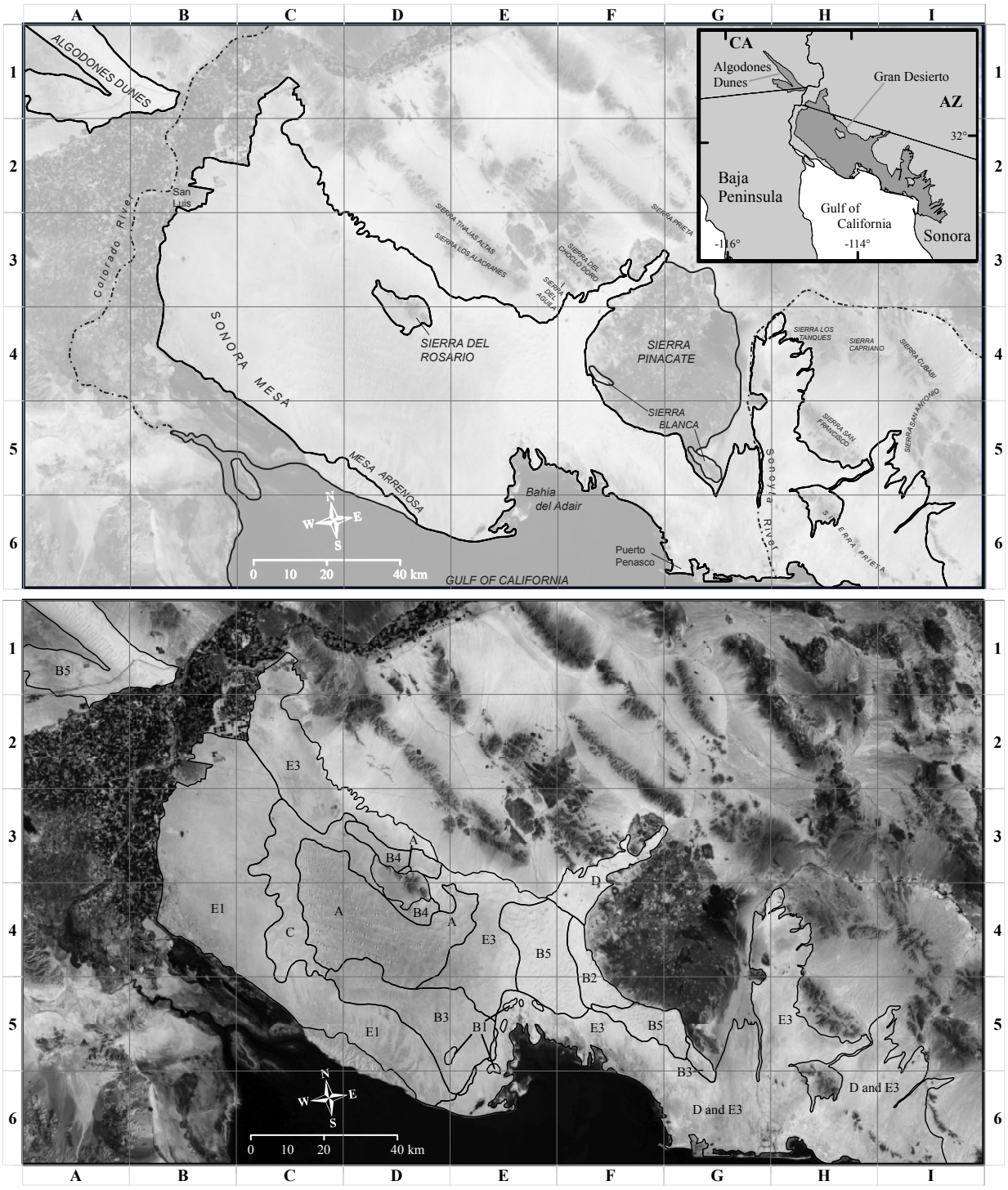

Figure 9. Location map of the Gran Desierto (upper map).
Dune patterns [after Lancaster [1995] (lower map). See previous page for key.

Compositional determination and the detection of major dune forming minerals (e.g., silicates, carbonates and sulfates) are possible because of diagnostic spectral absorption features (Figure 10) and the validity of linear mixing of emitted radiant energy as a function of their abundance [*Thomson and Salisbury* 1993; *Ramsey and Christensen* 1998]. Linear deconvolution of TIR emission spectra has been used as an effective tool for extracting the mineralogical composition of igneous and metamorphic rocks [*Feely and Christensen* 1999], meteorites [*Hamilton et al.* 1997], mafic and ultramafic igneous rocks [*Hamilton and Christensen* 2000], granites [*Ruff* 1998], volcanic rocks [*Wyatt et al*. 2002], feldspars [*Milam et al.* 2004] and glasses [*Byrnes et al*. 2007], among others. Martian surface composition was derived from the Thermal Emission Spectrometer (TES) [*Christensen et al*. 2000; *Christensen et al.* 2001; *Bandfield et al.* 2000; *Hamilton et al.* 2001] and the Thermal Emission Imaging System (THEMIS) [*Bandfield et al.* 2004; *Christensen et al*. 2004; *Hamilton et al.* 2007]. Likewise, airborne TIR remote-sensing observations were used to identify variations in surface composition on Earth from the Thermal Infrared Multispectral Scanner (TIMS) [*Kahle* 1987; *Gillespie* 1992; *Hook et al.* 1994; *Crowley and Hook* 1996; *Ramsey and Fink* 1992], specifically for dune surfaces [*Edgett et al*. 1995; *Ramsey et al*. 1999; *Bandfield et al.* 2002]. The airborne hyperspectral Spatially Enhanced Broadband Array Spectrograph System (SEBASS) instrument has also been used for compositional mapping of carbonate deposits [*Kirkland et al.* 2001].

The Advanced Spaceborne Thermal Emission and Reflection Radiometer (ASTER) instrument has a significant advantage in the remote sensing of Earth's geologic materials because of its high spatial resolution and enhanced multispectral capabilities [*Yamaguchi et al*. 1998]. The ASTER instrument records spectral radiance measurements in the visual-near infrared (VNIR, 0.52 - 0.86 μm), shortwave infrared (SWIR, 0.52 - 0.86 μm) and TIR (8.125 - 11.65 μm) wavelength regions. Detailed compositional mapping can be achieved using the full spectral capabilities of ASTER, where the utilization of the emissivity information in the TIR wavelength region was particular useful in discrimination of quartzose, mafic and granitic rocks and sediments [*Rowan and Mars* 2003] and classes of quartzose lithological units [*Rowan et al.* 2005]. In recent studies, examples of linear spectral deconvolution of ASTER TIR data have been used to map the distribution of surface composition at Meteor Crater, AZ [*Wright and Ramsey* 2006], the changing spatial relationship of playa mineralogy at Soda Playa, CA [*Katra and Lancaster* 2008] and the spatial relationships among different aeolian sand deposits at the

northern Coachella Valley, CA [*Katra et al.* 2009]. Most geologic mapping using ASTER data have been limited to a few scenes, but using mosaic techniques, ASTER data from different dates can be normalized and combined, minimizing difference due to season and atmosphere [*Scheidt et al.* 2008]. ASTER emissivity data have also been averaged over large areas to produce high quality mosaic data [*Hulley et al.* 2008; *Hulley and Hook* 2009]. The effect of mosaicking ASTER TIR data on the accuracy of compositional retrievals using linear deconvolution have not been tested or evaluated, however.

Figure 10. Library emission spectra used as end-members for this study in the linear deconvolution iterations of laboratory thermal emission spectra. The conversion of high resolution end-members to ASTER resolution (5 bands, shown as dotted lines with black points offset by +0.002) results in the loss of important spectral features for several of the end-member spectra (i.e., quartz and feldspar). Spectra shown on the left column of the figure (a-f) were detected in significant abundances from Gran Desierto samples. On the right column, spectra of important arid land and dune forming minerals are shown even though these were either undetectable, had low abundance or were limited to very small geographic areas and therefore deemed unimportant to the regional dune compositional trends in the Gran Desierto.

(See figure on following page)

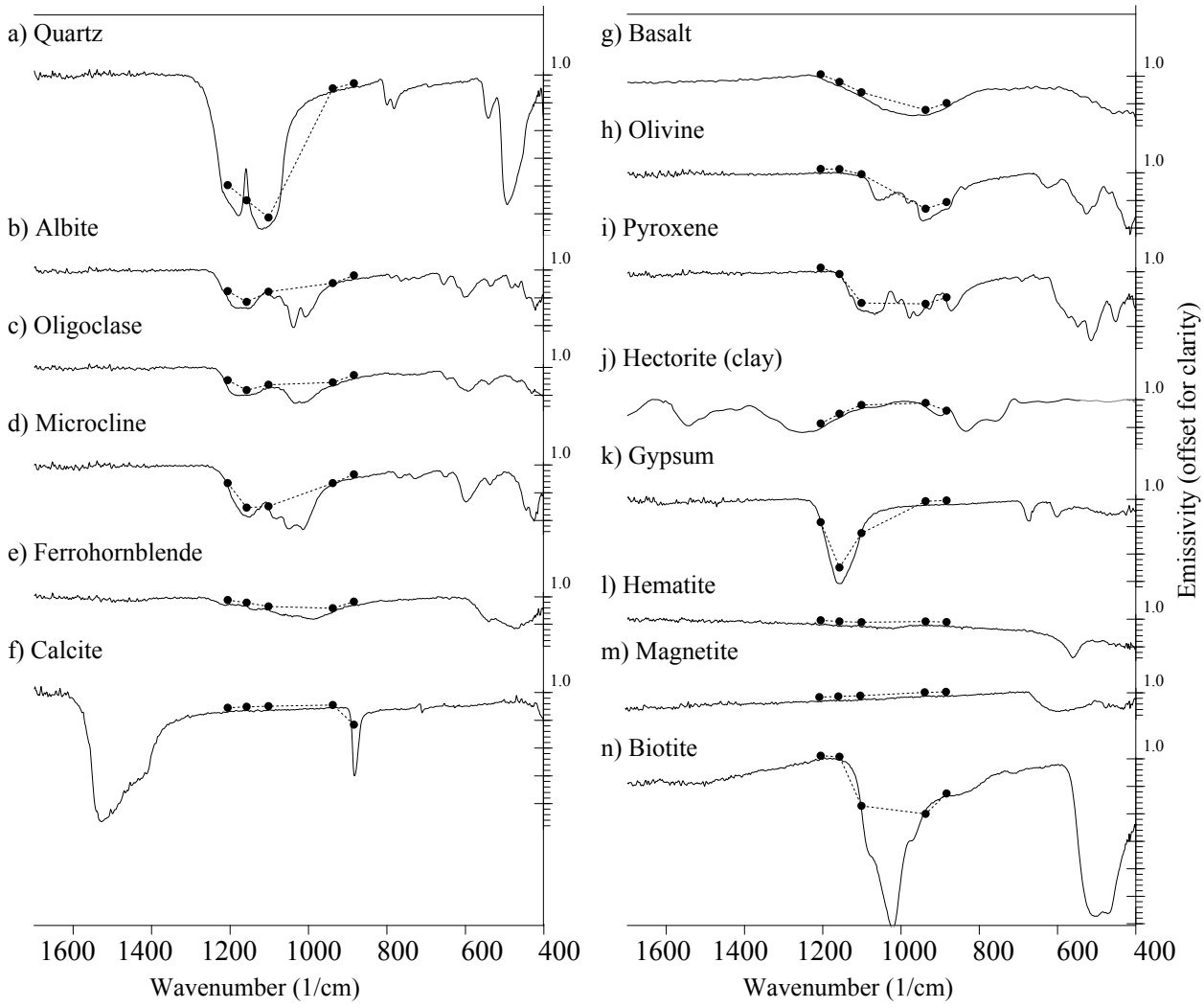

Figure 10. (See figure caption previous page)

3.2.2 Geologic Setting

The physiographic, tectonic and geologic setting of the Gran Desierto dune field has been presented in detail by a number of previous studies [*Blount et al*. 1990; *Blount and Lancaster*, 1990; *Beveridge et al.* 2006; *Kasper-Zubilliga et al.* 2007], but a summary is included here as it pertains to aeolian surface composition and potential sources of sand (Figure 9a). The majority of the dune field is located between the highly cultivated and populated Colorado River Valley to the west, the Basin and Range Provence to the north/northeast and the shores of the Gulf of California to the south. The center of the Gran Desierto is situated atop thick sequences of fluvial-deltaic sediments associated with the ancestral Colorado River, with two-thirds of the area covered by sand sheets, streaks and dunes. The western edge of the dune field is further separated from the Colorado River by a topographic high (z ~100m), the Sonora Mesa, which parallels the Colorado River and Delta. This topographic high was the result of uplift of Colorado River deltaic sediments. It coalesces with the Mesa Arrenosa (z ~ 120m) south along the coast east toward the Bahia del Adair ($z \leq 60$m), and composed of lag gravels and indurated silts and clays that extend underneath the superimposed sand sheets and dune forms. The desert pavement of the western plain is ubiquitous and composed almost entirely of well-rounded chert, epidote and quartzite. The coast is characterized by intermittent playa/sabkha surfaces (especially along the Bahia Del Adair), Pleistocene deltaic deposits [*Colleta and Ortlieb* 1984], raised beaches and coquina. These coastal areas contribute fine quartz sand, carbonate shell hash, gypsum sand and salts as aeolian sediments. The alluvial fans of the Sierra del Rosario, Tinajas Altas, Tule Agua Prieta Mountains and others along the northern edge of the dune field constitute a myriad of source lithologies of volcanic, sedimentary, metamorphic and plutonic origin [*Ortega-Gutiérrez et al.* 1992; *Nourse et al.* 2005], contributing bedloads of quartz, feldspar, biotite and hornblende into the margins of the sand sea. East of the main dune field is the Sierra Pinacate volcanic complex [*May* 1973; *Wood* 1974; *Greeley et al.* 1985; *Lynch and Gutmann* 1990; *Gutmann et al.* 2000], which is dominated by basalts and composed of numerous maar craters, lava flows, cinder and tuff cones. The Pinacate and its alluvial drainages (arroyos) contribute sediments of varied mineralogy as well, including grains of basalt, volcanic glass, olivine, phenocrysts of labradorite and weathering products, such as clays. Embedded and exposed among the Quaternary and Tertiary basalts are older quartzofeldspathic plutons, such as

the Sierra Blanca, and potassium-feldspar-rich trachytes. All of these surrounding rocks are potential source areas for aeolian sediments. There are many groups of dunes and dune forms in the Gran Desierto separated by sand sheets with minor dune forms, commonly stabilized by vegetation (Figure 9b).

Dune groups in the Gran Desierto are hypothesized to be genetically different aeolian accumulations separated by supersurfaces, which represent periods of dune stabilization and are stratigraphic boundaries between sand populations of different age, composition and/or periods of aeolian activity [*Lancaster* 1992]. The major groups of dunes are: (1) a central core of star dunes arranged in a linear pattern, recently described in *Beveridge et al.* [2006] as star dunes superimposed on relict linear dunes, (2) western crescentic dunes that onlap the sand sheets and desert pavement to the west, (3) longitudinal dunes that extend through a narrow passage between the Sierra Pinacate and the Basin and Range, (4) coastal parabolic dunes along the coast of the Bahia del Adair, (5) degraded crescentic dunes southeast of the central star dune complex, and (6) eastern crescentic dunes north of the Bahia Del Adair that wrap around the eastern and southern margins of the Sierra Pinacate. A summary of the grain size, grain sorting, texture and color of the major dune groups is found in previous studies [*Blount and Lancaster* 1990; *Blount et al.* 1990; *Lancaster* 1992]. The aeolian system extends further northwest and southwest around the perimeter of the Sierra Pinacate, consisting mostly of vegetated linear and parabolic dunes. These dune groups have largely been ignored in most prior studies of the Gran Desierto. The crests of these dunes are oriented in the northeast direction and terminate against the alluvial fans of the Tulles Mountains and the Sierra Pinacate. A detailed delineation of dune types in the central area of the Gran Desierto is shown here modified to also include these dune areas that extend out of the main dune field (Figure 9b, modified after *Lancaster* [1995]).

The large Sierra Pinacate volcanic complex (~1800 km^2) has been previously described as a topographic barrier defining the eastern limit of the dune field [*Blount et al.* 1990], but a group of crescentic dunes extends in coverage eastward to the Sierra Blanca (the "white mountain range") abutting the entire southern flank of the Sierra Pinacate. Between this group of dunes and the Puerto Peñasco coastline is a sand sheet with various coppice, parabolic and northeast-oriented linear dunes, which are mostly stabilized by vegetation and indurated with a surface crust. Active dune forms are present but are not as large in height or aspect ratio as the main dune groups, where these aeolian deposits extend to the eastern side of the Sierra Pinacate

along the ephemeral Sonoyta River and as far north as the Sierra Los Tanques. The coverage of these linear and parabolic dune groups includes an area that extends further than 120 km south from the Sierra Blanca at the southern end of the Sierra Pinacate to the Sierra el Alamo. All along the coastal plain, these dunes are visible with dune crests perpendicular to the northeast and eastern coasts of the Gulf of California, oriented in a general northeasterly direction from the coast extending landward to the base of alluvial fans that are further inland.

3.2.3 Approach

The main goal of this study was to use a combination of ASTER TIR remote-sensing data and laboratory TIR spectroscopy measurements to quantify and refine interpretations of surface compositional patterns of aeolian surface sand composition in the Gran Desierto. In order to accomplish this, several field campaigns provided a group of regionally and compositionally diverse sand samples for high resolution thermal emission lab spectroscopy measurements that were used to directly retrieve composition using spectral linear unmixing methods. The lab spectra were also used for a detailed, systematic analysis of composition and a comparison to satellite-retrievals of composition. The satellite data used were extracted from a seamless, multispectral, radiometrically balanced mosaic of the Gran Desierto [*Scheidt et al.* 2006; 2008]. (See Chapter 2.) Various transformations of thermal radiance were generated from the ASTER TIR image data, such as principle component analysis (PCA) and a decorrelation stretch (DCS) to examine spatial spectral variability. In-situ field observations, initial a-priori knowledge of composition and a thorough analysis of lab spectra (used for composition retrievals) served as the "ground truth" and as a basis for the selection of the end-members for the linear deconvolution of the ASTER TIR mosaic. The comparisons of high resolution laboratory data to satellite data were a secondary, but important goal of the work. This is critical information as the spectral data are significantly degraded at ASTER TIR spectral resolution, where some spectral information is lost using remote-sensing measurements. This is also important because it affects the accuracy and confidence of using ASTER satellite data alone in other regions and in areas with no samples for ground truth. The spatial continuity of mosaicked ASTER TIR data, although of lower spectral resolution than laboratory data, validates the spatial patterns interpolated between point source data from samples. Remote-sensing can also characterize the

distribution of surface materials on a different spatial and spectral scale, where the sampling of sand excludes surface materials in abundance at the 90m scale. Ultimately, the goal of this work is to compare these results to previous studies and hypotheses of depositional history, sand populations, regional transport pathways and source lithology.

3.3 LABORATORY SPECTROSCOPY OF SAND SAMPLES

3.3.1 Sample Collection and Analysis

Sand samples were collected by previous researchers [*Blount et al*,. 1990; *Lancaster* 1995] and archived at the Desert Research Institute (DRI) along with a database of grain size and sorting. Surface sand samples were selected from this archive for 203 different locations throughout the Gran Desierto. The geographic coordinates of these samples were determined by examining a combination of field maps, Landsat data and aerial photography within the accuracy of ASTER TIR data (90m). Another recent set of sand samples were collected from 76 additional locations during field campaigns in December 2004 and March 2005, which were accurately geolocated using a real-time differential global position system (GPS) (± 2 meters). The selection of these 2004 and 2005 sampling locations was based on several image products that were generated from Landsat and ASTER that characterized spectral variability of the sands. For example, the color variations of the DCS of mosaicked ASTER TIR data [*Scheidt et al.* 2006; 2008] were used as a guide to locate potential sample locations prior to field campaigns. Sand samples were collected from the upper surface of dunes (< 5mm depth), but some compositionally unique samples of sand and other materials were also collected to characterize local variability in composition, such as playa sediments, alluvial fan and outcrops of volcanic and granitic rock. Each sand sample represents a point measurement of surface composition at the sub-pixel scale of the ASTER satellite.

3.3.2 Laboratory Methods

Thermal emission spectra of all sand samples were measured at the University of Pittsburgh Image Visualization and Infrared Spectroscopy (IVIS) facility using a Nicolet Nexus 670 instrument. The samples were acquired at a 2 cm^{-1} wavenumber spectral resolution between 2000 and 400 wavenumber (≈ 5-25 μm wavelength). A detailed description of the instrument and setup are found in *Ruff et al.* [1997]. Sand samples were put in copper cups and heated in a temperature controlled oven for a period of 24 hours to 80º C. Each copper cup containing the sand sample was placed on a controlled heating stage within a sealed chamber, which is purged with nitrogen gas minimizing the spectral effects from carbon dioxide and water vapor during spectral measurement. Because the cup was actively heated and temperature was regulated at 80º C, temperature remains constant. The surface of the sand sample was scanned by the spectrometer (n = 512 scans) over a period of approximately five minutes per sample. These scans were subsequently averaged to reduce instrument measurement noise. The field of view of the instrument was approximately 2 cm in diameter at the sediment surface. Blackbodies at 70º and 100º C were used before and during laboratory sessions, and the acquired raw radiance data were then processed to emissivity spectra [*Ruff et al*. 1997]. A blackbody is an object (in this case a custom-designed, temperature-regulated conical cavity painted with a flat black paint) that absorbs all electromagnetic radiation incident upon it with little to no transmission or reflection, and it emits a temperature-dependent spectrum of electromagnetic energy. In this case, the peak energy was in the thermal infrared wavelength region.

The bulk mineralogy of the sand samples was determined by using a linear deconvolution algorithm, which models emissivity spectra as linear mixtures of pure spectral end-members. The best fit between the measured and modeled spectra was achieved by a Chi-square minimization. The spectral end-members from a library of chosen minerals combine in proportion to their areal fractions [*Ramsey and Christensen* 1998; *Ramsey et al.* 1999]:

$$\varepsilon(\lambda)_i \sum_{i=1}^{n} f_i \varepsilon(\lambda)_i + r(\lambda)_i; \qquad \sum_{i=1}^{n} f_i = 1.0 \tag{8}$$

where ε is the emissivity value of end-member i at a specific wavelength λ, f_i is the areal fraction of the end-member, n is the number of end-members and r is the residual error. The sum of the fractional abundances of the end-members was constrained to unity.

Because of the extensive size of the dune field and the number of variable source lithologies in the area, theoretically, a significantly large spectral library could be needed to explain sample compositions. An end-member library of minerals was chosen from the ASU TES library [*Christensen et al.* 2000] and the IVIS lab [*Scheidt*, unpublished data]. Several iterations of linear deconvolution were conducted, beginning with the entire combined ASU and IVIS spectral libraries. End-member that are not in significant quantities in Gran Desierto sands were eliminated in successive iterations, after which only 32 end-members were identified in linear deconvolution. For example, gypsum is an important constituent in sediments from the Bahia Adair playas, but this was limited to one laboratory sample spectrum and located in very limited areas in the ASTER data. The final selection was indicative of typical dune sediments and the field observations of composition in the Gran Desierto dunes and major surrounding source areas (Figure 10). Spectra on the left (Figure 10a-f) were significant end-member fractions found in Gran Desierto samples; spectra on the right (Figure 10g-n) were either non-detectable or significantly limited in geographic coverage. Ultimately, only a few possible end-members exist in significant abundance for all the sand samples. Even though the lab data have the spectral resolution to detect minor constituents, the accuracy of the laboratory spectra deconvolution is generally accurate for end-members that are greater than 5% in abundance [*Ramsey and Christensen* 1998, and others]. A blackbody was included as an end-member in deconvolution iterations because it allows for differences between the spectral contrast of library end-members and the sample's spectrum. Theoretically, no mineralogical information should be associated with the resulting blackbody abundance; therefore the blackbody percentage is normalized among the other fractional abundances [*Hamilton et al*. 1997]. The accuracy of modeling the mineralogy of a mineral mixture using linear deconvolution in this way is known empirically and varies between studies [*Ramsey and Christensen* 1998; *Feely and Christensen* 1999; *Wyatt et al.* 2001]. *Thomson and Salisbury* [1993] modeled fractional abundances of mineral mixtures within an accuracy of 5-12%; *Hamilton et al*. [1997] determined plagioclase content to within 5-10%; and Ramsey et al [1999] determined mineralogical abundances of dune sediments to within 3.1% where compared to point counts of sand samples of the Kelso Dunes.

Including minor accessory minerals less than 5% abundance should be avoided due to the modeling of noise in emissivity and these accuracy assessments [*Ramsey and Christensen* 1998]. With successful and correct linear deconvolution, the end-member fractions sum to unity, and the root mean square (RMS) error will approximately equal the RMS noise of the spectra. Fractional end-member amounts are reported as percentages between 0 and 100%.

3.3.3 Laboratory Spectra Results

The analysis results describe the components, composition and spatial distribution of sand deposition in the Gran Desierto. These results are separated into examining the spectral characteristics of different regions of the dune field (section 3.3.4), and the spatial distribution of composition determined from these laboratory spectra (section 3.3.5). Because of the significant number of samples and broad geographic coverage, the distribution of composition can be uniquely examined from spatial interpolations of the composition retrievals. All map locations are referred to by citing the Figure maps and the reference grid block(s); for example, the location of the Algodones Dunes is Figure 9a, block A1.

3.3.4 Spectral Variation of Gran Desierto Sands

Several sets of data and types of analyses were used to evaluate the spectral variation of aeolian sediments, which ultimately leads to the conclusion that distinguishing separate sand populations becomes very difficult. This difficulty arises from the nature of aeolian processes, which affect the physical redistribution of sediments by wind (i.e., deflation, winnowing, variable transport rate and direction) and variable resistance to physical weathering (i.e., high resistance for quartz vs. low for carbonate). This result is a scenario whereby adjacent sand populations do not always have distinct contacts such as those found in other sedimentary depositional environments or rock outcrops. Where variable materials exist, composition may vary across a single dune and with depth. For example, trenching in the dunes situated between the alluvial fans of the Sierra del Rosario and Sierra los Alacranes revealed alternating layers of light grains (quartzofeldspathic, 3-40mm thick) and dark grains (mafic minerals such as hornblende, biotite or magnetite, 1-3mm thick). Likewise, field observations from this and other studies observed

the mantling of granitic grus and feldspar grains atop the finer-grained, sediment surface [*Blount et al*. 1990; *Blount and Lancaster* 1990]. Coarse grains of feldspar (1-2mm diameter) were observed saltating between dunes in isolated patches in the Rosario dune area, and basaltic grains (0.5-1mm diameter) were found in a similar distribution in the crescentic dunes south of the Sierra Pinacate. In summary, significant local compositional variation exists below the spatial sampling interval of the laboratory samples and the spatial resolution of the ASTER data. Considering this local variation, a summary of laboratory spectra (Figure 11) and compositional retrievals (Table 3) of the samples were grouped into nine different regions. For each set, sample spectra are averaged to show a single spectrum as a black line, where the gray area above and below show the range of spectra variation for each set (Figure 11). All composition retrievals are shown as averages with upper and lower limits of their range (Table 3).

Figure 11. Laboratory thermal emission spectroscopy results from Gran Desierto samples displayed here as average spectra (solid black line) by geographic regions. The range of upper and lower limits of averaged emissivity is shown to examine the spectral variability of the samples (gray zone). Spectra were modeled successfully using the chosen end-member suite (average RMS error <0.007). Residuals can be seen where the average modeled spectra (dotted line) deviate from the averaged spectra. Refer to Table 3 for composition retrievals.

(See figure on following page)

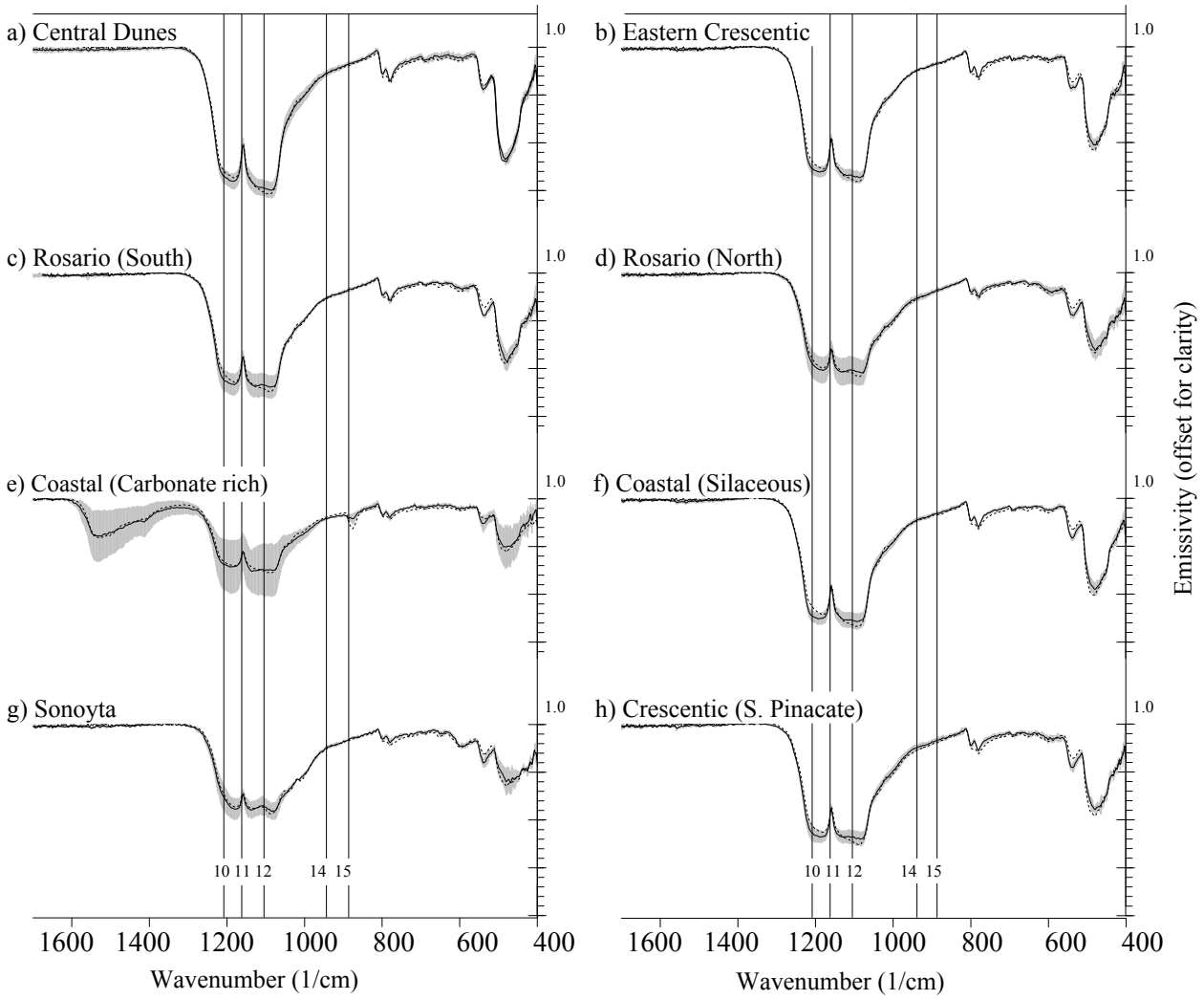

Figure 11. Spectral results for Gran Desierto sands.
(See caption on previous page.)

Table 3. Compositional Retrievals from Laboratory Spectra for Different Desierto Regions

Region	**Qt**	**Ft**	Fn	Fk	Albite	Olig.	An	Anorth.	**Lt**	CO_3	Ferro.	Lv	Iron	RMS
Central Dunes [n = 11]	**74 ± 5%**	**21 ± 4%**	21 ± 4%	--	16 ± 9%	5 ± 7%	D	--	**4 ± 3%**	--	4 ± 3%	--	--	0.0075
Eastern Crescentic [n = 9]	**68 ± 4%**	**29 ± 5%**	29 ± 6%	D	20 ± 11%	9 ± 8%	--	--	**2 ± 2%**	D	D	D	D	0.0073
Rosario (South) [n = 11]	**57 ± 8%**	**39 ± 8%**	36 ± 11%	3 ± 6%	22 ± 10%	13 ± 15%	--	--	**5 ± 4%**	D	D	2 ± 3%	D	0.0067
Rosario (North) [n = 23]	**44 ± 8%**	**45 ± 10%**	37 ± 13%	3 ± 6%	20 ± 11%	14 ± 14%	2 ± 5%	5 ± 11%	**11 ± 9%**	D	8 ± 7%	3 ± 3	D	0.0065
Coastal (CO_3 rich) [n = 7]	**38 ± 15%**	**26 ± 8%**	23 ± 9%	3 ± 8%	8 ± 12%	8 ± 11%	7 ± 9%	--	**36 ± 21%**	31 ± 22%	4 ± 7%	D	--	0.0067
Coastal (Siliceous) [n = 10]	**67 ± 5%**	**32 ± 3%**	32 ± 3%	--	22 ± 13%	9 ± 12%	--	--	**2 ± 3%**	D	D	D	--	0.0070
Sonoyta [n = 4]	**36 ± 7%**	**59 ± 6%**	40 ± 12%	19 ± 16%	16 ± 11%	19 ± 7%	4 ± 5%	--	**5 ± 2%**	--	4 ± 1	D	--	0.0058
Northern Pinacate [n = 4]	**53 ± 11%**	**41 ± 11%**	34 ± 8%	--	20 ± 16%	12 ± 12%	3 ± 6%	7 ± 13%	**6 ± 4%**	--	5 ± 4%	D	--	0.0079
Crescentic (S. Pinacate) [n = 5]	**53 ± 5%**	**41 ± 5%**	32 ± 4%	9 ± 7%	18 ± 6%	12 ± 3%	2 ± 5%	--	**6 ± 5%**	--	6 ± 5%	D	--	0.0058

D = detection reported only; average values is < 2%. Qt = Total Quartz; Ft = Total Feldspar; Fn = Na-Feldspar; Fk = K-Feldspar; Olig.= Oligoclase; An = Anorthite; Anorth. = anorthoclase; Lt = Total Lithics; CO3 = Total Carbonate Minerals; Ferro. = Ferrohornblende; Lv = Volcanic Lithics; Iron = Hematite; RMS = root-mean-squared.

3.3.4.1 Spectra of Quartz-rich Areas

The two main areas of dunes in the Gran Desierto [*Lancaster et al.* 1987], the Eastern Crescentic (Figure 9b, block E/F4) and the Central Dunes (Figure 9b, block 4C), have the highest quartz content retrievals found among the Gran Desierto samples. Quartz concentration is slightly higher for the Central Dunes (74%) than the Eastern Crescentic group (68%). Total feldspar (Ft) is higher than assumed by previous researchers and other results of point counts, and the feldspar content (according to these spectral results) is composed mostly of sodium feldspar (Fn) compared to potassium feldspar (Fk). The concentration of total lithics (Lt) for these samples is also low, where ferrohornblende was detected in small amounts for the Central Dunes (~3-7%) and a variety of lithics were detectable (but not in significant quantity) for the Eastern Crescentic dune area. These spectra have the greatest spectral contrast (as low as ε = 0.68) because of their high quartz content. The range of emissivity between samples is small in these spectra (Figure 11a and Figure 11b), resulting in a low range of variable compositions (Table 3, rows 1 and 2). The modeled spectra (shown as a dotted line) fit well to the measured spectra. An obvious residual error is seen at the main emissivity minima (9.1 μm or 1101 cm^{-1}) where the model spectra are roughly 1-2% lower. The quartz spectral library end-member has a steeper feature at 9.1 μm (Figure 10a), where this feature is shallower in Gran Desierto spectra. Though the composition retrievals are consistent with the observation of past researchers for quartz rich sediments, some differences are noteworthy. Central star dunes and western reversing dunes (Central Dunes group) are described as having a light brown to reddish-yellow coloration resulting from iron oxide coating [*Blount and Lancaster* 1990]; however, spectral deconvolution of laboratory spectra do not detect hematite consistently for these samples or others collected in the degraded crescentic dune area (Figure 9b, block D5). Eastern crescentic dunes were described as having a pinkish-gray to very pale brown coloration resulting from minor amounts of carbonate and labradorite. Labradorite was not detected.

3.3.4.2 Spectra from the Sierra del Rosario

The average quartz concentration decreases (~49-65%) and total feldspar increases (~31-47%) with distance from the central star dune area to the dunes south of the granitic Sierra del Rosario where aeolian sediments are more commonly admixed with granitic grus originating

from local sources (Figure 11c). Compared to quartz-rich samples, the emissivity spectra are shallower, and the quartz doublet centered at 9.1 μm is broader with increasing feldspar content, mostly Fn, although Fk is now detectable as high as 9%. Lithic concentration (Lt) also becomes slightly higher and additional detections of volcanic grains (Lv) appear, which is reasonable because of the closer proximity to volcanic outcrops in the Basin and Range. Dark green crystals were observed in alluvial fan sediments in these areas, which are most likely volcanic minerals. If composition retrievals from dunes between the Sierra del Rosario and the alluvial fans of the Basin and Range (Figure 11d) are compared to dunes south of the Sierra del Rosario (Figure 11c), the samples north of the Rosario are clearly more influenced by local sources as quartz decreases (~36-52%), feldspar increases (~35-55%) and Lt increases and becomes more variable (2-20%). Visual inspection of these dune sand samples also revealed a higher abundance of dark mafic grains. According to the composition retrievals, most of this is ferrohornblende, a reasonable result considering the proximity to granitic and metamorphic local sources. A small increase in Lv is noted, and this area also has the greatest variability in feldspar end-members with a small percentage being calcium feldspar (An, 0-7%).

3.3.4.3 The Bimodal Coastal Sediment Source

A significant amount of spectral variability was found in the samples collected along the coast of the Gran Desierto (Figure 11e and Figure 11f). These groups of samples were collected from dunes around the perimeter of Bahia del Adair, which also have a significant amount of variability in dune geomorphology (Figure 9b, blocks E5, E6 and F5). In this area, an extensive vegetated sand sheet with coppice, linear and a few star dunes is punctuated by smaller units of active quartz-rich simple crescentic dunes that appear to have migrated in a northerly direction. This area is further complicated by vegetated marshy coves and inlets, eroded marine paleosols, sabkhas and evaporite-rich playas. One laboratory sample retrieval indicated the presence of gypsum sand grains (~44%), and the most likely source is from gypsiferous playas detected by the ASTER data (gypsum abundance ~ 100%). Because of the very low strength of gypsum, gypsum is not a significant component of Gran Desierto sands. Shell hash (very small < 1 mm diameter) was easily and frequently seen in sand samples collected from this area. Some samples from this region had carbonate retrievals of 9-53% and showed significant variation in the carbonate feature (6.57 μm or 1520 cm^{-1}, Figure 11e). Other samples contained little to no

carbonate, had high quartz concentrations (62%-72%) and an average feldspar content (~30%). Other types of lithics were detectable, but in very low total quantity, unlike those of the samples closer to alluvial fans in the north. These results suggest a bimodal coastal sediment source which includes first, a biogenic carbonate-rich sediment source, probably from shallow-water sediments. The second source is siliceous sand possibly originating from quartz-rich neritic sands from the beach ridges along the Gulf of California. These quartz-rich beach ridges were clearly visible and distinguishable from DCS transformations of ASTER data. The amount of carbonate winnowed out of sand increases with distance from the coast. This is seen in both the decrease in carbonate spectral features and the composition of samples along a transect from the coast of the Bahia del Adair to the Sierra Pinacate (Figure 12). This transect is located at the boundary between the vegetated sand sheet and the crescentic dunes south of the Pinacate, where over a distance of 2 km, carbonate concentration reduced from 30% to 4% in the northeast direction (from Figure 12a to Figure 12d). In the crescentic dunes 5 km inland from the sand sheet, carbonate was not detectable by the linear deconvolution (Figure 12e).

Figure 12. Carbonate winnows out of Desierto sands with transport distance from coastal source and is expressed by the change in carbonate features of samples along a transect that crosses the boundary between E1 to B5 dune types in the area south of the Sierra Pinacate (location not shown). Each pie chart shows the relative portions of total quartz, Na-feldspar, K-feldspar, carbonate and the total of all other lithic grains.

(See figure on following page)

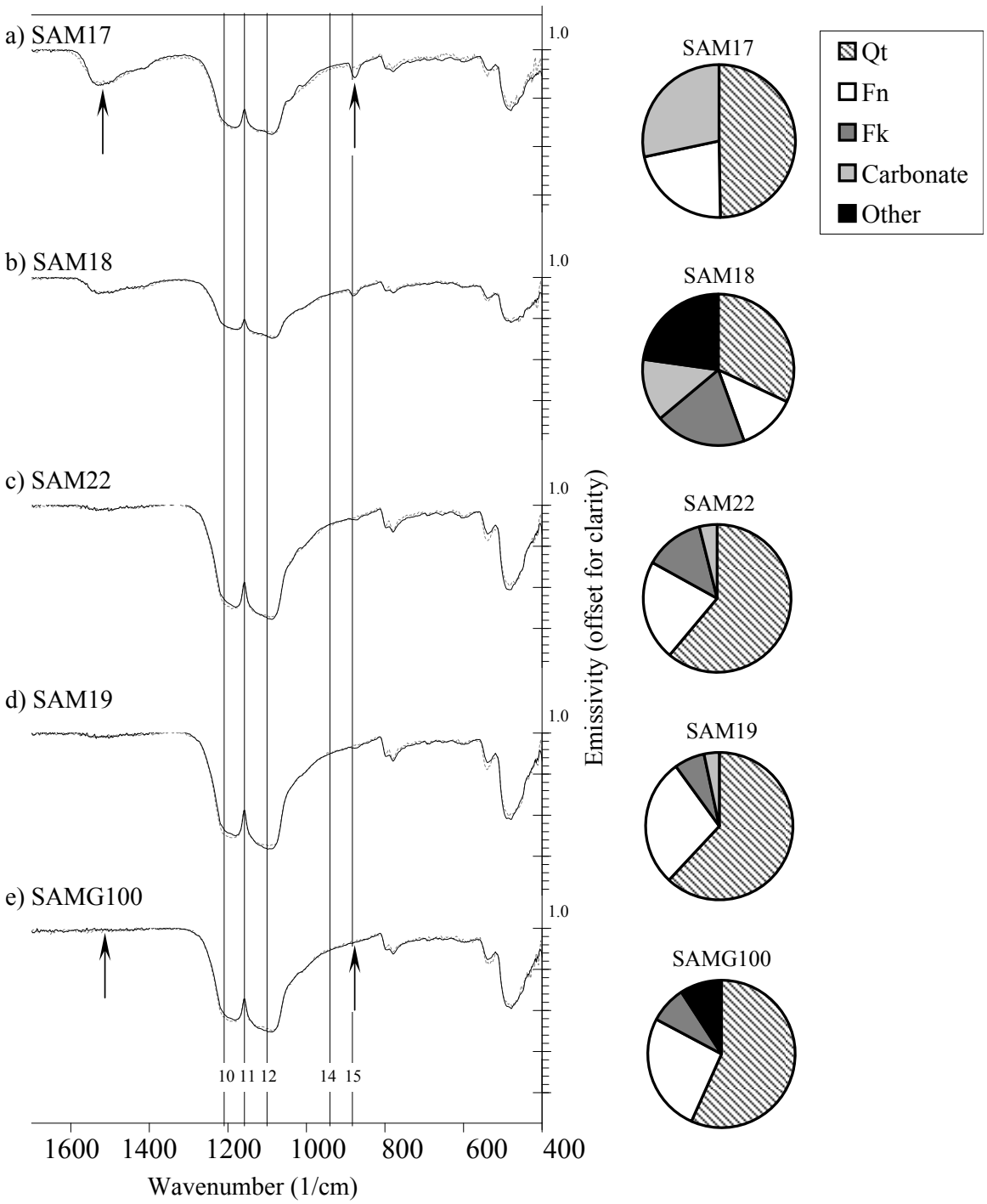

Figure 12. Spectra demonstrating a gradation change in carbonate.
(See caption on previous page.)

3.3.4.4 Sonoyta Dunes and Dunes Surrounding the Sierra Pinacate

The dunes that exist east and southeast of the Sierra Pinacate are a group of vegetated but still active linear dunes and have been named here as the Sonoyta Dunes, appropriately as the ephemeral, mostly dry Sonoyta River passes through this area as close as 2 km from the Sierra Pinacate as it travels south to the Gulf of California coast. Dunes exist on either side of the channel. The quartz spectral features visible in the Sonoyta area's average spectra are shallow (including the longer wavelength feature at 22 μm or 455 cm^{-1}). The spectral feature at 9.1 μm is significantly wider and has a different shape compared to other Desierto spectra (Figure 11g). These dunes had distinctly different composition retrievals with respect to feldspar. Quartz content is low and Ft is highest in these dunes (53-65%), where a significant portion (~50%) is potassium feldspar (Fk). Ferrohornblende is also found in minor amounts (3-5%) and volcanic lithics were detectable. The number of samples for this group is relatively low and was not recognized as a unique sediment source until after field campaigns in 2004 and 2005, nor have any samples been collected and archived at DRI. One sample was located at the northern extent of the Sonoyta Dunes, and three samples were from the coastal plain in the south surrounding the Sonoyta River. Samples were collected from the crescentic dunes west of this area, just south of the Sierra Pinacate and the Sierra Blanca (Figure 9b, block G5). Even though the average spectra from this location (Figure 11h) do not appear to be similar to the Sonoyta area, composition retrievals from these spectra are between 2-16% Fk. Examining the spatial pattern from the ASTER satellite data presented later suggests a very clear mixing relationship between different sand populations from the Eastern Crescentic area and the Sonoyta Dune area in the crescentic dunes south of the Pinacate.

The Northern Pinacate (Figure 9b, blocks 3/4F) is a group of vegetated linear dunes funneling between the southern extent of the Basin and Range alluvial fans and the western margin of the Sierra Pinacate at the northeastern end of the main dune field. The compositional retrievals of the Northern Pinacate (Table 3, row 8) are nearly identical to the Crescentic dunes to the south of the Sierra Pinacate (Table 3, row 9), except for the absence of Fk from a highly variable suite of feldspar retrievals. The average spectra of the Northern Pinacate (not shown) are nearly identical to the average spectra samples south of the Sierra Pinacate (Figure 11h). All of the dunes that are located in close proximity to alluvial fans of the Basin and Range and the Sierra Pinacate contain highly variable amounts of calcium feldspar (An), which may be

equivalent to field observations of labradorite. Labradorite is spectrally similar to anorthite; therefore if abundance is low and mixed with quartz and other feldspars, the linear deconvolution algorithm may have difficulty distinguishing labradorite.

3.3.5 Analysis and Discussion of Laboratory Results

3.3.5.1 Spatial Distribution of Composition

The modeled spectra (from which the composition retrievals are derived) compared to the measured spectra of the sand sample spectra described above have a low average root mean square (RMS) error of 0.0068. Even though those spectra represent end points of various sand compositions in the Gran Desierto, all of the other sample spectra in between these locations are considered to be mixtures, although local variation is expected. The interest of this study is the larger spatial trends in composition of the Gran Desierto. Furthermore, contacts between aeolian sedimentary units are expected to be gradual rather than abrupt. One exception is an example of local variation, where the contacts between star dunes and the underlying supersurface are abrupt, where dune composition is quartz rich and the exposed supersurface composition is variable. Considering the accuracy of the composition retrievals (and excluding samples with an RMS > 0.01, deemed to be inaccurate retrievals of composition), these data were combined into a database and imported into a geographic information system (GIS). The spatial distribution of each major compositional end-member-retrieval was calculated (or gridded) from the irregular array of sampling points (shown as "x" markers) using a weighted average interpolation algorithm (Figure 13 to Figure 18):

$$I_j = \sum_{i=1}^{N} w_{ij} f_i \tag{9}$$

where I_j is the interpolated value in the grid, N is the number of points used for interpolation, f_i is the end-member fraction of the sample and w_{ij} is the weight associated with the ith value used to compute I_j. Each I_j value in the resulting grid of 144 x 122 nodes (area shown within dotted line in Figure 13 to Figure 18) and weights were determined using the inverse distance weighted (IDW) technique, an exact interpolation algorithm [*Davis* 1986]. Because all samples were located on aeolian terrain, edges of coastlines and mountain ranges were input as barriers to the interpolation algorithm because these features are natural barriers to sand

transport. This has the effect of increasing the weighting distance between interpolated grid nodes if points exist on either side of a topographic barrier, such as the Sierra Pinacate. For example, this prevents the f_i value from the Northern Pinacate influencing the I_j value in the Sonoyta Dunes. Noise in the interpolation grid was eliminated by applying a 3 x 3 matrix smoothing function. Contour lines of surface mineral abundance (interval = 3%) were then drawn between nodes. The resulting contours show the spatially averaged distribution of minerals common to aeolian sediment in the Gran Desierto. These can be used to determine composition of different dune groups, trends of increasing and decreasing sand compositions, inferences of sediment transport direction, and source to deposition relationships. These data will also later be used to compare to the spatial distribution of composition retrievals determined from ASTER satellite data.

3.3.5.2 Quartz and Feldspar Distribution

Spatial patterns confirm that the central star dunes and reversing dunes at the western margin near the central area of the dune field are the most quartz rich sediments found in the Gran Desierto (Figure 13a, block 4b). Eastern crescentic dunes and the coastal sands north of the Bahia Adair are also found to be quartz rich as well. Quartz concentration decreases in the northerly direction in the central sand sea towards alluvial fans, as well as in the easterly direction toward the sand sheet between the star dunes and the Eastern crescentic dunes. The spatial distribution of total feldspar is inversely proportional to quartz abundance, where feldspar increases with shorter distance to the Sierra del Rosario and the Sonoyta Dune system (Figure 13b). The Sonoyta Dune area is heavily influenced by a bedload of granitic material from the Basin and Range to the north, as well as alluvial fans of the Sierra Pinacate.

Two spectral varieties of quartz were used as end-members and resulted in significant abundances: monocrystalline quartz (BUR-4120 from ASU's spectral library) and cryptocrystalline quartz (chert varieties analyzed at the IVIS laboratory). These varieties of quartz have broadly similar but slightly different spectral features. Including and excluding these quartz varieties resulted in similar deconvolution results, where differences were expressed mainly as slightly higher RMS error (~0.001-0.004) only. Monocrystalline quartz (Figure 14c) has a spatial pattern that coincides with total quartz. Cryptocrystalline quartz, or chert, varies between 35-38% in the whole of the main dune field (Figure 14d). Chert decreases in Sonoyta

Dune area, near the Sierra del Rosario, the Bahia del Adair and west of star dune area. Slightly higher values (~38%) are observed in the Central Dunes area (block 4c), the degraded crescentic dunes and sand sheet at block D5, the sand sheet west of Sierra Pinacate (block F4) and the linear dunes of the Northern Pinacate (block F3). Even though the data for the chert distribution is a weak trend, some potential hypotheses are: 1) Chert may be a tracer for older underlying Colorado River sediments. 2) Chert may be a tracer of desert pavements or older dune surfaces where the spectral features of quartz have been altered by desert varnish. 3) Lastly and certainly the least desirable, chert abundance may be a spectral artifact, compensating for an unmodeled end-member. An explanation for this weak spatial pattern has not been proposed. Other likely source rocks include nearby quartz-rich sandstones and quartzite. These varieties would also be favorable to include as end-members, but these samples were not collected or available for analysis.

Several end-members of feldspar were included in the laboratory deconvolution because each of the various minerals in the feldspar solution series has variable spectral features, as do Na- and K-feldspar. Likewise, single feldspar grains may exhibit intra-variable composition with the presence of twinning. Albite was the most abundant feldspar and the highest concentration was found between the Sierra del Rosario and the Sierra Pinacate (Figure 15e). Oligoclase abundance is low, but highest in the Rosario and Sonoyta Dune area (Figure 15f). In general oligoclase and the total amount of Na-feldspar (Figure 16g) follow the same spatial pattern as total feldspar. The total Na-feldspar is considered a more important result than the individual minerals detected. However, total average K-feldspar is in greatest abundance (6-18%) in the Sonoyta Dune area and has a unique spatial pattern in these data (Figure 16h). This was also found in ASTER data (discussed below).

3.3.5.3 Lithic Distribution

The examination of the spatial distribution of the lower abundance mineral percentages is only possible with the laboratory results because they are generally low in areal abundance and are difficult to model using spectral deconvolution of ASTER satellite data. The accuracy of laboratory data may be limited to end-members greater than 10%, reducing confidence in the quantification of minor constituents. With a high degree variation in composition from local sources, each of these fractions makes up a small amount of an already low abundance of total

lithics in the sample. Minor constituents must compete for a smaller percentage of estimated fractional abundance. Very low percentages of a minor constituent are likely to randomly be undetectable because of sample noise, laboratory error and of course, the limits of the deconvolution algorithm. With these limits considered, the compositional maps presented here show some unique spatial trends. First, total hornblende is highest in the Sierra del Rosario and averages 7% throughout the rest of the dune field west of the Sierra del Rosario and the Mesa Arrenosa (Figure 17i). Hornblende is an end-member associated with local granitic sources, and was absent from samples east of the Sierra del Rosario. An average, minor amount (~4%) is present in the Sonoyta Dune area. The average amount of volcanic lithics was expected to be much higher for samples around the Sierra Pinacate, but the average south and east of the Sierra Pinacate is only 1%; an average of 3% is found in the Sierra del Rosario (Figure 17j). Total lithic concentration is shown in Figure 18k, where the highest percentages are clearly a function of biogenic carbonate in the Bahia del Adair (Figure 18l). As was shown from individual samples from this area (Figure 12 and Table 3, row 5) with high values of 30-50% carbonate, the spatially averaged value is significantly decreased by the higher quartz content in siliceous samples (Table 3, row 6).

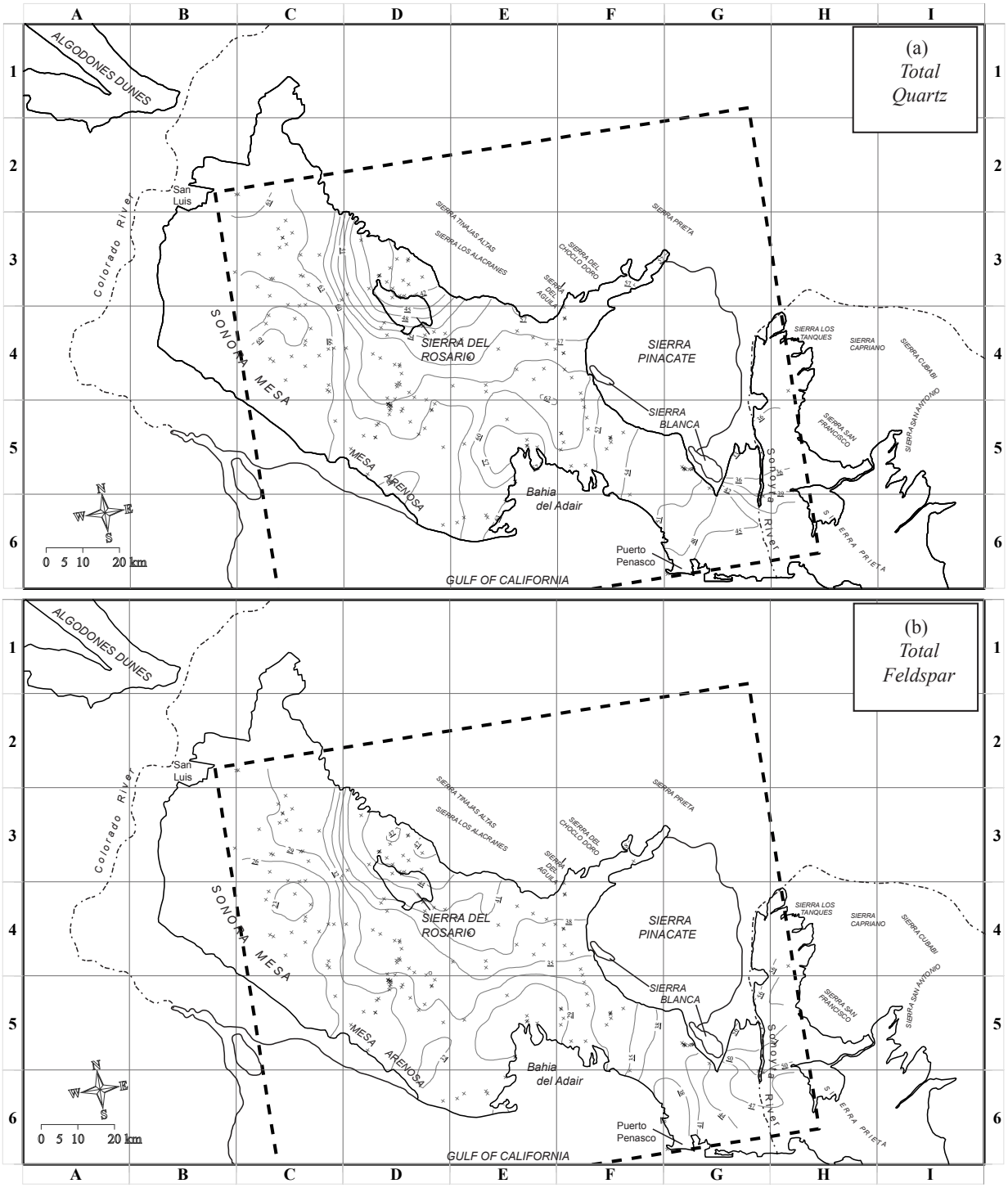

Figure 13. Spatial Interpolations of (a) Total Quartz and (b) Total Feldspar.

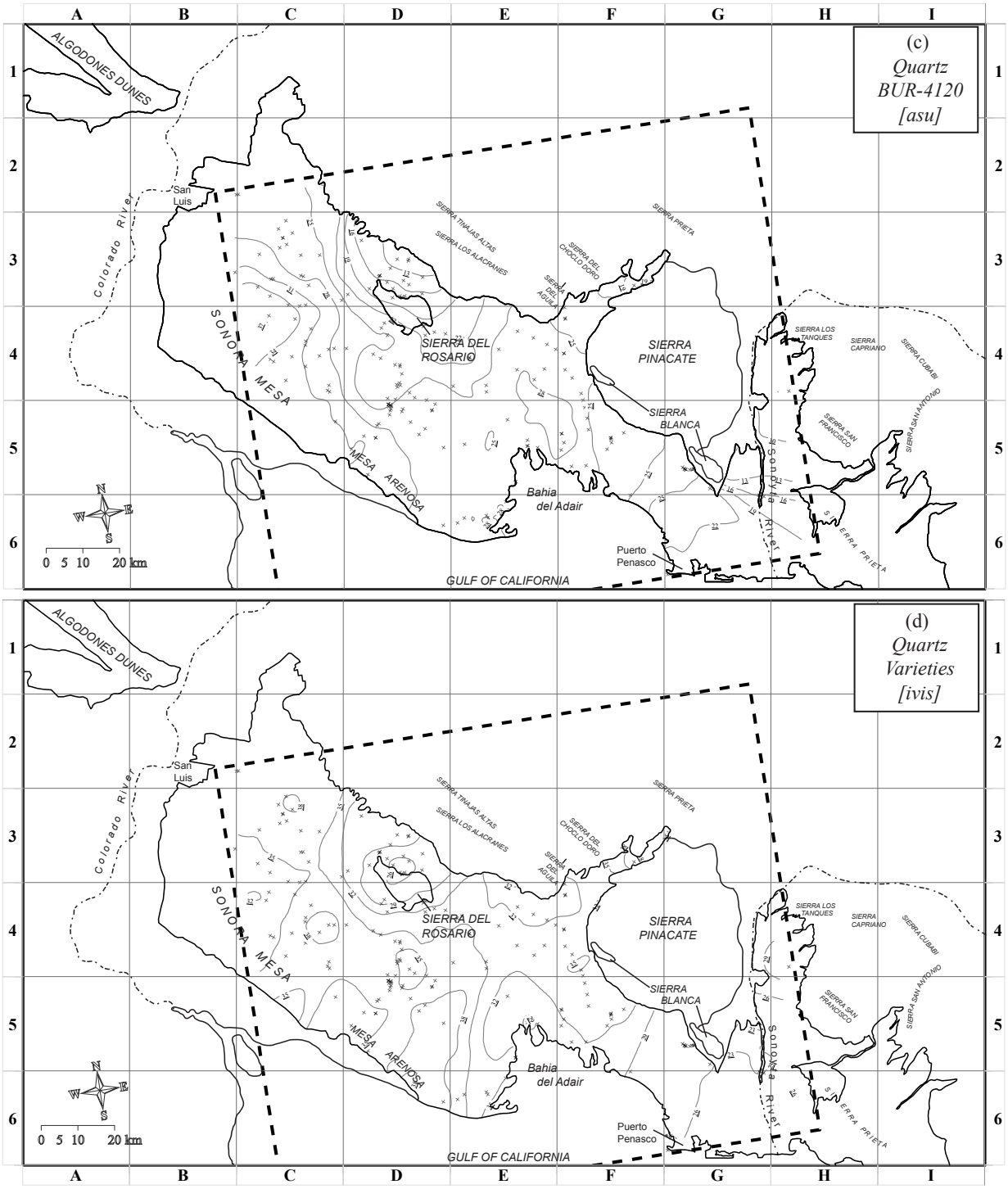

Figure 14. Spatial interpolations of (c) monocrystalline quartz and (d) cryptocrystalline quartz varieties.

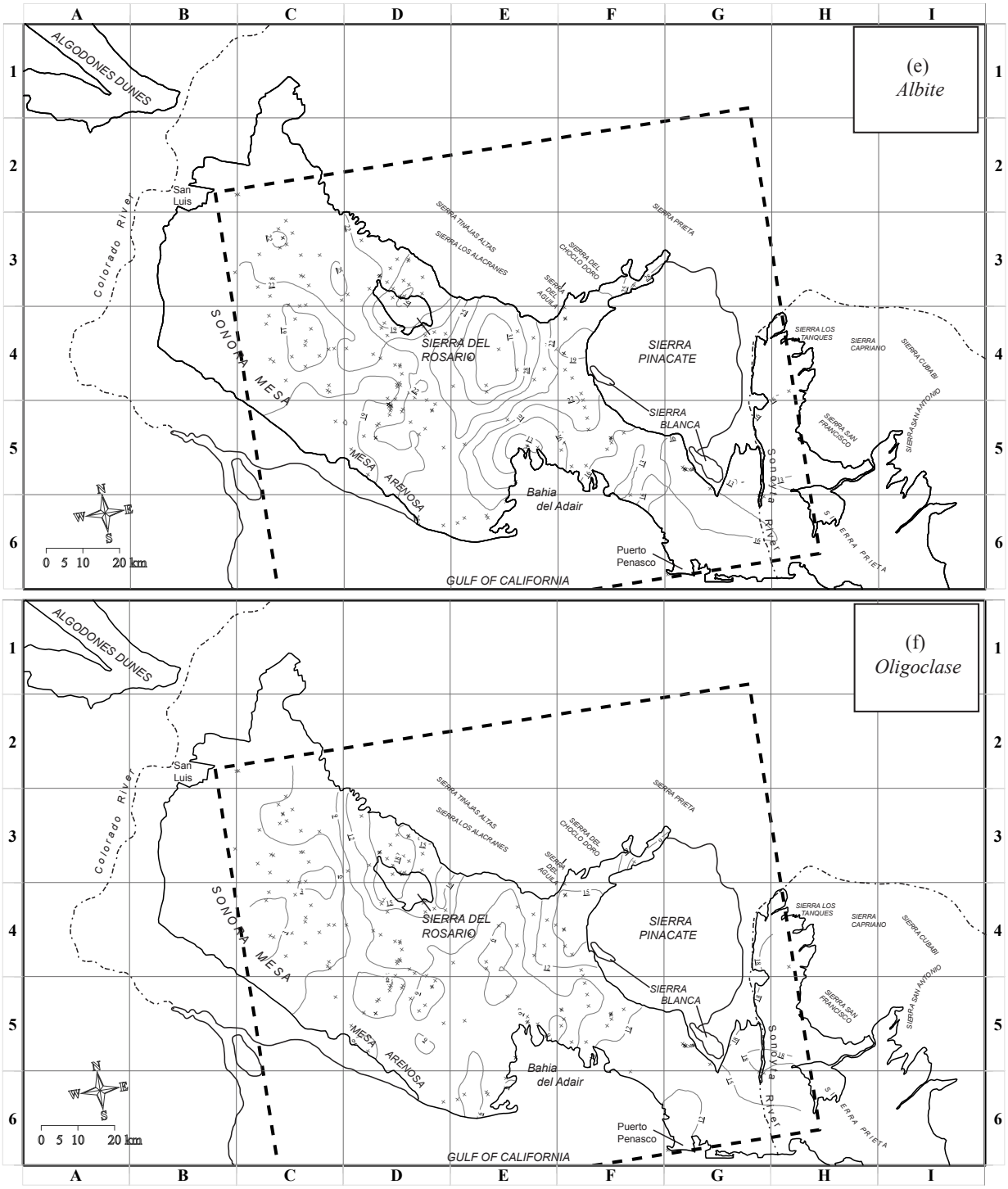

Figure 15. Spatial interpolations of (e) Albite and (f) Oligoclase.

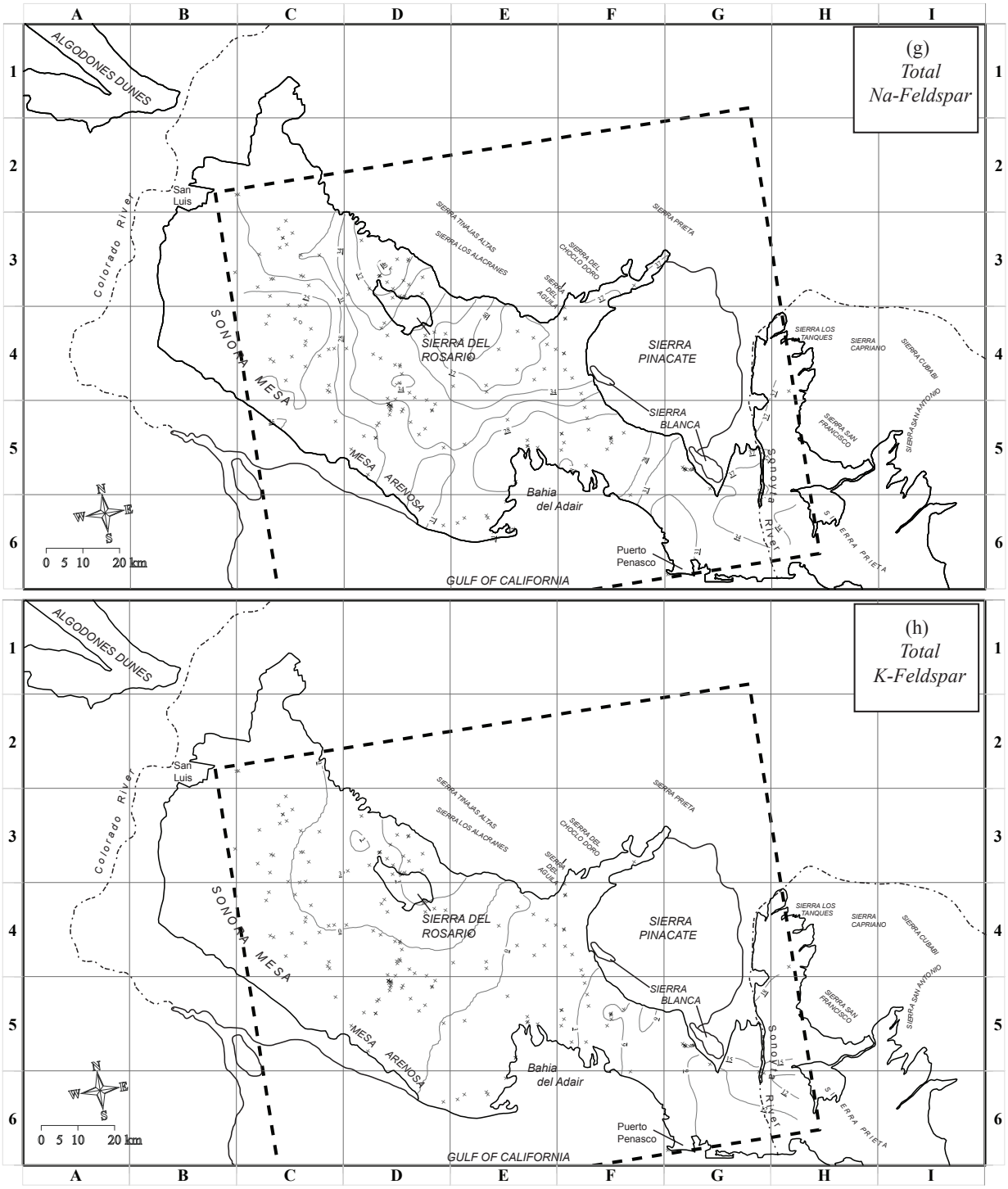

Figure 16. Spatial interpolations of (g) total Na-feldspar and (h) K-feldspar.

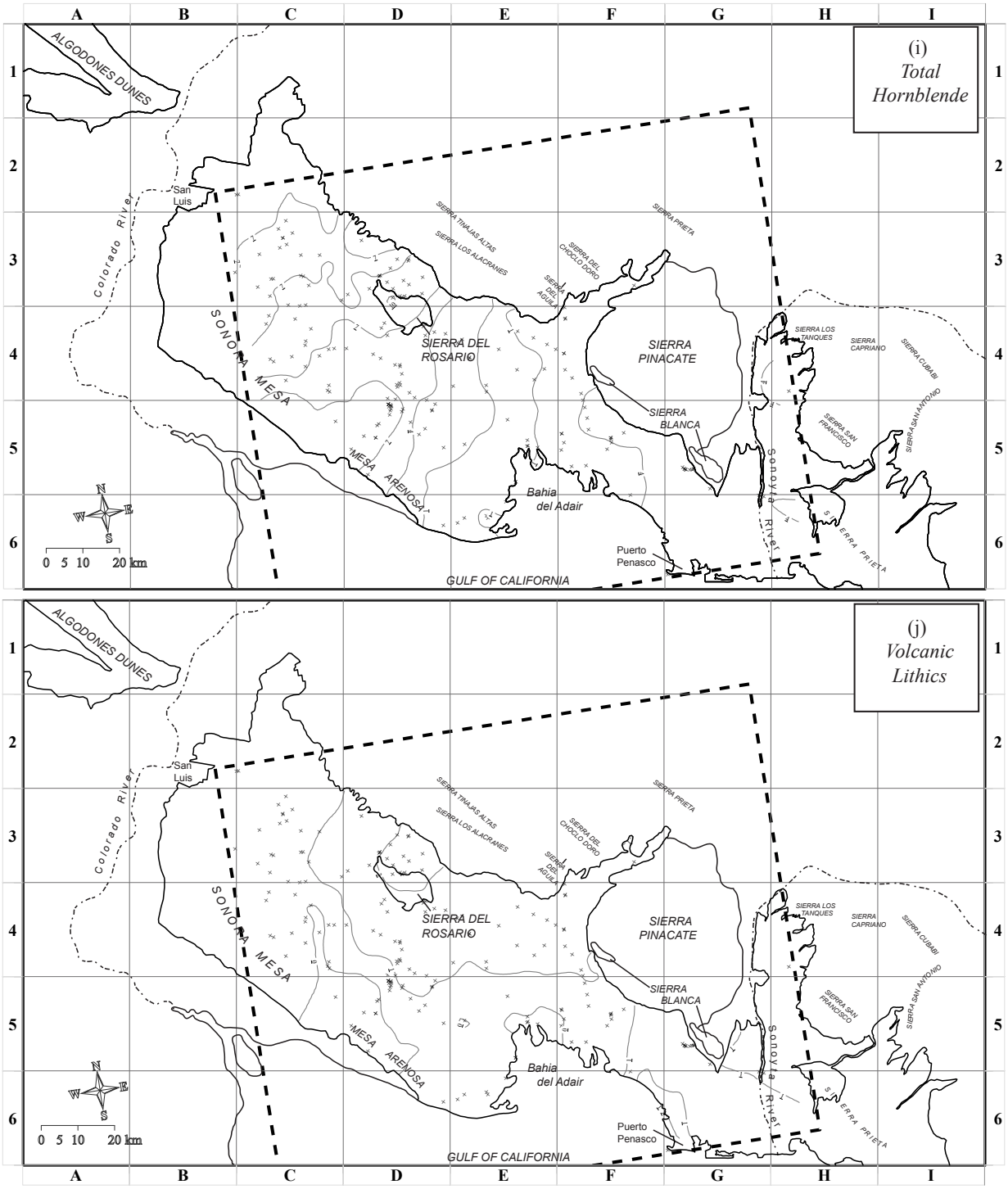

Figure 17. Spatial interpolations of (i) total hornblende and (j) volcanic lithics.

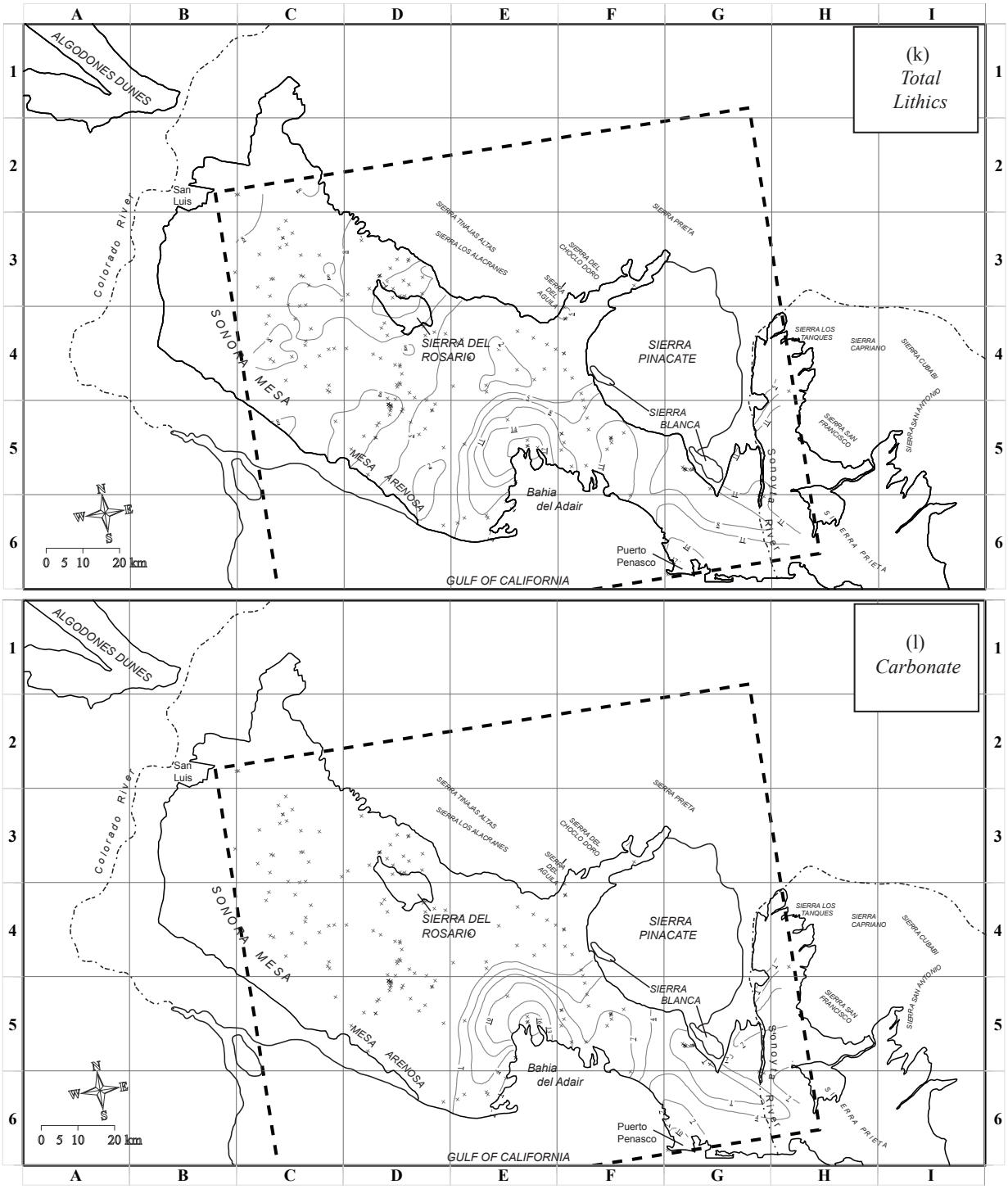

Figure 18. Spatial interpolations of (k) total lithics and (l) total carbonate.

3.4 ASTER IMAGE ANALYSIS

In this section, the ASTER derived composition is discussed and compared to the laboratory data. The treatment of ASTER data and methods used to determine surface composition at a larger spatial scale (~90m) and a lower spectral scale (~5 spectral bands). In the first section (3.4.1), the importance of combining several ASTER scenes using a radiometrically correct method for a mosaic is reviewed [*Scheidt et al.* 2008]. Additional atmospheric correction that much be applied to retrieve accurate emissivity ASTER standard data product is also discussed. The second section (3.4.2) discusses the linear deconvolution results and the process used to select the end-members, which is based on the results of the laboratory spectral analysis above. The linear deconvolution results of 3 and 4 end-member library suites are then presented and discussed with respect to variations of source lithology (section 3.4.3.1). The satellite retrievals of composition for the different regions of the Desierto from the mosaic product and the North American ASTER Land Surface Database (NAALSD) emissivity product are compared to laboratory results (section 3.4.3.2) and measured composition reported in the literature (section 3.4.3.3). The ASTER data results are presented in summary as a PCA image and a color composite of end-member fractions (section 3.4.3.4). We discuss the integration of laboratory and satellite data in section 3.5, where lastly, the conclusions with respect to sediment dynamics and mixing of aeolian sediments in the Gran Desierto follow.

3.4.1 ASTER Mosaic Processing and Atmospheric Correction of Emissivity

Each ASTER scene covers only 360 km^2; therefore, data must be combined, or mosaicked, from several different dates to provide a synoptic view of the Gran Desierto. Radiometric differences between scenes due to season, atmosphere and instrument calibration could cause a lack of seamlessness and limit spectral analysis of spatial patterns. There are several possible approaches to mosaicking these remote-sensing data, and only a few studies have described the process of normalizing and mosaicking [*Hewson et al*. 2005; *Scheidt et al*. 2008] or averaging [*Hulley and Hook* 2009] ASTER TIR data. Where scene differences are normalized, the resulting emissivity data are radiometrically accurate, seamless, have high spatial resolution and can be used for spectral analysis and geologic interpretation. *Scheidt et al.* [2008] developed a radiometric

normalization technique of ASTER TIR radiance data (AST_09T data product) and produced a seamless mosaic of the Gran Desierto that could be used directly for spectral analysis. (See Chapter 2).

The focus of this study relies on the use the spectral features of common dune-forming minerals in the thermal infrared (TIR) wavelength to determine composition of aeolian sands in the Gran Desierto. Concurrent with mosaicking of the data, other image processing tasks were completed in order to retrieve accurate emissivity, such as the correction for reflected downwelling radiance. Thermal radiance, a function of both emissivity and brightness temperature, is measured by the ASTER satellite (AST_09T product). The AST_09T product represents the thermal radiance at sensor (L_λ) at each ASTER pixel

The AST_09T data used for this study have been atmospherically corrected and are radiometrically accurate [*Thome et al.* 1998], but these data have not been corrected for reflected downwelling irradiance ($L_\lambda\downarrow$). This correction is important because the Desierto has an abundance of quartz rich dune sediments, and low emissivity values (≈0.7) are retrieved from ASTER bands 10, 11 and 12 (8.291, 8.634 and 9.075 μm wavelengths, respectively) from these areas. The downwelling irradiance ($L_\lambda\downarrow$) reflected from the land surface back to the sensor cannot be assumed to be negligible for these bands in areas of high quartz abundance (Kirchhoff's Law). Without the correction, the spectral contrast will be reduced for the spectra of these pixels and the spectral shape of the retrieved ASTER emissivity spectra will be adversely affected, especially for the quartz absorption features expressed in band 10, 11 and 12. This in turn affects the accuracy of the retrievals of composition from the spectra, resulting in an underestimation of quartz, for example. For the AST_09T thermal radiance data used in this study, an in-house correction for the reflected downwelling irradiance ($L_\lambda\downarrow$) was developed, which is similar to the iterative correction used by the NEM module of the TES algorithm described in *Gillespie et al.* [1998] and is equivalent to the "nominal correction" of reflected downwelling irradiance suggested for the TES algorithm by *Gustofson et al.* [2006] (see below). Quartz rich dune sediments in the core of the Desierto resulted in an average TIR radiance correction of no more than ≈ 0.7 Wm^{-2} μm^{-1} sr^{-1} for band 10-12 and can increase the depth of emissivity spectra for these bands by as much as ≈ 7% and improves spectral shape. Correction in bands 13 and 14 is insignificant because reflection of downwelling irradiance is low ($\rho << 1.0$)

and the emissivity is high. Overcorrection of reflected downwelling radiance is prevented by limiting the algorithm iterations to n = 3.

With accurate estimation of emissivity, normalization of satellite scenes should not be required and an emissivity mosaic can be used directly for compositional analysis. The ASTER emissivity product (AST_05) generated by the Temperature Emissivity Separation (TES) algorithm also corrects for the reflected downwelling irradiance [*Gillespie et al.* 1998], although the data's performance has varied through time with different versions of the TES algorithm [*Gustafson et al.* 2006]. TES generated emissivity (AST_05) was found not to mosaic well for the Desierto initially, leaving seam boundaries in the mosaic, therefore use of the AST_09T was preferential [*Scheidt et al.* 2008]. Various changes have been made to the TES algorithm [*Gustafson et al*. 2006], and the AST_05 may be considered an improved product since performance of the previous data versions were assessed in *Scheidt et al*. [2006; 2008]. The current AST_05 emissivity product compared well to the emissivity extracted from in-house corrected AST_09T [*Scheidt*, unpublished data]. The NAASLED is a mosaicked AST_05 emissivity product, generated by the ASTER Land Surface Emissivity Aggregation Algorithm (ALSEA), which averages overlapping ASTER emissivity scenes that have passed quality control parameters [*Hulley et al.* 2008; *Hulley and Hook* 2009]. NAALSED spectra of quartz-rich samples from the nearby Algodones dune field, CA compare well with field TIR reflectance spectra [*Hulley et al*. 2008]. The increased signal to noise ratio (SNR) of the averaged emissivity data is an advantage of the NAALSD dataset, reducing the amount of scan line noise inherent in ASTER TIR data. This advantage must be balanced with the negative effects generated from averaging scenes that may have incomplete atmospheric correction and land surface change from multiple images.

Both the mosaicked radiance and emissivity data are useful for different spectral analysis tasks, therefore a mosaicking technique that allows the utilization of both radiance and emissivity data was used [*Scheidt et al*. 2008]. The corrected AST_09T radiance data were used to generate a radiometrically normalized radiance-at-surface image, corrected for reflected downwelling irradiance. A quality reference image was used (i.e., clear scene, low vegetation, etc.), and the radiometric normalization technique used here eliminates scene to scene variations due to atmosphere and season [*Scheidt et al.* 2008]. The emissivity was extracted from the seamless radiance mosaic using a normalized emissivity approach [*Realmuto* 1990] and an emissivity

maximum set to 0.96. The extracted emissivity data were in agreement with non-normalized emissivity values, but the overall image of emissivity has the quality and benefit of seamlessness. A decorrelation stretch (DCS) [*Gillespie* 1992] and a Principle Component Analysis (PCA) stretch [*Richards* 1999] were generated from the radiance mosaic data to examine the spectral variability of the entire dune field. These analysis techniques were modified to include only the spectral data from arid land surface materials. Water, shade from mountain ranges and dense vegetation from the highly cultivated Colorado River Valley were excluded from the eigenvector statistics to enhance the spectral variability of geologic materials (i.e., the dunes, alluvial fans and rock outcrops). The DCS and PCA transformations of the original data both highlight compositional information as color variations and surface temperature as brightness variations [*Ramsey et al.* 1999; *Gillespie* 1992], although the DCS and PCA represent different dimensionalities of the ASTER TIR data. The DCS uses three rotated and stretched bands (commonly 14, 12 and 10 in R,G,B, respectively), but all 5 bands are used in the PCA transformation. These products were used to determine where composition varies throughout the dune field, which helped to select appropriate sampling locations during field activities and selection of sand samples from the Gran Desierto archived at the Desert Research Institute (DRI). The DCS can be found in *Scheidt et al.* [2006; 2008], and a version of PCA analysis for the Gran Desierto was previously described [*Scheidt et al.* 2006].

3.4.2 Composition Retrieval from ASTER Data

3.4.2.1 Selection of Spectral End-members and Linear Deconvolution Methods

The thorough analysis of laboratory samples was essentially a blind end-member investigation, computationally intensive and time-consuming. One purpose of the lab analysis was to provide a basis for narrowing down the possible spectral end-members used for the linear deconvolution of image data. A set of only 15 likely minerals produced hundreds of unique combinations of four end-members or less for the Kelso Dune system, where the resulting set of end-members used for linear deconvolution of TIMS imagery was based on the lowest overall RMS error [*Ramsey et al*. 1999]. Similarly, only a few combinations of end-members produce accurate, low RMS error results from the linear deconvolution of laboratory spectra from the Gran Desierto. These most likely end-members as a result of laboratory analysis were in

decreasing order of average abundance: mono/cryptocrystalline quartz > albite > oligoclase > microcline >> carbonate >> ferrohornblende >> anorthite.

In the deconvolution of ASTER TIR data, the number of end-members was limited to the number of spectral bands ($n \leq 5$). With the need to include a blackbody ($\varepsilon_n = 1.0$) to account for spectral depth between laboratory end-members and remotely sensed data, the number of possible end-members used in the algorithm is reduced ($n \leq 4$). Identification of composition from ASTER is also limited by the spectral features captured by the data, which is dependent on instrument characteristics, band detection limits, the band-to-band signal-to-noise-ratio (SNR) and the spectral contrast of target minerals [*Kirkland et al*. 2001 and others]. For example, carbonate, ferrohornblende, magnetite and hematite are all relatively difficult to detect at the sub-pixel level from ASTER data because they (a) are in low abundance and do not have a large impact on the measured emissivity, (b) have relatively few or no spectral features at ASTER wavelengths and lastly (c); the spectral contrast or range of emissivity values for band 13 and especially 14 is small. For example, the dune sands of the Gran Desierto varies by < 0.0015 emissivity for band 14, where in the basaltic Sierra Pinacate, this range increases to 0.0064 emissivity. Because of the SNR of ASTER (noise-equivalent-emissivity, $NE\Delta\varepsilon \approx 0.005$ at 300K), spectral features are not large enough at band 14 (i.e., carbonate) to be identifiable by the instrument in the dune field and approach the limit of detection in the Sierra Pinacate. Therefore, accounting for all these factors, the number of end-members may be further limited to ~three end-members for parts of the dune field. Image deconvolution was performed using suites of both three and four end-members, but the resulting agreement between laboratory and remote-sensing retrievals for dune field sands favored the use of three end-members for mapping dune sediments (Figure 19 to Figure 22).

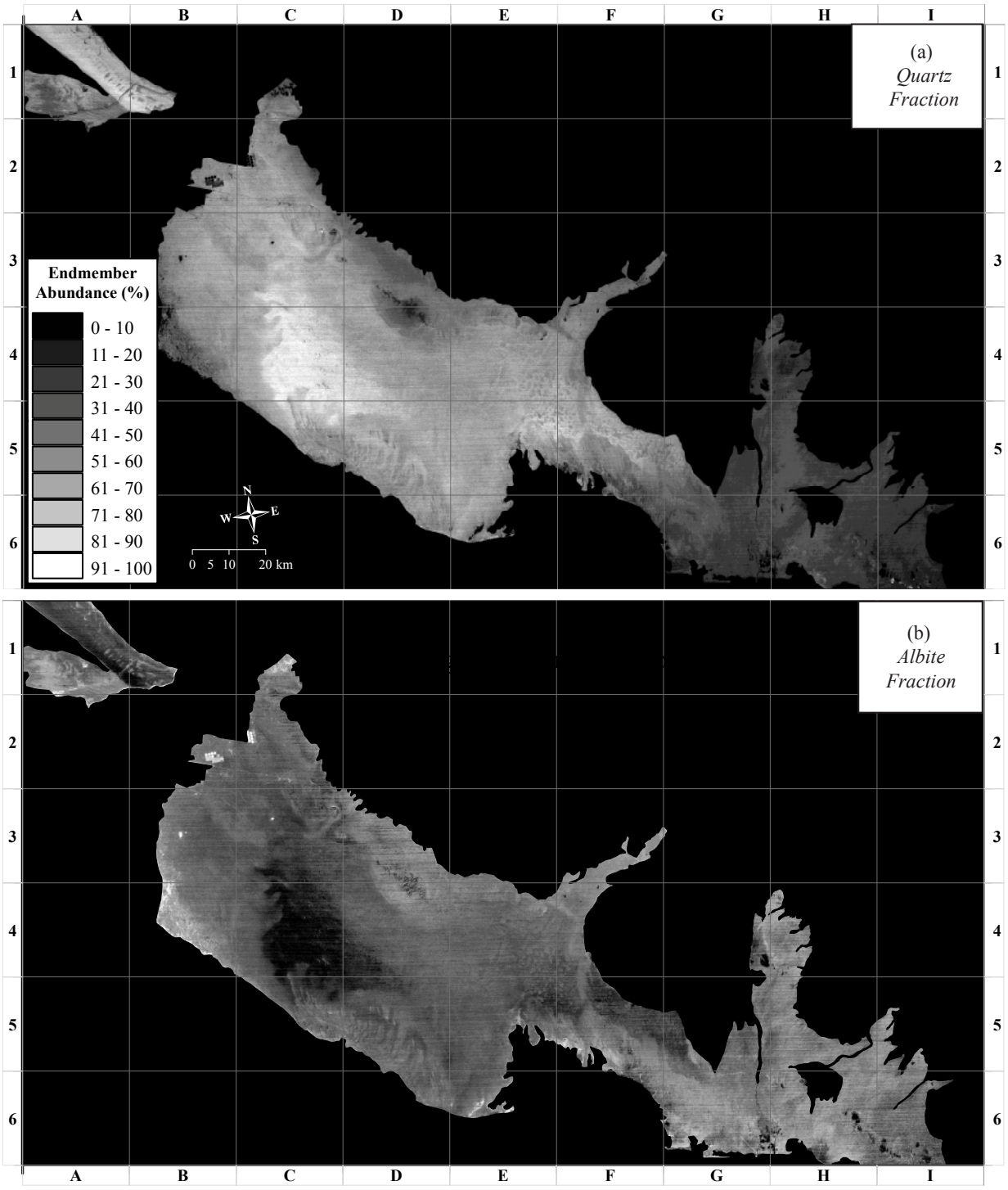

Figure 19. End-member images for the 3 spectral end-member suite: (a) total quartz and (b) albite (similar to total feldspar and total Na-feldspar distributions).

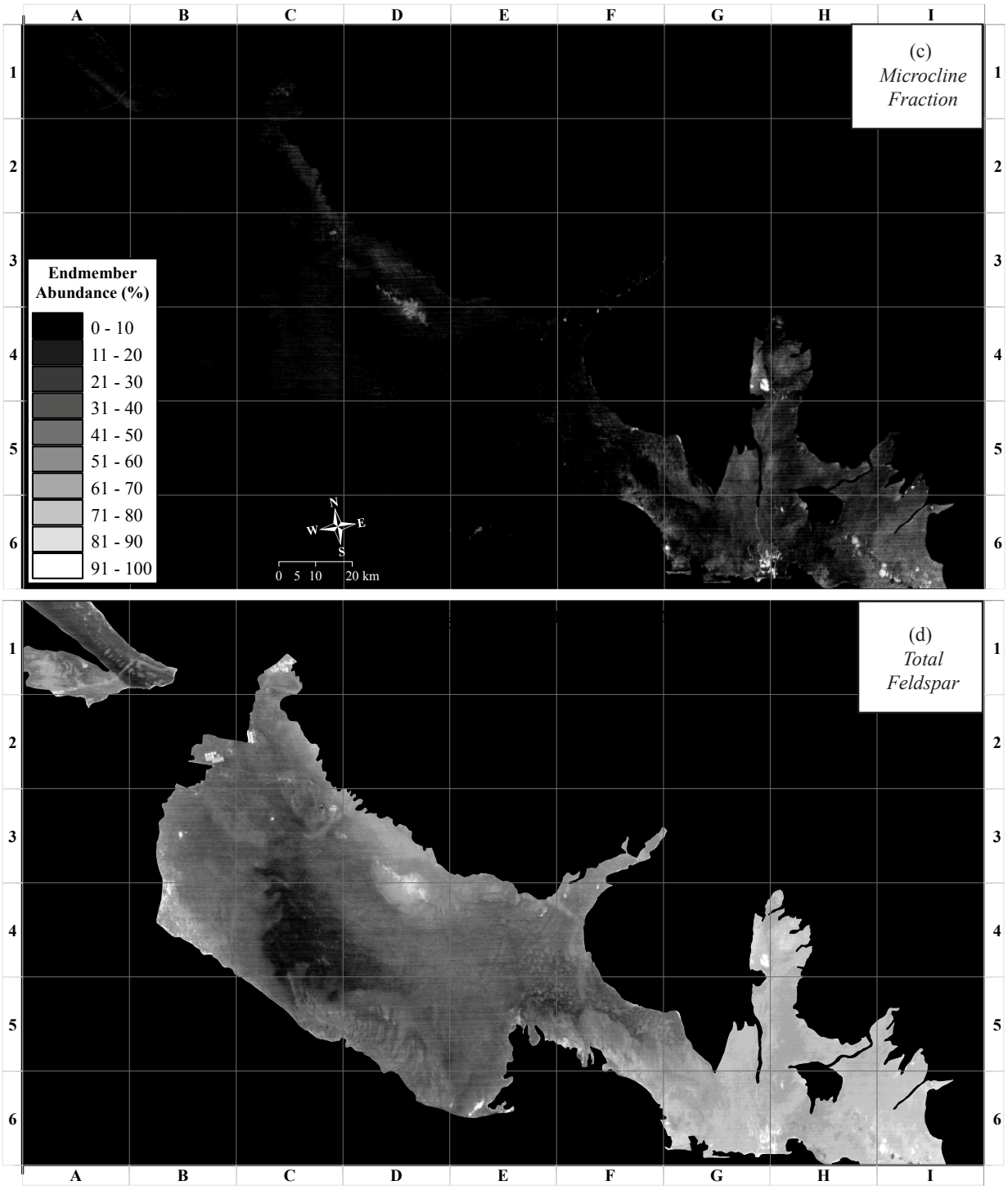

Figure 20. End-member images for the 3 spectral end-member suite: (c) microcline (similar to total K-feldspar distribution) and (d) total feldspar (albite+microcline).

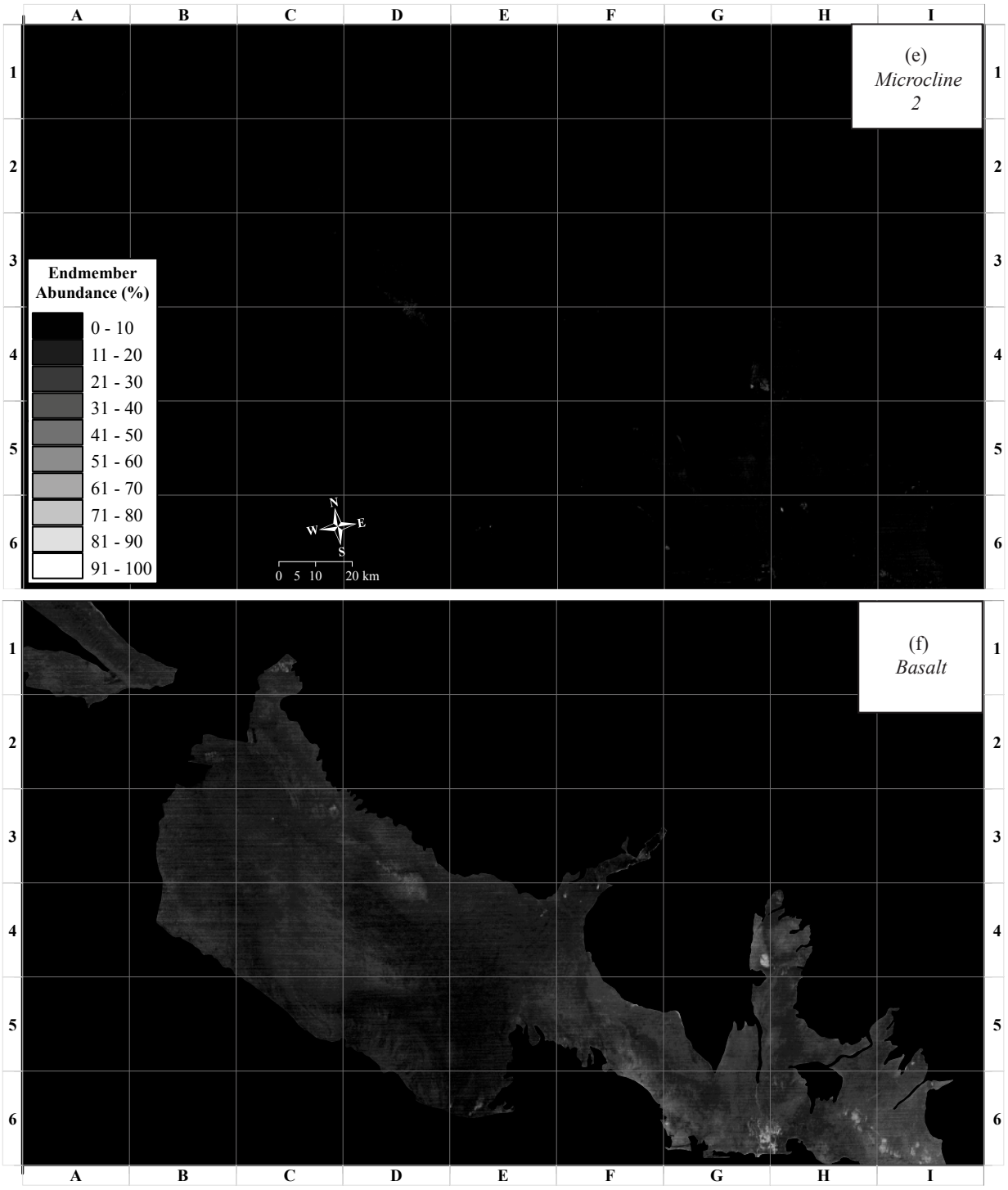

Figure 21. End-member images for the 4 spectral end-member suite: (e) microcline, (f) basalt, augite or "mafic" (Endmember-image results essentially differed for only these two fractional images using the 4 end-member suite).

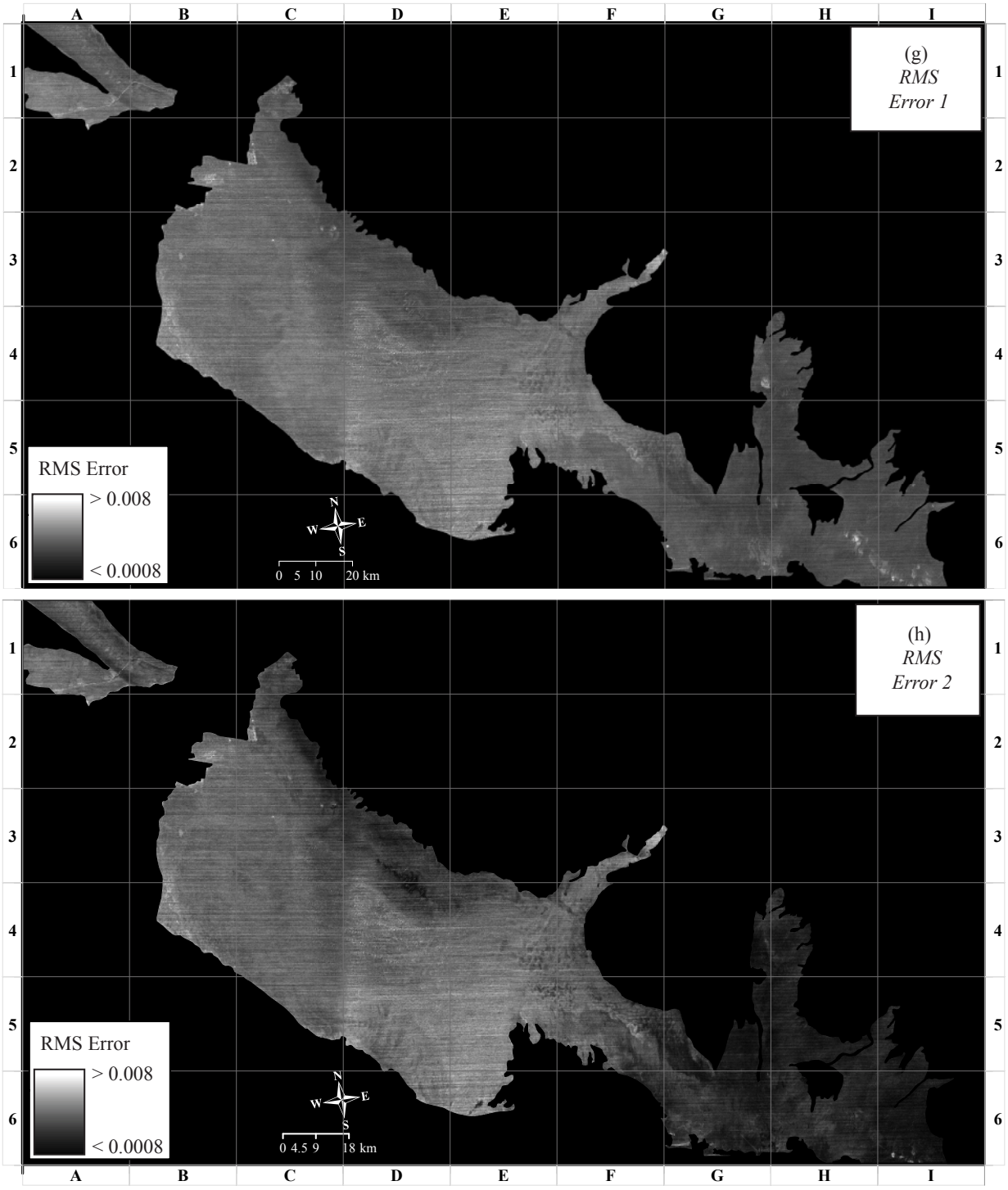

Figure 22. Spectral linear deconvolution results: (g) RMS error image resulting from the 3 end-member suite, where the average was 0.007 ± 0.001. (g) RMS error image resulting from the 4 end-member suite, where the average was 0.004 ± 0.003.

3.4.2.2 Image Analysis Results

The end-members chosen for image deconvolution, a quartz-albite-microcline-basalt end-member suite, resulted in the lowest RMS error (Figure 22h). The highest errors were found in areas of the image that were not modeled (non-aeolian sediments). These areas are in the vegetated Colorado River plain, the basaltic Sierra Pinacate and areas of evaporite deposits and playas. Some error is evident between blocks C and D (Figure 22g and Figure 22h) where scan line noise from the instrument did not mosaic well. The same deconvolution iterations were applied to NAASLED emissivity data, which resulted in a higher average, non-uniform, RMS error in the quartz rich dune fields of 0.0158 vs. 0.007. This error was probably dune to incomplete correction of reflected downwelling irradiance or dilution of spectral features due to averaging of scene variations. This did not significantly affect most of the composition retrievals (see below). Scan line noise effects NAASLED averaged emissivity less than mosaicked data.

3.4.3 Synthesis and Discussion of Laboratory and ASTER-Derived Composition

3.4.3.1 Analysis of End-member Images

The resulting fractional end-member images (Figure 19 to Figure 21) can be directly compared to the mineral abundance maps generated from laboratory data (Figure 13 to Figure 18). Because of the spectral similarities of some end-members at ASTER wavelengths, it is hypothesized that the single end-members used in the image deconvolution represent suites of similar end-members. For example, the quartz end-member will represent the total quartz, equivalent to quartz+chert (Figure 19a). Albite will reflect total Na-feldspars (Figure 19b), and microcline will show total K-feldspar (Figure 20c) Total feldspar (Figure 20d) is equivalent to the albite+microcline images. The end-members chosen captured the majority of the spectral variability at ASTER resolution, and appear to have spatial distributions of mineral abundance retrievals that are similar to laboratory results. Quartz abundance is highest in the central dune area (Figure 19a, block 4C) and the Eastern Crescentic dune group (Figure 19a, block F4/5). Albite or Na-feldspar images are inversely proportional to quartz with higher feldspar values occurring in the dunes surrounding the Sierra del Rosario and in the Sonoyta Dunes area (Figure 19b). The microcline (K-feldspar) fractional image shows higher abundance in the Sonoyta Dune area east of the Sierra Pinacate, similar to laboratory retrievals (Figure 20c). Examination

of the K-feldspar and RMS error image showed a clear overestimation (and false detection) of microcline occurring in the entire area for the Sierra Pinacate. These rocks are actually basaltic and some contain minor amounts of labradorite phenocrysts. These errors were masked, and only results of dune areas are shown.

If a "mafic" end-member, such as olivine, augite or vesicular basalt, was used as a fourth end-member, the linear deconvolution produces separate and different fractional images of microcline and "basalt" fractional end-member images (Figure 21e and Figure 21f, respectively). RMS error is shown in Figure 22h. Quartz and albite fractional images (not shown) are relatively unchanged compared to the results of the 3-end-member deconvolution. The Quaternary basalts are more correctly identified in the Sierra Pinacate and elsewhere in the Basin and Range, although this basalt end-member image, if compared to the previous microcline end-member image using 3 end-members, is very similar in areas of dunes. Because basalt or volcanic lithics were not identified in great abundance, it could be concluded that errors are present for the fraction of volcanic/mafic abundance in the dune areas. Volcanic composition was not identified in high abundance in these areas from laboratory spectra, although these components were detectable or visible in small quantities from hand samples. A high abundance of basaltic grains is plausible in dunes near the Sierra Pinacate as grains were readily observed in the field, actively saltating through topographic lows in dune topography. Interdune areas also had gravel to cobble size chunks of vesicular basalt in significant areal abundance (estimated at 20% from "pixel surveys" in the field). Therefore, the identification of basalt at the resolution of ASTER may be accurate. The fractional abundance of microcline in the 4-end-member deconvolution resulted in higher abundances in some of the rocks and alluvial fans of the Sierra Pinacate (5-50%) and the granitic and gneissic mountains of the Basin and Range. However, only some identification was found of 5-20% microcline in the Sonoyta Dune area in sporadic, noisy pixels (Figure 21e). Potassium feldspars (microcline, orthoclase and sanadine) are likely end-members from the source rocks surrounding the Sonoyta Dune area. The Sierra Blanca is a small group of Proterozoic metamorphic rocks (quartzites, gneiss, schist and amphibolites) mostly obscured by the much younger Quaternary basalts. Field observation and hand samples of the Sierra Blanca rocks contain a significant amount of K-feldspar [*Anderson*, unpublished data], whereas other assemblages in the area also contain significant amounts of K-feldspar [*Watkins* 2003; *Nourse et al.* 2005]. Trachytes, which are volcanic rocks that have an

aphanitic to porphyritic texture consisting mainly of sanidine, a high temperature K-feldspar, are exposed in limited areas within the basaltic fields of the Sierra Pinacate and have largely been unmapped in this region; trachytes are thought to once be more extensive in coverage prior to the emplacement of younger basalt flows [*Gutmann*, unpublished data]. A linear deconvolution analysis of ASTER TIR data using a different end-member suite (including a K-feldspar end-member) appropriate only to the Sierra Pinacate was conducted to explore the abundance of K-feldspar in the Sierra Pinacate. This resulted in the correct detections of higher K-feldspar abundance in small areas that probably indicate some of the largest deposits of trachytes in the Sierra Pinacate, which have not yet been mapped in the field [*Scheidt and Gutmann*, unpublished data]. The Sonoyta River carries a quartzofeldspathic bedload containing a host of varied source lithology from the Basin and Range as well as the Sierra Pinacate. Therefore, considering the very low quartz concentrations found in laboratory samples, the sediment of the Sonoyta Dune area is probably compositionally diverse and highly affected by local sources. The linear deconvolution using 4 end-members is at the limit for the number of end-members detectable by the instrument, where the smaller fractions of K-feldspar and volcanic lithics are difficult to resolve at ASTER's spectral and spatial resolution. Using both 3 and 4 end-members both produced acceptable and comparable low levels of RMS error. The 3-end-member suite was assumed to be correct with respect to dune sediments because of the agreement with laboratory composition retrievals. At the spatial scale of ASTER (~90m), the 4-end-member suite better characterizes the region's broader surface composition that includes, for example, un-sampled basaltic gravel and cobbles in interdune areas common to dunes south of the Sierra Pinacate.

3.4.3.2 Comparisons of Satellite and Laboratory Results

Using the results of the 3-end-member suite, the retrievals of average composition from the satellite were compared directly to the average laboratory results for the nine groups of samples separated by region (Table 4, Figure 23a-f). The satellite retrieval of the quartz end-member was compared to the total amount of quartz retrieved from lab data, and a general 1:1 direction relationship is observed indicating that ASTER retrieves quartz accurately (Figure 23a). The average variation of quartz retrieval ranges by ± 10%, and is within the accuracy expected of linear deconvolution methods. Total feldspar is similarly accurate (Figure 23b), with some exceptions found for coastal carbonate rich sands, which were 30% higher in total feldspar than

laboratory retrievals (Table 4-column 2). Because the mixing of spectral energy is linearly proportional to areal abundance, the depths of the spectral features are therefore linearly proportional to the end-member's fractional abundance. Considering the effects of reduced spectral contrast via satellite remote sensing (e.g., satellite spectra are always shallower than lab spectra), ASTER cannot as accurately retrieve carbonate because of the weak spectral contrast at band 14, even with the use of a blackbody. For example, in the case of the coastal carbonate sands, only an average of 40% of the spectral feature at band 14 ($\varepsilon \approx 0.032$) is initially available for detection by ASTER.

Table 4. Comparison of ASTER-derived Composition to Laboratory Retrievals

ASTER End-member	**Qt**		**Ft**		**Microcline**		**Albite**		**RMS**
Region	$\bar{x}$	σ	$\bar{x}$	σ	$\bar{x}$	σ	$\bar{x}$	σ	$\bar{x}$
Central Dunes	+5%	+4%	+0%	+5%	+3%	+5%	+2%	+8%	-0.0010
Eastern Crescentic	-3%	+1%	+6%	+2%	+1%	+2%	+14%	+8%	-0.0016
Rosario (South)	-4%	-2%	+8%	-1%	+1%	+0%	+21%	+0%	+0.0004
Rosario (North)	+2%	-2%	+9%	+1%	+4%	+5%	+27%	+2%	-0.0001
Coastal (CO_3 rich)	+9%	+5%	+27%	+7%	+7%	+6%	+35%	+2%	-0.0005
Coastal (Siliceous)	-7%	+0%	+8%	+4%	+2%	+0%	+18%	+8%	-0.0034
Sonoyta	-5%	-9%	+10%	+2%	+2%	-8%	+31%	+0%	+0.0001
Northern Pinacate	-2%	-7%	+8%	-4%	+11%	+4%	+27%	+2%	-0.0005
Crescentic (S. Pinacate)	-7%	-1%	+13%	+5%	+2%	+4%	+16%	+5%	-0.0005
End-member Average	-1%	-1%	+10%	+2%	+3%	+2%	+21%	+4%	-0.0008
Laboratory Endmember Compared	**Total Quartz**		**Albite + Microcline**		**Total K-feldspar**		**Total Na-Feldspar**		--

Carbonate was also not used as an end-member for the final endmember suites presented here, therefore what spectral variation is available due to carbonate and other scene components are not modeled. The use of a carbonate end-member was unsuccessful for image deconvolution, retrieving 0% abundance in all areas and having high residual error. In the area of coastal carbonate rich sands, the accuracy of feldspar was adversely affected because carbonate is not modeled correctly. Where individual end-members albite and microcline are compared to the

laboratory retrievals, greater variability in accuracy was observed (Table 4). These values compare satellite retrievals to the individual end-member abundances, where microcline was overestimated by an average of 3% overall (Figure 23c, Table 4-column 3), where albite and Na-feldspar was overestimated by 20% overall in most areas of the dune field. Central star dunes were accurate with respect to both quartz and feldspar. Comparing the ASTER retrieval of albite directly with the laboratory retrieval of albite shows the relationship was generally better with only a 10% underestimation, but the spread in the range of accuracy significantly increases compared to total Na-feldspar retrieval (Figure 23e, values not shown in Table 4). In summary, the use of the 3-endmember suite accurately retrieved the areal abundances of total quartz and total feldspar to within an average accuracy of 10% (Table 4). The suite slightly overestimates K-feldspar and Na-feldspar. Accurate retrievals are observed for microcline in the Sonoyta Dunes area, the Central Dunes and the Eastern Crescentic dunes. Inaccurate results are found consistently with an overestimation of feldspar and underestimation of carbonate in coastal regions. Most of the results of composition retrievals of the NAASLED product compare well to retrievals from these mosaic data (Figure 23f). Higher RMS error was observed; albite was similarly overestimated by 20%; Na-feldspar was underestimated using albite as an end-member, and microcline was undetected except for the Sonoyta Dune area. The average NAASLED retrieval of microcline were also accurate for the Sonoyta Dune area, but spatial patterns were highly altered by the averaging of multiple data sets used to create the averaged emissivity.

Figure 23. Average ASTER-derived composition is compared to composition derived from high resolution laboratory spectra. Each point represents a pixels averaged according to sampling locations of different areas reported in Table 3. The deviation of % composition from the laboratory data are reported in Table 4. The comparisons in these figures between laboratory vs. ASTER are: (a) Total quartz vs. monocrystalline quartz image end-member; (b) Total feldspar (Ft) vs. Ft image end-member; (c) Total Na-feldspar (Fn) vs. albite image end-member; (d) Total K-feldspar vs. microcline image end-member; (e) albite vs. albite image-endmember. (f) NAASLED vs. mosaic ASTER data for all the data.

(See figure on following page)

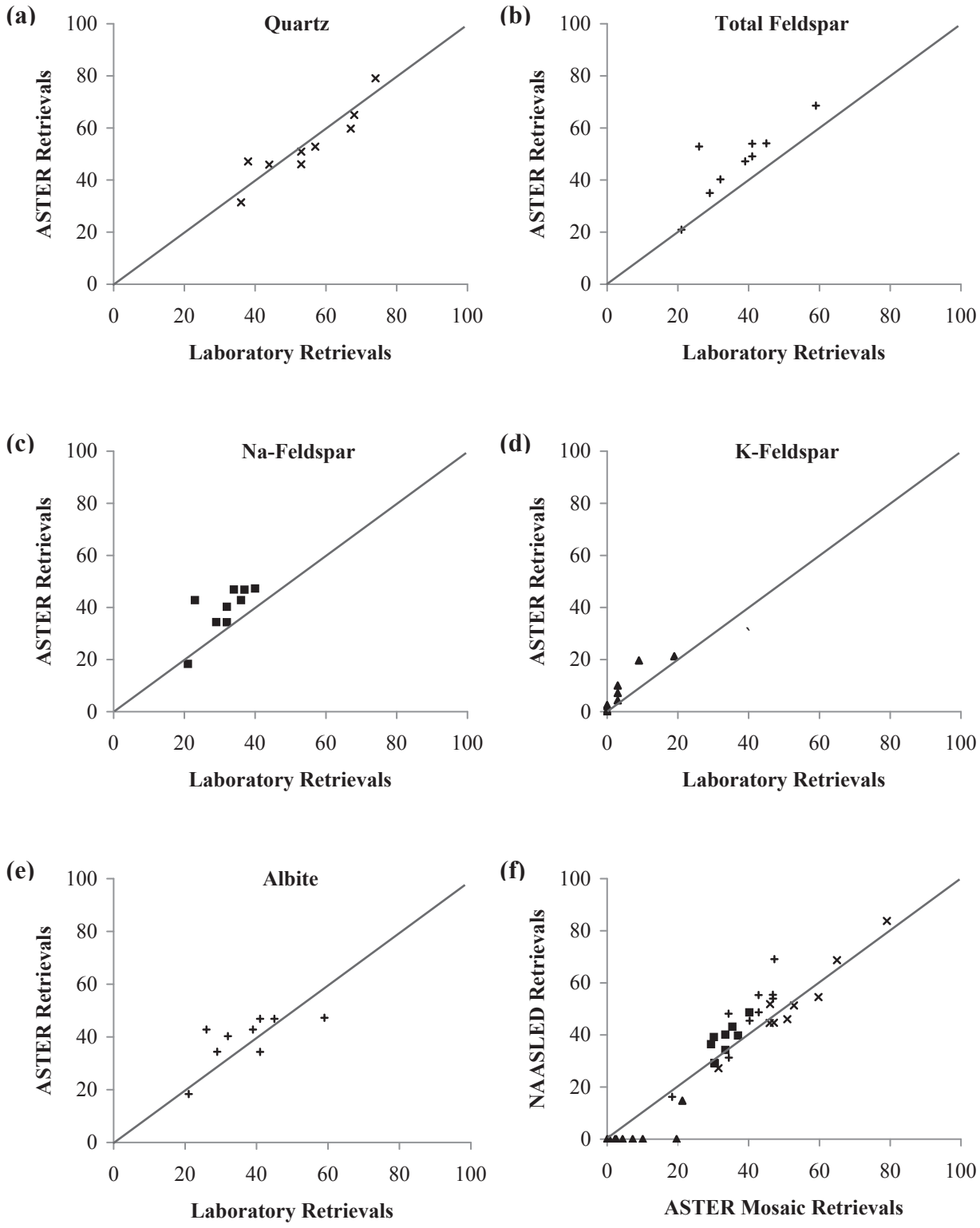

Figure 23. (See figure caption previous page)

3.4.3.3 Comparisons to Previous Composition Measurements

There are only a couple of studies that have analyzed the composition of the Desierto sands over the entire extent of the region. *Kasper-Zubilliga et al.* [2007] examined grain size distribution, mineral composition and geochemical characteristics of inland and coastal sand samples at four widely separated locations. Composition was determined by a combination of standard optical, petrographic modal analysis and energy dispersive X-ray analyses (EDXA), as described by *Rooney and Basu* [1994], to examine relationships of different sands to establish provenance. Their major conclusions important to this study were that (1) sands in the northwest dune field (Figure 9a, block B2 & B3) originated from Colorado River Delta sediment, (2) inland sand samples (Figure 9a, block F3 & F4) were significantly influenced by granitic local sources, and (3) coastal sand compositions were influenced heavily by contemporaneous input of quartz rich neritic sands (Figure 9a, block C5) also ultimately originating from the Colorado River Delta sediments, where sand near Puerto Peñasco is heavily influenced by carbonate (Figure 9a, block G6).

Table 5. Comparison of ASTER-retrieved composition to previous published data.

	[*Kasper-Zubillaga et al.* 2007]				[*Scheidt et al.* 2009]		
Region	**Qt**	**Ft**	**Lt**	**Lt***	**Qt**	**Ft**	**Lt***
El Pinacate	**82**	**7**	**9**	**11**	**50-75**	**15-37**	**10-18**
Golfo de Santa Clara	**79**	**6**	**12**	**15**	**58-81**	**21-37**	**5-15**
Puerto Peñasco	**69**	**5**	**5**	**26****	**34-56**	**0-48**	**5-42**
San Luis Rio Colorado	**77**	**8**	**11**	**15**	**55-71**	**10-35**	**8-21**

***Includes accessory lithics (heavy minerals and biogenic carbonates.)**
****High Lt due to biogenic carbonate.**
*****No carbonate endmember is modeled. Lt = Qt-Ft**

Thermal laboratory spectroscopy and ASTER-derived compositions do not conflict with these conclusions of source-deposition relationships. Our laboratory results cannot be compared to *Kasper-Zubillaga et al.* [2007] directly because sands were collected at different locations than this work. Instead, the ASTER-derived compositions were compared to the *Kasper-Zubillaga et al.* [2007] values at their general four sampling areas (Table 5). Total non-quartzofeldspathic material (total lithics or Lt) trends compare well (within 5%), but average feldspar retrieval from ASTER is greater than these previously reported values. This study showed an average 10% overestimation of feldspar from satellite data over laboratory spectra-

derived values, and the relative precision of laboratory spectra is between 3-10%. Another limitation of ASTER TIR data is the lack of a spectral band between 9 and 11 μm, where ozone absorption causes complications for orbital remote-sensing. The TIMS airborne instrument has a band at ~ 10 μm and could distinguish different feldspars (including microcline) very well. Considering this and the variation of values due to ASTER instrument noise (i.e., scan lines across the scene), previously reported values are close to the range of these ASTER values. It was noted that some of the highest quartz concentrations retrieved from ASTER data were located on beach ridges where "fresh" material is exposed and weathering rate is high. Inland ASTER retrievals are complicated by surface coatings, crust, vegetation and the integration of scene components at the 90 m spatial scale, which can conceal spectral contrast. Overall, we conclude that by considering the obvious errors in satellite retrieval, the ASTER results compare well to previously reported values of modal mineralogy. Our results also suggest that quartz has probably been overestimated by an average of 10%. Quartz percentage should not be assumed to be ≥ 90% for Desierto sands except in the most mature dune groups [*Muhs et al.* 2004]. The accuracy of point counting is about 10%, although it is not uncommon to over predict the number of quartz grains because of the difficulty in distinguishing quartz from some feldspar grains, let alone distinguishing between different feldspars, which is also very difficult [*Ramsey et al.* 1999]. The standard petrographic and sedimentological studies where establishing provenance usually emphasize a specific grain size fraction, and the finer fraction or matrix is ignored or assumed to be homogenous, which may contain important amounts of accessory, lithic, clay and silt-sized grains. Separation according to grain size is not practical if comparing lab spectra to remote-sensing measurements because the remote-sensing instrument integrates all scene components and grain sizes in its retrieval.

3.4.3.4 Visualization of Final Image Products

Compared to the traditional decorrelation stretch (DCS) of three bands, examination of a Principle Component Analysis (PCA) utilizes the full spectral variance of the ASTER TIR radiance data. For arid land surfaces, the DCS and other transformations create a reproducible color pattern that corresponds well to the general mineralogy of an area where vegetation, shade, water and other non-geological scene components are excluded [refer to *Scheidt at al.* 2008]. The variance of the first principle component (PC) band of ASTER TIR data is mostly

influenced by temperature, but the large spectral depth of quartz is also a strong influence [*Scheidt et al*. 2007]. The last PC band contains the smallest scale emissivity variations and contains the majority of noise in the data [*Richards* 1999]. The middle PC bands contain mostly emissivity information and represent composition variability. Here we display the PCA using bands 4, 3, and 1 in a RGB color composition (Figure 24a), where display of bands 4, 3, and 2 is not significantly different. The spectral contrast between ASTER radiance bands 10 through 12 is much less than between bands 14, 12, 10 used in the DCS of *Scheidt et al.* [2008]. The PCA shows similar spatial patterns as the DCS in addition to the variations observed in bands 10, 11 and 12. The color palette is also completely different from the DCS. The Sierra Pinacate quaternary basalts (Blt) is distinct from the rest of the dune field (white, pink, purple, cyan and light yellow colors, blocks F/G-3/4/5), and a significant number of different flows, craters and alluvial fans are distinguished that either highlight variations of basalt, granitic outcrops, K-feldspar rich trachyte deposits and weathering products. The crescentic dunes in the west and the southwestern portion of the star dunes (block C/D-4), and the eastern crescentic dunes (upper portion of block F/-5) have the highest yellow color value in the scene. These areas correspond to the highest quartz content, and compare directly to the red color in the composite image of fractional endmembers (Figure 24b). Linear and parabolic dunes southwest and west of the Sierra Pinacate have distinct green and blue color in the PCA (blocks G/H/I-456), which correspond to the admixing of granitic and volcanic material from local sources. Alluvial fans throughout the region have similarly quartz-poor composition. The complex crescentic dunes south of the Sierra Pinacate (between block F5 and G5) have a distinct green color to the southeast and transition to a yellow color at the northwest end of this group. This area is a transitional zone between sand populations of the K-feldspar rich Sonoyta Dune area and the quartz-rich Eastern Crescentic dunes. Color variations are highly varied along the coast, especially around the Bahia Adair, highlighting the various evaporite compositions and probably carbonate rich sands. At 90m pixel level, this area is also probably mixed with more significant amounts of vegetation. Feldspar content was overestimated from the pixels in these areas, which may be due to the higher vegetation and/or carbonate abundance, which would shallow quartz and feldspar spectral features. Vegetation and carbonate are responsible for the reddish color that appears in agricultural areas of the Colorado River (i.e., see active irrigation circles near San Luis) and the marshes of the Bahia Adair.

The Basin and Range mountains north of the Desierto have widely varying lithology ranging from older Proterozoic granites and gneiss to Tertiary basalts [*Nourse et al*. 2005]. For example, the alluvial fan of the Sierra los Alacranes (Figure 24a, block E3, aqua-green color) appears significantly different than the alluvial fan adjacent to the west of Cerro Pinto (Figure 24a, block D3, blue-magenta). In fact, differences in lithology can be distinguished between adjacent units in the Sierra los Alacranes [*Nourse et al*. 2005] using these linear deconvolution results (Figure 24b, block E3 and inset). Material weathering from the feldspar-rich leucocratic biotite granite has a greenish color (1), where to the west the more mafic units of hornblende-biotite quartz diorite, gabbro and diabase have a bluish color (2). The next unit west of this is a quartzofeldspathic gneiss, and a reddish color from quartz is present there (3). These materials are transported along the alluvial fans where it is enriched in feldspar at the dune-alluvial fan interface and dunes are quartz-rich in comparison. Considering these distinct observations of sediment transport from alluvial fans, local sources can be clearly seen as an important contribution to the spectral variation of aeolian sediments at the land surface. Based on the extent of total feldspar content surrounding the Rosario (greenish color in both Figure 24a and Figure 24b) and the prevalence of K-feldspar in the Sonoyta Dunes areas (greenish color in Figure 24b and greenish-blue in Figure 24a), local sources can be concluded to be a more abundant component to the composition of the dune field, especially because most of these source rocks are much older (excluding the basalts of the Sierra Pinacate) and have affected the composition of aeolian sediments throughout the dune field's younger existence. In Figure 24b, high RMS error occurred in areas of high vegetation and where mineralogical end-members were not modeled (i.e., the Sierra Pinacates). These areas were masked to show only the composition of aeolian sediments and dunes.

Figure 24. A principle component analysis (PCA) of ASTER TIR radiance data (PC bands 4,3,1 in RGB, respectively) (upper image). The average compositional distinctions between units are superimposed. Fractional abundance images are displayed in a color composition (lower image), where the color assignments are as follows: Quartz – red; total feldspar – green; basalt/accessory/Lt – blue. Superimposed on this mineral abundance map are dune groups [see Figure 9 (lower image), modified after *Lancaster* 1995]. ASTER has the ability to resolve and determine variable composition on alluvial fans from different sources at a high spatial resolution (inset). **(see figure on following page)**

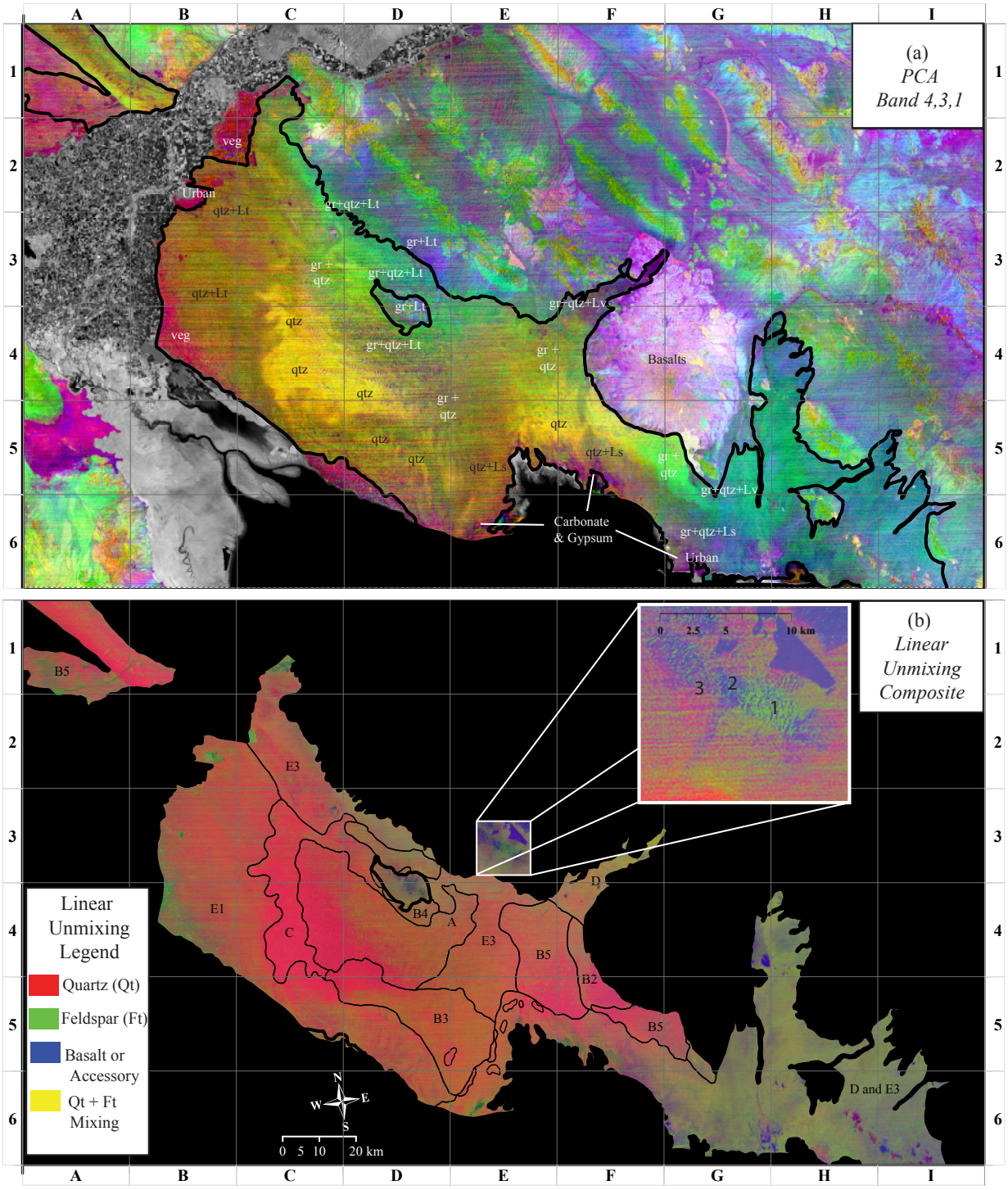

Figure 24. (See figure caption previous page.)

3.5 DISCUSSION AND CONCLUSIONS OF AEOLIAN SEDIMENT DYNAMICS AND MIXING

The goal of the analysis of thermal infrared laboratory and satellite data was to relate the spatial distribution of surface composition to the aeolian construction events of various dune groups in the Desierto. This study adds improved, more accurate spatial patterns of sediment composition to previous studies of dune patterns and morphology data. The previous remote-sensing study [*Blount et al*. 1990] did not accurately or quantitatively determine to what magnitude each of these potential sediment sources influence the sand populations of the Desierto. For example, *Blount et al.* [1990] recognized the importance of the low albedo grains in controlling the non-linear spectral response of VNIR data, but coverage of multispectral TIR data were not available at that time. For the first time, a combination of data sets were combined to examine aeolian sediment composition of the Gran Desierto, which included (1) high resolution thermal emission spectroscopy in a laboratory setting of an archive of samples representing a widespread geographic coverage of aeolian sediments and (2) spatially contiguous thermal remote-sensing data (although at a lower spectral resolution). Integration of the spatial scales of mosaicked ASTER data (90m) and the spatially interpolated, hyperspectral resolution of laboratory data was both a challenge and an advantage of the work. The complicating factor in analyzing these sand samples and remote-sensing data to understand the sand sea through time is that all results are derived from the surface only (< 5 mm). Each sample represents a small point measurement assumed to be representative of a broad area, which is a valid assumption in most parts of the dune field. Remote-sensing integrates the energy measured from a 90m area of land surface and from the uppermost surface of the sand, roughly ten times the wavelength used for analysis (≈ 100 μm). The forward assumption here is that the surface composition is generally representative of the underlying sand body. Sand transport pathways were determined using same methods used here for the Kelso Dunes where aeolian transport distance is relatively short [Ramsey et al. 1999]. For a large system such as the Gran Desierto with a very different model of sand accumulation, spatial pattern of composition did not directly reflect sand transport pathways or source-to-sink relationships, which may or may not at one time have been visible across a great distance.

In the Gran Desierto, the model for sand accumulation is unique. The emplacement history of the dunes previously described by *Lancaster et al*. [1987, 1992] has been supported by the analysis of dune morphology using a combination of a geomorphic back-stripping technique and optically stimulated luminescence (OSL) dating of sediments, which constraining the depositional history of the dunes [*Beveridge et al.* 2006]. According to Beveridge et al. [2006], the aeolian construction events have taken place in the past 25 ka. The forward sequence of events in time are: (1) late Pleistocene relict linear dunes in the central sand sea, (2) degraded crescentic forms at 12 ka, (3) early Holocene western crescentic dunes, (4) eastern crescentic dunes at 7 ka, (5) the central star dunes within the last 3 ka. The potential sediment supplies identified for these aeolian construction events were assumed to be: (a) previously stored fluvial and deltaic sediments of the ancestral Colorado River [*Merriam and Brandy* 1965], (b) coastal influx from the beaches of the Gulf of California and the Bahia Del Adair inlet [*Ives* 1959] and (c) contemporaneous influx from the lower Colorado River Valley. Other potential sources include the alluvial fan and ephemeral stream bed loads originating from the Pinacate and Basin and Range Province as major contributors [*Blount and Lancaster* 1990; *Lancaster et al*. 1989].

A "sand population" is a concept that has different meanings throughout the literature that describes a body of sediment (sand) characterized by distinct physical, geochemical and mineralogical characteristics. A sand population in an aeolian system is derived from a distinct source area, transported by wind via a transport pathway and preserved in the resulting accumulations of these sediments at the surface or in the geologic record. In this paper, the modern spatial pattern of composition at the land surface was observed and used to infer transport pathways and sources of sediment. Some complicating factors arise because the relationships between dune groups and sand populations are not straight forward. Sediment may be reworked in place several times over with changing wind patterns, altering the composition from its original, genetically related parent material. The reworking of sand by wind is responsible for essentially erasing the trace of sediment transport pathways between several source areas and dune deposition sites.

Sediment transport pathways can also be inferred from the rule of gross bedform-normal transport in dune morphology studies, but the same factors may alter the interpretation of source-deposition relationships by erasing previous dune patterns, especially for small, newer-dune forms that are easily reworked. A dune pattern reflects a stage of past climate and the wind

regime responsible for dune emplacement and its geomorphology, and overprinting of patterns of both mineralogy and dune patterns make interpretation of an aeolian system's emplacement history a formidable problem. For example, five aeolian construction events were determined from dune patterns in the Desierto [*Beveridge et al.* 2006], but these patterns do not correlate with the three potential sediment sources discussed in that work. Several morphological delineations of dune groups have been published, and even the detailed grouping presented here (Figure 9b) does not correlate exactly with the compositional variation determined here (Figure 24b). Our results suggest not all aeolian construction events directly correlate with patterns of sediment composition. A genetically unique sand population may span more than one dune pattern, and a single dune pattern may have several genetically unique sand types. Patterns and compositional trends are in fact independent. Lastly, this also leads to the conclusion that a dune pattern may be young, forming in older sediments.

A current working model of Gran Desierto dune groups are stratigraphically superimposed and juxtapositioned sand populations and/or dune patterns [*Lancaster* 1992]. The determining factor in determining these relationships from satellite data for the Gran Desierto is the ability of the instrument to resolve (1) the delineations of supersurfaces [*Lancaster* 1992] expressed as compositional/spectral variation at the surface and (2) gradational transitions between compositions of sand. The spectral variations may be subtle, non-compositional (i.e., textural, biotic plant communities, hydrology, etc.), or expressed by unmodeled end-members not used in the linear deconvolution algorithm. Gradational transitions of composition are important features in the Gran Desierto according to these results. Other abrupt spectral differences observed in remote-sensing data are commonly an effect of local variations in composition, such as dune and interdune areas throughout the dune field. The dune field has spatially diverse, heterogeneous patterns of dunes, and the aeolian system has responded to a number of external forcing factors, such as climate, tectonics and sea level. As a result, the adjacent sand compositions have both clear and non-distinct boundaries at the surface. The laboratory and ASTER thermal infrared results agree with the potential sources of sediment described by previous researchers and indicate that in general the method is working well. Moreover, the limits of precision in these techniques have been thoroughly examined with respect to mosaicked ASTER data and integrated with laboratory spectroscopy results over a large geographic area.

Coastal sands have the potential to be either rich in biogenic carbonate or enriched in quartz (siliceous sands) from the coastal area surrounding the Bahia Adair. Carbonate content winnows out quickly as sands saltate northward and sands mature quickly into the dune field. Carbonate content is indicative of a local source of sand, and is stratigraphically below the more active patches of mobile, crescentic dunes of siliceous sands and probably the Eastern Crescentic dune field. This underlying sand sheet that surrounds the Bahia del Adair contains as much as 50% carbonate, and extends along the coast to the southeast. Where carbonate content is confined to the coast, these sands are probably the parent material for parabolic and linear dunes.

Because of the significant spatial extent and high average feldspar abundance (21-60%), these results suggest that local sources are indeed a more abundant contributing source for much of the Gran Desierto than previously determined. This is especially true for dunes along the alluvial fans of the Basin and Range, surrounding the Rosario and Sierra Pinacate and in the Sonoyta Dune area. The composition of these dunes is probably more similar to other inland dunes that punctuate the Basin and Range as well as the Mojave and Sonoran Deserts where alluvial fans are major contributing sources of quartzofeldspathic sediments. For example, the Kelso Dunes system contains no more than an average of 50% quartz [*Ramsey et al.* 1999]. In the Northern Rosario dunes are close to topographic highs. These areas act as constraining barriers and source areas where plutonic and metamorphic mountain ranges contribute significant amounts of dark lithics to the dunes. Trenching in these dunes revealed pulses of dark lithic deposition through time. They do not only mantle the surface. These results suggest that these dunes are, at least partially, not characteristic of a singular quartz-rich parent material, such as the ancestral sediments of the Colorado River.

Feldspar is considered a younger source of sediment in an aeolian environment, whereas mature sands are considered to have had longer transport paths and become quartz-rich [*Muhs et al.* 2004]. Feldspar content is responsible for forming the northwest trending transition in the middle of the star dune area (Figure 24b, block D4), where feldspar (and probably hornblende and other accessory minerals) increases in concentration northeast toward the Sierra del Rosario and decreases to the southwest toward the middle of the star dune complex. In VNIR/SWIR remote-sensing data such as Landsat and ASTER, the star dunes and western crescentic dunes (Figure 24, block C4) appear as a triangular “yellowish” area, which is actually an effect of a greater abundance or reddish- and orange-colored grains in VNIR/SWIR wavelengths. Other

edges of this spectral feature are formed by a combination of geomorphic boundaries (at the southern and western edges). The northeast boundary is compositional due to local sources. In the field, the gradual compositional transition in the star dunes is unnoticeable. These data explain this transition as a gradational 30% decrease in feldspar with respect to quartz over a distance of 10 km from northeast to southwest across the star dune field.

The highest quartz content was found in the western crescentic dunes that transition to star dunes (i.e., some samples are as high as 90%), and the eastern crescentic dunes (i.e., averaging ≈ 70%). The oldest dune forms, late Pleistocene relict linear dunes, are the parent material for the youngest dune forms, star dunes, which are affected by a variable wind regime. Net sediment transport is low and significant reworking of sand is high in this depocenter. The parent material for these dunes may have been quartz-rich Colorado River sediments, but the northeast half of the star dune sediments have been affected by feldspar-rich sand from local sources. The southeastern margin is formed by the quartz-rich western crescentic dunes, and a gradual gradation in feldspar to quartz transition is not observed there. This leads to the hypothesis that the parent material of the western crescentic dunes was initially quartz-rich, characteristic of the Colorado River sediments. Likewise, the lowest feldspar abundance (and therefore highest quartz abundance) would be expected with greatest distance from sources, and these western crescentic and star dunes are the furthest dunes from alluvial fans. The entire surface of the surrounding mesa to the west and south is a deflationary, desert pavement, armored with fluvial-deltaic, gravel-sized clasts that also underlie the western crescentic dunes and western star dunes. This area, previously stored ancestral Colorado River sediments, was potentially a large "local source" of older, quartz-rich sand to the western crescentic dunes. These spectral data, i.e. bulk mineralogy, unfortunately cannot make that genetic distinction. Quartz-rich sediments are either matured sands, Colorado River sediment or both.

Quartz-rich eastern crescentic dunes can be easily explained by influx of quickly maturing (in the sense of *Muhs et al.* [2004]) siliceous sands from the coast traveling north-northwestward. The group of degraded crescentic dunes (Figure 9b, block D5) that formed at 12 ka have a composition that is difficult to explain from these data as it is relatively non-unique, lower in quartz compared to the adjacent quartz-rich star dunes to the north and sand streaks to the south. The orientation of these quartz-rich sand streaks (Figure 24b, block D5) could suggest either transport to or away from the degraded crescentic dunes. One hypothesis of the degraded

dunes and other areas of the central Desierto (i.e., sand sheets covering blocks D/E-4/5) is that these areas are deflationary or stabilizing, where sands accumulating in star dune areas and sand streaks are maturing in the direction of transport, increasing in quartz concentration and leaving older sediment of mixed composition behind. Alternatively, sand sheets and inactive sands, including the degraded crescentic dunes area, may be currently forming a stabilized surface and fine-grained crusts. Surface crust may be biogenic, an induration of silt/clay or an accumulation of salts, sulfate or carbonate. Regardless of the surface crust type, accumulation of these finer grained material at the surface imaged by ASTER (and collected from the surface in sand samples) would effectively obscure grains, reducing spectral contrast and in general shallowing spectral features of quartz and feldspar. Reduced grain size can also alter spectral features, reducing depth of spectral features. To determine these effects and to determine the original pre-stabilization sand mineralogy, spectral analysis of washed and unwashed samples should be compared in the future.

The coverage of the Sonoyta Dunes area includes an extensive area of linear and parabolic dune groups along the coastal plain between the Bahia Adair and far south to the Sierra el Alamo. The distinction between K-feldspar and Na-feldspar resulted in the determination that sands of the Sonoyta Dune area are unique, apart from the rest of both the Central Desierto dunes and the dune groups bordering the Rosario and most of the Sierra Pinacate. With this additional sediment supply to consider, the overall, geographically broader picture of the Gran Desierto revealed insight into the sequence of aeolian dune construction events of the main sand sea. The Sonoyta Dunes area has not received much, if any, attention in previous remote-sensing or other studies of Gran Desierto sand provenance. The hypotheses presented here for the Sonoyta Dunes area are: (1) an older, reworked local source of weather K-feldspar source rock, or (2) a stabilization surface, possibly related to other Gran Desierto supersurfaces, such as supersurface B of *Lancaster* [1992].

The Eastern Crescentic dunes coalesce and mix with the crescentic dunes south of the Sierra Pinacate, where these dunes admix with the compositionally distinct Sonoyta Dunes group. Here, gradational transitions in composition were observed from the remote-sensing data. Gradual transitions of composition between different dune groups generally suggests a different model of sand accumulation occurring in this area, different than the hypothesis of genetically

distinct aeolian accumulations separated by supersurfaces studied by *Lancaster* [1992] in the Rosario and Central Dunes.

Mentioned earlier, we hypothesized that Sonoyta sediment is a unique unit of sand and related to the surrounding source rocks that have a prevalence of K-feldspar. These possible local sources include currently exposed and/or eroded granitic and metamorphic rocks related to the Sierra Blanca and trachyte deposits in the Sierra Pinacate. The bed load of material from the ephemeral Sonoyta River is also a major source. The Sonoyta River transports material in pulses during wetter seasons that fluctuate with El Niño/Southern Oscillation (ENSO) cycles. The Sonoyta Dune area could represent an older, K-feldspar rich local source of sands that have been reworked in place. K-feldspar exists in source rocks near the Rosario and the Northern Pinacate dunes (e.g., Sierra del Choclo Doro), yet K-feldspar is absent as a significant component in laboratory retrievals. It is possible that the Sonoyta Dune area is able to maintain a typical suite of both Na- and K-feldspar minerals because it is far removed and topographically isolated from ancestral Colorado River sediments that would dilute (with quartz) K-feldspar concentration. Future work needs to be conducted to constrain the ages of these dunes perhaps through OSL dating techniques, measurement of sediment transport rates and including these dunes into back-stripping techniques of dune patterns. More samples throughout the area would also constrain the range and the spatial distribution of composition encountered throughout the Sonoyta Dunes area, as samples in this study were only collected from dunes immediately surrounding the Sonoyta River.

Overall, we can make some suggestion as to the relationships between sediment sources, the composition of dune sands in the Gran Desierto and emplacement history of various dune groups and patterns. These results are in agreement with previous models of the various local sources, contemporaneous influx of coastal sand and the ancestral sediments of the Colorado River. However, these results suggest that local sources were underestimated as major input to the dune field. Considering the extensive feldspar-rich sand deposits in the Sonoyta Dunes area, the overall higher than average feldspar concentration estimated in the most of the Desierto, and the gradual northeast-southwest trend of feldspar between the Basin and Range Province and the quartz rich dunes, we hypothesize that the major source of sediment is shared equally between the ancestral Colorado River sediments and the weathered quartzofeldspathic material from the alluvial fans of the Basin and Range. Dunes, thought to be genetically related to Colorado River

sediments, are most likely quartz-rich because of maturing sand populations based on the spatial patterns of composition. Western crescentic dunes have the highest likelihood of being quartz-rich ancestral sediments from the Colorado River.

This work presents a refinement to the concept of sand populations delineated by *Blount et al.* [1990] and *Blount and Lancaster* [1990]. Rather aeolian sand distribution is more appropriately represented by a continuous map of intermixing sand composition (Figure 24b). By superimposing different classifications of dune morphology types, the composition of different aeolian construction events can be evaluated. For example, the group of central star dunes (labeled as A) clearly shows a gradient of increasing quartz abundance from northeast to southwest compared to feldspar. Group B4 near the Sierra del Rosario is dominated by feldspar. Group C is dominated by quartz. The composition of eastern crescentic dunes (Group B5) transitions from high quartz abundance to feldspar abundance from south to north. The Sonoyta dune area is dominated by feldspar and local sources (Groups D and E3). These trends to not reveal the extent of abandoned ancestral Colorado River sediments as dune materials, but the pattern of local source input from the northern and eastern alluvial fans of Basin and Range mountain ranges is clear. Deflationary sediment from the desert pavements of the Mesa Arenosa and modern sand transported by westerly winds from the current Colorado River Valley is also not clear from these compositional results. Our laboratory results characterize coastal sands as a bimodal source from (1) an "underlying" sand sheet of carbonate-rich sands (Group E3) and (2) siliceous neritic sands from the coast that migrate in patches (Group B1) inland to multiple dune groups (i.e., the Eastern Crescentic, dunes adjacent to the southern Pinacate, and probably the central star dune and western crescentic dunes, prior to uplift of the Mesa Arenosa). This source is extensive throughout the Bahia Adair and probably contributes sand in other areas further southeast along the coast as source of sand to all of the linear dunes here, as well as the Sonoyta Dune group. Local sources significantly affect dunes north of the Rosario or the crescentic dunes that abut the southern rim of the Sierra Pinacate. Certainly a portion of Colorado River sediments contribute to these areas as well, but this source is masked by local source influence. The Rosario dunes are unique affected by high Na-feldspar and dark lithics, where Group B5 south of the Sierra Pinacate sands are characterized by an influence of Sierra Pinacate volcanics and K-feldspar (concluded partially by spectral variation in the PCA analysis). Ancestral Colorado River sediments, younger sand saltating from the present day Colorado River valley

and deflationary material from the Sonora Mesa and Mesa Arenosa are most likely reworked in-place in dune Groups A and C. It is concluded from this comparison that sand composition and dune patterns are independent. Certainly, correlation in some areas exists and in some cases, distinct compositions are characteristic and contemporaneous with the aeolian construction events.

The work in this Chapter demonstrated a comprehensive, quantitative approach to mapping compositional variations using ASTER TIR mosaic data. The Gran Desierto was used as an example, and the results contributed to a better understanding of aeolian system composition and how this relates to aeolian construction events and dune morphology. These mapping techniques can be applied to other dune fields and for other types of surface materials, including larger areas, such as the Sahara Desert (See Chapter 5). The limitations of mapping composition using a single mosaic of ASTER TIR data with these methods was found to be determined by spectral resolution and the unity constrain imposed in the linear spectral unmixing approach. For a dune field that is composed of 3-4 spectral endmembers (e.g., compositions), these techniques are ideal.

4.0 DETERMINING SOIL MOISTURE AND SEDIMENT AVAILABILITY AT WHITE SANDS DUNE FIELD, NM FROM APPARENT THERMAL INERTIA DATA

4.1 CHAPTER SUMMARY

Determinations of soil moisture and sediment availability in arid regions are important indicators of local climate variability, the potential for future dust emission events and the potential of desertification. Data from the Advanced Spaceborne Thermal Emission and Reflection (ASTER) radiometer are used to derive the relationships between potential soil erosion, soil moisture and thermal inertia at the spatial scale of aeolian landforms. To accomplish this, a series of cloud-free, day- and night-time ASTER image pairs were assembled between May 2000 and March 2008 for the White Sands Dune Field. The broadband albedo and brightness temperature of the land surface were derived from these data, and combined to extract apparent thermal inertia (ATI) of the land surface, a ratio of the incident to emitted radiant energy. Together with previously-developed models of soil moisture, the ATI data were extended further to derive an approximation of actual thermal inertia (TI) in order to then estimate the wind threshold velocity ratio (WTR), which is a ratio of the wind velocity thresholds at which soil erosion occurs for wet soil versus dry soil. The same data set was generated using the Moderate Resolution Imaging Spectroradiometer (MODIS) which has a higher temporal resolution but an order of magnitude lower spatial resolution in the thermal infrared (TIR). The spatial and temporal patterns of ASTER- and MODIS-derived retrievals of soil moisture compared well after scaling the ASTER albedo to that of MODIS. The ASTER-derived soil moisture retrievals and the changes through time were compared to local weather station data and independently modeled soil moisture predictions. These data sets were useful in explaining variability and the hydrologic forcing of soil moisture at White Sands, which was interpreted to be driven primarily by precipitation. The presence of a perched groundwater table may also

influence certain areas of the aeolian system. Using the related models of TI, soil moisture and the WTR, the sediment availability was determined to be consistently higher (WTR < 2.5) on dunes, active playa surfaces, and the margin of the alluvial fans adjacent to the active playas if compared to the average land surface (WTR > 3.0), including interdune areas. Sediment availability was highly variable on the playa surfaces and exhibits a trend through time similar to that of interdune areas. The sediment availability derived from ASTER can be primarily explained by the precipitation events and the number of dry days prior to the data acquisition. However other factors such as vegetation and the amount of surface crusting could also influence soil mobility, but were not measured in the field. This approach showed the highest modeled sediment availability values just days prior to the largest dust emission event at White Sands in decades. Such an approach could be extended to a global monitoring technique for arid land systems that are prone to dust storms and for other regional land surface studies in the Sahara.

4.2 INTRODUCTION

4.2.1 Geologic Setting

The White Sands Dune Field is located in the Tularosa Basin of the Rio Grande Rift in southern New Mexico and contains a central complex of crescentic dunes (Cd) that overlie sediments of Late Pleistocene pluvial Lake Otero (Figure 25) [*McKee*, 1966]. East and south along the edges of the main dune population are parabolic dunes (Pd). The aeolian system extends across the entire basin between the San Andres and Sacramento Mountains [*Fryberger* 2003; *Langford*, 2003; *Kocurek et al.* 2007]. Alkali Flat (AF), adjacent to the dune field, is a cementation surface, stabilized by the gypsum cement. The largest deflationary playa is Lake Lucero (LL), which is commonly inundated, resting in the southernmost and lowest elevation in an area of active playa surfaces (Ac). These playa surfaces are between Alkali Flat to the east and the alluvial fans of the San Andres Mountains to the west. They continue to supply new gypsum sand to the dune field, however the majority of gypsum sand has been derived from the deflation of Lake Otero during the Holocene Epoch [*Langford*, 2003]. Active sand transport is commonly observed on

both dune and playa surfaces today, and dust emission events have been documented in the field, as well as from orbital remote-sensing data.

The White Sands dune field has been interpreted as a wet aeolian system where soil moisture plays an important role in the sediment dynamics [*Kocurek and Havholm* 1994; *Crabaugh* 1994; *Kocurek et al.* 2007; *Langford et al.* 2009]. In a wet dune system, the capillary fringe of the water table is at or near the surface. Accumulation of evaporite minerals occurs with moist conditions, commonly corresponding to a relative rise of the dense, brine-rich groundwater table. During deflation, which occurs in dry conditions and a falling water table, the sediments become mobilized and the source of gypsum for the White Sands dune field. Therefore, sediment transport in this system is sensitive to changes in the regional climate that affect the hydrology of the playa [*Rosen* 1994; *Fan et al.* 1997]. The perched water table fluctuates seasonally in response to changes in precipitation, groundwater recharge/discharge and evapotranspiration within the Tularosa Basin [*Allmendinger* 1972; *Allmendinger and Titus* 1973; *Langford et al.* 2009]. *Fryberger* [2003] hypothesized that groundwater is controlling dune morphology at White Sands. *Langford et al.* [2009] confirmed this using a combination of GPS topographic surveys and groundwater measurements of water table height and salinity, and describe the parabolic dunes atop a topographic high relative to the lower crescentic dunes of the central dune field, an area of deflation. This topographic high contains a lower salinity groundwater lens recharged by precipitation, where the crescentic dune field is influenced by high saline brine [*Langford et al.* 2009]. The parabolic field is largely stabilized by vegetation, but sand is mobile on isolated parabolic dunes and ridges. Interdune areas are stabilized by vegetation and biotic soil crusts, where mobile sand has been observed as widely scattered 2 to 3 mm patches overlain on the thicker biotic soil crust [*Langford et al.* 2009].

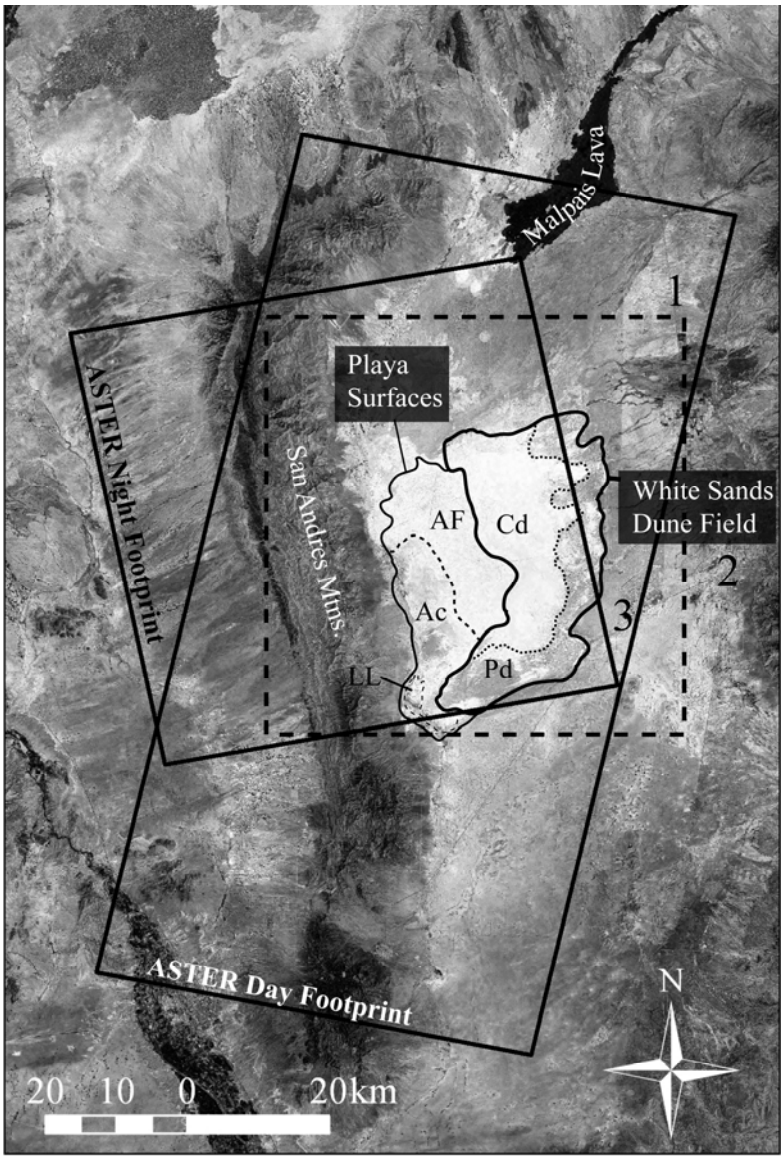

Figure 25. Location map of the White Sands National Monument study area centered at 32.9ºN, 106.3ºW generated from a panchromatic mosaic image acquired by Landsat ETM+ between September 1999 and August 2002 [*MDA Federal* 2004]. Complete spatial coverage of the region requires two consecutive ASTER daytime scenes (60km by 120km), whereas the night data is generally centered over the dunes and requires only one scene (60 km x 60 km). Important geographic areas are indicated: Lake Lucero (LL), Alkali Flat (AF) and the White Sands dune field, which includes the central core of crescentic dunes (Cd) and the parabolic dunes (Pd) to the south and east. Active playas (Ac) that continually resupply sediment to the dune field are south of Alkali Flat. The dashed inset box 1 indicates the area shown in Figure 29. The other numbers on the map indicate the locations of the local meteorological stations for the daily (2) and hourly (3) weather data.

4.2.2 Previous Remote-Sensing of Soil Moisture Studies

Several studies have examined the effect of soil moisture on the erosion potential of sediment [*Belly* 1964; *McKenna-Neuman and Nickling* 1989; *Saleh and Fryrear* 1995; *Shao et al.* 1996; *Chen et al.* 1996]. Aeolian erosion does not occur until the force of the wind exceeds the forces holding soil particles in place, including the cohesive force between particles due to soil moisture [*Chepil* 1956]. The velocity of the wind at which aeolian soil erosion takes place is the wind velocity threshold (u_{*t}). A parameterization for the large-scale simulation of dust emission events has been developed (i.e., the DREAM model) that attempts to predict the wet to dry erosion wind velocity thresholds for different soils [*Marticorena and Bergametti* 1995; *Fécan et al.* 1999; *Nickovic et al.* 2001; *Peŕez et al.* 2006a, 2006b]. The threshold wind velocity has a direct relationship to surface roughness and soil moisture, which are affected by the clay content because of its ability to retain soil water [*Fécan et al.* 1999].

Measuring soil moisture on large scales is important to hydrologic, aeolian and agriculture studies. However, field-based investigations in arid lands are difficult for several reasons. These areas typically experience a quick dry-down following rainfall, and soils in aeolian environments are commonly very permeable. With respect to soil mobility, the upper few centimeters are the most critical for understanding erosion potential and aeolian processes. Field measurements of soil moisture over a large geographical region are difficult and expensive, and require a significant amount of specialized equipment and man-power. Estimating soil moisture is desert regions is also highly problematic because of their remote location, difficult working conditions and the need for very sensitive in-situ sensors that can measure the low water content of desert soils. Accurate measurements for soil moisture in playas with high salinity are also difficult for standard soil moisture probes.

Synoptic regional to continental scale soil moisture mapping has been successful using spaceborne data, particularly with passive microwave remote-sensing instruments [*Jackson* 1993; *Jackson* 1997; *Bindlish et al.* 2003] such as the airborne Polarized Scanning Radiometer (PSR) and the spaceborne Advanced Microwave Scanning Radiometer (AMSR-E) where reasonable estimates have been obtained, even for vegetated areas [*Njoku et al.* 2003; *Bindlish et al.* 2006]. The future Soil Moisture Active Passive (SMAP) instrument planned for launch after 2011 will combine a passive microwave radiometer and high-resolution active radar and produce

data with a spatial resolution of 1-3 km and a temporal resolution of 12 hours. It will also retrieve measurements of the surface and vegetation roughness, which are useful for aeolian studies [*Entekhabi et al.* 2008]. Even though radar and passive microwave remote-sensing are effective in retrieving soil moisture at a high temporal resolution, the currently available AMSR-E data with a spatial resolution of 25 km per pixel limits the interpretation for smaller-scale aeolian landforms (i.e., dune, interdune and playas) at White Sands. The area of interest for this study is roughly 26 x 26 km, yielding approximately one pixel from AMSR-E per acquisition. The aeolian features of interest for this study are far below the spatial scale of the currently available spaceborne passive microwave remote-sensing instruments.

Soil moisture has also been retrieved from apparent thermal inertia measurements using visible and thermal infrared data. Previous studies have used Advanced Very High Resolution Radiometer (AVHRR) data to determine land surface thermal inertia [*Xue and Cracknell* 1995]. Relationships between thermal inertia and soil moisture have been derived from the Moderate Resolution Imaging Spectroradiometer (MODIS) data [*Cai et al.* 2005; 2007a and others]. Because relationships exist amongst thermal inertia, soil moisture and the erosion potential of sediment, aeolian sediment dynamics that are commonly controlled by the wetting and drying cycles can be directly extracted from these data. Quantification of aeolian sediment erosion potential at a high spatial resolution using satellite-derived data is particularly valuable to the validation of models that predict desert drying and dust cycles. The unique properties of the Advanced Spaceborne Thermal Emission and Reflection (ASTER) radiometer provide this capability to monitor and model the small-scale spatial variability of an active aeolian system. ASTER has been used to examine large-scale aeolian systems after mosaicking data [*Scheidt et al.* 2008a], and the temporal frequency of ASTER was leveraged to examine changes in sediment dynamics through time [*Katra et al.* 2008; *Katra and Lancaster*, 2008].

4.2.3 Approach

The approach presented here of determining the ASTER-derived sediment availability using the relationship between thermal inertia, soil moisture and the erosion potential of soil is unique in its ability to directly retrieve an approximation of the WTR. At the ASTER spatial resolution, the WTR is at the scale of the aeolian landforms found at White Sands. This paper investigates these

relationships for both ASTER and MODIS data, but focuses on ASTER to document the small-scale patterns of sediment availability through time. The main objectives are: (1) to present a methodology for applying the *Xue and Cracknell* [1995] thermal inertia model to multispectral high spatial resolution ASTER data, and compare the results to the higher temporal resolution/lower spatial resolution MODIS data, (2) to examine the spatial and temporal variation of thermal inertia, coincidently with soil moisture, the climate, and the geomorphology of the White Sands aeolian system, and (3) to demonstrate the potential of remote sensing as a predictive monitoring tool to retrieve the WTR, which is a quantitative measure of sediment availability and erosion potential.

4.3 BACKGROUND

4.3.1 Aeolian Sediment Dynamics

The prediction and monitoring of aeolian erosion is important for the management and conservation of natural resources, agricultural land, and the prediction of air pollution. The initiation of movement of sand and mineral dust has been extensively studied [*Nickling and McKenna-Neuman*, 1994; *Greeley and Iversen* 1985]. The initiation of sand saltation and dust emission occurs once the shear stress exerted by the wind onto the sediment surface overcomes the frictional and cohesive forces holding that sediment in place. Sediment that has a high potential for wind erosion and subsequent transport is defined as having high sediment availability [*Kocurek and Lancaster* 1999]. Sediment availability can also be defined as the percentage of surface soil particles for which the threshold wind velocity is exceeded under a given set of conditions [e.g. *Nickovich et al.* 2001; *Shao et al.* 1993]. The threshold wind speed or wind shear stress for entrainment of sediment depends on a number of complex and interdependent factors including the: grain size, presence of roughness elements (e.g., vegetation), soil moisture, soluble salts, crusting, and cohesion [*Nickling and McKenna-Neuman* 1994]. These factors determine the availability of sediment for transport in a basin-scale, sediment state model for an aeolian system [*Kocurek and Lancaster* 1999]. Sediment is

continually reworked within a single aeolian system on short time scales, resulting in considerable spatial and temporal variation in sediment transport, storage and availability.

Soil moisture plays a major role in affecting the erosion potential of sediment. Sediment availability decreases with increasing soil moisture because of the adhesive and capillary forces that bind wet sediment particles together [e.g., *Hotta et al.* 1984; *Sherman* 1990; *McKenna-Neumann and Nickling* 1989]. Soil composition, specifically the clay content, is an important factor in determining the degree of the soil's water retention and therefore the cohesion between particles [*Fécan et al.* 1999]. The effect of soil moisture on the erosion of wet sand and soil has been modeled theoretically and empirically by several researchers [e.g. *Chepil* 1956; *Belly* 1964; *Shao et al.* 1996; *Fécan et al.* 1999; and others]. *Cornelis and Gabriels* [2003] found that empirical models from *Chepil* [1956] and *Saleh and Fyrear* [1995] were good predictors because they use the soil moisture content of the upper most surface layer for the prediction of the threshold wind velocity. Soil composition and textural characteristics of an aeolian environment are expected to change in response to hydrologic and climatologic conditions, such as the flux of rainfall, soil moisture and groundwater. In a playa environment, for example, these changes can occur rapidly on the scale of minutes to days, where drought then becomes an important concern with respect to land use. The capacity of the surface to store water also varies spatially with the periodic inundation and drying of playa lake beds, the influx of fine silt and clay [*Reheis* 2006], and the crusting of evaporite minerals [*Kerr and Langer* 1965]. Dry conditions favor a higher degree of sediment availability, whereas wet conditions result in sediment immobilization [e.g., *Reynolds et al. 2007*; and others].

4.3.2 Thermal inertia-modeling

The prediction and monitoring of aeolian erosion is important for the management and conservation of natural resources, agricultural land, and the prediction of air pollution. The initiation of movement of sand and mineral dust has been extensively studied [*Nickling and McKenna-Neuman* 1994; *Greeley and Iversen* 1985]. The initiation of sand saltation and dust emission occurs once the shear stress exerted by the wind onto the sediment surface overcomes the frictional and cohesive forces holding that sediment in place. Sediment that has a high potential for wind erosion and subsequent transport is defined as having high sediment

availability [*Kocurek and Lancaster* 1999]. Sediment availability can also be defined as the percentage of surface soil particles for which the threshold wind velocity is exceeded under a given set of conditions [e.g., *Nickovich et al.* 2001; *Shao et al.* 1993]. The threshold wind speed or wind shear stress for entrainment of sediment depends on a number of complex and interdependent factors including the: grain size, presence of roughness elements (e.g., vegetation), soil moisture, soluble salts, crusting, and cohesion [*Nickling and McKenna-Neuman* 1994]. These factors determine the availability of sediment for transport in a basin-scale, sediment state model for an aeolian system [*Kocurek and Lancaster* 1999]. Sediment is continually reworked within a single aeolian system on short time scales, resulting in considerable spatial and temporal variation in sediment transport, storage and availability.

Soil moisture plays a major role in affecting the erosion potential of sediment. Sediment availability decreases with increasing soil moisture because of the adhesive and capillary forces that bind wet sediment particles together [e.g., *Hotta et al.* 1984; *Sherman* 1990; *McKenna-Neumann and Nickling* 1989]. Soil composition, specifically the clay content, is an important factor in determining the degree of the soil's water retention and therefore the cohesion between particles [*Fécan et al.* 1999]. The effect of soil moisture on the erosion of wet sand and soil has been modeled theoretically and empirically by several researchers [e.g., *Chepil* 1956; *Belly* 1964; *Shao et al.* 1996; *Fécan et al.* 1999; and others]. *Cornelis and Gabriels* [2003] found that empirical models from *Chepil* [1956] and *Saleh and Fyrear* [1995] were good predictors because they use the soil moisture content of the upper most surface layer for the prediction of the threshold wind velocity. Soil composition and textural characteristics of an aeolian environment are expected to change in response to hydrologic and climatologic conditions, such as the flux of rainfall, soil moisture and groundwater. In a playa environment, for example, these changes can occur rapidly on the scale of minutes to days, where drought then becomes an important concern with respect to land use. The capacity of the surface to store water also varies spatially with the periodic inundation and drying of playa lake beds, the influx of fine silt and clay [*Reheis*, 2006], and the crusting of evaporite minerals [*Kerr and Langer* 1965]. Dry conditions favor a higher degree of sediment availability, whereas wet conditions result in sediment immobilization [e.g., *Reynolds et al. 2007*; and others].

4.4 METHODS

This section describes the data used in the study, and how those data were used in the thermal inertia model. A detailed review of the ASTER and MODIS data sets and the thermal inertia models, soil moisture and the WTR are given. A list of parameters is given here for reference. The focus of this study is aeolian landforms on the spatial scale of tens to hundreds of meters, an ideal target for ASTER. However, MODIS data are compared to ASTER in order to assess the effects of high temporal versus high spatial resolution data.

4.4.1 List of Model Parameters

A_n	Fourier series coefficient
α	latitude of pixel
a	albedo, unitless
ATI	apparent thermal inertia
C_t	atmospheric transmittance
c	specific heat, J kg^{-1} K^{-1}
d_s	soil density, kg m^{-3}
d_θ	water density, kg m^{-3}
ρ	density, kg m^{-3}
K	thermal conductivity, W $m^{-2}K^{-1}$
k	attenuation constant
P	thermal inertia, J m^{-2} $s^{-1/2}$
TI	modeled thermal inertia, J m^{-2} $s^{-1/2}$ (or TIU)
p	precipitation, mm
S_0	solar constant, W m^{-2}
T_0	initial temperature, K
T_a	diurnal temperature amplitude, K
T_1	day temperature at t_1, K
T_2	night temperature at t_2, K
T_n	night atmospheric temperature, K
T_d	day atmospheric temperature, K
T_{max}	estimated maximum day temperature, K
T_{min}	estimated minimum night temperature, K
ΔT	brightness temperature difference, K
t_1	day satellite overpass time
t_2	night satellite overpass time
Δt	time difference between satellite overpasses
t_{max}	time of maximum daytime temperature
t_{min}	time of minimum nighttime temperature
$u_{*t\theta}$	wet soil threshold wind velocity (m s^{-1})

u_{*td}	dry soil threshold wind velocity (m s^{-1})	θ'	absorbed soil water, %
		x_n	reflectance or emissivity value of spectral band n
δ_n	phase difference terms		
δ	solar declination of pixel	ω	angular frequency of Earth
θ	volumetric soil moisture, %		

4.4.2 Remote-sensing Data of White Sands Dune Field

Several studies have compared ASTER and MODIS data products, such as retrievals of reflectance and radiance [*Miura at al.* 2008], emissivity and albedo [*Zhou et al.* 2003], and emissivity [*Jacob et al.* 2004] and temperature [*Liu et al.* 2007]. Good agreement was found between MODIS and ASTER temperatures [*Jacob et al.* 2004]. The resulting MODIS and ASTER reflectance values and vegetation indices compared well in the radiometric compatibility study of *Miura et al.* [2008]; however, (a) the values compared were resampled to a spatial resolution of 5 km, and (b) the study concluded that the method of the atmospheric correction for ASTER reduced the overall quality of the standard reflectance product. A detailed discussion of the different atmospheric correction methods used to generate standard reflectance products is given in *Miura et al.* [2008]. The radiative transfer code and approach to correcting scattering terms are different, as well as the sources of ozone and water vapor, and the lack of an aerosols correction for the ASTER reflectance product. The basic differences between the instruments relevant to this study are summaries in Table 6, and the separate treatment of temperature and reflectance data of the two instruments will be discussed in the following sections.

Table 6. The details and characteristics of the ASTER and MODIS instruments and data products used in this study are compared [after *Miura et al.* 2008]. The instruments have several spectral bands in similar locations; however differences are present between the atmospheric correction schemes, as well as the bands used for broadband albedo calculations.

Instrument Characteristic	ASTER	MODIS
Swath Width	60 km	2,330 km
Scanner	push-broom (VNIR/SWIR) whisk-broom (TIR)	whisk-broom
Spatial and Resolution at Nadir	VNIR bands 1-3: 15 m SWIR bands 4-9: 30 m TIR bands 10-14: 90 m	VNIR bands 1-2: 250 m SWIR bands 3-7: 500 m TIR bands 8-36: 1000 m
Radiometric Resolution	VNIR: NE$\Delta\rho \leq 0.5$ % SWIR: NE$\Delta\rho \leq 0.5 - 1.5$ % TIR: NE$\Delta T \leq 0.3$ K	TIR: NE$\Delta T = 0.25 - 0.05$ K
Geolocation Accuracy	± 15 m	± 50 m
Radiometric Accuracy	4%	2%
Radiative Transfer Code	MODTRAN	6S code
Ozone	NCEP TOVS	NASA TOMS
Water Vapor	NCEP GDAS	MODIS water vapor
Aerosol	No correction; $\rho = 0$	MODIS aerosols
Atm. Corr. Accuracy	14% for $\rho < 0.1$; 7% for $\rho > 0.1$	5-9% for clear-high ρ
Spectral Albedo Product	N/A	MOD43 (V5)
Reflectance Product	AST07XT	MOD09 (V5)
• VNIR	x_1 (0.52-0.60 μm) x_3 (0.78-0.86 μm)	x_3 (0.46-0.48 μm) x_4 (0.54-0.56 μm) x_1 (0.62-0.67 μm) x_2 (0.84-0.87 μm)
• SWIR	x_5 (2.15-2.18 μm) x_6 (2.18-2.22 μm) x_8 (2.29-2.36 μm) x_9 (2.36-2.43 μm)	x_5 (1.23-1.25 μm) x_7 (2.11-2.15 μm)
Thermal Radiance Product	AST09T	MOD021KM (V5)
• TIR	x_{10} (8.125-8.475 μm) x_{11} (8.475-8.825 μm) x_{12} (8.925-9.275 μm) x_{13} (10.25-10.95 μm) x_{14} (10.95-11.65 μm)	x_{29} (8.400-8.700 μm) x_{31} (10.78-11.28 μm) x_{32} (11.77-12.27 μm)

MODIS and ASTER collect coincident reflected and emitted radiance, but at much different spatial, temporal and spectral scales. ASTER acquires data at a repeat time of about 16 days, but this frequency depends on latitude and off-axis pointing. MODIS data are generally acquired twice every 24 hours (once daily and once nightly) for the White Sands study area. ASTER was designed to acquire repetitive, high spatial resolution, multispectral data over the VNIR, SWIR TIR portions of the spectrum [*Yamaguchi et al.* 1998; *Abrams* 2000; *Pieri and Abrams* 2004]. ASTER is comprised of three subsystems with three channels in the VNIR, six channels in the SWIR, and five channels in the TIR, and having spatial resolutions of 15 m, 30 m, and 90 m, respectively. ASTER acquires routine day and night time TIR data, as well as day time data in the VNIR and SWIR. However, after April 23, 2008 the SWIR data were no longer available due to a malfunction in the SWIR subsystem.

From 2000 to 2008, there were 54 day- and 70 night-time, cloud-free acquisitions of the White Sands area by ASTER. The satellite footprints of the day and night data acquisitions have different orientations and only the intersection of these over the White Sands study area were used (Figure 25). This reduced the large dataset to seven day-night image pairs for this study. Each image pair had a minimum time difference (Δt) of 36 hours (Table 7). Ideally, satellite acquisitions should occur very close to the times of maximum and minimum diurnal temperatures for modeling ATI. However, this is not possible with the ASTER orbits at this latitude. Furthermore, with a greater Δt, the probability increases of unexpected anomalies unrelated to the diurnal cycle of solar heating and cooling (e.g. rain, large wind events, etc.). The night image acquisitions occurred at about 22:10 local MST and the day image acquisitions about 36 hours later. MODIS data can be acquired with a $\Delta t \approx 12$ hours between day and night acquisitions, but only the MODIS data approximately nadir/coincident with ASTER were used in this study to allow direct comparisons between the instruments. The calibrated data sets from the MODIS and ASTER instruments were then used to calculate the key inputs of the thermal inertia model: albedo (a) and the day-night temperature difference (ΔT).

4.4.3 Temperature Retrieval

Day and night land surface temperatures (LST) were extracted from ASTER TIR data using the emissivity normalization method [*Realmuto* 1990; *Kahle and Alley* 1992]. The temperature difference (ΔT) was calculated for each of the day/night image pairs from both the MODIS and ASTER data. No manipulations or scaling calculations were applied to the temperature data, and the agreement between the average ΔT of MODIS and ASTER through time was within the MODIS overall accuracy (± 2 K). However, where compared to MODIS data, ASTER had a 15% larger range in temperature (ΔT) data most likely due to higher spatial resolution.

The LST & emissivity product (MOD11_L2) provided temperature retrievals without complete spatial coverage of the White Sands Dune Field (Figure 26a). This processing artifact is due to a false detection of cloud pixels because of the highly reflective gypsum composition of the playa and dune surface. A similar effect occurs over areas of mountain snow in the Sacramento Mountains just east of the dune field. Day and night land surface temperatures were retrieved using the emissivity normalization method [*Realmuto* 1990; *Kahle and Alley* 1992] from the calibrated top of atmosphere (TOA) thermal radiance from bands 29, 30 and 31 of the MOD021KM data product. Approaches to the accurate geolocation of MODIS data to achieve even sub-pixel accuracy are discussed in *Wolfe et al.* [2002], but the geographic coregistration between MODIS day and night temperature data for White Sands was found to be accurate at the 1 km spatial resolution. The AST_09T TIR standard data product has been radiometrically, geometrically, and atmospherically corrected *[Thome et al.* 1998]. Coregistration between day and night ASTER data was found to be poor [*Iwasaki and Fujisada* 2005a], with a spatial offset of similar land features by as much as 500 meters in some scenes. The night time ASTER TIR data's coregistration accuracy were quality checked. Errors were corrected by coregistering the data to daytime data with an accuracy of at least half of an ASTER TIR pixel (±45 m). Day and night land surface temperatures (LST) were extracted from ASTER TIR data using the emissivity normalization method [*Realmuto* 1990; *Kahle and Alley* 1992]. The temperature difference (ΔT) was calculated for each of the day/night image pairs from both the MODIS and ASTER data according to the TI model described below. The TIR bands used from the ASTER and MODIS satellites are compared in Table 6.

4.4.4 Broadband Albedo Estimation

Broadband albedo (*a*) was calculated directly from surface spectral reflectance products of both MODIS and ASTER data using the approach of *Liang* [2000]. Because of spatial resolution effects and differences in atmospheric correction techniques, ASTER broadband albedo was significantly higher than MODIS values. ASTER broadband albedo was scaled to that of MODIS for this study as a correction method for several reasons: (a) the MOD09 reflectance product was concluded to have a more accurate atmospheric reflectance correction than the ASTER reflectance product [*Miura et al.* 2008], (b) ASTER broadband albedo values were overestimated (> 1.0) in some areas of the dune field, and (c) the use of previously published relationships between the TI and soil moisture have been developed for MODIS data. After scaling, the ASTER broadband albedo data have the same mean but still have a larger dynamic range (~20%) than MODIS data, which is expected for an instrument of higher spatial resolution.

The preferred data input for narrowband to broadband albedo determination is the MOD43 spectral albedo product [*Liang* 2000]. The 1 km spatial resolution spectral and broadband albedo data from MODIS is generated from cloud-free, atmospherically-corrected, multi-angle reflectance data over a sixteen day period [*Schaaf et al.* 2002]. However, for all daytime satellite overpasses in the White Sands Dune Field area, spatial coverage of the albedo retrievals is limited, leaving gaps in the most critical area of the study (Figure 26a). These data were falsely flagged as cloud by the standard processing algorithm and ignored. In version 5 of the MODIS data, retrieval only occurs if there are at least three non-cloud acquisitions for a given location. The processing constraints on the MOD43 spectral albedo product are intended to produce a high quality, cloud-free product, and these constraints can be relaxed in order to generate data over bright targets that would normally be classified as cloud [*Schaaf*, personal communication]. However, even with a relaxation of these quality constraints allowing for the retrieval of albedo values, these data would be averaged over multiple dates and viewing angles over a several day period. Consequently, because of the time constraint needed for Δt in the TI model, the accuracy of the TI retrieval would be adversely affected. TI retrieval is dependent on a time constraint of 36 hours for these ASTER data (and potentially 12 hours for MODIS) in order to limit the temperature change to only the effects of diurnal solar heating and cooling. In order to avert this issue, spectral reflectance (MOD09) can be used if the surface is assumed to

be Lambertian for small viewing and solar angles [*Liang*, personal communication]. Therefore, the broadband albedo, *a*, was calculated directly from the MOD09 reflectance values using the approach of *Liang* [2000]:

$$a = 0.160(x_1) + 0.291(x_2) + 0.243(x_3) + 0.116(x_4) + 0.112(x_5) - 0.081(x_7) - 0.015, \quad (10)$$

where x_n is the reflectance value of spectral band *n* (Table 6). For ASTER, the AST_07XT standard surface reflectance product includes bands from the VNIR and cross-talk corrected SWIR spectral region [*Iwasaki et al.* 2002; *Tanooka et al.* 2003; *Iwaski and Tanooka* 2005b]. Assuming a Lambertian surface, the broadband albedo, *a*, was calculated using the methodology of *Liang* [2000] directly from the AST_07XT values:

$$a = 0.484(x_1) + 0.335(x_3) + 0.324(x_5) + 0.551(x_6) + 0.305(x_8) - 0.367(x_9) - 0.015, \quad (11)$$

where x_n is the reflectance value of spectral band n (Table 6). This method of calculating broadband albedo would not be possible for ASTER data after April 23, 2008. Beginning in May 2007, ASTER SWIR data was observed to have anomalous saturation of values in bands 5 through 9 due to increasing SWIR detector temperature which reduces the dynamic range of the data. This is a potential problem for bright desert scenes such as the White Sands Dune Field. The data acquired for this study were reprocessed with the current radiometric correction, and no saturated pixels or anomalous striping were observed. The last date of the data used in this study was March 10, 2008, where data after April 23, 2008 exhibited saturated values in the SWIR bands due to the rapid degradation of the detectors. Data after April 2008 were determined to be unusable; ASTER SWIR detectors were no longer functioning after January 13, 2009.

Preliminary analysis revealed differences between the broadband albedo calculated from MODIS and ASTER, even though these values should be similar because the data are acquired at approximately the same time from the same satellite. The maximum and average values of broadband albedo of the White Sands Dune Field calculated from ASTER data were consistently higher than those calculated from MODIS data. In some isolated areas of the very bright playa surface (less than 100 pixels), the albedo was greater than 1.0. These effects are due to the original data and not the broadband calculations. Where similar bands were compared from

common areas at White Sands, the AST07XT data were higher than the MOD09 reflectance data for the White Sands data. The mean differences were between 10-30% for TOA radiance and 30-70% for corrected reflectance values. *Miura et al.* [2008] found a mean difference of ~3% between ASTER and MODIS red and near-infrared reflectance (NIR) bands at 5 km spatial resolution. Some of this variability was expected due to the differences between the ASTER and MODIS spatial resolutions and atmospheric correction techniques. With lower spatial resolution, dynamic range was also expected to be lower because less mixing of scene components in each pixel occurs in data from an instrument of higher spatial resolution. The difference in broadband albedo between the two instruments was also likely due to the result of different atmospheric correction schemes. ASTER broadband albedo was scaled to the MODIS broadband albedo for this study. This linear scaling shifted the peaks of the data (a bimodal frequency distribution) into agreement (Figure 26b). After scaling, the ASTER broadband albedo data had the same mean but still had a larger dynamic range (20%) than MODIS data, which was expected for an instrument of higher spatial resolution.

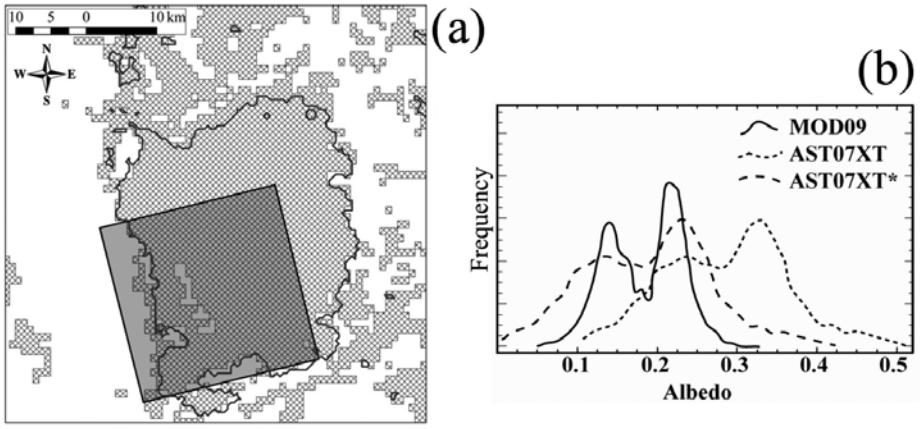

Figure 26. (a) The standard MODIS product, MOD43 broadband albedo, has missing data in the White Sands study area because of the quality constraints used to create the cloud-free data product. The area of missing data retrievals from the standard albedo product is indicated on the map with a solid line, where the hatched areas represent missing temperature retrievals from the MOD11 standard LST and emissivity product. The gray inset box indicates the Figure subset used for Figure 29. (b) ASTER albedo data were scaled to MODIS data: the frequency distributions of MODIS reflectance from the MOD09 product (solid line), ASTER reflectance from the AST07XT product (short-dashed line) and the resulting, scaled ASTER reflectance (long-dashed line with asterisk).

4.4.5 Thermal inertia model

The temperature difference and broadband albedo results were used as input to the simplified thermal inertia model given by *Xue and Cracknell* [1995] that can be used for areas of variable soil moisture. The model was reproduced for this study in the Interactive Data Language (IDL) for use in Environment for Visualizing Images (ENVI) software using the MODIS and ASTER data and metadata as inputs. Applying this model to remote-sensing image data resulted in thermal inertia unit (TIU) maps at a spatial resolution equal to that of the input data (i.e., 90 m/pixel for ASTER). The data produced in this paper are reported and discussed as approximated TI data, which represents ATI at the scale and units of real thermal inertia (*P*). Where compared to MODIS results, ASTER data values had a 25% larger range in TI retrievals directly related to the larger range of albedo values.

Xue and Cracknell [1995] presented a simplified TI model that can be used for areas of variable soil moisture. They also present a sensitivity analysis to input parameters and an example of its operational use to derive ATI and an approximation of TI from AVHRR data, utilizing phase angle information and the magnitude of the diurnal temperature change [*Xu and Cracknell*, 1995]. A thorough description of the model's applications utilizing MODIS data can be found in *Cai et al*. [2005; 2007a]. The model is shown below for clarity of the method used in this paper and to correct discrepancies between previously published versions of the equations in *Cai at al.* [2005] *and* [2007a]. From *Xue and Cracknell* [1995] thermal inertia (*P*) is defined as:

$$P = \frac{(1-a)S_0 C_t}{\Delta T\sqrt{\omega}}\left\{\frac{A_1\left[\cos(\omega t_2 - \delta_1) - \cos(\omega t_1 - \delta_1)\right]}{\sqrt{1+\frac{1}{b}+\frac{1}{2b^2}}} + \frac{A_2\left[\cos(\omega t_2 - \delta_2) - \cos(\omega t_1 - \delta_2)\right]}{\sqrt{2+\frac{\sqrt{2}}{b}+\frac{1}{2b^2}}}\right\} \quad (12)$$

where, S_0 is the solar constant (W/m^2), C_t is the atmospheric transmittance (assumed for this study to be 0.75), ω is Earth's angular frequency, a is the broadband albedo derived from satellite image data, and b is dependent on the time of maximum daytime temperature t_{max} estimated from the nearest ground based weather station at the White Sands Dune field:

$$b = \frac{\tan(\omega t_{\max})}{1-\tan(\omega t_{\max})} \quad (13)$$

Phase difference terms are calculated from b as:

$$\delta_1 = \arctan\left(\frac{b}{1+b}\right) \tag{14}$$

$$\delta_2 = \arctan\left(\frac{b\sqrt{2}}{1+b\sqrt{2}}\right) \tag{15}$$

The coefficient of Fourier series (A_n) is calculated as:

$$A_n = \frac{2\sin\delta\sin\alpha}{\pi}\sin(n\psi) + \frac{2\cos\delta\cos\alpha}{\pi\left(n^2-1\right)}\left[n\sin(n\psi)\cos\psi - \cos(n\psi)\sin\psi\right] \tag{16}$$

where, δ is the solar declination, α is the latitude and:

$$\psi = \arccos\left(\tan\delta\tan\alpha\right) \tag{17}$$

t_1 and t_2 are the times of maximum and minimum temperatures, typically considered to be 14:00 and 2:00 local time. However, the satellite overpass times obtained from satellite metadata are at ≈11:00 and ≈22:10 local U.S. MST respectively. The general diurnal temperature cycle of the land surface is driven by insolation, and an accurate estimation of the LST temperature wave was needed in order to predict the maximum and minimum temperatures at other times. The shape of the LST wave has been described the increasing temperature according to a single cosine function, followed by a period of cooling where the shape of the temperature curve is modified by an exponential decay in temperature:

$$T(t) = \begin{cases} T_0 + T_a\cos\left(\dfrac{\pi}{\omega}\left(t - t_{\max}\right)\right), & t < t_s \\ T_0 + T_a\cos\left(\dfrac{\pi}{\omega}\left(t - t_{\max}\right)\right)e^{-\frac{t-t_s}{k}}, & t \geq t_s \end{cases} \tag{18}$$

where, T_0 is the initial morning temperature, T_a is the diurnal temperature amplitude, t_s is the start time of the attenuation function, and k is the attenuation constant [*Schädlich et al.* 2001]. Improvements have been made in fitting remote sensing data to this type of model [*van den Bergh et al.* 2007], but only the simple cosine model was used to determine the actual maximum (T_{max}) and minimum (T_{min}) temperatures in *Cai et al.* [2005]. Therefore, the diurnal temperature difference (ΔT) was determined from the day (T_1) and night (T_2) time temperature ASTER images using $T_{max} - T_{min}$, where:

$$T_{\max} = T_1 + \frac{(T_1 - T_2)[\cos(\omega t_{\max}) - \cos(\omega t_1)]}{\cos(\omega t_1) - \cos(\omega t_2)}$$
$$T_{\min} = T_2 + \frac{(T_1 - T_2)[\cos(\omega t_{\min}) - \cos(\omega t_2)]}{\cos(\omega t_1) - \cos(\omega t_2)} \quad (19)$$

$T_1 - T_2$ is the temperature difference between the 11:00 and 22:10 satellite overpass times. $T_1 - T_2$ is always less than $T_{max} - T_{min}$ in the case of these ASTER data, and would result in an underestimation of TI if not scaled using equation (12).

Applying this model to remote-sensing image data resulted in TI maps in thermal inertia units (TIU) and a spatial resolution equal to that of the input data used. The *Xue and Cracknell* [1995] model was modified in *Zhenhua and Yingshi* [2006]. They describe the model as more accurate, needing only the daily maximum temperature instead of the day-night temperature difference and the model accounts for sensible and latent heat [*Zhenhua and Yingshi* 2006]. Comparison of the soil moisture retrievals for both models using MODIS data showed similar results to actual soil moisture measurements in *Zhenhua and Yingshi* [2006]. The data produced in this paper are reported and discussed as approximated TI data, which represents ATI at the scale and units of real thermal inertia (P).

4.4.6 Estimation of erosion threshold velocity ratio from soil moisture

Soil moisture of bare or sparsely vegetated surfaces as a function of thermal inertia is given by *Ma and Xue* [1990]:

$$P = \left[2.1 d_s^{\left(1.2-0.2\frac{d_s}{d_\theta}\theta\right)} e^{\left(-0.007\left(\frac{w d_s}{d_\theta}-20\right)^2\right)} + d_s^{\left(0.8+0.2\frac{d_s}{d_\theta}\theta\right)} \right]^{1/2} \bullet \left[\frac{\frac{0.2\theta}{d_\theta} d_s^2}{0.001} \sqrt{100} \right] \quad (20)$$

where, d_s is the soil density, d_θ is the water density, and θ is the volumetric soil moisture. Using this relationship, lookup tables were generated for soil moisture as a function of density and thermal inertia. Because this model is used in the context of remote-sensing, density must be assumed. The variation of density in the model between 2.30 – 2.65 g/cm^3 results in slightly different but similar relationships between soil moisture and TI (Figure 27a). For arid lands where the actual soil moisture is low (0 ~ 15%), the density is assumed not to significantly affect soil moisture retrievals. For the data analysis here, a density of 2.65 g/cm^3 was assumed for the calculation of the TI.

An operational parameterization of the wind erosion threshold as a function of soil moisture for semi-arid soils is given by *Fécan et al*. [1999]:

$$\frac{u_{*t\theta}}{u_{*td}} = 1, \qquad \text{for } \theta < \theta'$$

$$\frac{u_{*t\theta}}{u_{*td}} = \left[1 + 1.21\left(\theta - \theta'\right)^{0.68}\right]^{0.5}, \qquad \text{for } \theta > \theta' \quad (21)$$

where, θ is the percentage of volumetric soil moisture, θ' is the absorbed soil water percentage dependent on clay content, and $u_{*t\theta}/u_{*td}$ is the ratio of the wet to dry threshold wind velocity or WTR. With this relationship between soil moisture and WTR, the lookup table defined by equation (13) was refined to determine WTR directly as a function of TI (Figure 27b).

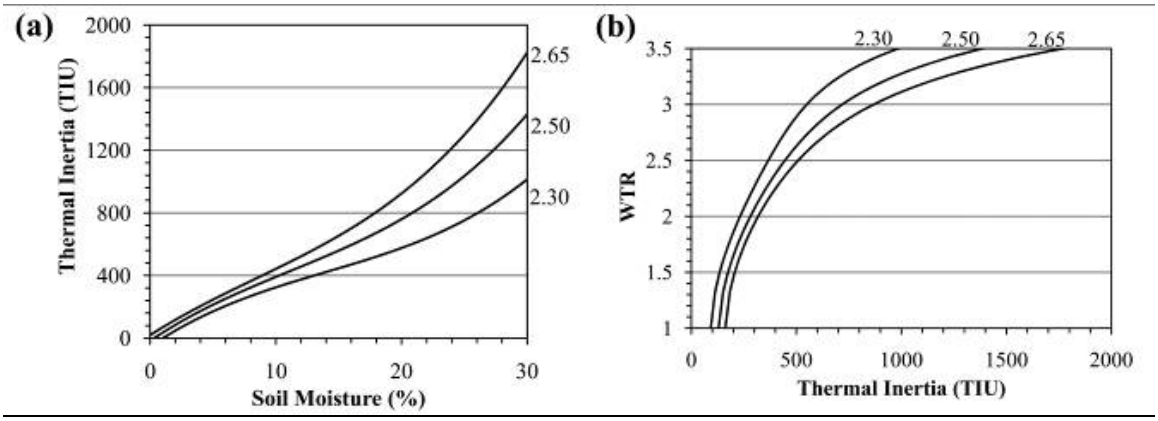

Figure 27. The model relationships between soil moisture and thermal inertia and WTR as a function of soil density (g/cm^3) used for the ASTER data in this study. (a) Thermal inertia plotted as a function of soil moisture. The assumed density used for the study is 2.65 g/cm^3 (reproduced from lookup tables by *Ma and Xue* [1990]). (b) The erosion threshold velocity as a function of soil moisture and density [*Fécan et al.* 1999]. These relationships were combined in order to show the threshold wind velocity ratio (WTR) as a function of thermal inertia.

4.4.7 Climate Conditions and Data

Temperature and precipitation data were collected from historical sources, but no known field work had been conducted on soil moisture or aeolian sediment erosion during any of the historical overpass dates and times. Weather data for the White Sands Dune field were gathered from local stations to determine if correlations exist amongst precipitation, modeled soil moisture and remote sensing retrievals, specifically for the time periods prior and coincident with the Terra satellite overpasses when ASTER and MODIS data were collected. Hourly precipitation data were available from U.S. Air Force (USAF) station No. 722693 located at 32°50'N, 105°59'W [*http://cdo.ncdc.noaa.gov/CDO/cdo*], and daily data were available from National Climate Data Center Cooperative [*NCDC COOP*] weather station No. 299686 located at 32°47'N, 106°10'W.

Total precipitation in the White Sands area is about 22 cm/year, with the peak rainfall amount occurring in August and the minimum in May. Maximum rainfall in this area is in late summer to early autumn with a second maximum in the winter. Precipitation events have a major impact on the results in two distinct ways: (1) to produces an error in thermal inertia calculations due to changes in surface temperature and (2) it serves as to replenish the soil moisture of the system. Examination of the hourly precipitation data for White Sands showed that precipitation events did not occur between day and night overpass times, therefore no error

of this type is expected. Time-series of precipitation are reported here, which include: (1) the total monthly precipitation trend during the study period (Figure 28g) with respect to the ASTER overpasses and (2) the daily precipitation trends 48 days prior to each of the satellite overpass times (Figure 28a-f). The number of consecutive dry days without a precipitation event in the White Sands area, and the predicted soil moisture data interpolated for the study area (bounded between 33.3–32.6ºN and 106.9–106ºW) are reported in Table 7. The predicted soil moisture data were produced by a one-layer, hydrologic model, referred to as H96, at a resolution of 0.5º across the entire U.S. from disperse meteorological measurement stations [*Huang et al.* 1996; *van den Dool et al.* 2003]. The H96 model accounts for precipitation, runoff, groundwater loss and evaporation, and is utilized for soil moisture prediction for the real-time National Drought Monitor [*Svoboda et al.* 2002].

Temperature data were used to determine the time of maximum daily temperature or t_{max} for the thermal inertia model, aid in the interpretation of TI and soil moisture retrievals, and to detect a source of error in the TI retrievals that could be due to season or weather. An attempt was made to find relationships between the data and MODIS water vapor retrievals as well, but these MODIS data were found to be unreliable because of inconsistent spatial coverage. Using the atmospheric temperature data from both the hourly and daily local weather stations, we determined that the study area experienced normal diurnal temperature fluctuations during the satellite acquisitions. The satellite overpass times (t_1 and t_2) and the daily maximum (T_{max}) and minimum (T_{min}) atmospheric temperatures occur at roughly the same time for each date, with one exception on April 6, 2006 when the maximum temperature occurred at 01:12 MST local time. The atmospheric temperatures at t_1 and t_2 are reported here as T_d and T_n (Table 7). T_{max} is always greater than T_d, and T_{min} is always less than T_n. Although the LST wave is expected to have higher amplitude, the average LST change is assumed to have tracked the average atmospheric temperature wave. The available climate/weather data show that no abnormal local weather conditions (i.e., frontal weather systems) occurred during or between satellite acquisitions of day and night image pairs, which would have adversely affected TI calculation. From these available data, it was concluded that the ΔT is therefore unlikely to be considered a source of significant error in the calculation of TI.

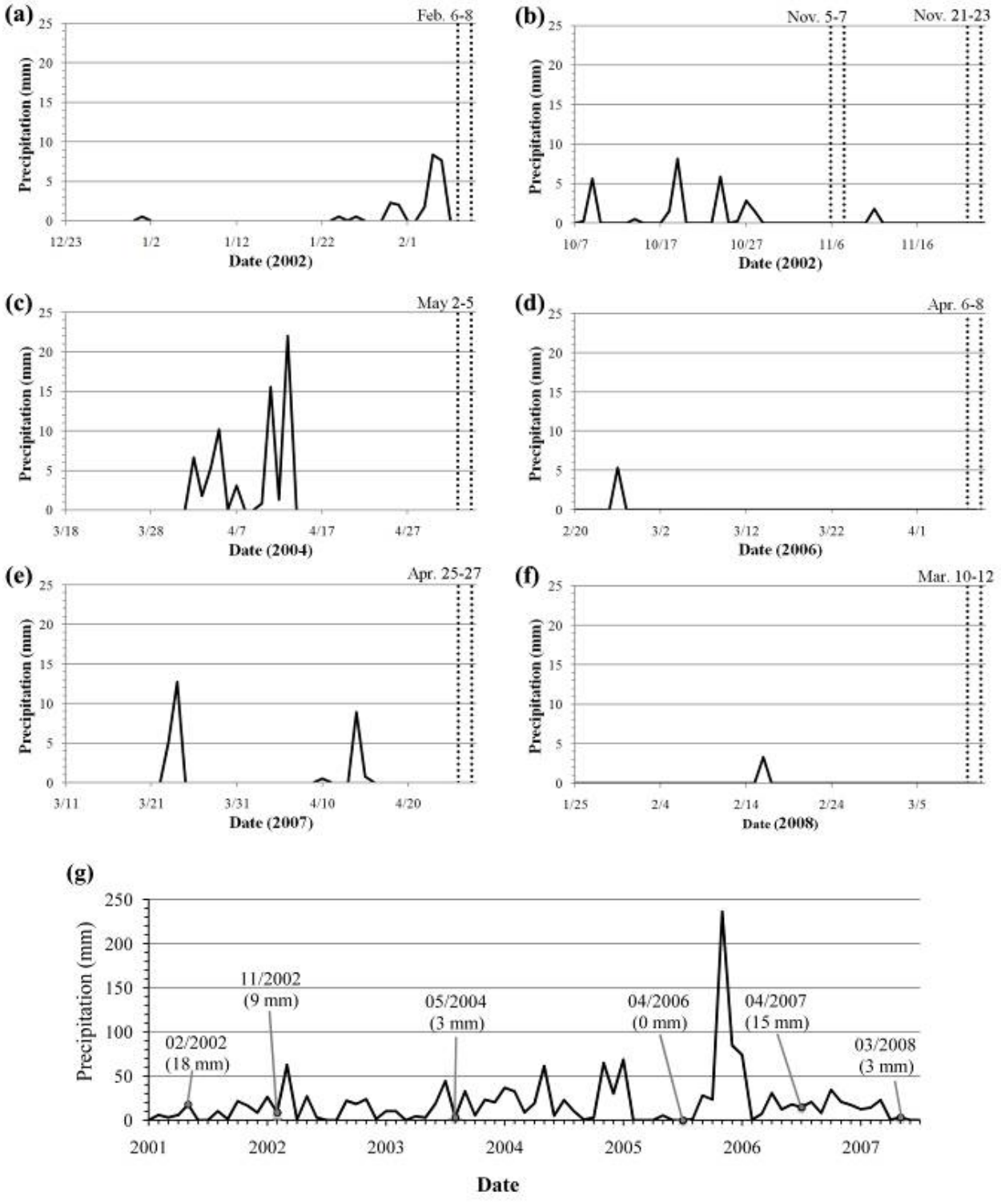

Figure 28. Daily precipitation totals 48 days prior to each of the ASTER data acquisitions that were used to retrieve thermal inertia and soil moisture in Figure 31. (a) – (f) Precipitation totals from station 296886. the days of the satellite overpass used in this study are shown by the vertical dashed lines. (g) Monthly precipitation totals for the entire timeframe also compared with the satellite overpass dates (vertical lines).

Table 7. ASTER acquisition dates/times (MODIS times are within several minutes) and the associated relevant climate data for the seven image pairs.

No.	t_1	t_2	T_d	T_n	t_{min}	t_{max}	T_{max_h}	T_{min_h}	T_{max_d}	T_{min_d}	$\overline{\theta}$ (%)	dry (days)
1	02/08/02 10:58	02/06/02 22:12	287	275	06:52	16:31	291	270	288	265	17	1
2	11/07/02 10:57	11/05/02 22:11	289	278	05:10	16:30	294	274	294	271	23	10
3	11/23/02 10:57	11/21/02 22:11	288	281	05:50	15:10	296	272	295	266	22	12
4	05/04/04 10:56	05/02/04 22:10	300	287	04:53	16:30	305	280	301	277	20	22
5	04/08/06 10:56	04/06/06 22:09	292	289	01:12	16:30	298	279	298	273	15	42
6	04/27/07 10:56	04/25/07 22:10	301	289	04:31	15:30	ND	282	302	286	29	12
7	03/12/08 10:56	03/10/08 22:10	291	280	05:05	16:30	295	275	294	270	18	25

t_1 and t_2: sensor overpass time, day and night, respectively.
T_d and T_n: atmospheric temperature (degrees Kelvin), day and night, respectively.
t_{max} and t_{min}: local time of the maximum and minimum air temperatures
T_{max} and T_{min}: maximum and minimum hourly *(h*) and daily (*d*) air temperatures (degrees Kelvin) from local weather stations
θ: average estimated regional volumetric soil moisture for White Sands from U.S. climate data.
dry (days): number of days without precipitation prior to satellite overpass and data acquisition.

4.5 RESULTS AND ANALYSIS

4.5.1 Comparison of MODIS and ASTER Results

The differences in VNIR reflectance between a dry (April 2006) and wet (April 2007) period are readily apparent in the regional scale ASTER and MODIS color composite images (Figure 29). The inundation of the largest playas, including Lake Lucero, is observed in both data sets. The large-scale changes in the albedo patterns of the gypsum sands and vegetation on the surrounding alluvial fans is also clear in MODIS data. However, the 15 meter spatial resolution of ASTER is able to better resolve the features and processes of interest within the dune and playa system (e.g., the inundation of many smaller playas and alluvial drainages, dune and interdune surfaces, and changes in the spatial pattern of gypsum and evaporite deposits, especially in active playas).

The study area had full coverage in the ASTER and MODIS reflectance data (AST07XT and MOD09 standard reflectance products, respectively). The broadband albedo calculations from MOD09 data had a difference of less than 1% compared to the MOD43 broadband albedo where spatial coverage of MOD43 was available. Comparison of the ASTER and MODIS albedo is difficult because of the difference in spatial resolutions. AT MODIS resolution, ASTER and MODIS have the same mean and general spatial pattern in the temperature and albedo data. The differences in the input data for the thermal inertia model were best recognized by examining the broadband albedo and temperature difference images calculated from MODIS (Figure 30a and Figure 30b) and ASTER (Figure 30c and Figure 30d). The area of Figure 30 corresponded to the inset box from Figure 29d labeled *zoom*. Temperature data from ASTER are 11 times sharper and albedo data are 16 times sharper compared to MODIS.

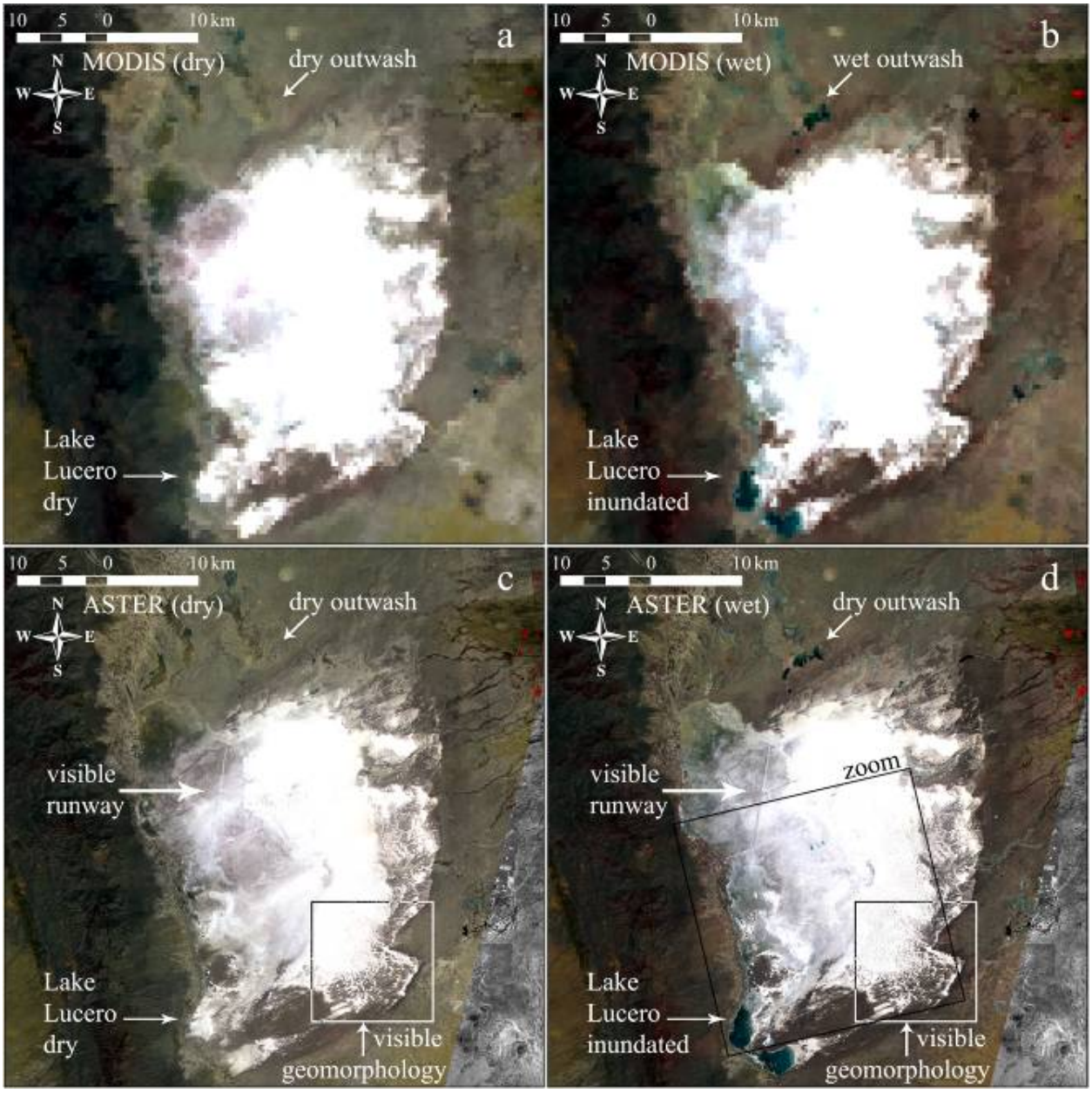

Figure 29. ASTER and MODIS color VNIR data for a typical dry period (April 6, 2006, left hand column) and a wet period (April 27, 2007, right hand column). (a – b) The MODIS data product (MOD09) color composites (bands 2, 1, and 4 in Red, Green, Blue, respectively). (c –d) ASTER color composites (bands 3, 2, and 1 in Red, Green, Blue, respectively). The typical extent of inundation of Lake Lucero can clearly be seen during the wet period (indicated by white arrows). ASTER data also show a higher level of detail in dune morphology and changes in the playas surfaces. The inset box labeled *zoom* denotes the area shown in Figure 31, whereas the smaller box denotes an area where parabolic dunes are resolved by ASTER but not MODIS.

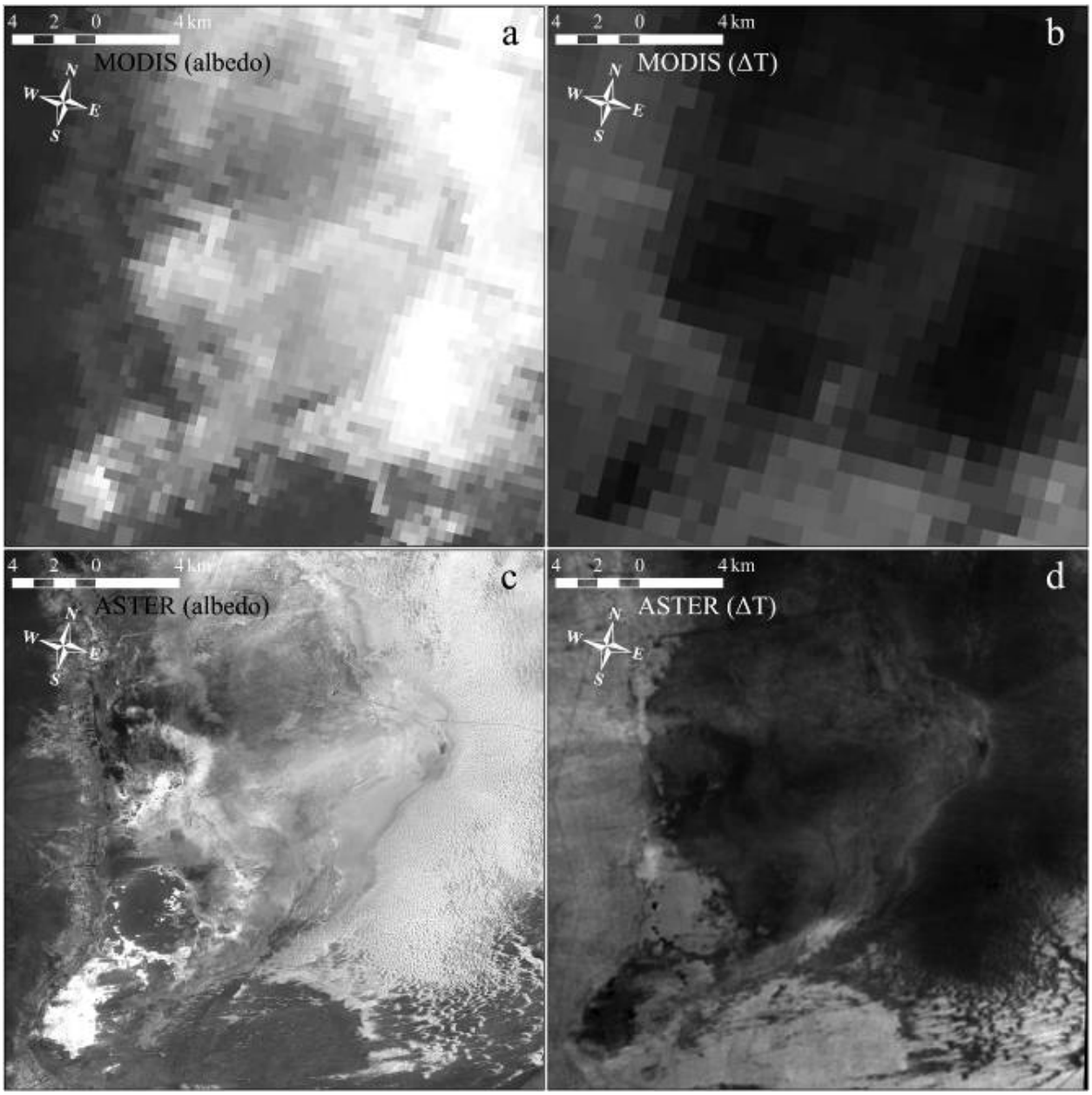

Figure 30. Comparison of MODIS and ASTER derived image products acquired on April 6, 2006, which were used to calculate TI. (a) MODIS-derived broadband albedo. (b) MODIS-derived *ΔT*. (c) ASTER-derived broadband albedo. (d) ASTER-derived *ΔT*. Broadband albedo values range from 0 to 0.60 and *ΔT* values range from 25 to 60 K. Both image pairs are linearly stretched equally for greatest image contrast.

The results of the TI modeling using ASTER data were expected to be more useful because of the ability to distinguish small-scale thermophysical differences in aeolian geomorphology. Nonetheless, TI was retrieved using both ASTER and MODIS data at their native resolution in order to compare the results over time and assess the benefits of high spatial versus high temporal resolution. This comparison was useful for several important reasons. First, the similar capability and accuracy of the instruments allowed for variations due to instrument effects to be separated from real temporal and spatial trends. For example, the highest average TI values were calculated for the entire image data on February 6, 2002 compared to other data. Because the same general temporal and spatial trends were observed by MODIS, an individual sensor or instrument effect was ruled out for these high values. Second, previous studies that retrieve TI and soil moisture using the *Xue and Cracknell* [1995] model relied on MODIS data at different study sites [*Cai et al.* 2005; 2007a]. The retrieval using MODIS for this study of White Sands demonstrates valid values (~ 400-2000 TIU) similar to those reported previously and that the model is working correctly.

4.5.2 Spatial Patterns of Thermal Inertia

TI retrievals of the White Sands dune and playa aeolian system from seven different dates between 2002 and 2008 show significant spatial and temporal variation (Figure 31a-g). In the figure, the data are shown as a subset of the White Sand dune field and playa area in order to focus on smaller scale aeolian features (shown as an inset box on the map in Figure 29d). The majority of the ASTER TI data fall within the range of 400 – 1400 TIU with 95% of the data falling within the range of 900 – 2000 TIU. The highest TI was associated with very wet surfaces, such as those found at the inundated Lake Lucero and playa (area A5). Full inundation of areas like Lake Lucero is denoted by the dark blue color in Figure 31d and Figure 31f, whereas the lake was partially inundated in Figure 31b, Figure 31c, and nearly or completely dry in Figure 31e and Figure 31g. Close examination of the ASTER TI images revealed that many other small persistent playa lakes can be found within the region (e.g. Figure 31f, areas C1, D1, and E2), several of which occur as higher TI areas in the interdune areas (e.g., Figure 31b, area 4E). Several of these inundated interdune areas correspond to the spectral characteristics of water, seen as the light blue color in the ASTER VNIR reflectance. The western portion of the

image subset represents the termination of the Andres Mountain alluvial fans abutting the edge of active playas and Alkali Flat (Figure 31, portions of area A1, A2, A3, A4 and A5). This area has a pattern of consistently lower TI at the distal edges of the fans, and is interpreted as fine-grained sediments deposited at the edges of the playa.

Other regions have a spatially complex and temporally variable pattern of TI. Several of the active playa surfaces have extremely low values in some areas (Figure 31g, area B2-B4, C2-C4), which corresponds to very dry conditions and the high-albedo gypsiferous evaporite. The opposite trend is observed in the previous date of the time-series Figure 31f), when the same area was wet. Just northeast of Lake Lucero is a circular area of consistently lower TI (see Figure 31b, 31c, 31d, 31f and 31g, area B4), but in Figure 31e this area has an average similar to that of its surroundings. This circular feature is frequently rimmed by a very low TI area that is interpreted as a significantly fluctuating amount of evaporite crust in the active playa. For example, in Figure 31e, this region has an average TI (green color), a thin zone of low TI (red color) rims the southern edge. This feature is interpreted as a high albedo gypsiferous evaporite surface. Clouds can also cause anomalously higher TI values, an example of which is found at the top center of the image in Figure 31g (area C1). This propagates into the average TI image as an overestimation of TI and soil moisture (Figure 31h, area C1), and demonstrates the models susceptibility to atmospheric conditions.

Dune ridges consistently have lower values of TI due to the dry, mobile, high albedo gypsum sands, including the larger parabolic dune forms at the southern edge of the dune field (e.g., area D5 and E5). Large areas west of the dunes also have persistently low TI values (see Figure 31b, 31d and 31g, area B5 and C5). In other areas of the dune field, some interdune areas persist as high TI regions despite the soil conditions in the rest of the image. These areas are interpreted to have consistently higher soil moisture and interdune vegetation cover or biotic crust. An increase in the areal coverage of vegetation is expected to increase TI retrieval values because of water content in vegetation. Likewise, the lower albedo may also increase TI values for these particular pixels if vegetation is a major scene component. Some interdune areas are covered by a clay-rich crust that has a slightly lower albedo, causing an increase in TI retrieval. Unique to the composition of the White Sands area, the interdune areas and stoss slopes of the dunes also have a higher cohesion and bulk density due to the partial cementation of gypsum

sand grains. The effect on TI is not known where the hard and compact cores of these dunes are exposed by erosion of loose sand.

The average TI image (Figure 31h) shows the persistent spatial patterns of the White Sands aeolian system. For example, the crescentic dunes in the south of the dune field have a much lower average TI (100-200 TIU) than the adjacent interdune areas (400-600 TIU). Interdune areas are affected by the interaction of the groundwater table with the surface [Kocurek et al. 2007; Langford et al. 2009]. Playa surfaces were also found to have high standard deviation of TI values, similar to the interdune areas. Several smaller playas and persistently wet interdune areas with higher TI are easily identified throughout the dune field. The mean and standard deviation of the seven image dates were generated and represent a range of soil moisture conditions. The standard deviation of each pixel is a relative estimate of the variability of TI, and therefore, soil moisture variability. As expected, a higher standard deviation is observed on playa and interdune areas compared to dunes, indicating a higher degree of variability in soil moisture through time in these areas. However, the data constitute a limited temporal subset and therefore the interpretation of longer term trends is difficult. For example, exclusion of the image data shown in Figure 31a (a very wet time period) biases the statistics showing the greatest amount of variability in dry areas of Alkali Flat. Exclusion of image data shown in Figure 31e or Figure 31g removes the influences of very dry conditions, and the wet areas appear more significant. Therefore, even though the average of all seven images gives the best available representation of the average TI (and soil moisture), additional data would further aid the refinement of the temporal trends in the dune field.

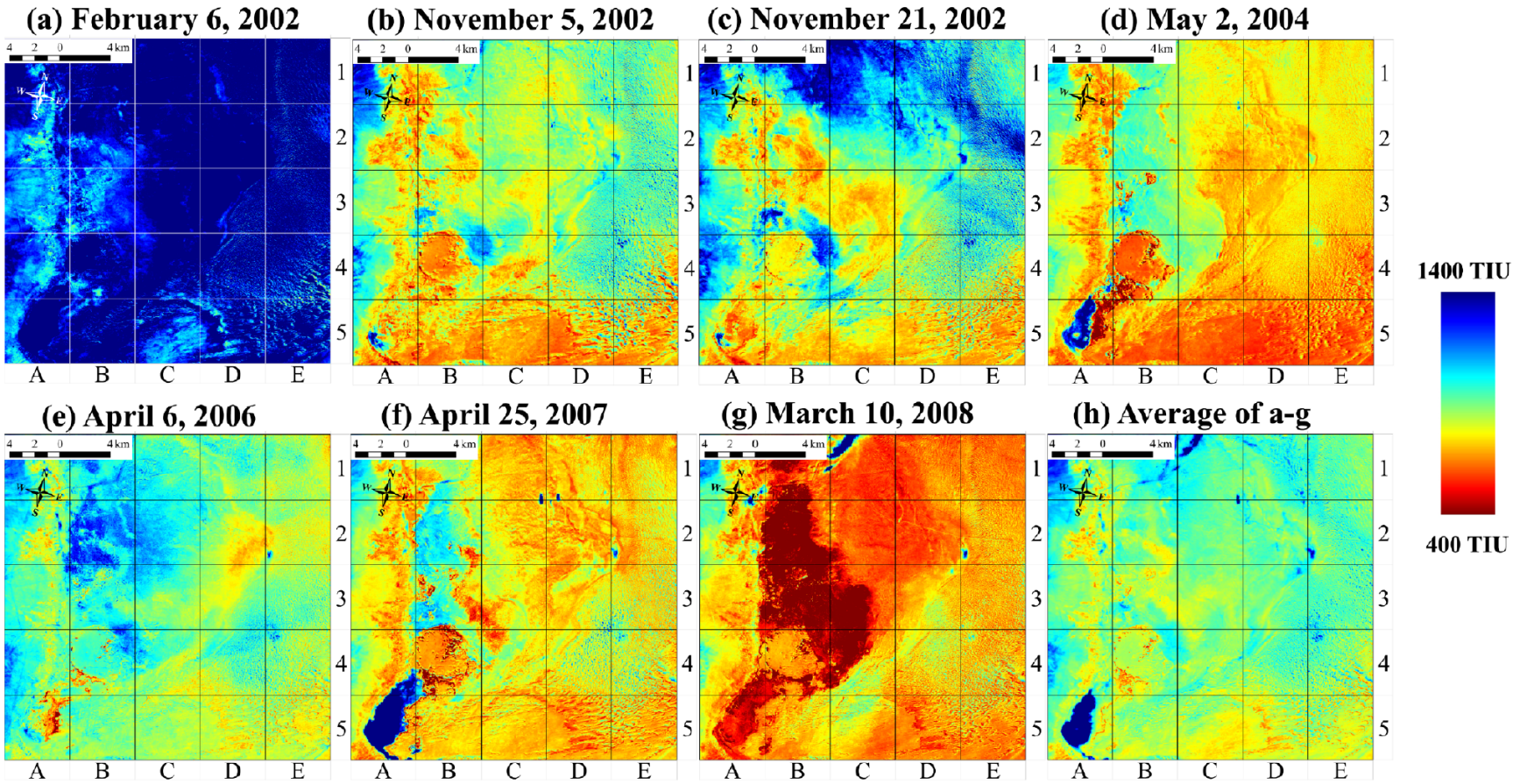

Figure 31. TI derived from the ASTER data, which corresponds to a range of soil moisture from 9% to 25%. Regions in blue are surfaces with higher soil moisture and therefore immobile sediment, whereas areas in red are drier surfaces that are more susceptible to wind erosion via sand saltation or dust emissions. (a – g) the seven time periods detailed in this study. (h) The averaged image product of all seven image pairs showing the TI trend over time.

4.5.3 Temporal Trends of Soil Moisture

Independent in-situ soil moisture measurements were not available for these ASTER data acquisition dates, which would have provided ground truth and an accuracy assessment of soil moisture retrievals. However, the time-series of ASTER-derived soil moisture can be compared to the modeled H96 soil moisture at a regional scale. The meteorological stations used by H96 are not located directly in the dune field, and the gridded data products do not have the spatial resolution to match ASTER or even MODIS data. The time-series of H96 soil moisture were extracted from the meteorological stations surrounding the study area and spatially interpolated to give the best possible comparison of H96 model data to ASTER-derived data (Figure 32a). In addition to the differences between them in spatial resolution, obvious differences in these two data sets arise because of the very different methods by which soil moisture is derived. However, because the H96 model predicts soil moisture based on a specific set of hydrologic variables and for average soil conditions, some comparisons to the ASTER derived data result in new hypotheses of hydrologic forcing on soil moisture that specifically occurs in an arid, wet-aeolian system of dunes and playas. For example, the H96 soil moisture data can be compared to measured precipitation from the local weather stations (Figure 32a-g) giving possible insight into the effects on ASTER-derived data (discussed below).

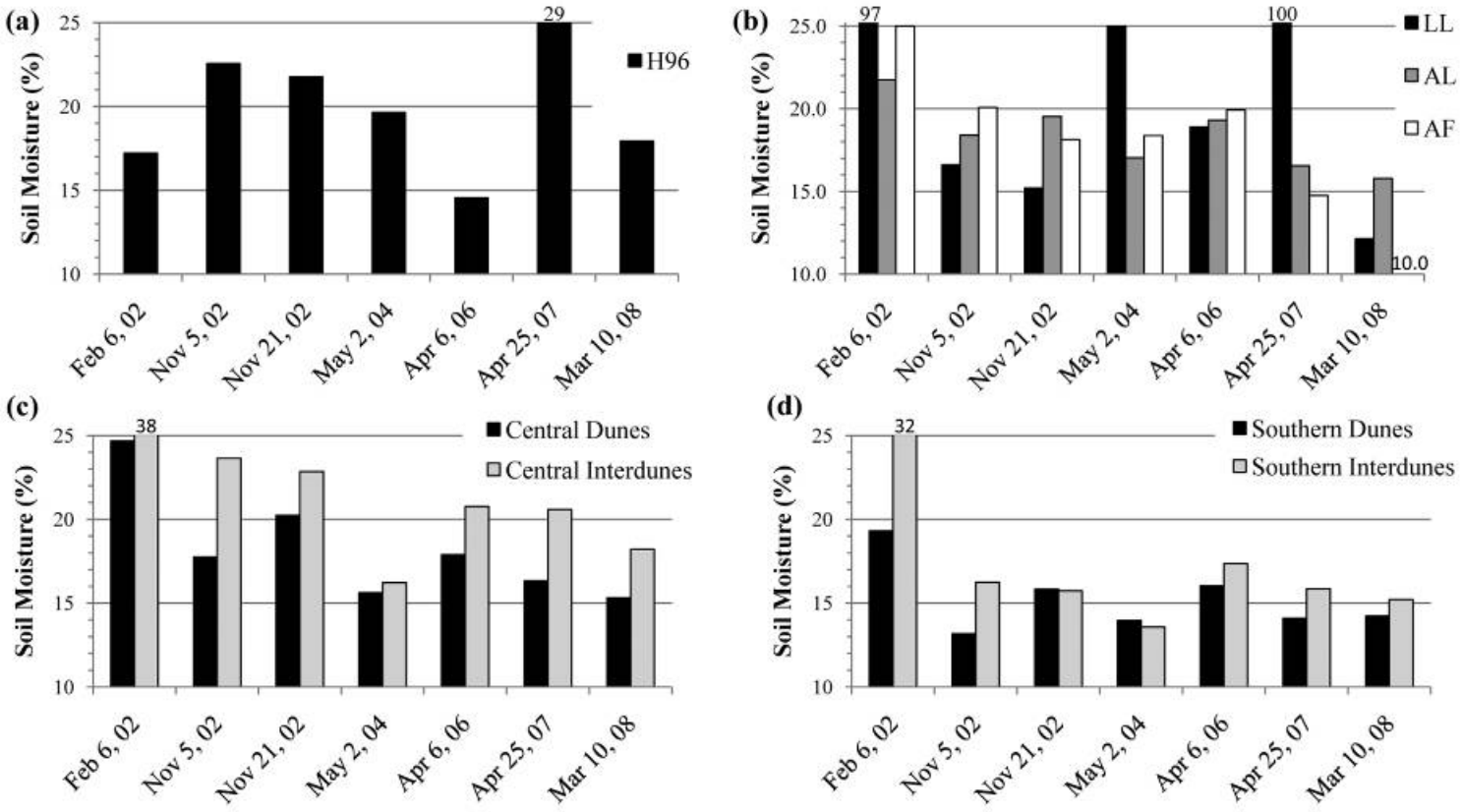

Figure 32. Temporal trends of soil moisture for various geomorphic features and surfaces at White Sands. (a) The predicted average soil moisture extracted from U.S. climate data for the White Sands Dune region [*Huang et al.* 1996, *van den Dool et al.* 2003]. (b) Lake Lucero (LL), Alkali Flat (AF), and the lower San Andres alluvial fans (AL) west of the dune field. The variation is high for Lake Lucero and Alkali Flat, ranging from complete inundation of the lake to very dry. The alluvial fan variation is low and more typical of the average soil moisture conditions. (c) Central crescentic dunes and interdune areas. (d) Southern parabolic dunes and interdune areas. Higher soil moisture conditions were predicted for the central crescentic dunes and the majority of the interdune areas consistently had higher soil moisture retrievals than dunes.

Image statistics show that the ASTER-derived data have a greater range of soil moisture values through time than the H96 model data. ASTER-derived data range from < 10% to 100%, and these values are highly spatially dependent as previously discussed. Average H96 data range from a minimum of 14% on April 6, 2006 to a maximum of 29% on April 27, 2007 (Figure 32a). Average ASTER-derived soil moisture values were highest for February 6, 2002, and the driest values were for March 10, 2008. In general, the comparison of the land surface soil moisture data between H96 and the ASTER-derived data for the seven ASTER acquisition dates are between 10% and 30% (periodically inundated playa and interdune surface areas are excluded), but the data do not correlate well through time (Figure 32). These results are not surprising considering the greater spatial resolution of ASTER, which captures such a high degree of local variation in soil moisture. The time-series data from ASTER are spatially variable and depend greatly on the location in the White Sands system from which the time-series data are taken (Figure 32b-Figure 32d). The H96 soil moisture values predicted for each of the dates examined in this study were compared to the monthly totals of precipitation (from Figure 28g) in a simple least-squares regression. H96 soil moisture predictions were directly related to the amount of precipitation ($R^2 = 0.92$) if the February 6, 2002 data point was excluded. The February 6, 2002 soil moisture was the result of a localized precipitation event and not captured by H96.

The time-series of ASTER-derived soil moisture was extracted from various regions of interest that represent different geomorphic settings within the aeolian system (Figure 32b-Figure 32d). Different trends of soil moisture were expected and were observed from these areas. Large playa lakes, like Lake Lucero (LL), are periodically inundated, reaching complete saturation at times, and complete desiccation at other times (Figure 32b). Other playa and interdune areas show similar trends, but do not reach complete saturation (Figure 31c and Figure 31d). Alluvial fan (AL) and dune areas had the lowest variation of soil moisture (6% and 8%, respectively) and similar trends through time. Dune areas almost always had lower soil moisture than their adjacent interdune areas. Parabolic dunes at the southern end of the White Sands dune field had lower soil moisture and less variability than crescentic dunes located in the central part of the dune field (Figure 32c and Figure 32d), although locally these differences were small. The pattern of high interdune and low dune soil moisture is much less than the soil moisture variation found at LL, playas and AF. Dune and interdune variability is also somewhat dampened in the time-series because of the spatial averaging where regions of interest were created for the time

series. Not all interdune areas experience the same wetting and drying cycles, and therefore some differences between adjacent dune and interdune areas may be greater than others (Figure 31). Lower soil moisture in the dune field may also be due to greater sand thickness. In general, the dunes sit on top of a sabkha surface that is connected to and interacts with the underlying groundwater table. Dune cores are commonly cemented at White Sands, and my also contain perched groundwater. Where sand thickness is low, the underlying moist soil will increase TI retrievals relative to thick, dry sand cover. Dune TI and therefore soil moisture are at their lowest at the top of the dunes where these areas are well drained and not very well connected to groundwater fluctuations. The southern dunes have the least amount of soil moisture variation (13 to 16%) over time, not including the very wet conditions present on February 6, 2002 (see also Figure 31a).

The wet conditions on February 6, 2002 were considered to be anomalously high where compared to all of the other ASTER-derived soil moisture data, but the H96 hydrologic model did not predict wet soil conditions for February 6, 2002. This was not due to an effect of high spatial resolution (e.g., capture of a typical playa lake signature). The image wide ASTER-derived soil moisture was higher than any of the other ASTER image data from any other date (Figure 31a). Examination of the daily precipitation record from weather station No. 299686 at White Sands showed that a total of 23 mm of precipitation was recorded in the days prior from January 24 to February 5, 2002 (Figure 28a). The majority of this precipitation occurred February 4th and 5th for a total of 16 mm. Therefore, the local rainfall recorded at weather station No. 299686 better explains the resulting ASTER derived soil moisture on February 6, 2002 and highlights the weakness of the regional H96 model in this application.

Both ASTER-derived and H96 data predicted relatively wet condition for April 25, 2007. Observation of the monthly precipitation in Figure 28g shows the highest rainfall in the year prior to April 25, 2007, however this did not have an impact on surface soil moisture conditions. The April 25, 2007 ASTER image data do not show widespread wet soil conditions, but several smaller areas of very wet conditions exist, such as in playas, interdune areas and some alluvial outwashes. Significant precipitation events occurred on 14 and 35 days prior to the image acquisition (9 and 12 mm, respectively) and may be responsible for recharging subsurface water and Lake Lucero (Figure 28e). This is interpreted as a period in which the subsurface soil moisture remained persistently high and the groundwater table was also persistently high. The

upper soil and sand layers are dry due to evaporation, rapid dry-down and the persistent arid conditions. Low monthly precipitation was observed prior to the March 12, 2008, April 6, 2006 and May 2, 2004 ASTER data acquisition dates (Figure 28g). Monthly precipitation was high in May 2004, but because the data acquisition occurred early in the month, precipitation during April 2004 was responsible for forcing high soil moisture values shown in Figure 31d. Significant precipitation events in the month prior to the satellite data acquisition on May 2, 2004 raised Lake Lucero levels during which time soil surfaces experienced a quick dry-down due to evaporation (Figure 28c). This was consistent with the dry soil conditions determined from ASTER for the region. However, the ASTER-derived data show drier conditions on March 12, 2008 (Figure 6h) than April 6, 2006 (Figure 31e). April 6, 2006 represents very dry soil moisture conditions, and March 12, 2008 shows the driest conditions relative to all the other dates. H96 does not show this trend, and the reason for this difference cannot be explained by the available precipitation data. Evaporation rates and groundwater levels could possible lead to a better understanding the ASTER-derived soil moisture. It is logical to conclude that duration and amount of precipitation has a major control on soil moisture, as well the number of dry days experienced since the last precipitation event (Table 7 and Figure 28). Otherwise, some of the discrepancies between model soil moisture and these ASTER data may be related to differences in spatial and temporal resolution. This suggests that whereas the H96 data may be representative of the region, the dune field and unique surrounding aeolian environment probably respond differently to hydrologic forcing.

4.5.4 Erosion Threshold Velocity Ratio

The relationship between TI and the wind erosion threshold velocity ratio (WTR) is not linear (Figure 27). However, the shape of the curve between the erosion threshold velocity ratio and TI is similar and comparable to those presented as a function of volumetric soil moisture [*Fécan et al*. 1999]. To observe the spatial pattern of erosion potential, the average TI data were recast into the distribution of WTR values (Figure 33). The relationship varies for different soil textures, and the erosion threshold velocity ratios range between 1.0 and 2.0 for pure sand with soil moisture between 0 and 5%. An erosion threshold velocity ratio for gypsum sand has not reported in the literature, but if it is similar to quartz sand, the modeled values range from 2.5 to

3.0, and correspond to modeled soil moisture content of between 8 and 18% (*Fécan et al*. 1999). The dunes and several areas of the playa surface have a wind threshold velocity ratio ≤ 2.5, indicating that these areas have the highest potential for aeolian transport or sediment availability relative to other areas of the dune field. The lower relative values of the WTR correspond to the

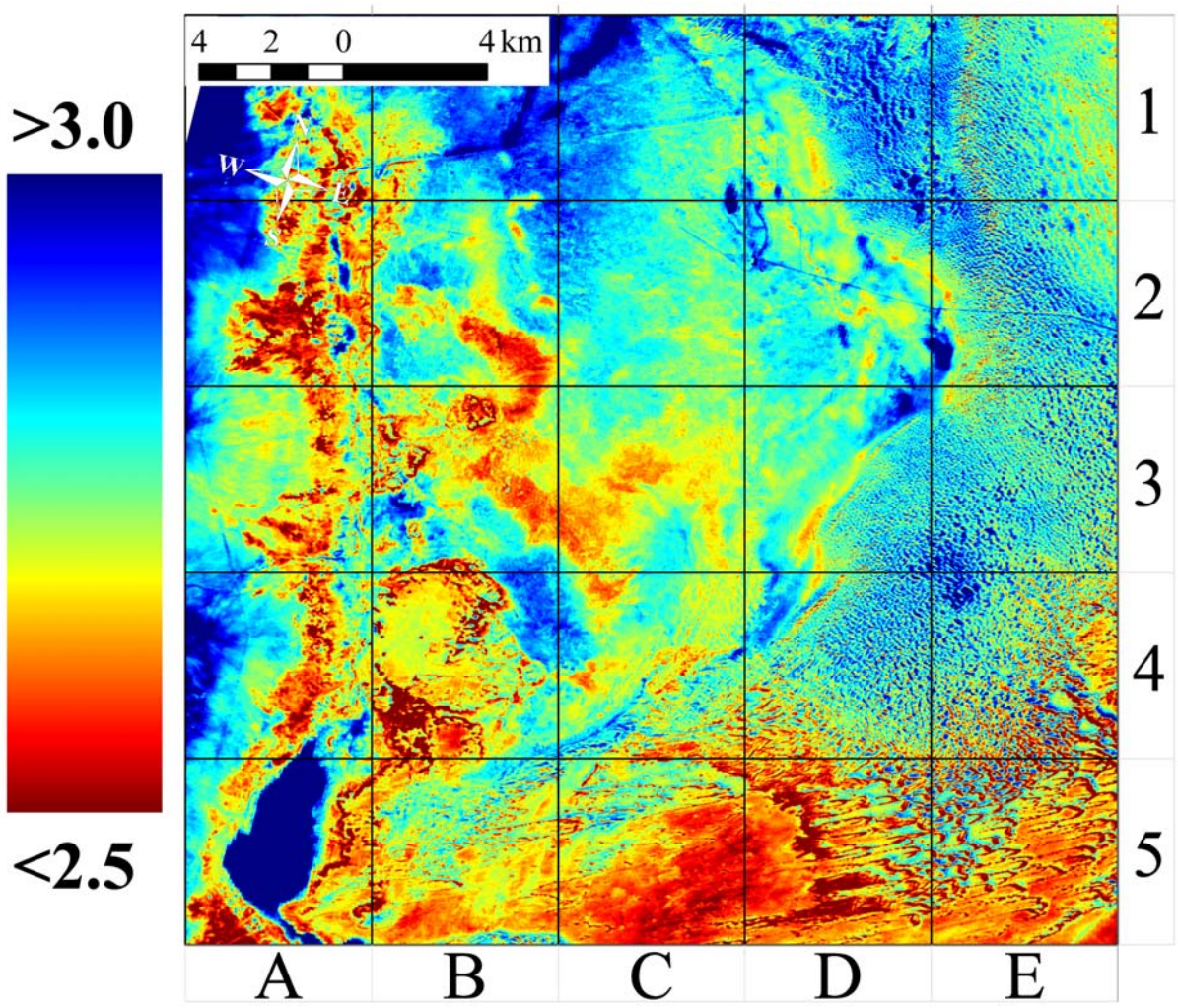

Figure 33. The average unitless erosion threshold wind velocity (WTR) derived from the average ASTER TI image (Figure 7h). Areas that have a high susceptibility to aeolian erosion are shown in red, whereas areas in blue (higher TI) frequently have higher soil moisture and thus a lower susceptibility to wind erosion. Note the higher WTR values for the southern parabolic dunes as compared to the central crescentic dunes.

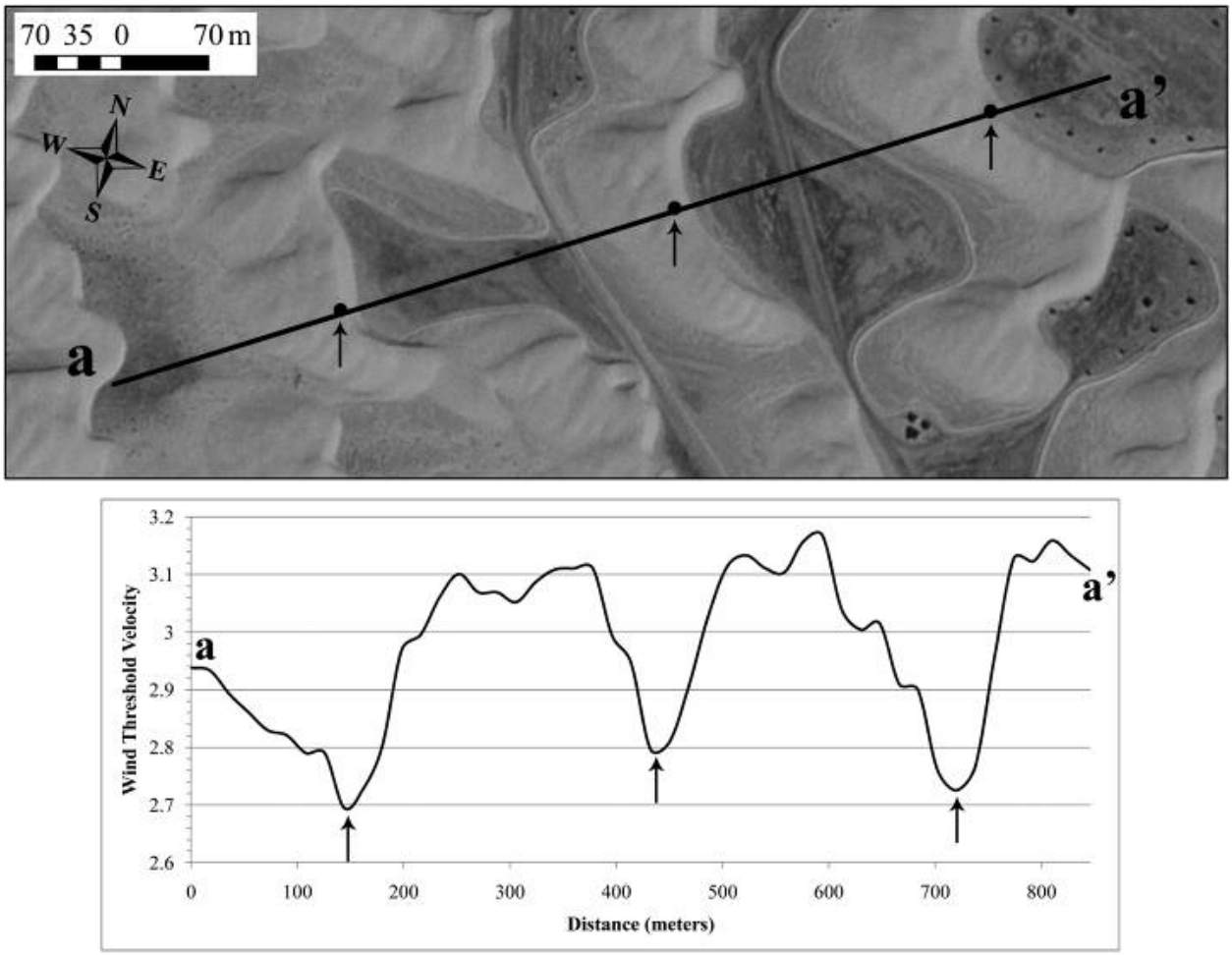

Figure 34. The WTR plotted along the transect a – a' (32.8103° N, 106.9364° W to 32.8143° N, 106.2619°W) across a series of dune and interdune areas at the White Sands National Monument access road. The image is a digital orthophoto quarter-quad (DOQQ) acquired January 4, 2003 [*USGS* 2002]. Arrows correspond to dune crest positions, where WTR values are lower relative to interdune areas.

position of dune centers and/or crests compared to the higher values found in the interdune. The variability of the average wind velocity threshold ratio was observed along a transect (a – a') oriented in the dominant wind direction (SW to NE) across a series of dunes (Figure 34). The dunes are easily accessible from the White Sands National Monument park area and access road. Several areas at the bottom of the alluvial fan adjacent to the dune field also have high sediment availability. Other areas that have high sediment availability include an area west of the southern crescentic dunes, interpreted as sand mantling the surface supplied from the eastern margin of Lake Lucero where gypsum evaporite is readily resupplied for transport. Interdune areas and the periodically wet playa surfaces appear to have the least sediment availability from the averaged

data, however during dry conditions interdune areas may be activated in the crescentic dune field (for example, during dry conditions shown on March 12, 2008 in Figure 31g, and the wind threshold velocity ≈ 1.0 – 2.0).

The erosion susceptibility of the White Sands aeolian system as derived by this approach was validated two days after the last image pair in March 2008. On March 14, 2008, a large dust storm occurred and was captured by MODIS Aqua (Figure 35). Plumes from the playa and dune field can be seen emanating from the area, inundating the city of Alamogordo, NM and traveling over 200 km to the ENE. At least for this particular case, the ASTER-derived WTR correspond very well and was shown to be a good predictor for the subsequent dust emission event. Because of the high spatial resolution of the data, it can by hypothesized that the dust emissions originated from the aeolian features with low WTR values, such as the active playas north of Lake Lucero, the edge of the alluvial fans to the west and the parabolic dunes as well. The low spatial resolution of MODIS makes it difficult to deduce the exact source of dust emissions from features imaged by ASTER. Later field observations on May 2, 2008, when similar dry and windy conditions prevailed and aeolian processes were observed at multiple locations at the White Sands aeolian system, provided some insight into the probable surface conditions present at that time of the large dust emission event. Wind velocities were measured and averaged between 10 to 15 mph, gusting to greater than 50 mph. Sand saltation was observed originating from all dunes in all areas, the adjacent alluvial fans to the west of active playas and the playas themselves. Several patches of friable surface crust composed of gypsum and silt were observed to be removed from the playa surface, although specific dust emission sources could be seen only from a distance. The surface crusts observed on the playa were inflated (lower bulk density) from the lower, moister soil conditions 2-3 cm below the upper surface. It is probable that these types of surfaces appear as low TI and low WTR in the ASTER-derived images. The WTR parameter derived from ASTER does not distinguish between loose dry sand susceptible to saltation, a dust emission source or dry, low density, surface-crusted sediments. Under high wind conditions, it is likely that fine-grained surface crust material (on dunes and playas alike) will break apart and become easily entrained by the wind to generate saltating particles or dust emissions.

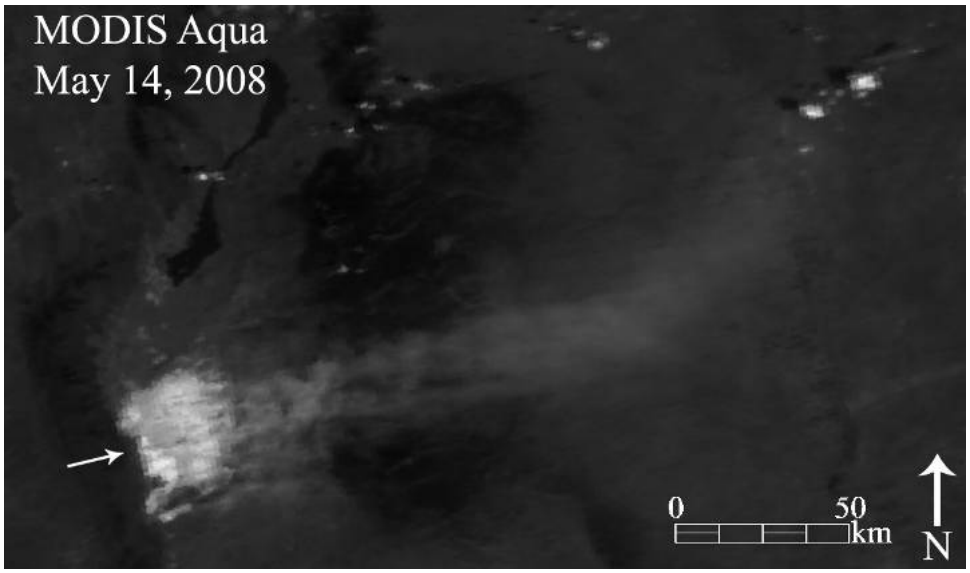

Figure 35. On May 14, 2008, two days after the period of lowest predicted WTR values in this study, a large dust storm was capture by MODIS Aqua from the White Sands Dune aeolian system. This image shows the MODIS albedo. The image is stretched linearly to prevent saturated pixels in areas of gypsum ground cover and dust. This allows the visualization of the dust plume structure emanating from the whole of the aeolian system. Winds are from the west-southwest.

4.6 DISCUSSION

Aeolian sediment availability in the absence of vegetation and stabilizing biotic soil crusts is highly dependent on the soil hydrology of any specific location. Evaporation rates are important in predicting soil moisture, which are strongly influenced by wind. Several factors (i.e., precipitation and groundwater) affect the soil moisture in this perched groundwater system beyond the influence of solar heating and evapotranspiration. The interdune and playa soil moisture is affected by water table fluctuations due to variable precipitation anywhere within the basin. The White Sands aeolian system is situated between steep, high elevation mountain ranges and broad alluvial fans. This implies that snow melt or rainwater from a distance could influence groundwater hydrology in the low-lying basin. The subsurface variation in topography of the underlying sabkha surface is also likely to affect the groundwater flow dynamics. A detailed examination of the groundwater conditions that impact soil moisture is beyond the scope

of this paper and has been previously explored by *Langford et al.* [2009], where dune morphology at White Sands was found to control dune morphology. Where local precipitation data or modeled hydrology (i.e., H96 data) cannot explain wet soil conditions through time, the influence of groundwater fluctuations becomes a plausible scenario for explaining anomalously high soil moisture. In this case, the forcing of precipitation on soil moisture levels is apparent from examining the timing between precipitation events and satellite data acquisitions, the number of dry days between precipitation events and the total amount of precipitation.

Retrieval of the erosion threshold via TI modeling from spaceborne thermal infrared remote-sensing measurements has some limitations. The TI data from multiple dates are at the same scale of real thermal inertia units (TIUs) and were comparable to each other in this study. Despite the efforts put forth to model real thermal inertia from remote-sensing, retrievals from any satellite-based system are still an approximation and subject to the same limitations [*Scheidt et al.* 2008b]. The relative values of ATI could also be related to soil moisture and wind threshold velocity ratio; however, this study using ASTER builds on previous work using the MODIS-derived values of soil moisture from modeled TI data. The real thermal inertia of the land surface is affected by the heterogeneity of material properties (i.e., K, ρ and c). The remote-sensing TI retrievals, which should be but are not always proportional to the real thermal inertia, are affected by composition (e.g., reflectance and emissivity variation), topography and surface roughness, vegetation and variable atmospheric conditions. Specifically for the White Sands dune field where dry sand has been stripped away, the algorithm may not detect the difference in bulk density between dry cemented dune surfaces and wet sediment. These areas are small however, and occur seasonally. Based on this study, in order for the derivation of sediment availability from modeled TI data to be useful, it must be assumed that (a) all environmental effects are described or assumed to be negligible with respect to soil moisture, (b) soil moisture contributes a high degree of variability to the relative values of TI retrieved by the algorithm, and (c) sediment availability is significantly controlled by soil moisture. Some of the exceptions and important points (including temporal scale, subsurface moisture effects, soil composition and texture) for the interpretation of the data are discussed below.

The approach presented works well for the overall relative field conditions on the dates presented in this study, specifically for the main dune complex that consists of crescentic dunes and interdune areas (Figure 31). Areas outside the main dune field, such as in the parabolic dune

area, Alkali Flat and the alluvial fans to the west, raise some concern. In these areas, erosion potential appears to be a function of other factors in addition to soil moisture. For example, the water table in the parabolic dune area is lower and does not exert a significant influence on soil moisture. The low values of WTR for these dunes suggest that they are active, however this area is considered a stabilized-vegetation system and the dunes do not appear to be mobile [*Kocurek and Lancaster* 1999] especially interdune sediments stabilized by biotic soil crusts [*Langford et al.* 2009]. These dunes may be quite dry and far less mobile than crescentic dunes, and the sediment state of surfaces does not necessarily reflect the state of the dune field as a whole or the mobility of the dunes in general. Active sand transport occurring from the sediment supply generated by Lake Lucero and other active playas feed the central dune core as well as the parabolic dunes. This sediment supply is available only in pulses with the periodic dry-down of the playa areas. The WTR results generated here appear to capture sand transport atop areas where stabilized interdune areas occur in the parabolic dune field area. Because these areas are stabilized by biotic crusts, they cannot be interpreted as source areas of sediment, rather an indication of a sediment transport/bypass region, which may help to maintain parabolic dunes. Alternatively, the WTR may simply indicate that a high potential for aeolian erosion exists for these dunes in the absence of vegetation, but the actual transport rate is far less. Alkali Flat is a hard gypsum-cemented surface and likely not an erosive surface. However, it was modeled as having a low WTR during dry periods. Under these conditions, this area will not be an area of sediment accumulation, rather an area of sediment transport/bypass. Alluvial fans may contain both vegetation and cemented (or armored) surface characteristics. This is certainly true for the upper portion of these areas, but alluvial fans adjacent to the playas have a sufficient supply of loose sand and silt sized particles available for transport by wind. As mentioned previously, saltation and dust emission were observed from these areas under dry windy conditions. In summary, caution should be applied in the interpretation of the WTR results because other factors can influence soil erosion.

The timing of the data acquisition is also an important variable influencing the interpretation of the results and their context. Long periods of time exist between each of the image dates and several wet and dry cycles have occurred. Each TI image in Figure 31 represents a 36 hour time difference between day and night image acquisition, and we assume the results are consistent with a ½ period ($\omega/2$ = 12 hours) of the LST wave, ideal for

determining a remote-sensing derived retrieval of TI. Therefore, the data here reflect pseudo-daily TI from different times of different years. This time scale is useful for examining the sediment states that occur at the White Sands Dune field and playa aeolian system as a whole, as well as within the system. Even though presented as a time-series representing six years, the sediment state and configuration of wet and dry surfaces varies on several temporal scales. Both the day- and night-time satellite acquisitions occur at roughly the same time of day, which allows for a direct comparison between different dates. Atmospheric conditions, such as the thermal structure of the atmosphere (i.e., such as a temperature inversion in early morning), vary through the day. Similarly, soil moisture in the upper cm of the land surface varies throughout the day (e.g., precipitation, dew formation). If the same dates are used, but images are acquired at different times, the results would be different. Fortunately, the day acquisition takes place well into the LST wave and the night acquisition occurs early enough that surface moisture variability from day to day is probably similar, favoring drier conditions.

The depth at which soil moisture affects the results of the WTR is not known, but it is hypothesized to be sensitive the only the upper few centimeters of sediment. The soil moisture and the rate of temperature fluctuation at the surface are partially driven by solar heating and cooling. An assumption is made that the retrieved TI represents an integration of soil moisture to some depth within subsurface soil, and we are observing the surface using optical remote-sensing that is mostly sensitive to the uppermost sediment surface (~ 100-200 μm). The amplitude of the daily LST wave is expected to be greatest at the sediment surface, decreasing rapidly with depth [*Sabol et al.* 2006]. Heating and cooling may occur rapidly on the time scale of minutes to hours, fluctuating with atmospheric humidity, the formation of dew, heat waves and wind. Pore space at the sediment surface will lose or retain moisture faster than the subsurface soil, and in a wet aeolian system, it is not uncommon to find this soil moisture to be stable and persistent in both the playa and dune subsurface. What is not known from the remote-sensing measurements is the degree to which the spatial variation of subsurface moisture correlates with the sediment surface. A reasonable assumption would be that the geomorphology, soil composition and cementation are significant factors in determining the soil moisture depth profile. For example, the uppermost sediment surface of a relatively wet playa surface will dry out quickly in the day during intense land surface heating, rapidly forming a friable surface evaporite or silt crust. The surface within a few centimeters may be quite erodible where this occurs and therefore have a

low wind threshold velocity. Subsurface soil moisture, which could lower the ΔT due to the higher heat capacity of the moist subsurface, would give a relatively higher TI and soil moisture retrieval, resulting in a falsely higher wind WTR with respect to the dry skin. Therefore, caution must be taken if applying the results of these TI retrievals to the bulk of the dunes. However, this study was concerned with sediment availability and dust emission events. These two factors would be most concentrated in the uppermost sediment layer and therefore the use of this technique may actually be more appropriate and more accurate than other techniques (i.e., microwave-based approaches) which measure the deeper levels of soil moisture.

The surface albedo may also fluctuate with soil moisture on short time scales for soils of variable composition, including a playa environment. For example, as the playa surface dries and minerals precipitate, the albedo of the sediment may increase. Where soils are different in total evaporite mineral content, the amount of highly reflective crust will also vary. Soils that have the same moisture content should have a similar thermal inertia, but the difference in albedo independent of the thermal inertia will affect the ATI calculation, lowering the TI retrieval for the higher albedo soil surface. The albedo of a clay or silt rich soil may not fluctuate with soil moisture as much as gypsum-, carbonate- and bicarbonate-rich sediment. At White Sands, where gypsum forms as a highly reflective evaporite crust, these areas can be expected to have relatively low TI retrievals and a lower WTR. However, the cohesion of the soil is also an unknown parameter, and the remotely sensed data provide no means to detect how much this cohesion contributes to the strength of the surface soil and the resistance to erosion. If the surface formation of high albedo gypsum is indicative of a stable surface crust, the WTR will be underestimated. Future and more detailed field observations can determine soil strength properties and better correlate sources of erodible sediments with the orbital data.

4.7 CONCLUSIONS

The approach presented here using ASTER-derived TI to estimate soil moisture and the wind threshold velocity ratio (WTR) of an aeolian dune system at a high spatial resolution from

optical remote-sensing data is unique. Furthermore, the data are sensitive to the surfaces most directly involved in saltation, sediment transport, and dust emission events. For the study of White Sands, small scale variability of soil moisture was retrieved without the use of sparse weather station data or the limitations of a hydrologic model. However, modeled soil moisture and precipitation data sets were important in determining the hydrologic forcing that affects soil moisture, and to explain the events that occur between satellite data acquisitions. These data helped to partially explain variations in the modeled soil moisture and correlated them with the timing of precipitation events. Trends in soil moisture were difficult to explain using the monthly precipitation, but the daily precipitation data provide a finer temporal scale from which to compare the soil moisture maps. Dry-down of surface sediments probably occurs quickly, and soil moisture responds to precipitation on the scale of days rather than months with respect to these ASTER results. In wet aeolian systems such as White Sands, soil moisture exerts an important control on increasing the WTR, sediment availability and aeolian erosion. The results for White Sands represent the best possible TI retrievals at this spatial resolution, and local weather data verified that normal diurnal cycles occurred with little to no clouds, precipitation or frontal activity interfering with the ΔT estimation of each image date. Based on previous studies and field observations at White Sands, spatial and temporal variation of TI are strongly affected by soil moisture, which is in turn affected by precipitation. The model for retrieving TI and, subsequently, soil moisture and the WTR, has limitations and is in need of further refinement using ground truth and accuracy assessment at the spatial resolution of the ASTER instrument. Overall soil moisture retrievals (10-25%) were higher than expected for arid lands and dunes (0-10%), reinforcing the need for calibration of the model, incorporating field measurements of soil density, volumetric soil moisture, and soil composition (e.g., percent clay). However, these higher percentages did not impact the spatial patterns or the overall calculation of the sediment availability.

The potential exists to use this approach to estimate sediment availability and soil moisture in other playa, dune, and sparsely-vegetated environments (e.g., fallow agricultural fields), especially if these regions are influenced by subsurface water. A need also exists to conduct these studies for different soil compositions with different albedo, as White Sands has uniquely high albedo. Where small-scale spatial variability is less important, such as the large dune systems of the Sahara, MODIS can be leveraged to examine aeolian sediment availability at

a lower spatial resolution but higher temporal resolution. This study demonstrates a viable approach to soil moisture mapping that may be conducted with ASTER, MODIS or future VSWIR-TIR instruments such as the Hyperspectral Infrared Imager (HyspIRI). The spatial resolution of HyspIRI is planned to be 60m for all the wavelength regions and the temporal resolution for the TIR will be as low as 5 days, which will provide much better resolution for ATI studies. Additionally, apparent thermal inertia modeling using these instruments would complement future high spatial resolution SMAP retrievals of soil moisture, vegetation and surface roughness of arid lands.

5.0 MULTI-SENSOR DATA FUSION, DIRECT MEASUREMENT AND MODELING OF AEROSOL LONGWAVE RADIATIVE FORCING

5.1 INTRODUCTION

5.1.1 Background

Atmospheric aerosols are composed of solid or liquid particles that are suspended in the air. Different types of aerosols exist at different concentrations and particle sizes. They vary significantly in space and time, and are a function of both natural land-atmosphere interactions and anthropogenic emissions. On a global scale, the largest amount of loading is derived from sea spray and mineral dust. Volcanic eruptions are also a significant point source of aerosols, which can impact public health of nearby populations and the safety of aircraft by reducing visibility and increasing the risk of engine failure. Aerosols have significant and profound impacts on public health, where size fractions that are less than 2.5 μm are easily inhaled and deposited in the lungs. Despite these hazards, the impetus for the research described here is driven by the impact of Saharan dust on the Earth's climate. The interaction of these particles affects the incoming solar and outgoing terrestrial energy and the net radiative effect varies because of differences in aerosol shape, size and composition. Each type of aerosol exerts a different effect (i.e., radiative forcing) on the energy budget, which in addition to clouds, drives the planet's climate. The different types of radiative forcing are summarized as direct (e.g., scattering, absorption and emission of radiation), indirect (e.g., modification of physical and radiative properties of clouds) and semi-direct effects [*Twomey* 1974; *Haywood and Boucher* 2000; *Lohmann and Feichter* 2004]. The net energy flux in each of the many scenarios can be either positive in sign (i.e., net downwelling is greater, a gain of energy occurs and the Earth

experiences warming) or negative (i.e., net upwelling is greater, a loss of energy from the Earth and cooling). Constituents in the atmosphere alter the relative proportion of solar and terrestrial energy fluxes, thus the net upwelling or downwelling energy flux (measured as Watts/m^2). The interactions of radiation and aerosol particles are inherently complex; however the prediction of aerosol radiative forcing is extremely important to the accuracy of climate predictions. Greenhouse gases and ozone exert a positive radiative force by absorbing radiant energy, causing a warming of the Earth's climate. The historical record and the effect of anthropogenic gaseous emissions, such as carbon dioxide, on the Earth's climate are known with relative accuracy, but the effect of aerosols on total radiative forcing and climate sensitivity is not well constrained (Figure 36).

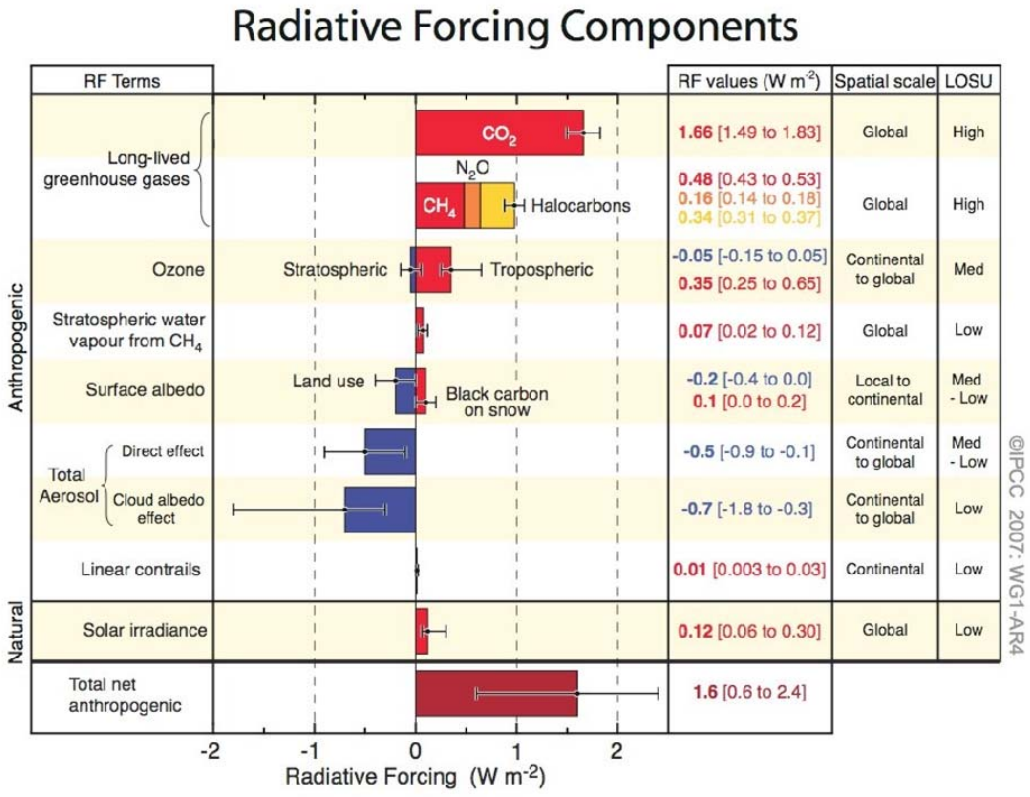

Figure 36. Radiative forcing components from the 2007 International Panel of Climate Change report.

On a global scale, a major assumption is made that the energy powering the Earth's climate is in equilibrium [*Kiehl and Trenberth* 1997], where outgoing terrestrial radiation balances with the incoming absorbed solar radiation. Transmitted solar visible and shortwave energy is absorbed or reflected by the Earth surface. Absorbed energy is transformed into various forms (i.e., sensible and latent heat, potential and kinetic energy) before thermal emission occurs at longer wavelengths. Researchers continue to improve the models that predict this flow of energy through the global climate system (Figure 37), and a number of surface, airborne and satellite observations have been used to validate, constrain and reduce the uncertainty of these models (described below).

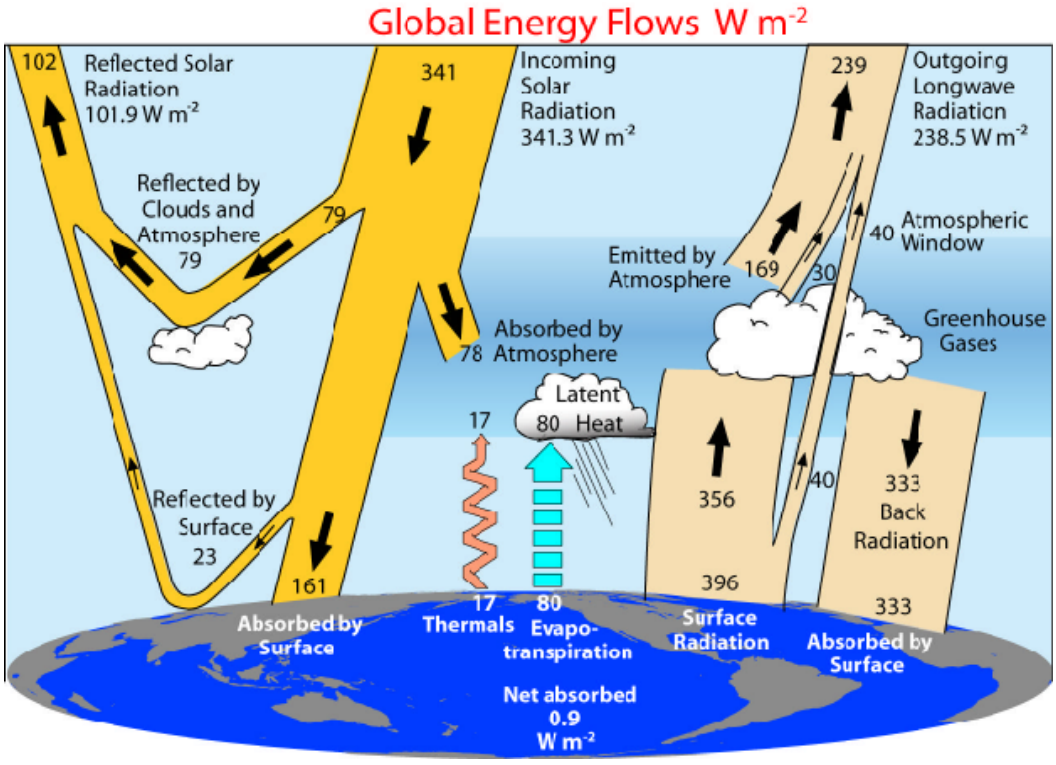

Figure 37. Radiation budget [*Trenberth et al.* 2008].

Aerosols remain one of the largest uncertainties in radiative forcing [*IPCC* 2007]. Some of the most recent satellite measurements of the Earth's radiation budget are from the Clouds and the Earth's Radiant Energy System (CERES) instruments. *Zhang and Christopher* [2003] used a synthesis of MISR, MODIS, and CERES, comparing the spatial variability of dust aerosols and the LW radiative forcing over the Sahara, which showed that Saharan dust counteracted a portion of the incoming shortwave energy by the contribution of longwave radiation. Studies of this net

energy balance using combined CERES and MODIS Single Satellite Footprint (SSF) data stress the importance of the effect of dust on the longwave radiation budget [*Christopher and Jones* 2007, 2008]. The use of CERES and MISR data in *Gupta et al.* [2008] is anther example of data fusion that addresses the longwave radiative effects due to mineral dust loading. The total aerosol loading can be separated into mineral dust, marine and anthropogenic components from the optical depth (AOD) as well as the radiative effects due to the different aerosols [*Bellouin et al.* 2005; *Kaufman et al.* 2005]. Several values of the shortwave radiative effects have been reported, but few values of the longwave radiative effects over the Atlantic Ocean were available according to *Christopher and Jones* [2007]. Several other instruments, such as those in the NASA A-Train, a series of six satellites flying in close proximity following Aqua, can be used to study mineral dust aerosols. For example, the Cloud-Aerosol Lidar and Infrared Pathfinder Satellite Observation (CALIPSO) instrument has the ability to map the vertical distribution of dust. MODIS has been used to retrieve mass and size particles in sandstorms in China [*Gu et al*. 2003]. *Hsu et al.* [2004] estimated aerosol properties over bright-reflecting source regions using MODIS and compared them to ground-based Aerosol Robotic Network (AERONET) radiometer measurements of dust. MODIS was also used to enhance the spatial extent of dust storms over water and land [*Hao and Qu* 2007, *Miller* 2003].

Uncertainty still remains as to the direct effect of dust loading on temperature feedback in the atmosphere and at the Earth surface. Understanding the longwave radiative effects due to mineral dusts and its modeling uncertainties is important to our understanding of weather and climate [*Sokolik et al.* 2001, *Haywood et al*. 2001, *Yoshioka et al*. 2005, and others]. For example, the interaction of the dusty air layer with tropical cyclones is thought to suppress convection within hurricanes [*Dunion and Velden* 2004]. *Miller and Tegen* [1998] have shown that Arabian dust has caused reduced temperatures in Australia as well as the northern hemisphere. In contrast, *Zhang and Christopher* [2003] have shown a different concept, a "warming effect" over the Sahara due to mineral dust loading. Their study used data from MISR, MODIS, and CERES to compare the spatial variability of dust aerosols and the longwave radiative forcing over the Sahara. For September 2000, they showed a reduction of the outgoing longwave (OLW) radiative flux with an increase of aerosol optical depth (AOD), counteracting the "cooling effect" that occurs from the reflection and scattering of solar energy in the visible

and short wavelength region. Furthermore, the LW flux was found to double if surface temperature was increased from 300 K to 316 K, which is a nonlinear response.

Recent research has addressed the need for more accurate parameters to model dust inputs, such as size distribution and chemistry/mineralogy of the dust [*Meloni et al.* 2004, *Luo* 2003]. Several campaigns have been conducted to study Saharan dust and aerosol emissions, many including aircraft missions and direct dust sampling. These missions include the Saharan Dust Experiment (SHADE) [*Tanré et al. 2003* and others], Mediterranean Dust Experiment (MEIDEX) [*Alpert et al.* 2004], the Bodele Experiment 2005 [W*ashington et al.* 2006], the Dust and Biomass Experiment (DABEX), the African Multidisciplinary Monsoon Analysis (AMMA), and the Saharan Mineral Dust Experiment (SAMUM) [*Knippertz et al.* 2009]. Understanding the effect of aerosols on climate, specifically, the longwave (LW) radiative forcing due to mineral dusts and the modeling uncertainties is very important to climate studies [*Sokolik et al*. 2001; *Haywood et al*. 2001; *Yoshioka et al*. 2005]. Recent research addressed the need for more accurate parameters to model dust inputs, such as size distribution and chemistry/mineralogy of the dust (e.g., *Meloni et al.* 2004; *Luo* 2003]. Mineral dust was also found to be the source of discrepancy in LW radiative forcing by 50 W/m^2 in Meteosat-7 and numerical weather prediction (NWP) modeling for July 2003 data [*Haywood et al.* 2005 and others]. Scattering and absorption properties of mineral dust aerosols are not accounted for in the NWP model, and *Haywood et al.* [2005] concluded that inclusion of the radiative effects of mineral dust will lead to significant improvements of modeling. Broadband surface emissivity (ε) is coarsely approximated in the NWP model, leading *Haywood et al.* [2005] to conclude differences in emissivity alone cannot explain modeled variability in LW radiative flux. *Ogawa et al*. [2003] showed there are large variations of broadband emissivity using ASTER, which can better resolve this variability over traditional classification based determinations [*Wilber et al.* 1999]. Regressions between lab spectra, ASTER and MODIS data allowed continental scale mapping of broadband emissivity using MODIS [*Ogawa et al*. 20004].

Because sea surface temperature affects the generation of hurricanes in the North Atlantic, it is suggested that the dusty Saharan air layer (SAL) could also be a forcing for storm severity [*Dunion and Velden* 2004; *Karyampudi et al.* 2002]. This impact of aerosols obviously occurs on relatively short time scales and have a direct human impact by affecting the frequency of hurricanes on the eastern coast of North America and the Caribbean. Many hurricanes and

tropical storms in the Atlantic originate from convective waves that travel westward from the Eastern Atlantic near the coast of Africa. The energy of these weather systems depend on several parameters, including atmospheric stability, wind patterns, sea surface temperatures, atmospheric water vapor and the interaction with other weather systems. Large dust storms occur in the Sahara and Sahel region of North Africa, which generate a dry, warm and dust-loaded layer of air. The air is driven out over the Atlantic Ocean as the Saharan Air Layer (SAL) between one and six kilometers high, over the more humid and cooler marine boundary layer (MBL). The mineral dust in the SAL reflects or scatters visible and shortwave solar radiation by increasing the albedo of the atmosphere, thereby creating a negative radiative effect (cooling). Indirectly, mineral dust forms cloud condensation nuclei, increasing clouds and cloud brightness, which is also a negative radiative effect. This also reduces energy received at the Earth surface, reducing temperatures and thus minimizing energy available for cyclogenesis. Further reduction in energy for cyclogenesis occurs by the prevention of upper level convection as a temperature inversion layer and an increase in vertical wind shear [*Sun et al.* 2008].

5.1.2 Research Objectives

An underlying hypothesis for the dissertation work described in this Chapter is that the composition of dust sources and aerosols that regularly disperse over the North Atlantic affects the variability of LW radiative forcing. Dust sources in the Sahara are widespread, yet there are specific locations that are considered to be "hot spots" (e.g., locations where dust emissions are regularly generated by winds from readily available sediment). Winds initiate dust emissions from several sources simultaneously over these hot spots, but then the dust is mixed along the direction of transport. Therefore, it is difficult to make connections between dust sources (and their composition) and atmospheric measurements of aerosols. To address this problem, the composition of the dust aerosols must be better understood through the analysis of multiple, concurrent datasets, including modeling. Indeed, many studies have attempted and succeeded in connecting observations of atmospheric dust to dust sources from the Sahara, as referenced and described above. The research here attempts to address possible gaps in understanding of the SAL system by characterizing dust sources and atmospheric dust with previously unutilized data. There are two datasets that have not been employed to study the SAL: orbital ASTER TIR data

and ground-based Forward Looking Infrared (FLIR) data. These both have the capabilities to examine longwave radiation and dust composition simultaneously. The research objectives here were to (1) use ASTER data to examine dust source composition and characteristics and also to (2) determine the effect of aerosols on longwave radiative forcing in the atmosphere. FLIR data were used to measure and model longwave radiative forcing due to aerosols, which is a new experimental approach for SAL dust studies.

There are three main sections for this Chapter that each relate to a quantitative understanding of the properties and transport of Saharan dust aerosols in the Earth's atmosphere: (1) the cycle of atmospheric dust and its radiative effects, (2) mapping dust source composition, and (3) measuring emitted longwave radiation from the dusty atmosphere. As a broad approach, an attempt was made to synthesize two very different applications of remote-sensing. On one hand, there exists a lineage of traditional instruments for studying dust on a global scale that monitor the Earth with near complete coverage and regularity (i.e., TOMS, MODIS, and AERONET). On the other, there are high spatial and spectral resolution data sets that are used to map surface composition and geomorphology (i.e., Landsat, ASTER, and Google Earth™ mapping service data), although these data are discontinuous in time. The work in this Chapter attempts to synthesize and relate these datasets. A number of different supporting datasets are also used which are not the focus of the work, but they were needed to put ASTER and FLIR measurements into context.

The field site, the various instruments and their datasets are introduced and described in section 5.2. In section 5.3 the variability of mineral dust aerosols in the atmosphere and their effect on the Earth's radiation budget through time is addressed. Data were simultaneously acquired from both orbital and ground-based sources between July 4 and August 4, 2009. Ground-based data are from the Izaña Atmospheric Observatory (IZO) on the island of Tenerife, Spain. This facility houses the ground-based network of AERONET instrumentation, which measures aerosol and atmospheric properties on a continual basis. These measurements are related to orbital data, modeled dust loading and the wind patterns within the SAL for the month of July. ASTER data were acquired to demonstrate its their use as a high spatial and spectral resolution focus for dust studies. In section 5.4, ASTER is used further to identify dust source composition and the characteristics of dust hot spots. Syntheses of thermal infrared remote-sensing, laboratory and field based measurements are used in an attempt to relate dust source

composition (small scale) to the larger scale of atmospheric dust. The effects of dust on the Earth's outgoing longwave radiation are controlled by particle size and composition, therefore ASTER can be used to examine the TIR optical properties (emissivity) of Saharan dust sources directly. In the thermal infrared wavelength region, the spectral emissivity of dust sources can be derived to determine composition.

Lastly, in section 5.5, a new experimental approach for dust studies is presented. A method was developed using the application of side-looking FLIR to measure atmospheric LW radiation (7 – 13 μm wavelength region) emitted by aerosols. These data were collected from the observation tower at IZO on the island of Tenerife in July 2009 simultaneously with Aqua and Terra satellite overpasses, where because of the location and elevation, the longwave radiance measurements can be directly compared to other dust measurements and properties described in section 5.3 and 5.4. In this atmospheric window, absorption due to water vapor, carbon dioxide and stratospheric ozone are minimal. Preliminary results of the raw, uncorrected data are presented in section 5.5, and how these data can be used to study the SAL is also described.

5.1.3 Study Site and General Local Climate

The Canary Islands are a unique place to study the effect of aerosols for several reasons (Figure 38). First, the location is close to the source of mineral dust emissions from the Sahara desert, which are frequently transported over the islands. Dust events are frequent, but they are intermittent enough to allow measurement of a variety of conditions (dusty and clear). Second, the Izaña Atmospheric Observatory (IZO), located on the largest island of Tenerife, maintains extensive instrumentation networks (AERONET, and the aerosol monitoring program conducted by the Agencia Estatal de Meteorología, AEMET) that monitor climate, weather and atmospheric properties, including aerosols concentration, size distribution and composition.

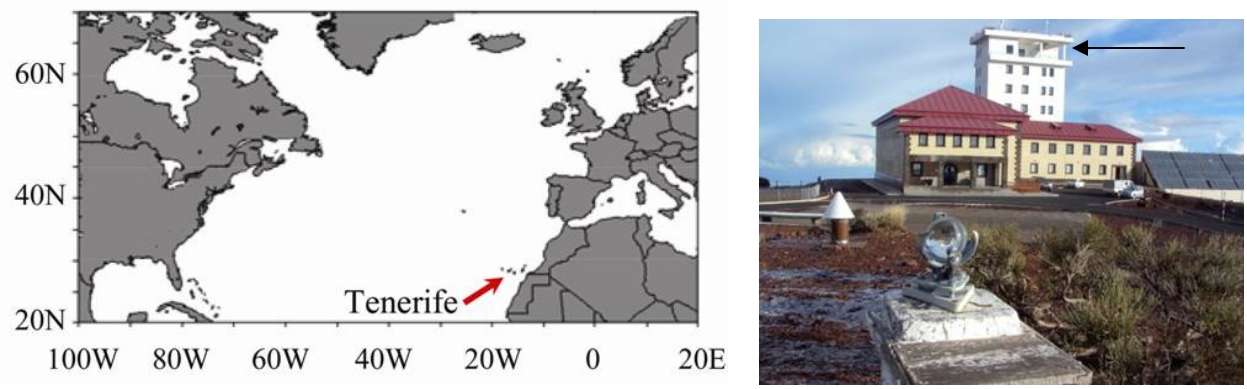

Figure 38. Geographic location of study site for dust measurements (left image) [*AEMET* 2009]. Measurements were acquired from the observation tower (indicated by arrow in right image) [*AEMET* 2009].

Thirdly, the geographic location (16.499°W, 28.31°N) and elevation of the observation tower (2391 m.a.s.l.) allow measurements above a stable atmospheric temperature inversion layer in the lower free troposphere (FT) where sky conditions are generally clear, have consistent prevailing winds most of the year and are separated from the influence of marine aerosols and anthropogenic aerosol emissions. The MBL below the FT is humid and cool with trade winds consistent in the north northeast direction. A layer of stratocumulus clouds characterizes the top of the MBL (between 800 to 1800 m.a.s.l.) just below the temperature inversion. Dry air subsides with northwest winds in the FT. During the summer dusty season, a cycle of large Saharan dust plumes are carried by southeast winds in the FT to the Atlantic Ocean. Consequently, this location is an ideal place to study the pulsing of the SAL where the sampling and measurement of atmospheric aerosols can be assumed to be predominantly influenced by Saharan dust.

There are numerous studies describing the meteorology that controls dust storm generation in North Africa [*Engelstaedter and Washington* 2007], the mobilization and transport of dust to the Atlantic [*Carlson and Prospero* 1965, 1972; *Knippertz et al.* 2009; *Karyampudi et al.* 1999] by African easterly waves [*Carlson and Prospero* 1969; *Burpee* 1972; *Cook* 1999], the effects on tropical cyclogenesis [*Karyampudi et al.* 1999; *Reid et al.* 2003; *Dunion and Velden* 2004; *Evan et al.* 2006] and the radiative effects of the dust [*Carlson and Benjamin* 1980]. However, despite the large volume of literature on the subject, many aspects of the SAL system are still be poorly understood. In general, the SAL is an elevated layer of mixed dry air with high dust loading that originates from various regions in the west and central Sahara. It emerges from the Atlantic coast of West Africa moving west at a base height of about 850 mbar (~ 1.5

km) extending to 500 mbar (~ 6 km). African easterly waves, troughs of low atmospheric pressure, move form east to west along the equator side of the subtropical ridge of high pressure, which lies north of the Intertropical Convergence Zone (ITCZ). These waves travel westward with the prevailing winds near the equator and can lead to the formation of tropical storms or hurricanes in the Atlantic. The waves and the SAL are intimately related as tropical waves lead to deep atmospheric convection and atmospheric instability. The result is gustiness, which is thought to be a control on dust generation in the Sahara [*Engelstaedter and Washington* 2007]. The SAL commonly follows easterly waves, where the SAL then leads to reduced cloud cover, strengthens the temperature inversion above the MBL and limits atmospheric convection in the Atlantic.

5.1.4 Supporting Data Sets

The ASTER and FLIR IR measurements of the SAL dust must be placed into context by using other ground-based satellites datasets. Measurements of incoming shortwave (0.34 – 1.02 μm) solar energy and optical properties of aerosols were collected and derived from AERONET instruments, obtained from the Level 1.5 data product on the AERONET web site. The radiative forcing of the SAL aerosol loading was examined by describing and ultimately comparing ground observations and satellite derived values. MODIS and AIRS data parameters were obtained through the GES-DISC (Goddard Earth Sciences Data and Information Services Center) Interactive Online Visualization ANd aNalysis Infrastructure (GIOVANNI) system [*Acker and G. Leptoukh* 2007]. Dust loading was predicted by the Dust Regional Atmospheric Model (DREAM) [*Nickovic et al*. 2001; *Pérez et al*. 2006a, 2006b], and the average vector wind fields at 3000 m were derived from NCAR/NCEP weather reanalysis data. This wind data provides one dimension of the synoptic weather patterns important to distributing dust over the Atlantic and in relation to the IZO. This model operated by the Barcelona Supercomputing Center in the Earth Sciences Department, maintained daily 72 hour prediction data online. Orbital and AERONET datasets are described below.

5.1.4.1 The Spinning Enhanced Visible and InfraRed Imager (SEVIRI)

SEVIRI data are collected from the geostationary Meteosat Second Generation (MSG) satellite, and are available in near real-time every 15 minutes over the whole of Europe and Africa. SEVIRI is a 50 cm diameter aperture, line by line scanning radiometer, which provides image data in four Visible and Near InfraRed (VNIR) channels and eight InfraRed (IR) channels [*http://www.eumetsat.int/Home/index.htm*]. The SEVIRI dust product algorithm enhances the visual appearance of dust, which utilizes brightness temperature differences in the infrared bands at 12, 10.8 and 8.7 μm wavelengths and a specific color stretch transformation to enhance the appearance of dust. This allows a very good visualization tool to observe the timing of dust storms and SAL formation. DREAM model predictions have shown to compare well to the spatial distribution of dust obtained by SEVIRI [*Basart et al 2009*].

5.1.4.2 The Moderate Resolution Imaging Spectroradiometer (MODIS)

The MODIS instrument began collecting data from the NASA Terra spacecraft in December 1999 and from the Aqua spacecraft in May 2002 [*Parkinson* 2003; *King et al*. 1992; *King et al*. 2003]. MODIS measures radiance at 250 to 1 km spatial resolution in 36 channels spanning the spectral range from 0.44 to 15 μm. The advantages of MODIS are its spatial coverage over a large geographic area, where between MODIS Aqua and Terra, measurements are acquired 4 times every 24 hours. Day and night overpass times for MODIS Terra occurred at approximately 11:30 and 23:30 GMT respectively, and MODIS Aqua data were collected at approximately 14:45 and 2:45 GMT. Aerosol retrieval makes use of seven solar spectral channels (0.47–2.1 μm) at 250- and 500-m spatial resolution [*Tanré et al.* 1997; *Kaufman et al.* 1997; *Levy et al*. 2003]. MODIS has a wide spectral range and can measure aerosol optical depth (AOD) over both ocean and land and give quantitative estimates of aerosol size [*Tanré et al.* 1997]. Previous validation of global MODIS AOD and aerosol size products have compared well to retrievals from ground-based sun photometers at coastal AERONET sites ($r^2 = 0.95$) [*Holben et al.* 1998; *Remer et al.* 2002]. Aerosol size retrievals have errors in dusty regions however due to inaccuracies of the spectral dependence of AOD measurement [*Levy et al.* 2003]. Generally, AOD is overestimated for low dust loading and underestimated for high loading [*Chu et al*. 2002]. Time series data of AOD were extracted from MODIS-derived products from both Terra

and Aqua (MOD08.D3.005 and MYD08.D3.005 data products respectively) and were combined to give a full time-series trend during the data collection period of July 3 – August 3, 2009.

5.1.4.3 Thermal infrared data from the Atmospheric Infrared Sounder (AIRS)

AIRS is a cross track scanning instrument aboard the Aqua spacecraft (along with MODIS) in NASA's A-train constellation of polar orbiting satellites. AIRS has been operational and providing 80% daily coverage of the globe since 2002 [*Aumann et al.* 2003]. Thermal infrared data are hyperspectral in the 8-12 μm atmospheric window, where day and night radiance measurement is sensitive to the spectral features of mineral dust, including quartz and feldspar, over ocean or land [*Pierangelo et al*. 2004; *Carn et al.* 2005; *De Souza-Machado et al.* 2006]. AIRS has a 13.3 km footprint at nadir and 2378 bands covering three spectral ranges (≈ 3.8 to 4.6, 6.2 to 8.2, and 8.8 to 15.4 μm), where the noise equivalent change in temperature (NEΔT) < 0.2 Kelvin. Several different products are generated from the AIRS data, where for this study, AIRS retrievals of temperature and water vapor profiles (g/kg of dry air) were extracted from the daily standard product (AIRX3STD.005) for day and night overpasses between July 3 and August 3, 2009. Total column ozone (in Dobson units), total column water vapor (cm) and the measured and clear-sky outgoing LW radiative fluxes (W/m^2) were also extracted. Clear sky radiation fluxes are estimated using the AIRS-RTA radiative transfer algorithm [*Aumann et al.* 2003; *Strow et al.* 2003]. These longwave radiative fluxes and modeled clear sky radiation fluxes can determine the net radiative forcing for top of atmosphere (TOA). Syntheses of AIRS and CALIPSO data also have the ability to retrieve dust due to the absorption features of mineral dusts within the 8-12 μm atmospheric windows [*De Souza-Machado et al*, (submitted); *De DeSouza-Machado et al.* 2006]. AIRS data were also useful in producing a dust-flag algorithm implemented in the AIRS version 5 data product that relies on brightness temperature differences from narrow thermal infrared bands that exceed specific thresholds [*De Souza-Machado et al.* 2006]. For AIRS data, the brightness temperature differences were between 10.4 and 8.1 μm and between 10.4 and 12.2 μm.

5.1.4.4 ASTER Thermal Infrared

The ASTER TIR data products have largely been used in this Chapter to examine land surface properties, where here an attempt is made to use the instrument to derive atmospheric parameters, leveraging its higher spatial resolution. ASTER measures spectral radiance in five TIR bands between 8.13 and 11.65 μm, has a spatial resolution of 90 m/pixel and a NEΔT value < 0.3 K. The data used for this study include the L1B data products. Instrument calibration is applied to Level-1A (L1A) data, which is based on the sensor stability over time in order to create the geolocated and radiometrically accurate L1B data, resulting in an absolute accuracy of 2% and a relative accuracy of 1% [*Yamaguchi et al*. 1998]. The L1B data show radiance at top of atmospheric (TOA). The AST_09T product, created from the L1B, has been radiometrically, geometrically, and atmospherically corrected [*Thome et al.* 1998]. Here in this section, the use of ASTER L1B data was tested in its ability to provide atmospheric information. The TIR bands in the AST L1B standard data product represent the TOA surface leaving LW spectral radiance. Several dust algorithms exist for different data products, like MODIS [*Miller* 2003]. Similarly, the SEVIRI dust detection/visualization algorithm is also a useful dust detection product that relies on brightness temperature differences between 12 and 10.8 μm and between 10.8 and 8.7 μm. Using ASTER's L1B data, the combination of band brightness temperature differences from dusty and clear conditions are used to test a similar dust detection product designed after the SEVIRI algorithm. The linear deconvolution approach using ASTER data [*Ramsey et al*. 1999] was also used to attempt relate dust observations at IZO to dust sources in the Sahara.

5.1.4.5 AERONET

The AERONET station was partially developed as a collection of ground-based radiometers for satellite data validation [*Holben et al.* 1998], but it is also used to study aerosols in the atmosphere directly. Spectral sky-scanning radiometers accurately retrieve aerosol measurements, including aerosol size distribution and the refractive index at four optical wavelengths [*Dubovik and King* 2000; *Dubovik et al*. 2000]. Specifically, the time series of aerosol optical thickness (AOT) at solar wavelengths, volume of dust particles (total, course and fine fractions), the solar radiative forcing (or net flux), particle size distribution and total column water vapor were examined. The derivation of these inversion products, or aerosol optical

properties from direct and diffuse solar radiation, are described in the papers by *Dubovik and King*, [2000], *Dubovik et al.* [2000], [2006], and others.

5.2 THE CYCLE OF ATMOSPHERIC DUST AND ITS RADIATIVE EFFECTS

5.2.1 Time-Series of Satellite and AERONET Data

MODIS and AERONET both detect the largest AOD SAL dust event in the month of July beginning July 20 affecting the island of Tenerife (Figure 39a). The AOD peak on July 20 was at the same time but different in magnitude for MODIS and AERONET. The MODIS AOD was 2.35 and the AERONET value was 0.56. The time trends in the two data sets are similar, but the magnitudes of the AOD events are generally greater from MODIS data compared to AERONET. Regression analysis between the MODIS AOD at 550 nm and the AERONET AOD at 500 nm resulted in an r^2 equal to 0.54, excluding the July 20 outlier, where MODIS was 60% higher than AERONET observations. Dusty conditions were observed on the first day (July 10) of in-field observations, and local researchers confirmed the hazy conditions as a typical, but mild, SAL event. AERONET data show a sharp peak in AOD above background (0.3), but only a broad increase is seen over the course of a few days in the MODIS retrieval (increasing from 0.16 to 0.45). Some of this discrepancy may be because the AERONET is measuring AOD in the atmosphere heights between 2.39 and 120 km. MODIS is measuring AOD for the entire atmospheric column, which includes the lower MBL AOD. Another factor is the MODIS values extracted using GIOVANNI are from an area integrated over 1° of latitude and longitude. Therefore, high concentration (or low concentrations) anywhere else in the area may skew the time-trend for the Tenerife location. AERONET is a point measurement and can be assumed to be most representative of the exact location and the SAL. Accepting some of the general differences between the data sets, the relative time-series both document the cycle of dust and clear conditions. ~~We~~ can also compare the AOD values to the trends of water vapor and ozone from AERONET and AIRS to determine to what degree aerosol or non-aerosol absorption and scattering correlate. According to the regression between water vapor and AOD, 50% of the

AOD could be due to water vapor, but these values are generally not well correlated, indicating a good separation of the two measurements (r^2 = 0.5). .For the July 10 event, a peak aerosol volume occurs but water vapor and ozone are also high as measured by AIRS. In general, SAL dust events are expected to be dry and dust-loaded; therefore, the July 10 event perhaps goes against the usual SAL trend because a component of the AOD value is not due to aerosols. Image data demonstrate variability in the general character of SAL events, where dust plumes commonly spur cloud formation, as seen in SEVIRI data sets show later. In contrast, the largest MODIS AOD event on July 20 corresponded to classic conditions of SAL dust events, where water vapor decreases with the onset of dust as measured by both orbital and ground-based data. Ozone however, is higher than average on the July 20.

The second largest event (AOD = 0.9) detected by MODIS is on July 30, but data are not available from the AERONET station at that time. AERONET and MODIS also do not collect night time data in the VNIR and SWIR wavelength regions. The trend in the AERONET data shows increasing AOD before and decreasing AOD after the MODIS peak on July 30. The second largest peak from AERONET data occurred on July 26, where MODIS only picked up a broad increase over a few days (similar to the comparison of data between MODIS and AERONET on July 10). The clearest sky conditions were observed on July 13 and 14 when AOD, water vapor, ozone and aerosols were measured at their lowest values.

Assuming that the trends in water vapor and ozone were properly estimated, ~~we~~ the AERONET inversion products give accurate physical dust properties that have been modeled from the multi-angle spectral measurements. Dust concentration (Figure 41) as well as the solar radiative forcing due to aerosols (Figure 42a) is determined by an inversion algorithm adapted for AERONET sky measurements [*Dubovik and King* 2000]. To determine the total net radiative effect due to aerosols, it is important to examine both the balance between longwave and shortwave energy. AERONET does not measure or model the outgoing longwave radiance. Longwave radiative forcing is determined by AIRS orbital data, which is the outgoing longwave radiance minus modeled clear sky radiance and the radiative forcing data are with respect to aerosols (Figure 42b). Regression analysis confirmed that radiative forcing was found not to correlate with AIRS measurements of water vapor or ozone ($r^2 < 0.33$), and AIRS longwave radiative forcing was found to not correlate with the AERONET shortwave radiative forcing as well (r^2 = 0.03). Shortwave radiative forcing (Figure 42a) is correlated with dust concentration

where the r^2 is equal to 0.92 (Figure 41). Therefore, these data show that shortwave radiative forcing is affected by aerosol loading, whereas the AIRS longwave radiative forcing is not. This is not a surprising result because AERONET values are modeled from measurements in the short wavelength region (0.34 – 1.02 μm). Just as MODIS measured the total AOD from orbit, AIRS also integrates the entire atmospheric column. On three instances July 16, 24 and 31, the decrease in shortwave radiation correlated with the increase in longwave radiance as a result of upper level clouds ($r^2 = 0.92$).

The time-series of volume concentrations of dust is modeled as a bimodal source of coarse and fine modes (particle size) of dust [*Dubovik and King* 2000]. The fine size fraction of dust is generally an order of magnitude less than the coarse fraction, and the trends through time are similar (Figure 41). One notable deviation occurs on July 20 where the fine mode of dust particles was absent in the measurement (Figure 43). On July 10 and July 26 when other dust events occurred, a fine mode of dust was present and the relative peaks of fine and coarse modes were similar (Figure 41). Where the particle size distribution becomes coarser and unimodal, the aerosol type is more typical of a SAL event dominated by mineral dust [*Rodriguez*, unpublished data]. In summary, of the dust concentration trends in the month of July, five dust events occurred were ≥ 0.15 $\mu m^3/m^2$.

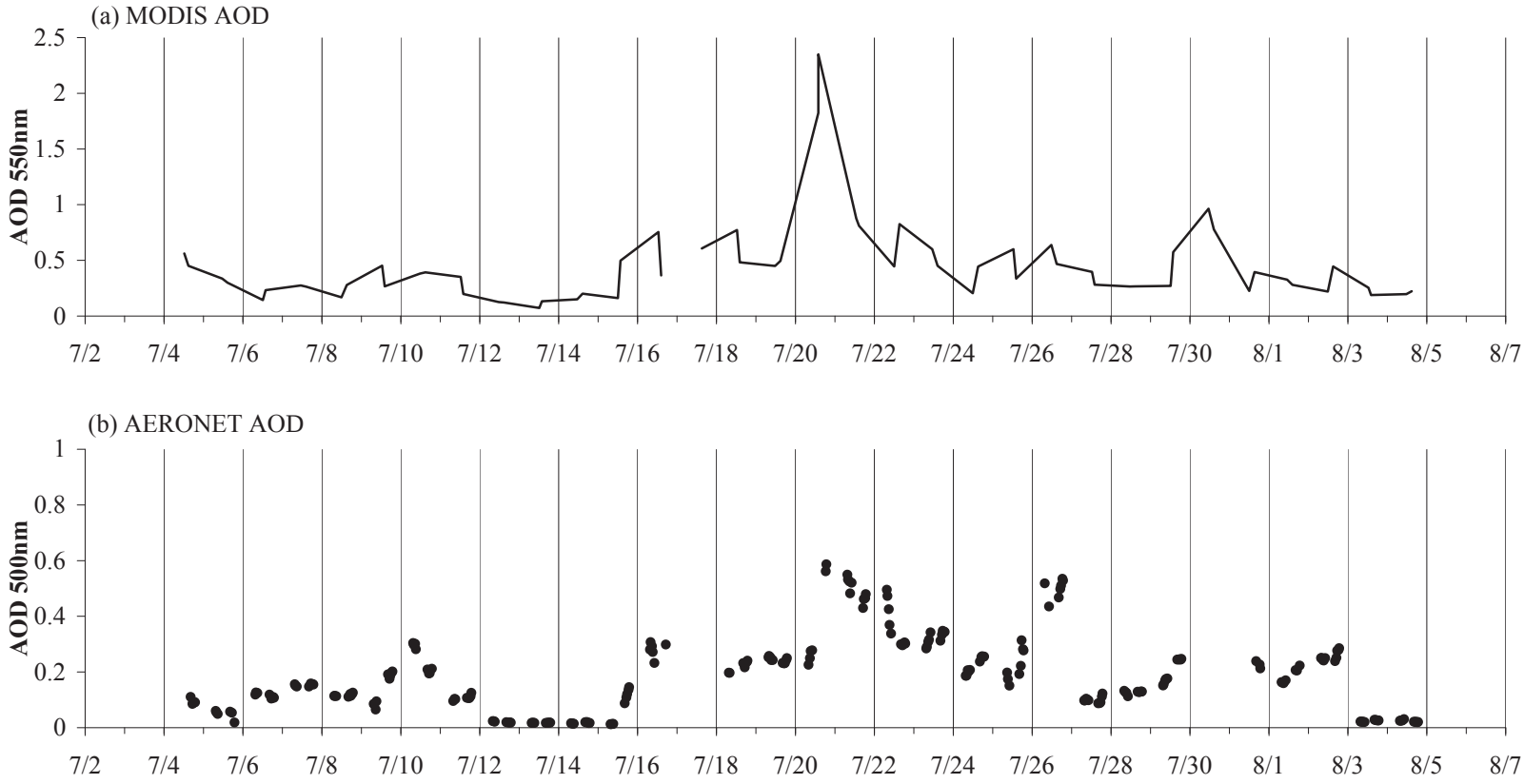

Figure 39. (a) Combined time-series of aerosol optical depth from MODIS Aqua and MODIS Terra. (b) AOD at solar wavelengths from AERONET.

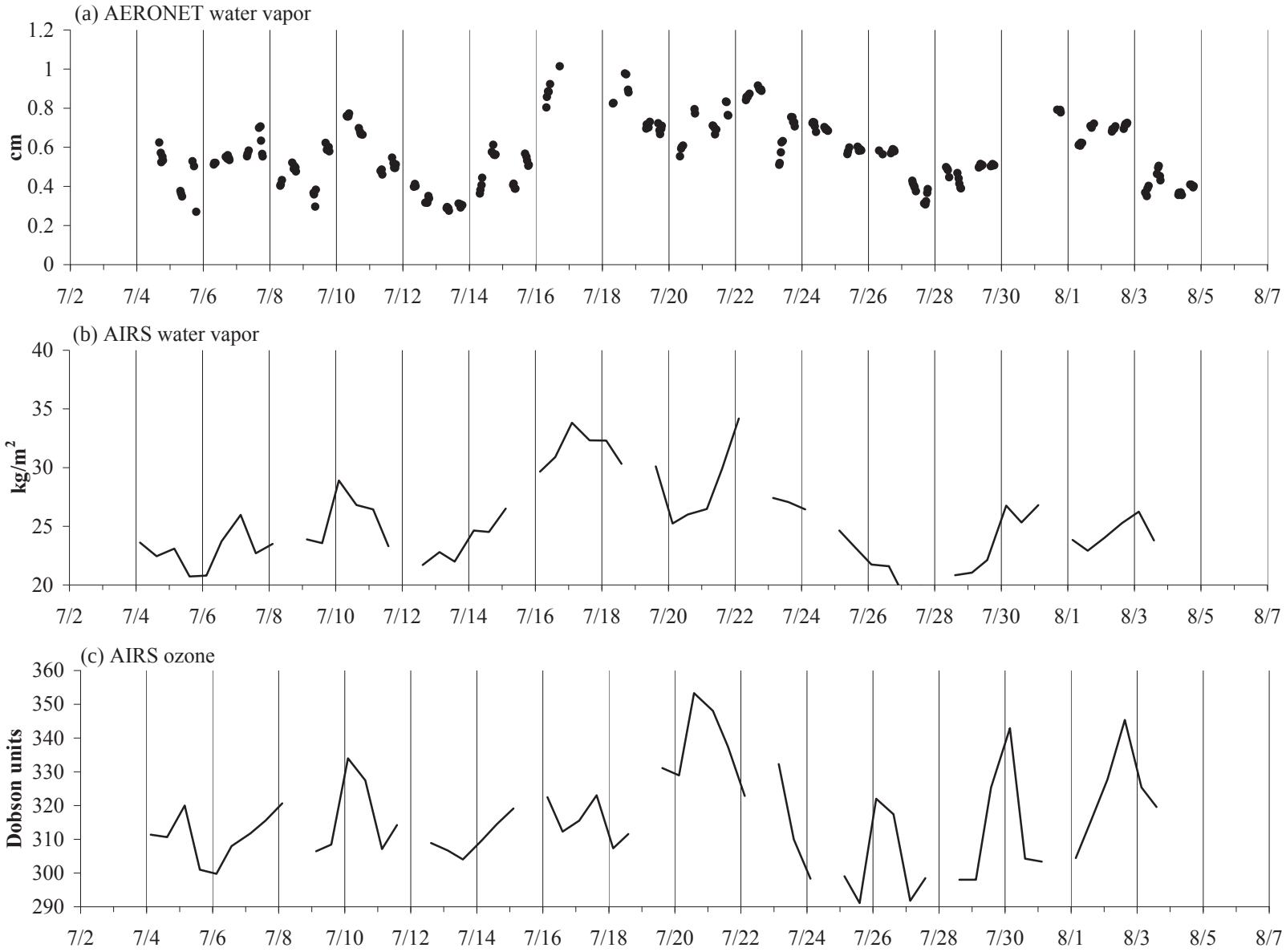

Figure 40. Total column water vapor from (a) AERONET measured in cm and (b) AIRS measured in kg/m^2. (c) The time series of total column ozone (Dobson units).

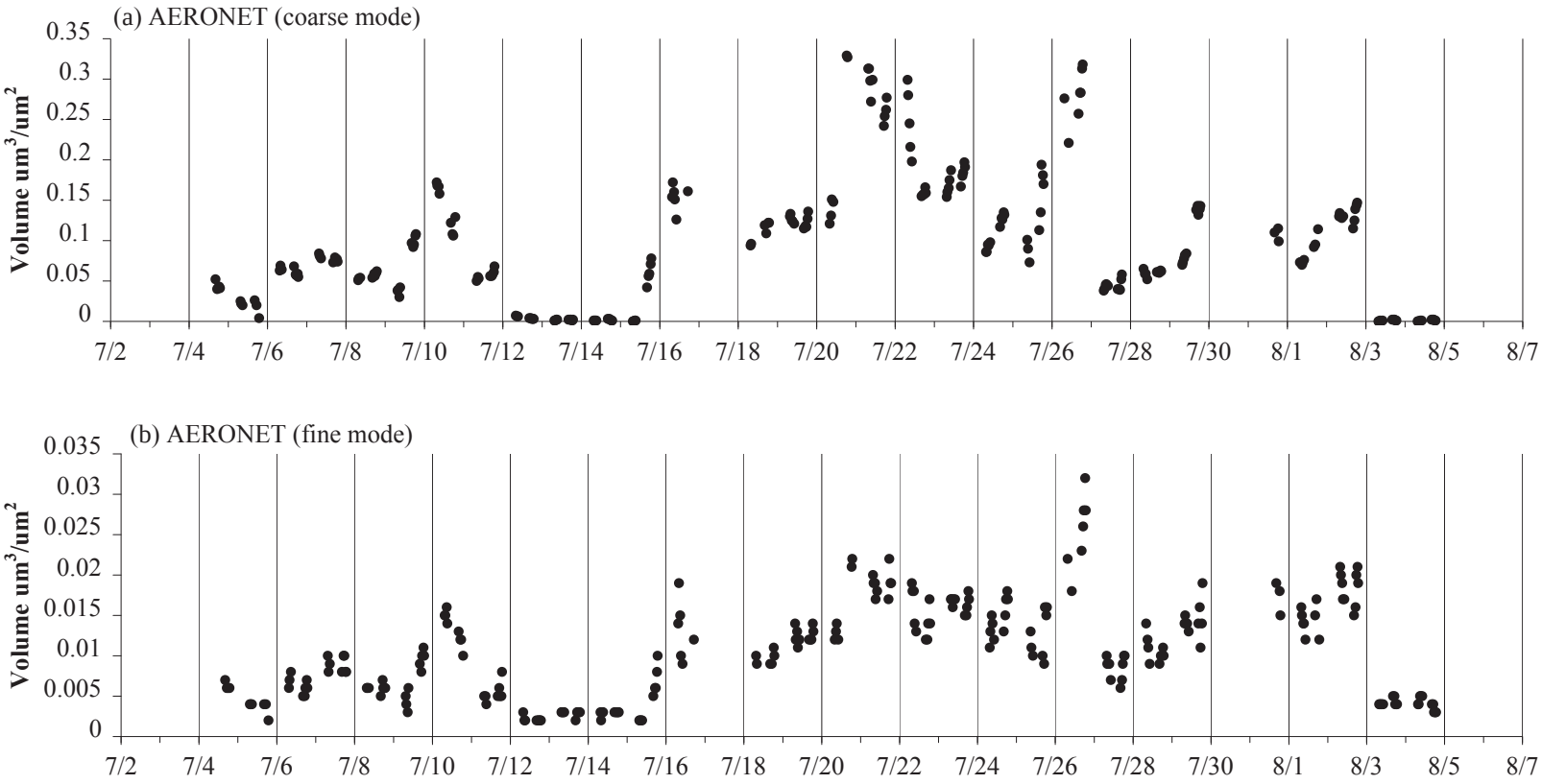

Figure 41. AERONET derived volume concentration of aerosols ($um^3/um^{2)}$ for the (a) coarse and (b) fine mode fractions of the total.

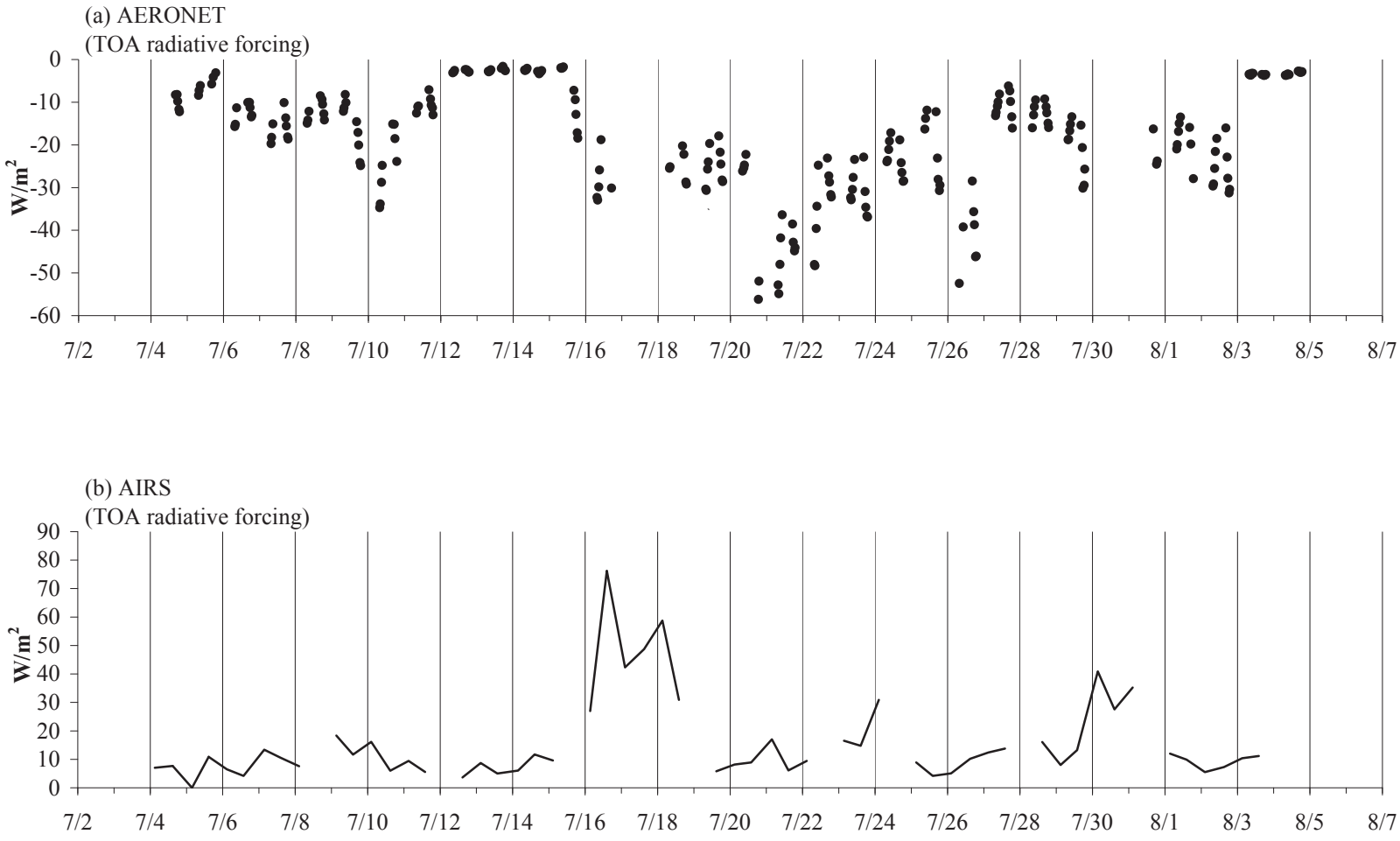

Figure 42. (a) AERONET radiative forcing of shortwave solar and (b) longwave terrestrial radiance measured from AIRS.

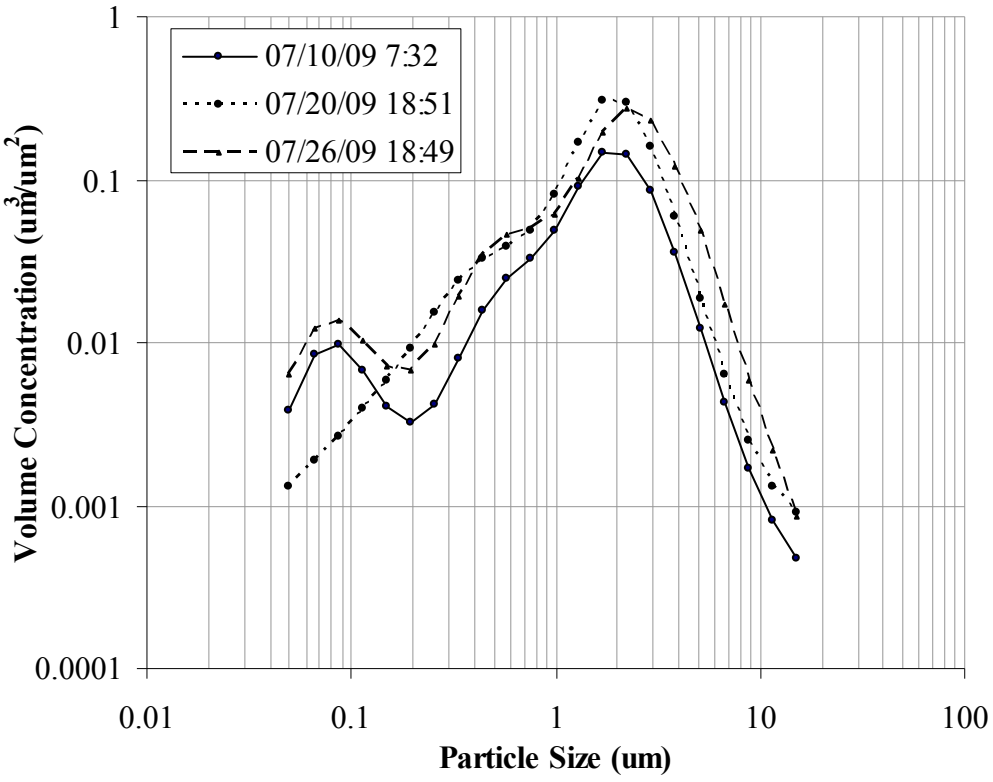

Figure 43. Particle size distributions of SAL dust derived from AERONET [*Dubovik and King* 2000].

5.2.2 Comparison to DREAM model output

Different paths of atmospheric circulation and synoptic weather patterns are responsible for the dust events (Figure 44). The elevation of the IZO observation tower (where AERONET and FLIR sky radiance measurements were collected) is 2390 m.a.s.l. Therefore, the winds at 3000m generally describes the movement of the air mass and the transport of dust that affects measurements at IZO. For the peak in AOD on July 10, wind direction is due west over the island of Tenerife. The prediction of the DREAM model indicated that a SAL dust event was not directly impacting the island. Rather, observations in the field and the higher dust values measured by IZO researchers explained the event as a result of dust being recirculated from the south or southwest in this wind regime. At this stage, where dust has recirculated out over the Atlantic from the southwest, the dust has had a longer residence time in the atmosphere. The air mass interacts with a moister air mass over the Atlantic and with increased residence time coarse

particles fall out of suspension and fine particles serve as nuclei for cloud condensation or other chemical reactions that occur. During clear sky conditions on July 13, winds at Tenerife were primarily from the north, bringing dust-free air to the IZO. Dust in the SAL is transported from the continent due north from the western Sahara directly over the Iberian Peninsula and away from the IZO. On July 20 when dust volume peaked at the IZO, winds were from the south southeast transporting dust as a characteristic SAL directly over the IZO. The SAL air flow disperses north and south as it extends over the Atlantic near the latitude of IZO (28°N), west of the island at 20°W. On July 26, winds at IZO again shifted to due west, and the trajectory of the dust-laden SAL is directly over Tenerife. Looking at the time-series of dust volume, it was shown that these changes in 3000m winds are responsible for the pulses of dust loading measured at the IZO. However, the DREAM model simulations at 6 hour intervals through the month predicted continuously high dust loading in between some of these events. The range of AOD from July 20 to August 3 measured by AERONET was between 0.5 and 0.6, where DREAM AOD values at the same wavelength was between 0.15 and 1.6.

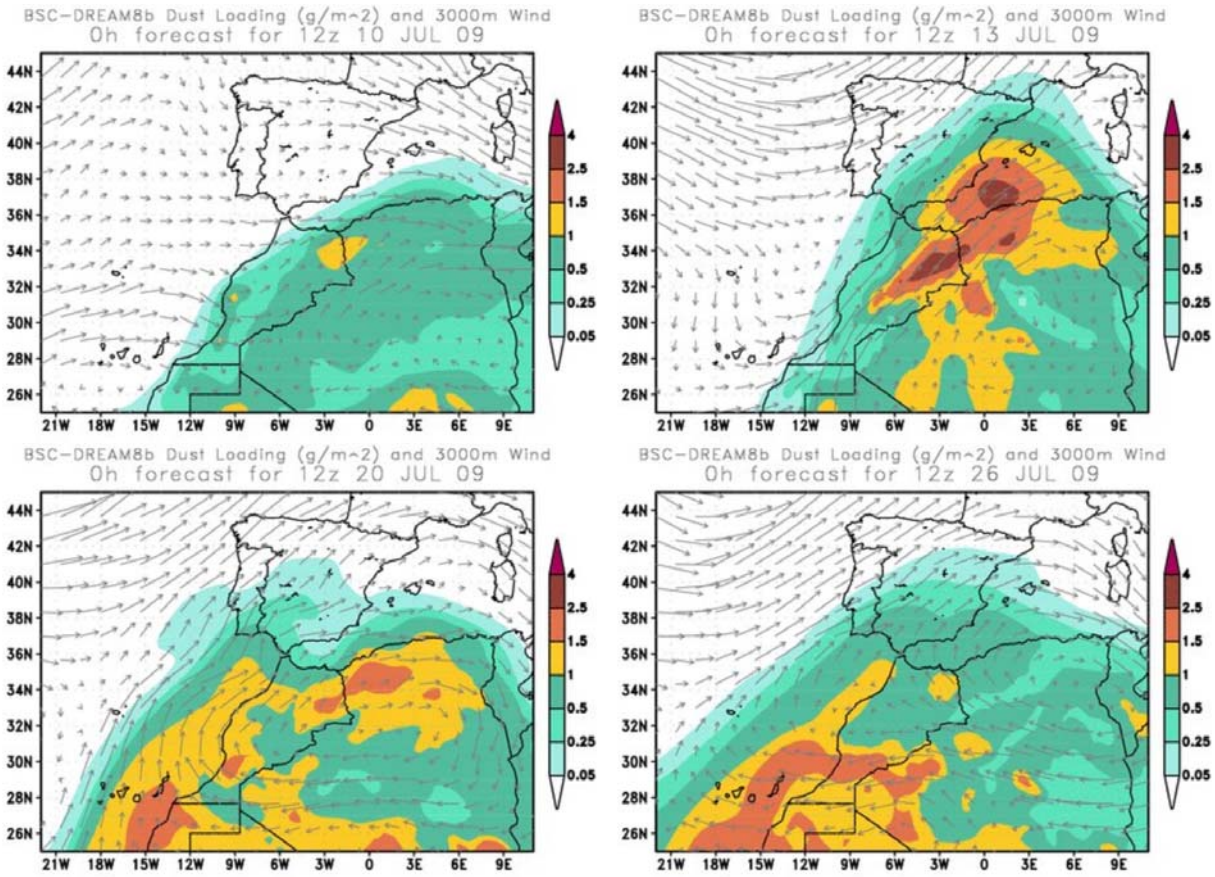

Figure 44. DREAM model predictions of dust loading for four different time periods.

5.2.3 Tracking dust using SEVIRI orbital data

It is possible to visually track Saharan dust from satellite data, where the best available data set is the high temporal resolution SEVIRI data. Visualization of the SEVIRI dust detection data led to identification of the most probable sources of dust for the stronger events that occurred during July 2009, as well as the transport path and dynamics. Large dust plumes in the SEVIRI image of July 10 appear as a bright magenta color (Figure 45). These plumes are forming at their source in central Niger and Mali. The delineation of a dust plume affecting IZO is difficult to determine because low lying clouds or humidity in the MBL also produce a light magenta/pink coloring. Nonetheless, the diffuse dust front could be identified, shown as a dashed green line between 10-20°N, centered at 20°W. Conditions continue to clear after July 10, which resulted in the clearest conditions observed at Tenerife on July 13. Dust plumes at hot spots can be seen to be starting to form over the border between Mauritania and Mali (Figure 46).

The largest dust event (according to the AERONET and MODIS data) took place on the July 20. Days prior, wide spread outbreak of dust plumes occurred throughout the west central Sahara. On the map in Figure 47, several of the plumes that directly affected the IZO measurements on July 20 are indicated. The largest dust plume over the coast of southern Mauritania dispersed west, and did not recirculated back to IZO. On the next day, high intensity surface winds dispersed dust plumes northward. The 15 minute time-step data clearly show several dust fronts that merge and form one large dust front, which is indicated by the dashed green line in Figure 48, and stretches some 1500 miles from the eastern border of Mauritania to the northern border between Niger and Libya. As the dust is dispersed and mixed, it is then transported by easterly winds and continued dust entrainment at the surface. On July 20, the classic SAL has moved off-continent to the west with the IZO in its path (Figure 49). According to the DREAM model simulation, the greatest dust concentration at the IZO is between 0.6-1.0 $\mu g/\mu m^3$ at a height between 1000 and 2200 m.a.s.l. The leading edge (indicated by the dashed green line) of the SAL was redirected north and south over the Atlantic just west of the Canary Islands. The back edge of the SAL dusty air is indicated with a dashed yellow line, showing the

general spreading out of the dusty air, which appears to be redirected to the northeast and southwest. The maximum dust volume rose from 0.096 $\mu m^3/\mu m^2$ on the July 18 at 8:00 to the recorded maximum of 0.329 $\mu m^3/\mu m^2$ on the July 20 at approximately 13:30 GMT. Dust concentration then declined (with some intermittent smaller dust events) to a low dust volume of 0.073 $\mu m^3/\mu m^2$ on July 25 at 10:14. On the same day, a dust plume was generated and quickly moved in the northwest direction from a dust source in northeastern Mauritania. In this situation, a clear, singular plume and dust front was visible moving toward the Atlantic coastline of the Western Sahara province (indicated by a dashed green line in Figure 50). On July 26, the same upper level wind pattern as occurred on July 20, with the plume being dispersed to the southwest and northeast, creating similar distribution of dust as July 20 in plan view (Figure 51). The dust volume concentration on the July 26 at IZO was measured by AERONET instruments to be 0.318 $\mu m^3/\mu m^2$, nearly as high as the July 20 event. Therefore, the July 20 and 26 events resulted in similar dust concentrations at the IZO, where the initial distribution of dust emission at dust sources imaged from SEVIRI appeared to be quite different. On July 20, it appeared that several dust sources formed different plumes that converged as one SAL. On July 26, one large plume appeared to be responsible for dust at the IZO.

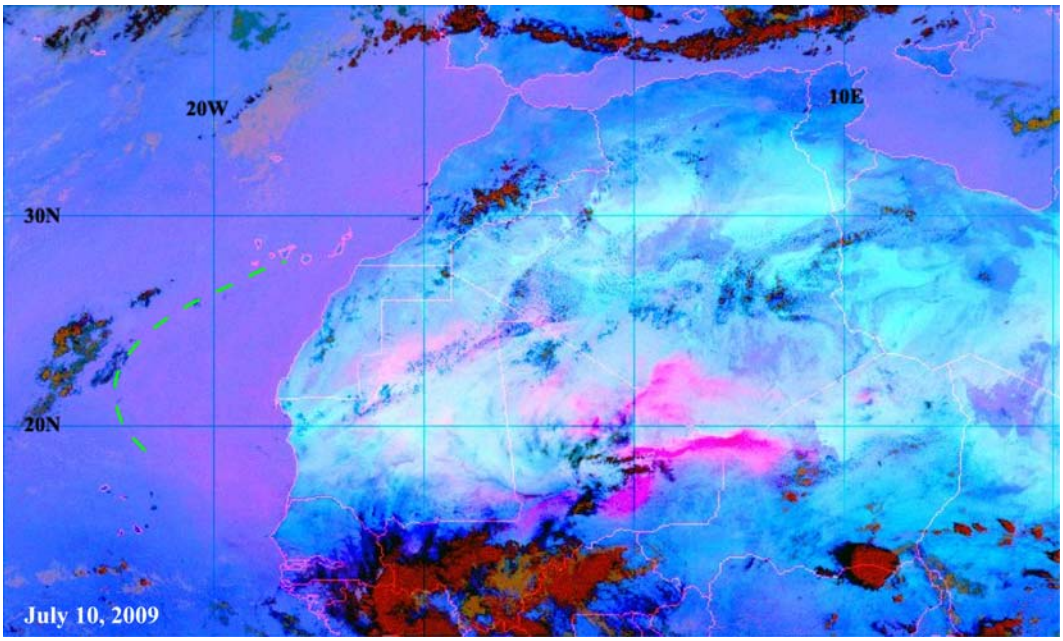

Figure 45. July 10, 2009 SEVIRI time step. The green dashed line indicates the dust front increasing AOD at the IZO.

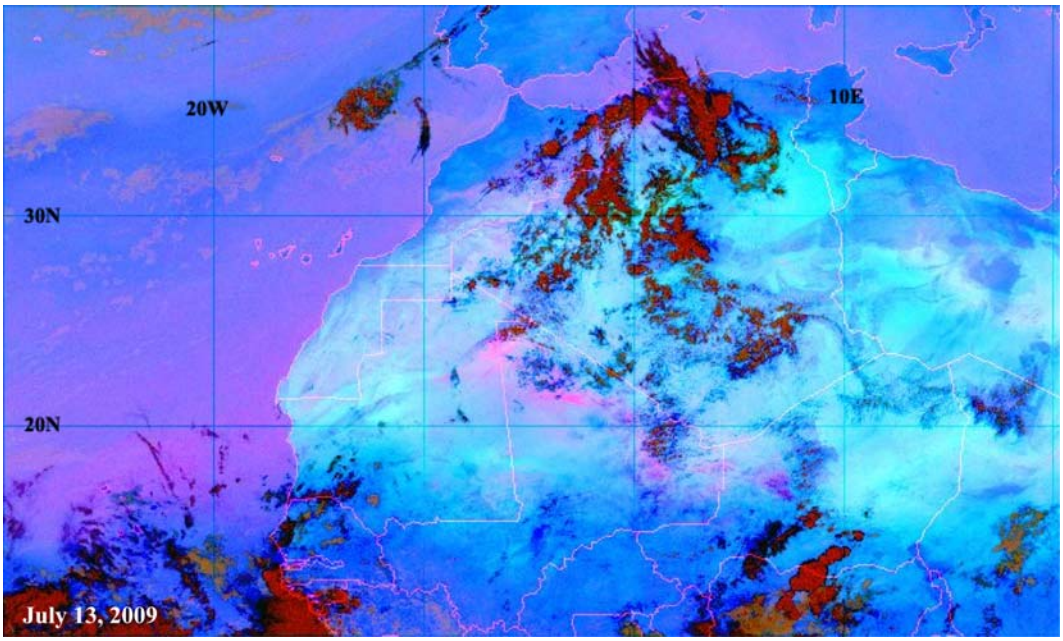

Figure 46. July 13, 2009 SEVIRI time step, indicative of clearer conditions over IZO.

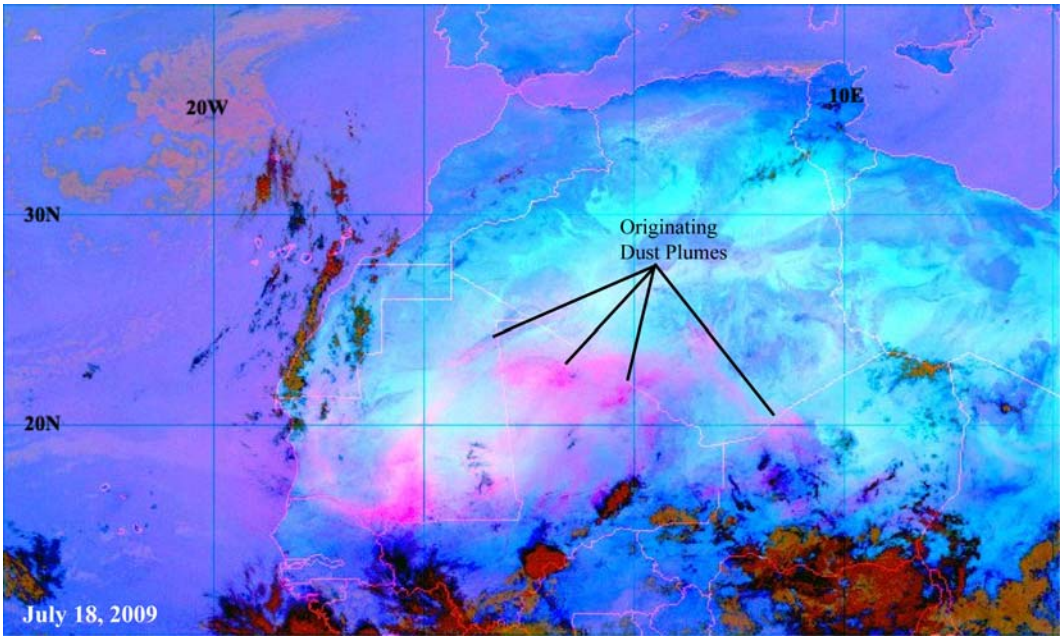

Figure 47. July 18, 2009 SEVIRI time step.

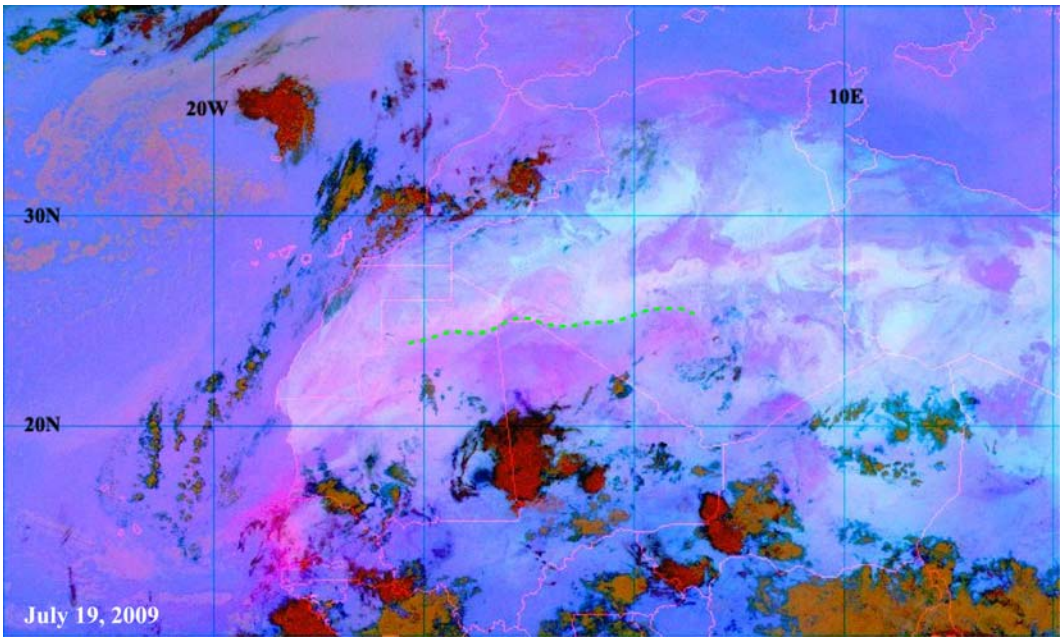

Figure 48. July 19, 2009 SEVIRI time step

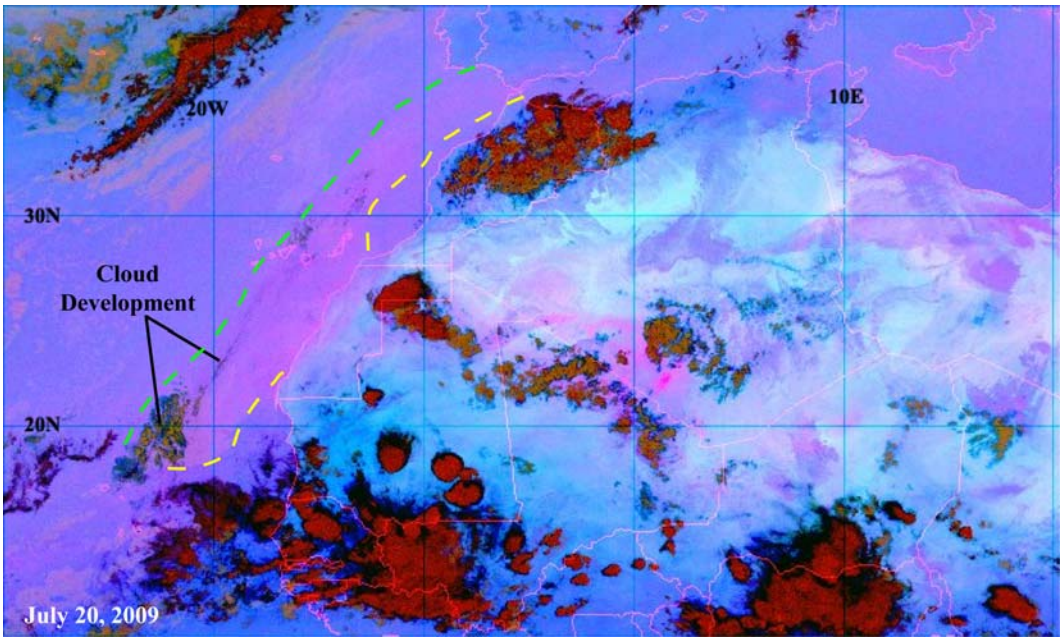

Figure 49. July 20, 2009 SEVIRI time step. The green dashed line indicates the leading edge of the dust storm, and the yellow dashed line indicates the trailing edge. These outline the general plan-view shape of the mega-dust plume.

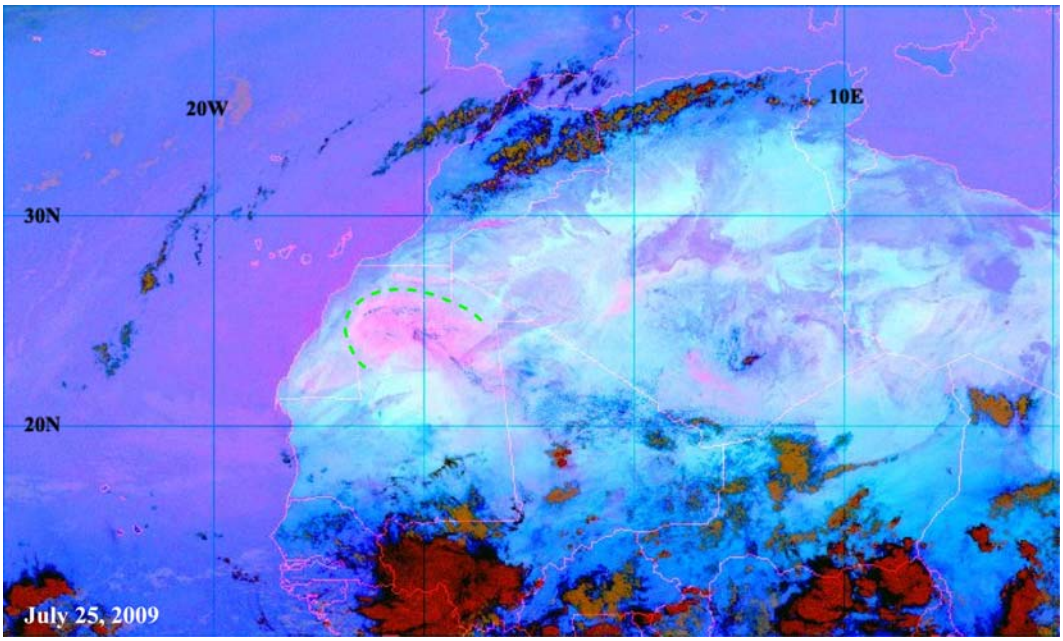

Figure 50. July 25, 2009 SEVIRI time step. Green dashed line indicates a dust front.

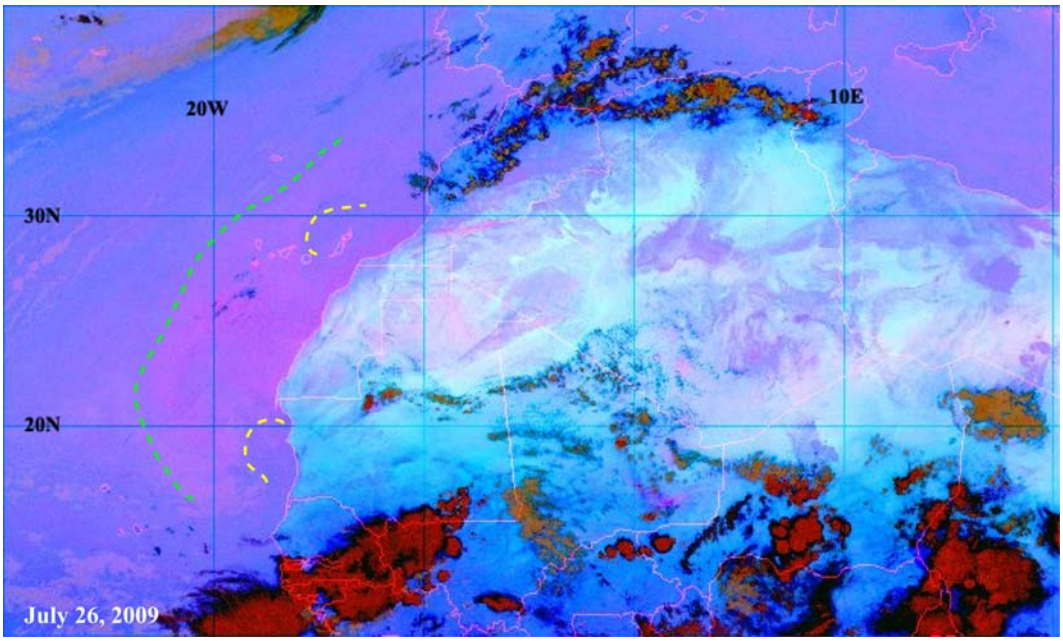

Figure 51. July 26, 2009 SEVIRI time step. The green dashed line indicates the leading edge of the dust storm, and the yellow dashed line indicates the trailing edge. These outline the general plan-view shape of another mega-dust plume.

5.2.4 ASTER dust detection algorithm

A higher spatial resolution dust detection product was explored using ASTER data. Over the course of July, four images were collected of the IZO study site: July 4 at 23:16, July 8 at 11:53, July 20 at 23:17 and July 24 at 11:53. Two images were collected during night-time overpasses and have TIR data only, whereas the daytime images have both VNIR and TIR wavelength data. Dust concentration was not retrieved at the same time as the ASTER nighttime overpasses, but AERONET and MODIS retrieved daytime sky measurements at 500 nm retrieving AOD measurements before and after the ASTER overpasses. MODIS Terra retrieved an increase in AOD from 0.5 on July 19 (at 14:50) to 1.8 on July 20 (at 11:50) on July 20 just prior to the peak of 2.35 AOD later that day (at 13:55). AERONET measurements showed an increase in AOD from 0.22 to 0.56 before and after the night time overpass on July 20. The other ASTER image acquisitions occurred during much less dusty conditions. The ASTER data were examined in two ways: (a) the SEVIRI dust enhancement technique was applied to ASTER TIR data and (b) by examination of the emissivity difference between clear and dusty sky conditions. ASTER has similar but not the exact band passes as SEVIRI. The ASTER dust detection algorithm used the closest bands to SEVIRI in the brightness temperature images derived from atmospherically uncorrected TOA radiance from the L1B data product, is:

$$\begin{aligned} &BT_{\lambda=11.318} - BT_{\lambda=10.657} && \text{-4.1 to 1° K, Red} \\ &BT_{\lambda=10.657} - BT_{\lambda=8.634} && \text{-3 to 5° K, Green} \\ &BT_{\lambda=10.657} && \text{260 to 289°K, Blue} \end{aligned} \tag{22}$$

Where, the resulting data are stretched between temperature values for the indicated ranges in the red, green and blue channels respectively. This produces similar results to the SEVIRI algorithm, and the color interpretation is also the same. Magenta/pink indicates atmospheric aerosols, where the blue color indicates clear conditions. Cold clouds appear red and orange, but lower, warmer clouds will appear light blue to light pink (Figure 52). The dust detection results are similar for generally clear days on July 8 and July 24 where dust volume concentrations were 0.05 and 0.09 $\mu m^3/\mu m^2$ respectively. The ocean surface is both light pink and blue due to scan line noise, but in general the light pink color is expected based on the SEVIRI data results. The

resulting dust enhancement for the July 20 image correlated well with dusty conditions. The dust volume concentration was equal to 0.328 $\mu m^3/\mu m^2$, where the more intense magenta color correctly enhances dust between colder cumulous clouds (red color).

The effect of dust on the ASTER TIR dust algorithm and the SEVIRI algorithm enhance dust by computing the brightness temperatures of each of the bands separately. Essentially, each radiance band is simply scaled to temperature. It was hypothesized that the difference between clear and dusty scenes in the ASTER TIR data is a result of a change in atmospheric composition and would be represented by a change in emissivity. The algorithm was performed on emissivity for July 20, and produced a similar result, although clouds were not as enhanced. Cloud enhancement occurs because the algorithm capitalizes on brightness temperature differences of the cloud, but the algorithm also takes advantage of the compositional differences in aerosols as well. ~~We~~ can observe the difference between clear and dusty conditions by extracting the spectral emissivity from ASTER data. Emissivity was derived using the emissivity normalization approach with an assumed emissivity of 0.97 [*Realmuto* 1990]. On July 8, when the atmosphere was clear of aerosols and the ocean surface can be seen, the resulting spectra represents mostly atmosphere and ocean water (Figure 53). The decrease at shorter wavelengths in the overall spectra is probably due to atmospheric water vapor. On July 20, the emissivity spectra over ocean is altered with a relative decrease in ASTER band 12 (9.075 μm) and increases in ASTER band 11 (8.634 μm). The spectra of dusty atmosphere over the ocean appear to look more like land surface spectra, which is not surprising considering the source of aerosols is the Sahara Desert. The spectra of the atmospheric dust were related to land spectra (of dust sources) in section 5.4 below.

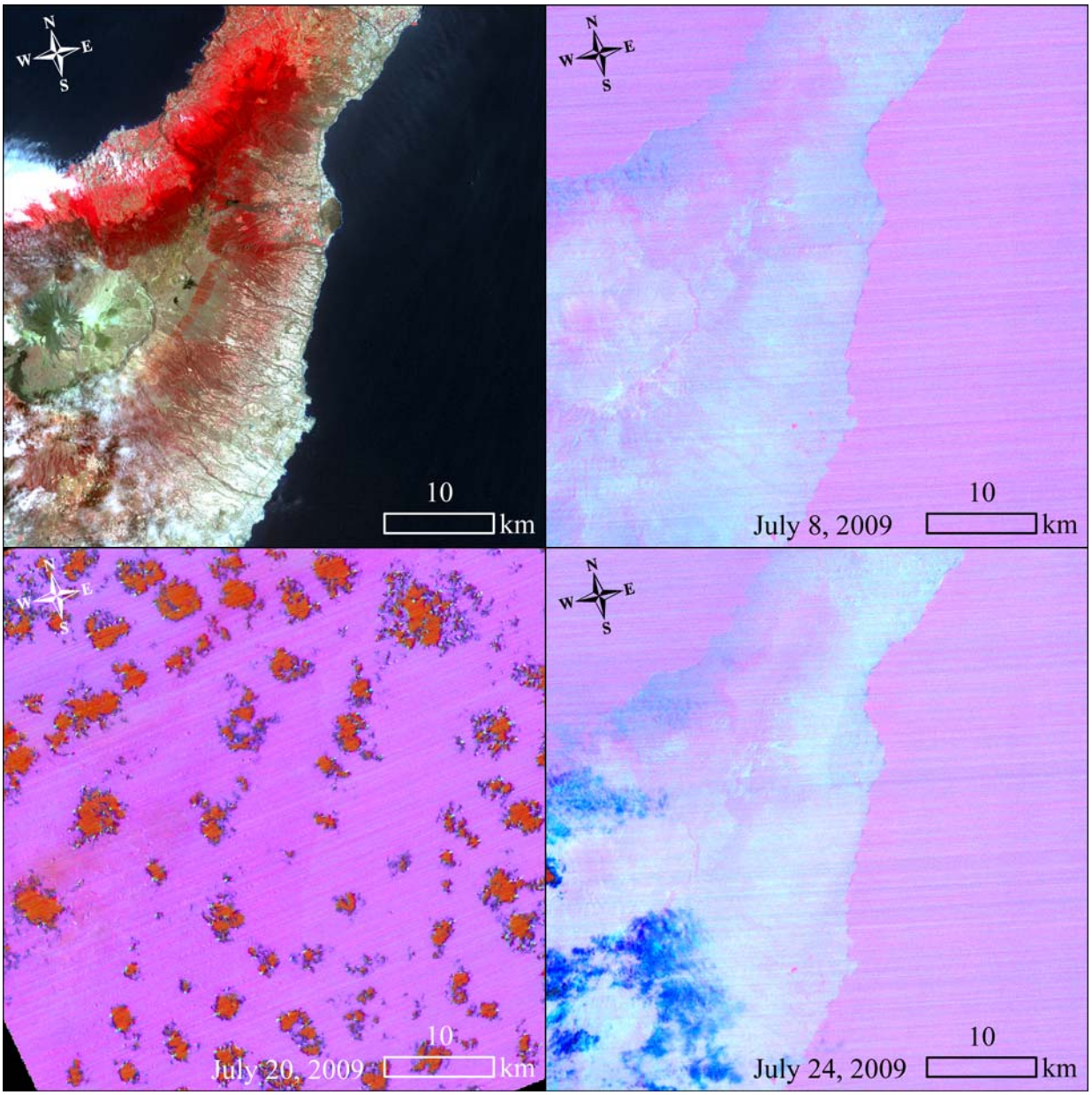

Figure 52. The first upper left time is a reference image for the island of Tenerife, and is a clear sky, ASTER VNIR false composite of bands 3,2,1 in RGB respectively. The images on the left are from generally clearer skies, where the July 20 dust event is captured in the bottom left image.

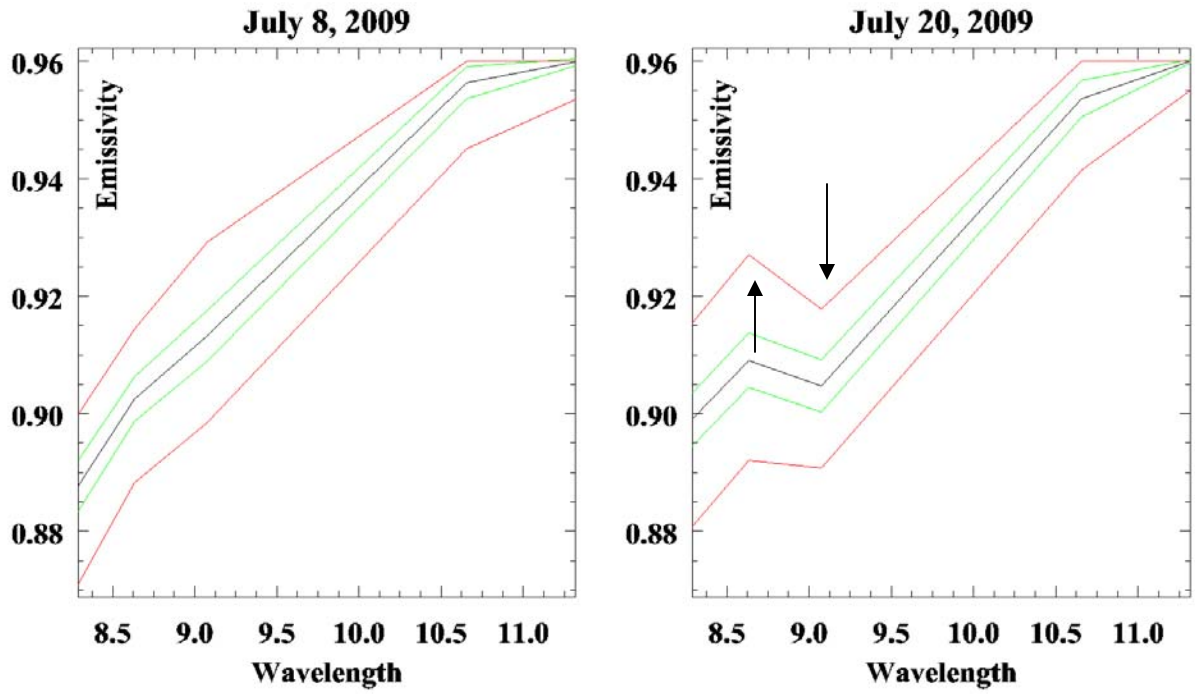

Figure 53. Emissivity spectra of ocean water (left) and dusty sky over ocean water (right). The black line indicates the average of a 25 x 25 pixel area; red lines are maximum and minimum emissivity; green lines represent standard deviations. Arrows in the left image indicate the change in emissivity as a result of dust contamination.

5.2.5 Radiative Forcing

The AIRS outgoing longwave radiative flux (OLW) was compared to the outgoing shortwave radiative flux (OSW) from AERONET. The OSW is a broad band flux (0.2 – 4 μm) modeled from the aerosol properties retrieved from AERONET measurements. The OSW is estimated using the real n(λ) and imaginary k(λ) parts of the complex refractive index, to extrapolate and interpolate the spectral response for the radiative transfer model [*Dubovik and King* 2000]. These data were reported in the inversion products that were downloaded from the AERONET website. AIRS OLW radiance is accurate data with the inclusion of cloud effects. The AIRS OLW radiative forcing due to aerosols is (Figure 42b):

$$\Delta OLW_{aerosols} = OLW\uparrow_{clear\ sky} - OLW\uparrow_{measured} \quad (23)$$

To determine the OLW due only to aerosols (i.e., the direct effect), radiative forcing values would be underestimated. Longwave, outgoing terrestrial radiation values are reported as positive, demonstrating that the net flux is toward the Earth. The AIRS radiative forcing values (as well as AERONET's shortwave radiative forcing values) are computed by modeling clear-sky atmosphere and then differencing these with the actual measurements. The time series AIRS data are shown along with the SW radiative forcing modeled from AERONET data (Figure 42). AIRS values are positive representing terrestrial radiance that has been absorbed or scattered back to the Earth. AERONET data show the net effect of aerosols on the balance of shortwave solar radiance. AERONET values in Figure 42a are:

$$\Delta OSW_{TOA} = OSW\uparrow_{TOA} - OSW\uparrow_{TOA\ clear\ sky} \quad (24)$$

The resulting values of ΔOSW_{TOA} are negative because $OSW\uparrow_{TOA\ clear\ sky} > OSW\uparrow_{TOA}$ due to the reflectance and scattering of aerosols. The total net radiative effect of aerosols can be determined by the addition of the positive LW and the negative SW radiance forcing values. In most cases during the month of July, the magnitude of ΔOSW_{TOA} is greater than $\Delta OLW_{aerosols}$, resulting in a net loss of radiance. On the 16th, the ΔOLW force offset the ΔOSW_{TOA} significantly, due to clouds. This date is also coincident with an increase in water vapor and cannot be attributed only to aerosols.

For the ASTER satellite overpass times, radiative forcing can be compared between different instruments, such as AIRS, AERONET and ASTER. The AERONET TOA OSW radiative flux is 25% of the TOA OLW radiative flux of ASTER. The shortwave radiance measurements are dependent on scattered solar radiance and are modeled only for daytime, but shortwave flux during night can be assumed to be neglible. AIRS OLW averages 305 W/m^2, where the AIRS radiative forcing on July 20 was not affected significantly by the dust event. The AIRS outgoing LW radiance value was lowest (282.8 W/m^2) on July 24 because of cloud cover. The AIRS footprint is large compared to ASTER, and as can be seen on July 20 from the ASTER dust algorithm product in Figure 52, a significant amount of intermittent cloud cover was also observed, lowering the AIRS value (302.9 W/m^2). The areas of red are clouds in the July 20 image and have a lower average OLW radiance measured by ASTER (264 W/m^2). Clouds reflect energy back to the Earth surface or absorb radiant energy and therefore appear

cooler than the Earth surface to orbital instruments in this scenario. Regional cloud cover on July 4 would have been integrated into the AIRS measurement as well, but these clouds were lower and warmer (407 W/m^2) in the MBL compared to clouds on July 20. The average OLW radiance excluding clouds was measured from ASTER at 436 W/m^2, 43% higher than the AIRS average. These values extracted from ASTER are free of cloud contamination, and the OLW is measured from areas of the image that are directly from the ocean surface between clouds. The larger AIRS footprint integrated both clear and cloudy areas where measuring the OLW flux.

Table 8. Outgoing Terrestrial Radiation

Date	ASTER TOA Outgoing LW (W/m^2)	AIRS TOA Outgoing LW (W/m^2)	AERNOT TOA Outgoing(W/m^2) [0.2 – 4μm]
July 4 (night)	438.6	310	ND
July 8 (day)	439.3	306.3	127.1
July 20 (night)*	428.8	302.9	ND
July 24 (day)	441.0	282.8	134.0

*Dust conditions were observed on July 20; other dates were relatively clear.

To determine the direct effect of LW radiative forcing due to aerosols, cloud-free areas are desired. The average clear-sky ASTER OLW is 440 W/m^2 (using July 4, 8 and 24 as clear conditions for the average, Table 8). If the atmosphere is assumed to be aerosol free, which is a conservative assumption because of low levels of dust, the longwave radiative forcing due to aerosols on the July 20 dust event would be 11 W/m^2. This represents the terrestrial radiation absorbed or scattered back into the atmosphere due to aerosols, and considered the "warming" effect of SAL aerosols. However ozone, biogenic aerosols and molecular absorption have not yet been documented in these ASTER values, so this warming value is likely overestimated. The OLW radiance from cloud free ASTER data is 40% greater than AIRS, and represents the direct radiative effect.

5.3 DUST SOURCES

5.3.1 Introduction

In the previous section, the cycle of dust and the effect on the radiation balance of the atmosphere was examined. In this next section, the focus is on the identification and characterization of major mineral dust source areas from the Sahara Desert. Understanding their composition is important to the understanding of global dust production, models of atmospheric emission and transport, and determination of radiative properties of dust plumes. The distribution of dust sources have been described from the analysis of various remote-sensing data of aerosols [*Middleton and Goudie* 2001; *Miller et al*. 2006; and others], including the Multi-angle Imaging SpectroRadiometer (MISR) [*Meloni et al.* 2004], MODIS [*Kaufman et al*. 2005], and the Total Ozone Mapping Spectrometer aerosol index (TOMS AI) [*Herman et al*. 1997]. These data show that regions of dust emissions are identified as dust "hot spots" (DHS) and are commonly coincident with topographic depressions where alluvial sediments accumulate [*Gillette* 1999; *Prospero et al.* 2002]. Dust hotspots are locations of frequent and high volume dust loading to the atmosphere. Models have used these satellite-based retrievals, as well as topography, to constrain the geographic extent of dust emission sources [*Zender et al.* 2003]. Studies have arrived at different and occasionally conflicting delineations of Saharan dust sources. Uncertainties remain with respect to dust sources because their distribution and characteristics vary with time [*Bryant et al.* 2007 and others], and the geomorphic environment is a major control on dust emission source and process. Small but numerous dust sources that give a weak value of TOMS AI also vary seasonally [*Prospero et al.* 2002]. The locations of many of these dust hot spots, including west and central Africa, were determined using data such as the TOMS AI, where several are located in west and central Africa [*Engelstaedter et al.* 2006, *Engelstaedter and Washington* 2007, and others].

The emission of dust at these sources and the rate of emission are controlled by several factors, such as surface properties, wind shear, gustiness [*Engelstadter and Washington* 2007] and sand saltation [*Shao* 1993]. Most eolian dust is generated by the impact of sand size grains on playa or dry lake bed surfaces [*Shao* 2001; *Shao et al.* 1993], which ontain abundant fine-

grained material (i.e. silt, clay, salt, sulphates or diatomite) and are abundant in the low lying basins of arid lands. Dust emissions are proportional to the horizontal flux of sand size particles [*Shao* 2001], a function of wind shear, and highly dependent on surface characteristics, moisture content, degree of crusting and cohesion, mineralogy, and vegetation. Because of the interest in the mechanisms of dust emissions that are initiated or controlled by sand saltation, especially at the Bodele Depression, an enhancement technique using the ASTER TIR data was used to examine sand transport pathways in relation to global dust sources [*Scheidt et al.* 2007].

The hypothesis tested was that other dust emission sources would also be linked to sand transport along defined pathways, resulting in dust storms activated by sand saltation. Mosaicked TIR data from ASTER were integrated and compared with high spatial resolution, mosaicked visible (VNIR) data available from the Google Earth™ mapping service. The geomorphic environment, surface composition and their relative magnitude as dust sources were assessed using the high resolution data, and the controls on dust emissions were explored. The locations that were analyzed are at predefined dust hot spots determined by the TOMS AI values. In the next sections, the various techniques explored in mapping Saharan sand transport pathways and dust source areas are described. These techniques can be applied to other field studies of aeolian processes, especially in the Sahara. In fact, the ability to study Saharan dust sources has grown substantially from the time this work was initiated in 2007. As of November 2009, most of the Sahara Desert has been imaged at very high spatial resolution in the VNIR range, where these data are currently readily available for visualization through the Google Earth™ mapping service. The increase in the availability of these data since 2007 is estimated at roughly 95%. ASTER data have also become more readily available. An unprecedented opportunity now exists to study large-scale aeolian composition, dynamics and dune geomorphology on Earth (and as Martian analogues). In this section, some techniques and the results of mapping sand transport pathways and dust sources are described.

5.3.2 Methods to Observe Saharan Dust Hot Spots

ASTER has the ability to map composition on very small spatial scales, especially with the fusion of other remote sensing data sets and techniques that indicate dust emission to the atmosphere. Cloud free data were acquired for most of the Sahara imaged between 2000 and

2006 (Figure 54). All the daytime ASTER TIR data were archived and processed into a GIS, although these data were not combined into a complete, radiometrically balanced mosaic because of computer resource limitations. Creating a sub-continental mosaic of these data for the Sahara at high spatial resolution would be highly resource and time intensive and impractical for several reasons. Most importantly, the physical geography of the Sahara desert is highly varied, and it is not in its entirety a dust source, therefore full coverage of the spectral data are not needed. Likewise, today's global dust models do not have the spatial resolution to accommodate an ASTER dust source model scheme. Instead, the ASTER data were used to determine dust source composition on a case by case basis for the highest priority targets of ASTER TIR data mosaicking, such as the Bodele Depression, to examine sand transport and dust emission interactions [*Scheidt et al.* 2007].

To determine targets for ASTER analysis, the subset of Saharan dust hot spot locations from *Engelstaedter and Washington* [2007] were examined. These points were modified by ranking the locations from highest to lowest according to the average June TOMS Aerosol Index data (1980-1992), which have a low resolution of 1.25 x 1.0 degree grid cell [*Engelstaedter and Washington* 2007]. Each grid cell with a high AI value is likely to contain several important, globally significant dust source(s). It is also important to note that the TOMS signal is measured from dust that is translated downwind from source because TOMS atmospheric dust detection is not sensitive at altitudes less than 1 km [*Xie and Xie* 2008]. The dust hot spot locations and the contours of average AI values (Figure 55a) were compared to several land surface spectral data sets in order to characterize the geomorphology of dust sources and the sand transport pathways that initiate dust emissions. This resulted in the delineation of broad areas of interest that may contain potential dust sources in Figure 55b, which are outlined in red. For each hot spot identified from TOMS AI, the area was visualized using several combined data sets, including: (1) image data from the Google Earth™ mapping service, which utilized a mosaicked natural color composite base image data from Landsat 7 ETM+ circa 2000 with some areas having very high resolution data (< 3 meter) from other sensors, such as Quickbird and IKONOS; and (2) Landsat GeoCover Mosaics, which is a combination of bands 7, 4, and 2 (2.22, 0.825 and 0.565 μm, RGB, respectively) in a false color composite (Figure 56). At each of the dust hot spot locations, the color of the mosaic data corresponded to blue and cyan colors (Figure 56). Typically, these dust hot spot areas were lacustrine deposits that probably contain dry, fine-

grained sediments. These were located across the Sahara and the Middle East. Saharan paleolake beds were also found to correspond with some dust source areas [*Drake and Bristow* 2006]. These paleolake beds are shown as blue polygons in Figure 55b. The delineation of dust source areas for the five major dust hot spots with a TOMS AI average greater than 2.0 were used as a guide for further analysis of ASTER thermal infrared (TIR) mosaics. A DCS transformation was applied to each ASTER image mosaic, and the resulting color values were related to sand or dust source areas. The mosaicked areas are identified as three major regions shown by white inset boxes on Figure 56. The largest three dust hotspots occur in Mali and western Mauritania, and are labeled as DHS1, DHS2, and DHS3. DHS4 is a coastal playa in Mauritania. DHS5 is located on the border of Mali and Niger, and DHS6 is the Bodele Depression. This study first focused on the Bodele Depression because of available sediment samples and field observations. The unique characteristic about the Bodele Depression is that sand saltation on the playa surface is known to actively generate dust emissions. It had been described in the literature as one of the world's largest dust source; however it ranks as the sixth largest dust source in the Sahara according to the TOMS AI hot spot data set used here.

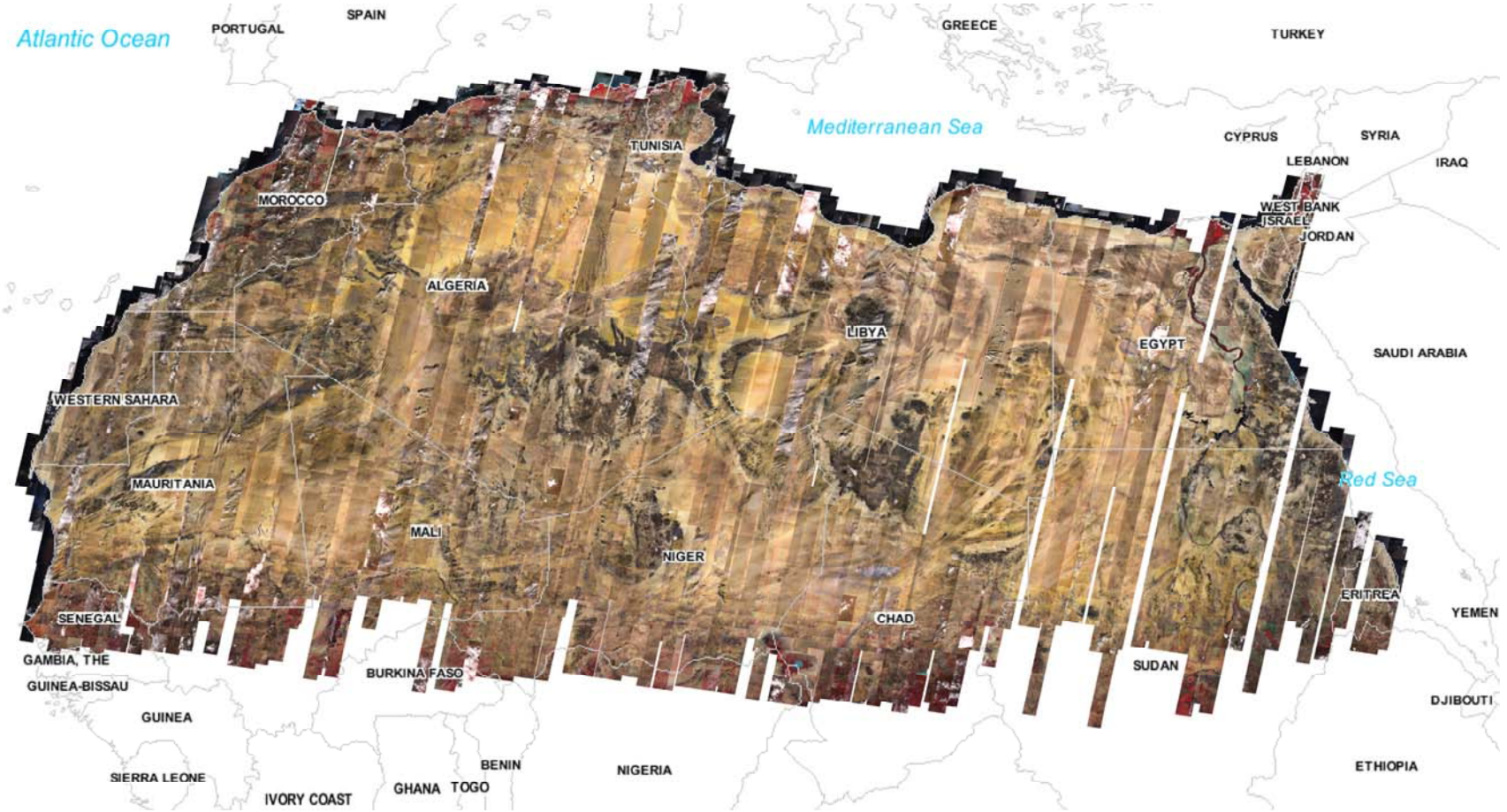

Figure 54. Low resolution mosaic of non-radiometrically balanced ASTER VNIR.

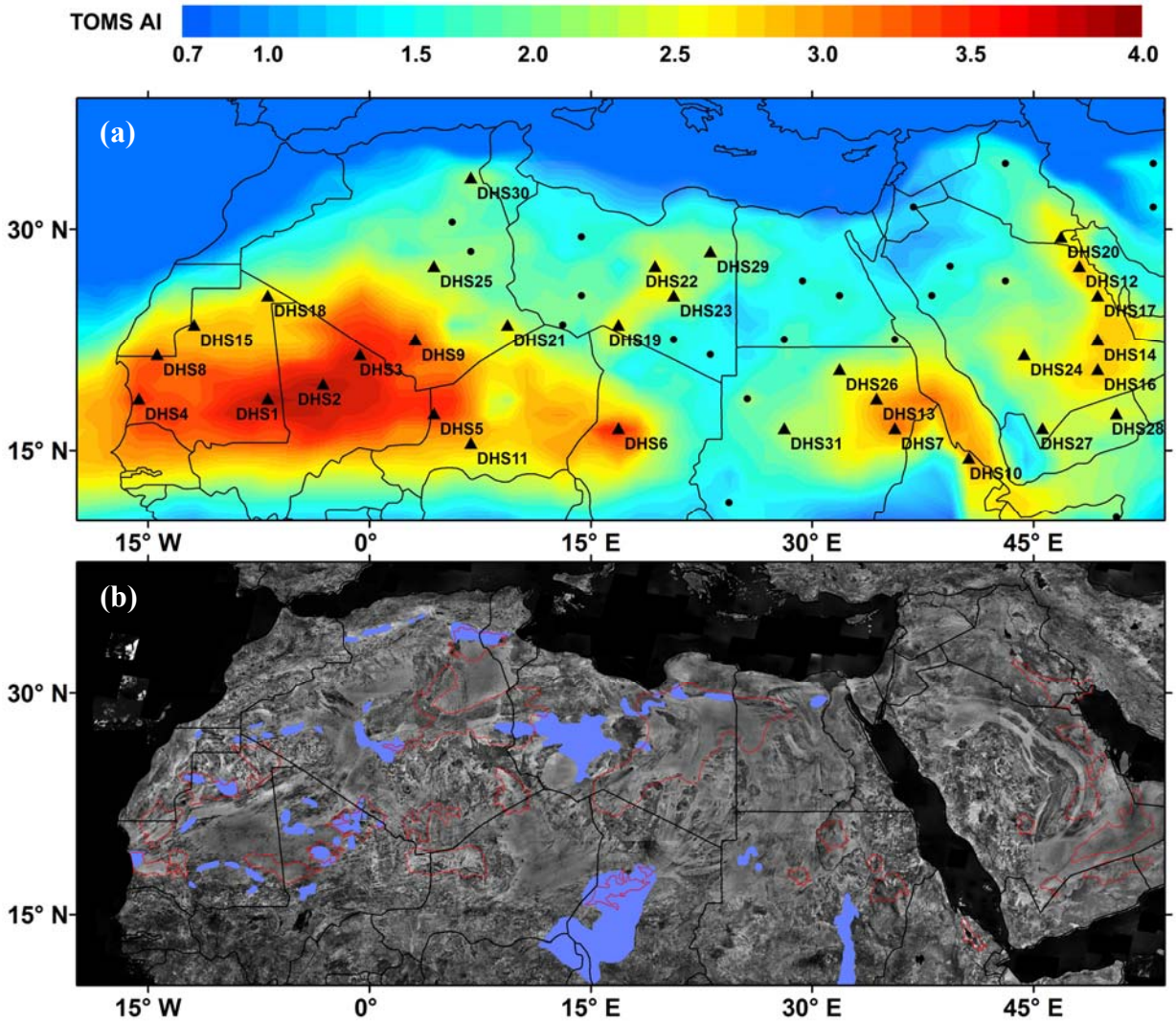

Figure 55. (a) TOMS AI contours and the locations of the largest dust hot spots. (b) Delineations of potential dust source areas (red outlines) and paleolake beds from *Drake and Bristow* [2006] (blue polygons).

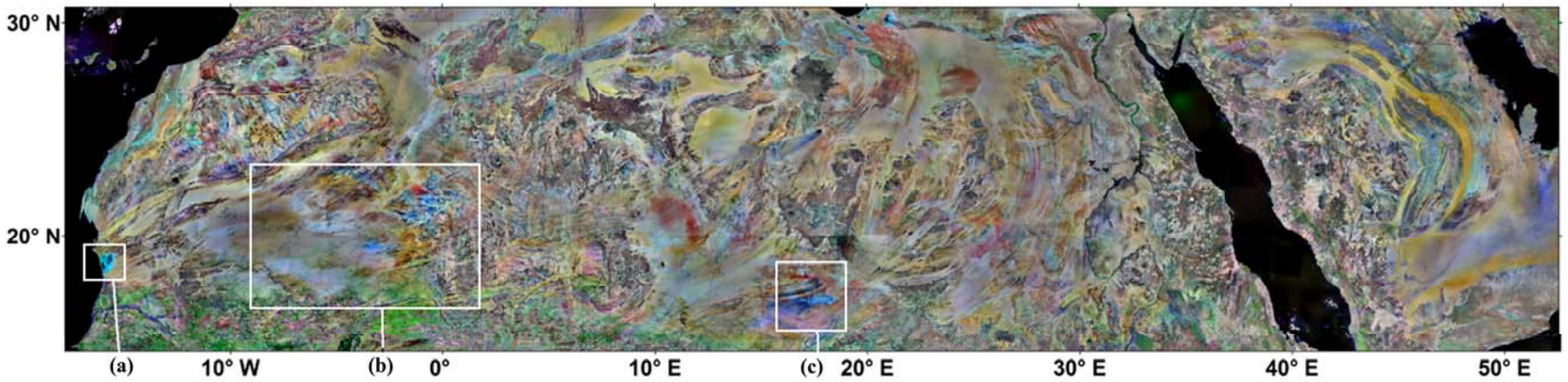

Figure 56. Landsat mosaic of the Sahara. Areas mosaicked by ASTER are shown in white inset boxes which are associated with the largest dust hotspots. (a) Dust hot spot DHS4, (b) DHS1, DHS2, DHS3, and (c) DHS6.

5.3.3 Results and Analysis of Dust Hotspots

For arid land surfaces with little vegetation, the decorrelation stretch (DCS) transformation of ASTER radiance using bands 14, 12 and 10 (11.318, 9.075, 8.291 μm, RGB, respectively) produces a consistent color pattern that correspond well to bulk mineral composition for arid lands [*Gillespie* 1992]. For example, sand transport pathways of quartzofeldspathic rich sediments of the Erg du Ténéré in Niger are clearly visible here from the red and magenta color of the decorrelated ASTER data overlain on VNIR Landsat TM data (Figure 57).

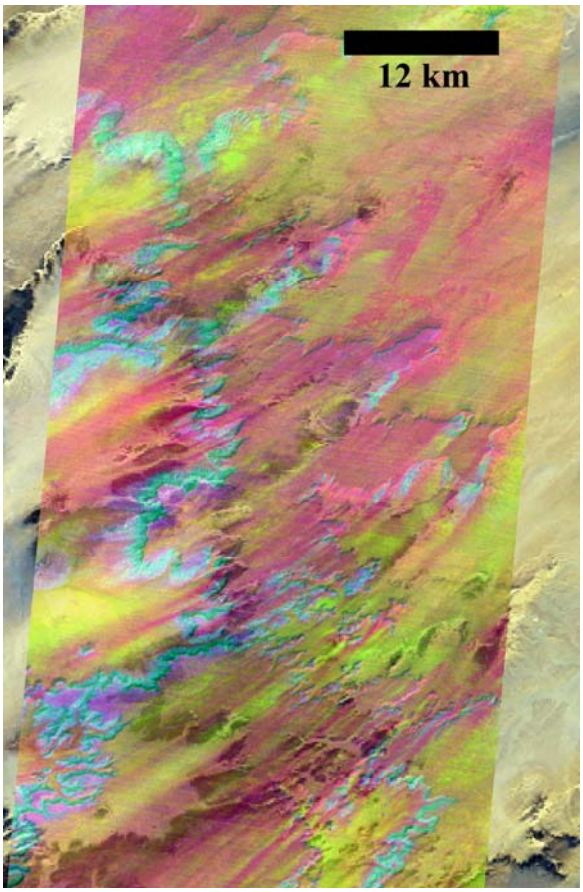

Figure 57. An example of a DCS transformation of ASTER TIR data in the Sahara.

The same interpretation of red/magenta color as a tracer for quartzofeldspathic material can be used for the DCS mosaic of the Bodele Depression (Figure 58). The DCS data were overlain onto the Landsat TM mosaicked albedo. The light cyan and blue color in the center of this image delineates the boundaries of the lucustrine deposits that generate dust in high wind

conditions. The lucustrine deposits form both the playa surface and dunes of saltating flakes and granules of diatomite. The depth of the main absorption feature at 9.075 μm and a high areal abundance of quartz increase the intensity of the resulting red channel in the DCS transformed data. The larger, regional sand transport pathways north and south of the Bodele stand out from the main dry lake bed. Sands transported into the Bodele mix with the fine-grained lacustrine sediments and change the spectral character of the material. The resulting green color indicates mixed material that is transported out of the dry lake bed to the southwest of the Bodele.

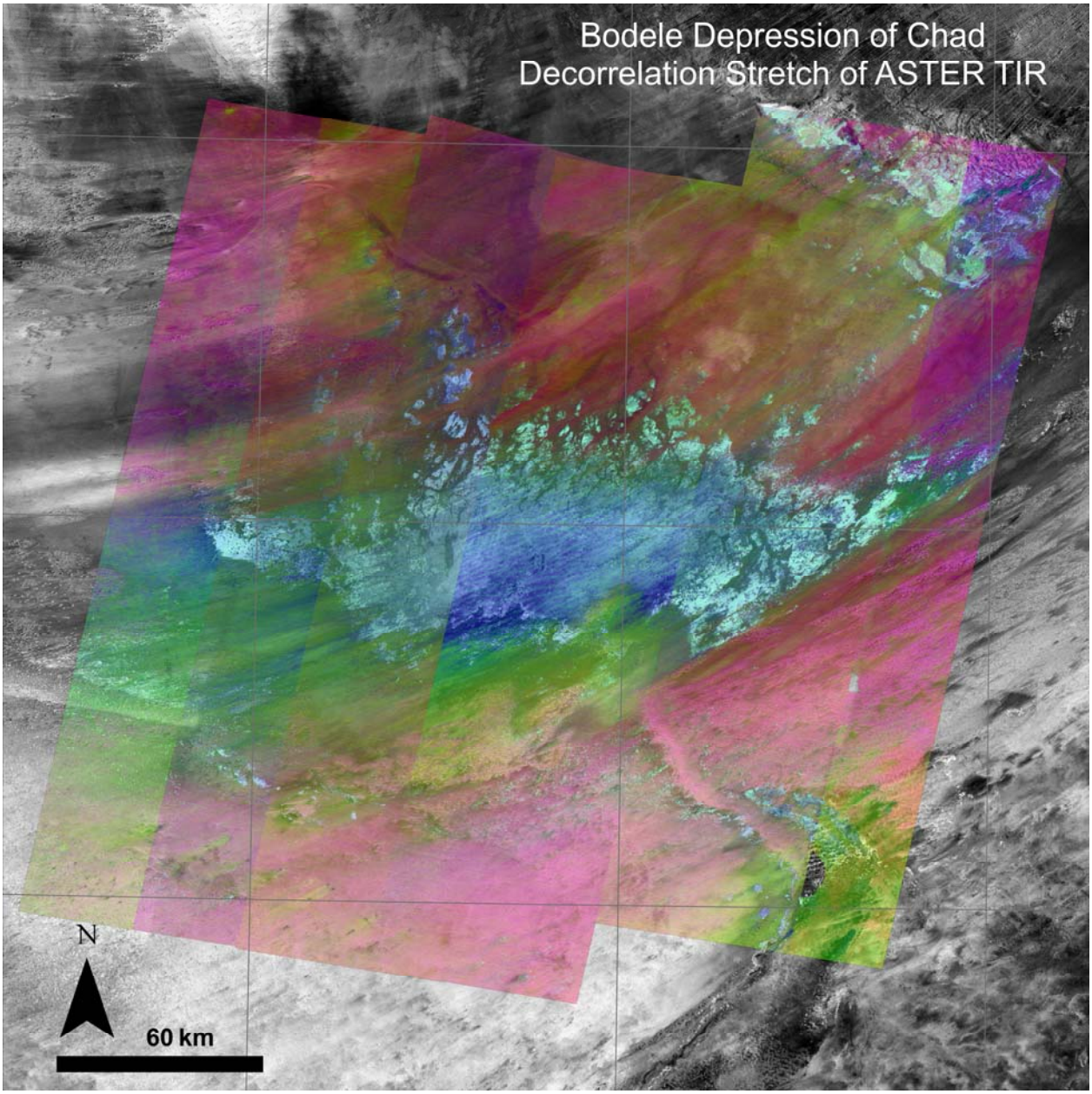

Figure 58. DSC transformation of ASTER TIR data.

The spectral characteristics of quartz sand in the thermal infrared were used to relate sand transport pathways to the relative abundance of coarse quartz sand particles. These results were compared to the initial dust source area delineations shown in Figure 55b to validate locations of dust and sand transport interactions. At these locations where sand transport direction leads to dust sources, dust emissions are affected by the saltation of sand particles, which impact and abrade finer grained material, initiating dust emission. Using spectral linear deconvolution of

image data [*Ramsey and Christensen* 1998] to confirm the relationship of color values in the DCS transformation to composition, the red areas of the DCS data were found to directly relate to the actual areal quartz abundance. These data were useful for identifying sand transport pathways at different spatial scales, taking advantage of the relative differences in composition in image scene data. For a large area of 10^5 km^2, regional statistics of the data are more revealing of the pattern of regional sand dune systems (Figure 59). Blue colored regions on this figure indicate areas of elevated quartz concentration, whereas the red indicates the highest areal abundance. By stretching data values to their scene statistics in smaller subsets, greater detail in the relative abundance of quartz sand was examined on the playa surface in the Bodele. For example, the relatively higher quartz abundance of the dunes was enhanced in the overall lower quartz region of the Bodele dry lake bed to reveal smaller sand transport pathways and dune patterns at the scale of 10^2 km^2 [*Scheidt et al.* 2007].

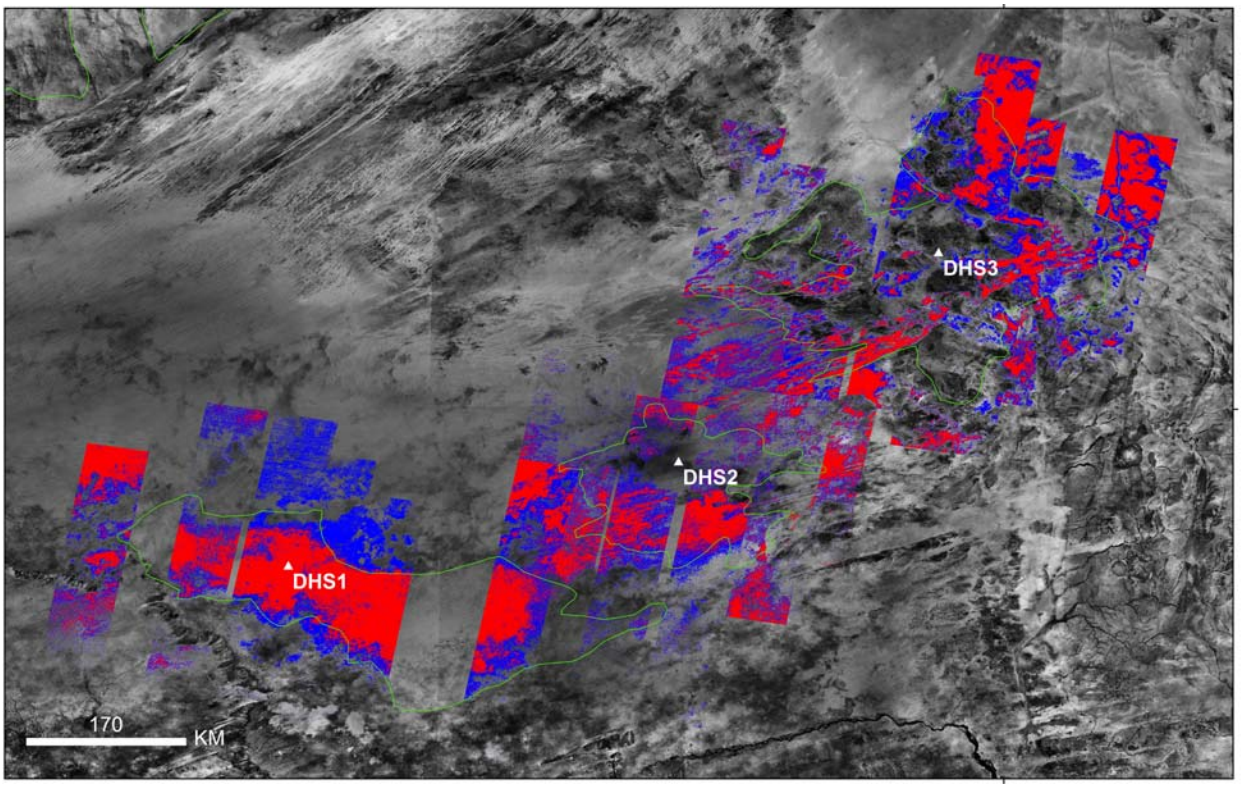

Figure 59. Areas of high quartz concentration delineated by DCS and linear spectral unmixing. Red indicates the highest relative quartz areal abundance relative to blue. Green lines indicates the outline of potential dust source areas.

These methods were similarly used to highlight lacustrine deposits using the other color values of the decorrelation stretch. Common dust generating sediments (i.e., clay, diatomite,

carbonate, etc.) have shallower spectra at 9.075 μm, unlike the areas where deposits of coarse quartz particles exist. The restrahlen feature also becomes shallower for quartz particles that are dust sized, between 40 and 2.5 μm [*Wenrich and Christensen* 1996; *Ramsey and Christensen* 1998; *Mustard and Hayes* 1997; *Cooper and Mustard* 1999; *Hamilton* 1999; *Hudson et al.* 2008]. The DCS is useful for discerning between dust deposits and quartz sand transport pathways in this type of dry, arid aeolian geomorphology.

Dust storms are frequent in the Bodele Depression. One that occurred in the region on February 3, 2009 was imaged by MISR and ASTER, located on the Terra spacecraft (Figure 60). The data from MISR show dust emissions being transported westward of the Bodele, where the color scale on this figure indicates dust plume height extracted from the multiple look angles of MISR using the MINX software tool [*Garay*, unpublished data]. The MINX program also retrieved the vertical profiles of the plume and wind fields by using the twelve look angles of MISR data, and can be viewed as a function of distance from dust plume source (Figure 61). From the MISR data, the resultant winds were also determined to be 18 m/s from the northeast and compared well with reported wind speeds that were measured in this region (generating dust plumes). The plume height reached 700 meters above mean sea level only a limited distance from emission source. This height is significant considering that the TOMS AI (and probably other dust monitoring satellites) is insensitive to dust below the 1 km height in the atmosphere. Comparisons of the plume heights with LIDAR heights from CALIPSO were found to be in good agreement [*Garay*, unpublished data].

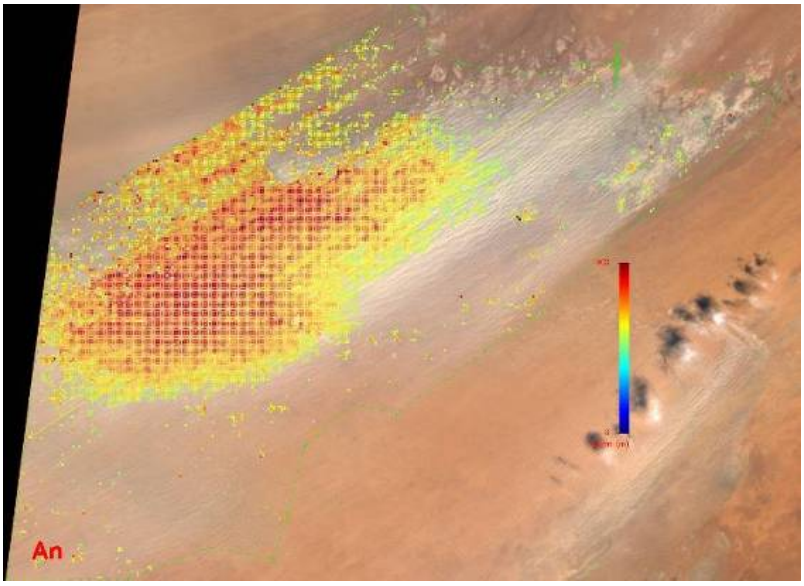

Figure 60. Plume heights were obtained from the MISR instrument for the dust storm occurring on February 2, 2002. The wind direction is from the northeast, and plume height is indicated by the color scale, where red is the highest height (maximum = 750m) [*Garay*, unpublished data].

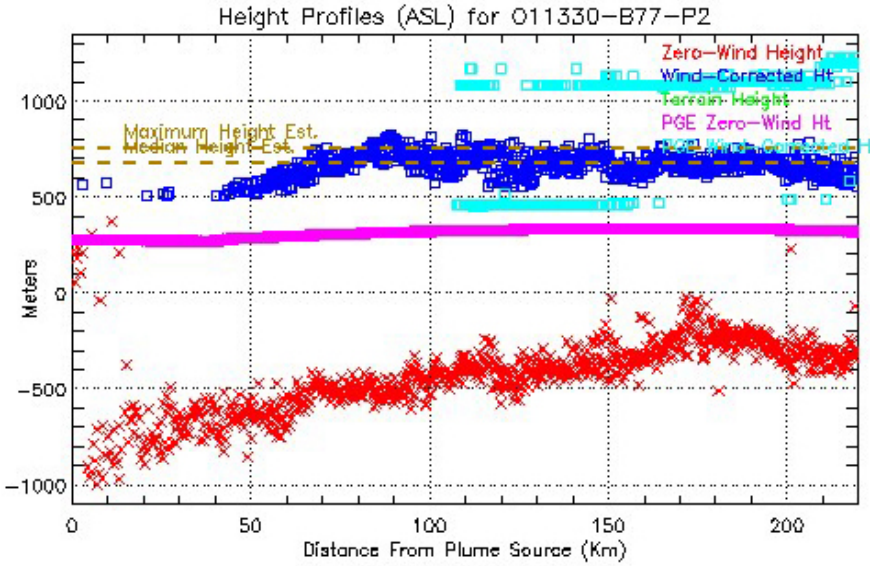

Figure 61. Vertical profiles of the plume are shown here, indicating a maximum plume height of 750 meters, trailing from the dust source downwind from the northeast [*Garay*, unpublished data].

Using the ASTER VNIR data to examine a small subset of the same area prior to the event on February 3, 2009 where dust emissions occurred shows diatomite and carbonate rich deposits (blue and white colors respectively), which are intermixed with the surrounding quartz rich sands (yellow color) (Figure 62). In Figure 63, ASTER VNIR data on February 3, 2009

showed multiple dust clouds from the land surface that are far more extensive than the field of view shown here. Using the DCS of TIR data processed above, the carbonate and diatomite deposits were delineated using the third DCS band. The third DCS band enhances surface materials that are low in spectral contrast in the thermal infrared wavelength region. These areas are either likely to be non-quartzofeldspathic or have small particle size. In Figure 64, the deposit delineations are compared to the plume structure at a high spatial resolution, far below the resolution of MISR. Because the dust outbreak is so widespread, it was difficult to relate plume structure to the deposits in this example. Dust appears to be generated throughout the image example, but this is highly plausible considering the mechanism for dust emission at the Bodele. The process by which dust emissions are generated in the Bodele Depression is an interaction between sand saltation and the fine grain deposits, whereby dust source material is ingested by traveling quartz-rich barchans dunes and the granular dust material also forms dunes. Therefore, because of the widespread area of mixing sediments, it is likely that areas besides the lucustrine deposits shown in the pre-dust storm example (Figure 62) are also strong emitters of dust. The two larger white areas appear to be generating slightly more dust than the surrounding plumes, indicated by arrows (Figure 63).

Figure 62. Pre-dust storm surface from ASTER VNIR, bands 3,2,1 in RBG respectively.

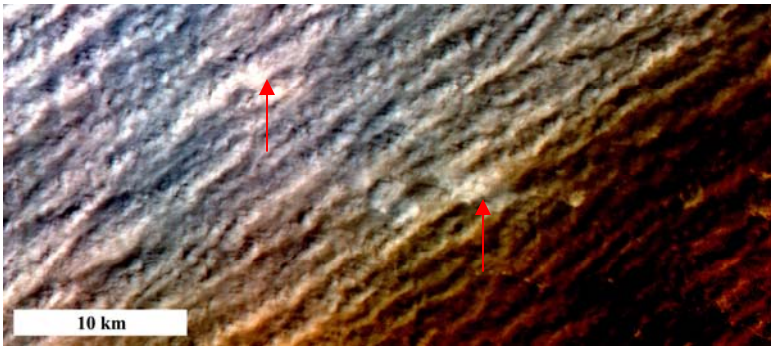

Figure 63. Active dust emissions viewed from ASTER VNIR on February 3, 2009.

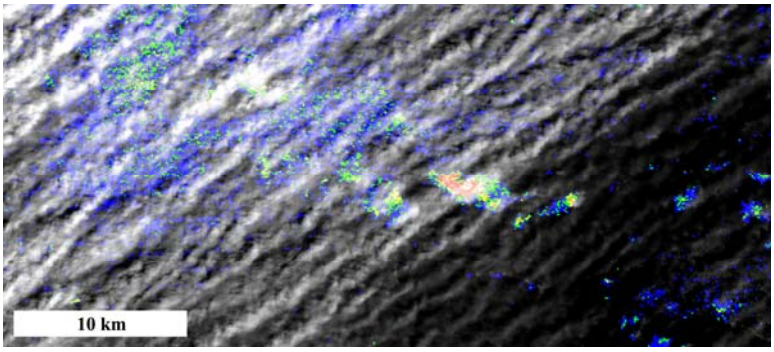

Figure 64. The potential dust source areas at this location are superimposed as colored areas on the February 3, 2009 image. Blue, green, yellow and red colors indicate increasing areal abundance of lucustrine, dust source material.

The interpretation of dust sources identified by ASTER TIR processing was aided by examining the high spatial resolution data of Google Earth™ mapping service. This helped to visualize and validate dust sources at a smaller scale (>5m), where otherwise undetected surface features and geomorphology could be seen, especially for other areas in the west central Sahara discussed in [*Scheidt et al*. 2007]. For example, some of the interdune areas in the region of DHS1 have the visual appearance of having standing water (Figure 65). (This would not be expected in the Sahara Desert, and th the interpretation cannot be confirmed since the date of the data cannot be determined from the Google EarthTM mapping service data. If water existed during the image acquisition, it would not be persistent due to the arid climate unless fed by a groundwater source.) In that example, interdune spacing (750 m) and area (2 – 5 km^2) were also measured. These areas are close but not below the limit of ASTER's TIR spatial resolution of 90 m. The visualizations were suggestive of a wetting/drying process that commonly generates erodible sediments similar to Mojave playa systems in the southwestern U.S. as well as White Sands, NM. Groundwater interaction at the surface could be problematic in causing error in spectral algorithms that identify composition because spectral features become shallower with the spectral mixing of water at the 90m pixel scale. This creates an interesting opportunity for temporal studies, such as thermal inertia and sediment availability techniques used with ASTER or MODIS data at White Sands, NM (see Chapter 4). The validation of the ASTER data analysis using images from the Google Earth™ mapping service was important for making distinctions between the characteristics of the three largest dust hotpots in the west central Sahara. In general, these distinctions were either between (a) dust sources that are clusters of many small, highly erodible deposits or (b) a contiguous, expansive area like the Bodele Depression. Both

areas have equally high average value of TOMS AI, but appear to have different geomorphic processes by which dust emissions occur.

Figure 65. Anomalous interdune areas in the area of DHS1 as shown from a combination of high resolution image data and topography as viewed by the Google Earth™ mapping service.

The DCS image of dust source areas was validated using high resolution thermal infrared spectroscopy of material in the Bodele Depression (Figure 66). These samples were provided by Dr. Charlie Bristow of University College London, a participant in the BodEx experiment at the Bodele in 2005. The high resolution thermal emission spectra of dust and sand samples from the Bodele Depression were done at the IVIS spectroscopy lab (Figure 67) [*Scheidt et al*. 2006; *Scheidt et al.* 2007]. The comparisons of spectra show the obvious mixing of dust and sand material, and these correlate well to the modeled change in composition from ASTER satellite-

derived emissivity. The enhancement techniques used here for sand and dust sources was based on the exploitation of the major spectral absorption feature of quartz. Mature aeolian sands are quartz rich, and therefore can be used to trace the major sand transport pathways. This technique was found to be equally useful in enhancing the dust sources in the complementary colors of the enhancement technique (described above). The dust materials that were enhanced had lower spectral contrast in the 8-12 μm wavelength region because the typical sedimentary composition of clays, evaporites, carbonates, etc. as well as the finer grain size of the sediments.

These comparisons between sample spectra and ASTER image data provide insight into the properties of dust, the effect on the spectral emissivity in the TIR and the strategy for mapping other dust sources. Lacustrine deposits of the Bodele are rich in diatomite, but a spectral library end-members of diatomite was not available for use in the linear deconvolution approach. Diatomite is amorphous silica, and the samples collected from dust source deposits do not indicate any quartz content (samples CH9, CH50, CH65, and CH20). Only CH15 was identified to have a very high abundance of quartz (Figure 67), where CH2 was determined to be a mixture of quartz sand and diatomite (Figure 67). The variety in texture, particle size and shape are shown in these images of the samples (Figure 66). Comparison of these spectra to the ASTER TIR data show that few spectral features occur within the dust source regions and the quartz was correctly identified in sand transport pathways, admixing with diatomite material. CH50 was also shown to have a narrow spectral feature at 7.6 μm, which is at a longer wavelength from the calcite feature at 6.7 μm. The spectra were compared to library end-member spectra in the ASU spectral library [*Christensen et al*. 2000], but no match could be found that contained this spectral feature. Linear deconvolution of the dust sample material yielded retrievals of clays and minor amounts of carbonate. RMS error was found to be high, therefore composition was not retrieved. CH50 and CH65 spectra also may show some affects of particle sizes less than 50 microns, where the emissivity decreases at wavelengths less than 7 μm. These spectral results suggest that imaging of dust sources in the 8 – 12 μm wavelength region will have low spectral contrast due to the small particle size fraction that becomes airborne. However, particle size effects are not known for all minerals, and therefore low spectral contrast may not always be the result. These areas were identified in the Bodele (diatomite dunes and playa surfaces), which appeared unique in the decorrelation stretch as blue and cyan colors (Figure 58), indicating a clear, distinct compositional difference from sand

transport pathways of quartz. Quartz rich areas have high spectral contrast, with low values of emissivity at the 9.1 μm wavelength region. In summary, the high resolution spectra agree with the ASTER spectra at degraded resolution. However, for the Bodele's dust source material, further investigation is needed to determine the exact relationship between TIR spectra and composition. For this analysis, the spectral identification of low spectral contrast of dust source materials was sufficient.

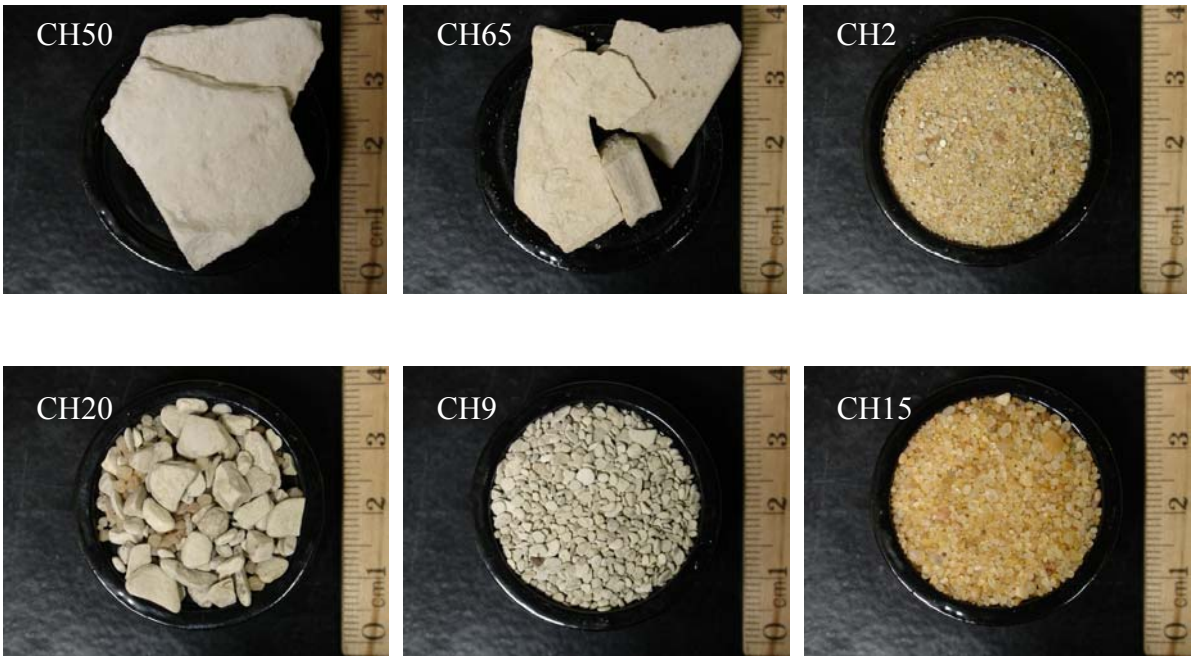

Figure 66. Sample preparations of Bodele sample materials for thermal IR emission spectroscopy.

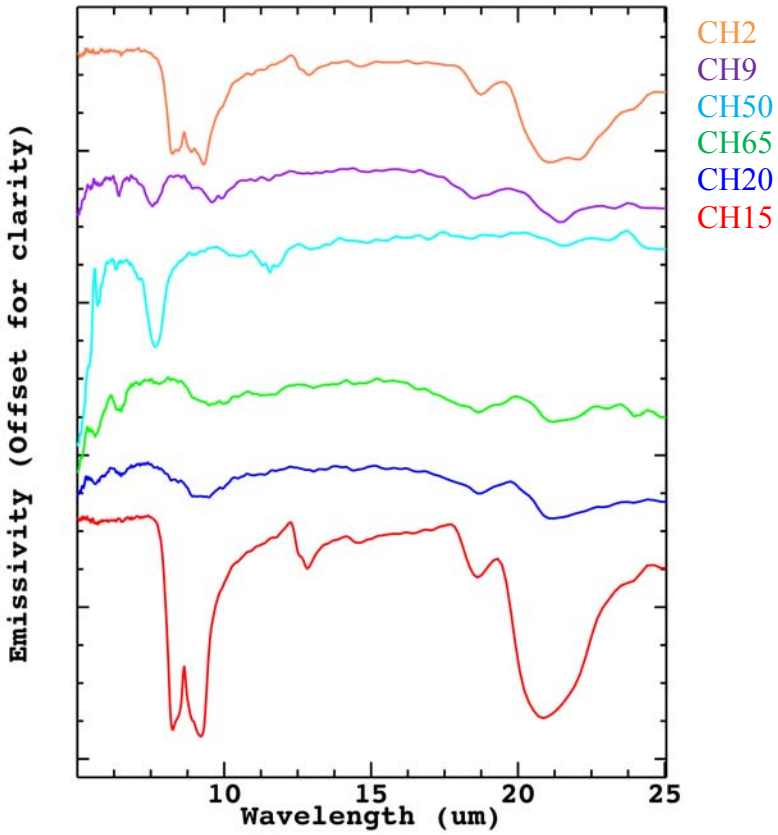

Figure 67. TIR emission spectra of Bodele aeolian sediments.

5.3.4 Tracking Dust Sources Using ASTER

In Chapter 3, the effectiveness of ASTER TIR image data transformation techniques such as the decorrelation stretch (DCS) and the principle component analysis (PCA) to distinguish between different compositional units in the Gran Desierto sand sea was demonstrated. These techniques were then modified to map sand transport pathways in the Sahara and identify potential dust sources, discussed in the previous section. Linear deconvolution was effective in mapping sand composition for the Gran Desierto, and it was also useful in validating quartz sand deposits as well as low spectral contrast, fine grained materials in the Bodele Depression. By employing these techniques in concert with the time-series analysis in the section 5.3, a connection can be made between dust sources and the measurement of SAL dust at the IZO. Analysis of SEVIRI data for the month of July showed the majority of the dust sources affecting IZO to be between

0-10°W and 20-30°N. In general, dust is emitted from thousands of square miles at a time, but the SEVIRI data provide significant evidence for dust hot spots in the Sahara.

One of these dust hot spots was observed on the July 16, 2009 image in Northern Mali (Figure 68a). The dust storm could be tracked over 600 km upwind to the Northeast, but a concentrated plume began to form when winds reached a location pinpointed at ~ 22.75°N, 4°W. This general location is responsible for emitting dust that contributed to plumes throughout July, including the July 20 and July 26 SAL events noted at the IZO. Clear sky data were acquired to examine the surface composition at the sight of the large plume. These ASTER data were from a much earlier date (March 2006), but surface conditions are expected to be similar because this is a persistent dust source. Three images were mosaicked in the ASTER orbital path, and a PCA transformation was applied. The same band combination used for Gran Desierto surface composition analysis is displayed (Figure 68b) showing significant diversity in the outcrop of granitic crystalline rocks, aeolian deposits and several other unidentified sedimentary units A number of peculiar dune forms and surface features can be found in this area as well. The DCS transformation was processed, and emissivity was extracted to examine land surface spectral variability. These products and visualization of the land surface using the Google Earth™ mapping service suggested that the cyan color in Figure 68b was indicative of a paleolake surface, where dry, friable lucustrine sediments are easily eroded by sand saltation from northeast winds on July 16, 2009. Small, meter scale dune forms suggest active aeolian processes are ongoing in the area. Other ASTER image data captured from this location documented outbreaks of widespread dust emissions (not shown here). Using a similar version of the dust detection method described previously in section 5.3.2, areas of the most likely dust emission source locations were identified by looking for materials that had the lowest spectral contrast, hypothesized to be due to a combination of composition and small particle size (Figure 68c). The areas such as those identified in Figure 68c are likely, but not confirmed to be dust sources.

Using the ASTER surface emissivity data, the average five point spectra of these deposits was identified (Figure 68d). This dust spectrum was used to determine the aerosol optical depth (AOD) on July 20, 2009 of the SAL dust event at the IZO by employing the linear deconvolution approach. This application of the linear deconvolution method has not been previously done, and must therefore be treated as an experimental approach. Determining the areal abundance of

atmospheric dust over ocean may or may not behave as a spectral linear mixing scenario. The hypothesis is that the areal coverage of dust over ocean can be determined by deconvolving the image data with a spectral library. This library contains the dust spectra of the probable source (determined from the Mali location in Figure 68c), the spectra of ocean water during clear sky conditions and the inclusion of a blackbody. The average ocean water spectrum was obtained from the clear sky ASTER data on July 8 and 24, and is compared to the dust spectra in Figure 68d. The significant slope of the water spectrum is commonly seen in areas of warmer water and significant atmospheric water vapor. Linear deconvolution resulted in a retrieval of 0.22, with a very low RMS error equal to 0.0024. This value is an average of a 25 x 25 pixel area over cloud free ocean water, where the variation in the values due to scan line noise was 6-25%. This areal abundance can be described as the ASTER-derived AOD value and applies to the TIR wavelength region. Before and after the ASTER overpass (the evening of July 19 and the morning of July 20) the AERONET station at IZO retrieved an AOD of 0.25, which is measured from solar scattering at shorter wavelengths. These values compare well and imply that the linear unmixing might be a successful approach in retrieving the correct AOD value. However, further analysis is needed to determine the effects of variable spactral shapes of the water and dust.

Figure 68. (a) SEVIRI image time step for July 16, 2009. The green inset box indicates the March 2006 ASTER TIR data displayed as (b) a PCA image of bands 4,3,2 in RGB respectively. (c) The probable dust sources were located and the spectra of the dust sources extracted, and (d) the emissivity spectra of dust and water used to deconvolve the ASTER image of the July 20 dust event. Ocean water spectra was obtained from clear ASTER imagery. (See figure next page).

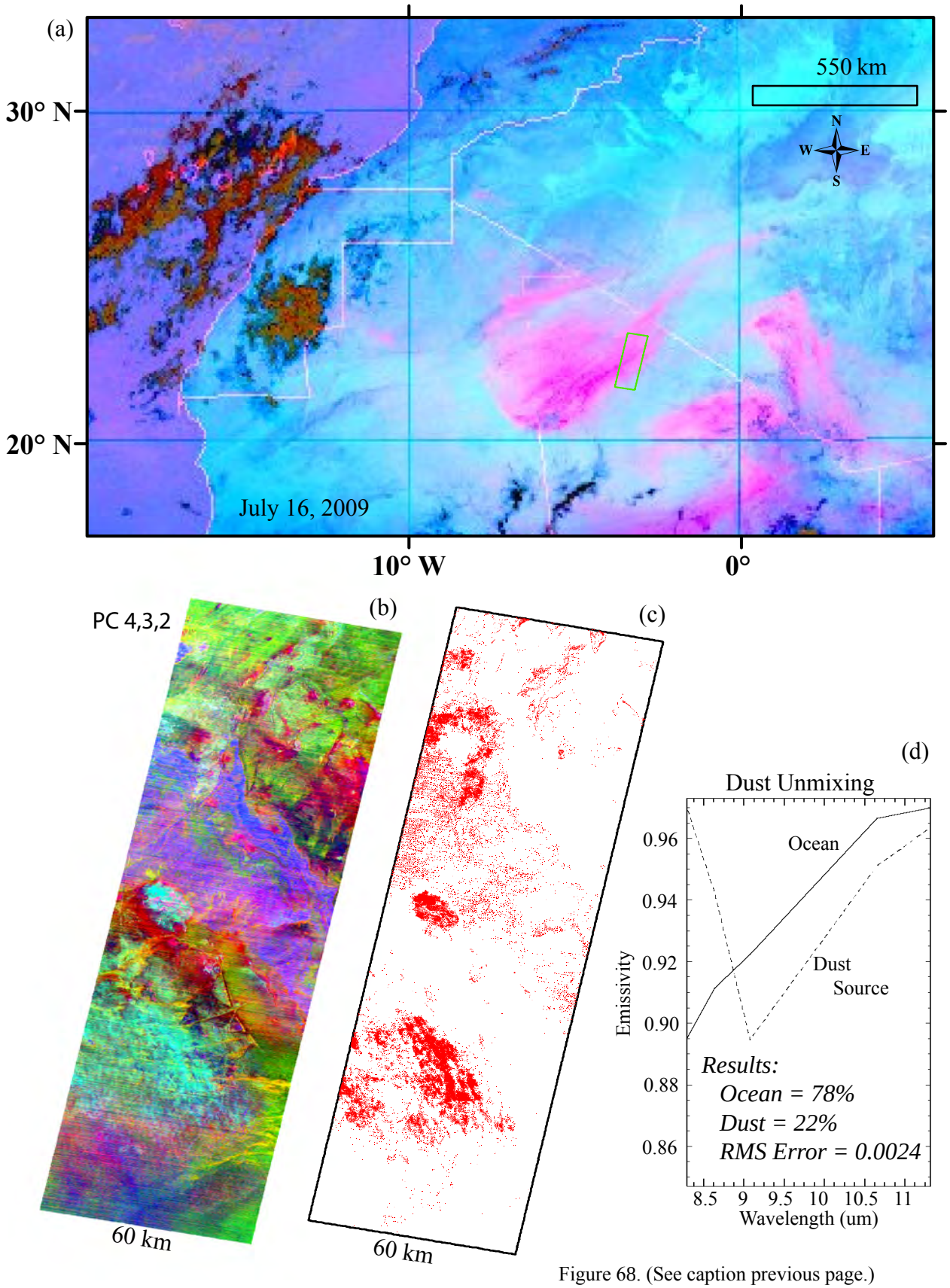

Figure 68. (See caption previous page.)

5.4 FORWARD-LOOKING INFRARED RADIOMETER (FLIR) DATA

In the previous sections of Chapter 5, the cycle of Saharan dust during the month of July was examined, and the dust sources that generate Saharan dust were explored using orbital data sets. Ground-based measurements of atmospheric dust are measured by AERONET, where dust properties rely on radiation measurements at solar wavelengths (0.34 – 1.02 μm). The real $n(\lambda)$ ($1.33 \leq n(\lambda) \leq 1.6$) and imaginary $k(\lambda)$ ($0.0005 \leq k(\lambda) \leq 0.5$) parts of the complex refractive index are retrieved for wavelengths corresponding to sky radiance measurements at multiple angles [*Dubovik et al.* 2006a]. These properties are used for calculating broad-band fluxes in the spectral range from 0.2 to 4.0 μm, spectrally extrapolating and interpolating from the $n(\lambda)$ and $k(\lambda)$ values using the correlated-k distribution based on line by line simulations [*Scott* 1974]. Gaseous absorption is accounted for using a radiative transfer model [*Dubuisson et al*. 1996]. AERONET however does not calculate the longwave (LW) radiative flux from the atmosphere, which prompts the use of other means to obtain these data. The infrared optical properties of the SAL directly affect the performance of remote-sensing systems, including the thermal infrared, and a need exists for a method to validate atmospheric longwave radiance measurements from orbital data. The following section describes the aspects of field work using the side-looking measurements of a FLIR camera to determine LW radiance in the atmosphere, as well as the theory behind the measurements, the tools and models that will be used to determine LW radiative flux due to aerosols and the expected data products. In addition to the validation of orbital LW measurements, this technique can be used directly to study the emitted LW radiative flux from the atmosphere, and with the aid of modeling, radiative properties of aerosols in the TIR wavelength region.

The primary focus of the associated field work was to use the FLIR imaging camera to directly measure atmospheric LW radiation (7 – 12 μm wavelength region). In this atmospheric window, absorption due to water vapor, carbon dioxide and stratospheric ozone are minimal (Figure 69). These data were collected over a one month period (July 3 – August 3, 2009) from the observation tower at IZO on the island of Tenerife. Because of the location and elevation, this new experimental approach for dust studies can be directly compared to other dust measurements and properties from ground and orbital instruments. These measurements include the time-series of aerosol optical depth, shortwave and longwave radiative forcing and the spatial

distribution of aerosols. The frequency of FLIR observations was paced according to the timing of ASTER, MODIS-Aqua, MODIS-Terra and AIRS satellite overpasses. Dust sample collection was coordinated with AEMET Aerosol Monitoring Program personnel. As the primary science objective is to quantify the longwave radiative forcing of SAL dust, clear-sky and dusty-sky radiance measurements were compared.

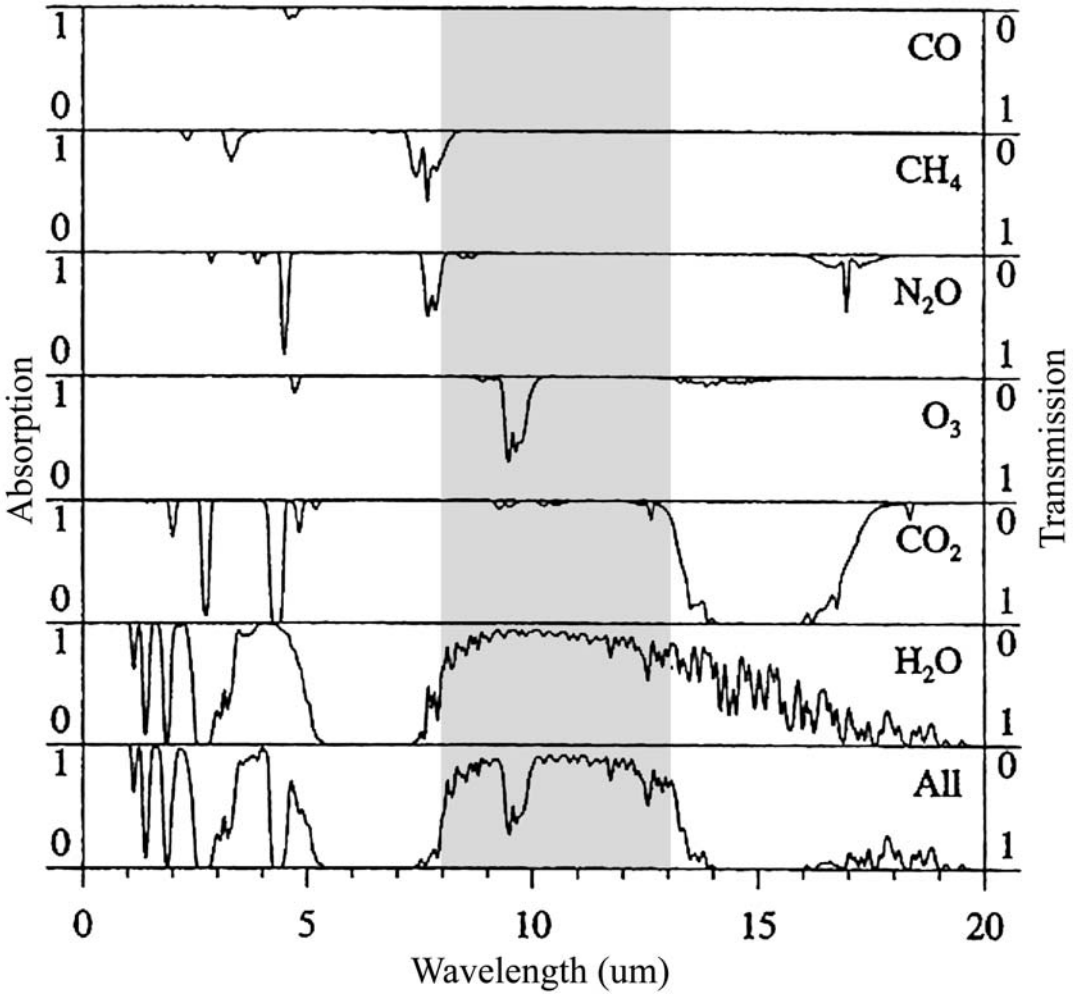

Figure 69. Absorption/transmission spectra of important gaseous species in the atmosphere. The gray box shows the wavelength region for the FLIR camera.

5.4.1 FLIR Sky-Measurement Setup

As described above, the IZO is an ideal location to make radiation measurements directly associated with suspended dust in the SAL. Using a ThermaCAM S40 FLIR camera, the flux of thermal sky irradiance was directly measured. Because the ThermaCAM S40 is also an imaging device, returning data from a 2-dimensional focal plane array of uncooled microbolometers, the spatial distribution of sky irradiance was also determined. The acquisition of side-looking FLIR TIR sky irradiance data was hypothesized to be helpful in the validation of remote-sensing data, radiative transfer models and dust models that rely on dust properties. Relatively few studies utilizing this method have been found with the exception of *Law et al*. [1988]. This source was a non-peer reviewed report distributed from the Naval Ocean Systems Center out of San Diego, CA, whose sole purpose was the performance evaluation of a FLIR system in the marine boundary layer. This work suggested that only the LW infrared (as opposed to the SW infrared) wavelength region could be used reliably to determine aerosol transmittance along the horizon line of sight (LOS). Actual determination of aerosol transmittance relied on radiative transfer modeling to determine initial clear sky conditions in the LW infrared wavelength region. Comparison of the measured to modeled values determined the atmospheric transmittance results for the marine boundary layer at very low elevation angle. Another study used FLIR camera data to study different stages in the life cycle of tornadoes based on the measured thermal characteristics of the tornado and surrounding cloud base [*Tanamachi et al.* 2006].

Potential exists to combine FLIR TIR measurements with orbital data as well. Combining upward-looking ground radiance measurements and orbital nadir-looking viewing geometry has been used with success on Mars to acquire a "top and bottom" view of the Martian atmosphere. Thermal infrared spectra of the Martian atmosphere, taken by the Miniature Thermal Emission Spectrometer (Mini-TES), were used to determine the atmospheric temperatures in the planetary boundary layer, as well as the column integrated optical depth of aerosols [*Smith et al.* 2004]. Mini-TES TIR observations were also used to infer boundary layer thermal structure, the movement of warm and cool parcels of air moving through the field of view and retrieved dust optical properties. Combining mini-TES and Mars Global Surveyor (MGS) orbital Thermal Emission Spectrometer (TES) data retrieved indices of refraction, dust particle size distribution and the degree of vertical atmospheric mixing [*Wolff et al.* 2006]. A

drawback to using the FLIR TIR data are that only broadband thermal IR measurement were possible.

The intended application of the FLIR data was to retrieve aerosol optical thickness/depth in the 8-12 μm atmospheric window and to study direct measurements of the variation of radiant LW energy in the vertical structure of the atmosphere under dusty conditions. An eventual goal stemming from this work is to compare these measurements to ASTER, MODIS, AIRS and AERONET data. Because this is a generally new application, the first priority was determining the feasibility of the FLIR data for the purposes of studying dust properties and dust storms. Trends in the uncalibrated FLIR data collected over the one month period of measurements in dusty and non-dusty settings were examined. Some limitations are immediately recognized for these measurements, which are discussed below. According to the diagram of the globally averaged longwave radiation portion of the Earth's energy balance presented earlier (Figure 37), 169 W/m^2 is emitted by the atmosphere to space and 333 W/m^2 is radiated back to the Earth surface. These numbers are in balance with solar energy, and other heat transfers that occur between the Earth surface and atmosphere. Measuring the longwave energy distribution using the method described below provides a relatively new method for studying climate and radiative forcing, demonstrated by these measurements of SAL dust. Measuring the emitted LW radiance is only one component of the Earth's energy budget, but these measurements have not been common or previously reported from FLIR data.

5.4.2 Field Setup

The FLIR camera was set up on a solid aluminum/plastic tripod and concrete platform on an observation tower at IZO using standard camera equipment. The tripod and camera were leveled and stabilized. Data were collected each day, coincident with overpasses of Aqua and Terra spacecraft and other sensors of the NASA A-train. Each FLIR measurement consisted of a series of horizontally adjacent images along a 180° field of view rotating from due North to due South, towards the East. On clear days, the island of Gran Canary could be seen on the horizon. With the exception of the 11:30 data collection time (a time of solar interference), a profile was also acquired in a 60° vertical field of view from the land-ocean interface to a 45° angle above the

horizon. Approaching zenith $z = 0°$ (pointing straight upwards), atmospheric opacity is low and there was no cloud cover, the FLIR camera's limit of detection is reached as it points directly into cold space. The spot size, or instantaneous field of view (IFOV) is 1.33 mRad for each pixel in the 320 x 240 image array of the ThermaCAM S40 with a 24 degree lens. The slant distance from the IZO observation tower to the eastern coast of the island in the field of view is ~12km away. At 12 km, the pixel IFOV is 15m, where the image dimensions in the focal plane is roughly 5.1 x 3.8 km. The FLIR camera focused at this distance has the contrast to resolve surrounding land features (including the coastline). The sharpness in the image data was necessary for image to image coregistration to create panoramic views, but the FLIR camera was set at or near the hyperfocal distance, giving a depth of field near infinity. The calculated field of view was actually much greater than 6000 km. The path length (l) to the apparent horizon based on simple geometry is less, which is about 180 km.

5.4.3 Model for Sky Radiance Measurement

The side-looking FLIR camera can be used to derive sky irradiance ($W/m^2/sr$). The images were centered at a zenith angle $\theta \approx 90°$ (e.g. the horizon) and were not scaled to height (z) or atmospheric pressure levels (P). In order to compare the side-looking FLIR measurements to vertical distributions and column-integrated TOA measurements from orbital data, including radiosonde measurement, LIDAR retrieval and AIRS data, a model must be developed. Longwave radiation is at its greatest intensity at the land surface, as measured by pixels in the field of view. At the elevation of the FLIR observation (2391 m.a.s.l.), the land and ocean are commonly obscured by clouds and haze at the top of the marine boundary layer at ≈ 900 m.a.s.l. As the camera tilts up from the ocean surface towards the horizon, radiance values from areas of ocean stay relatively consistent but vary with cloud cover or ocean surface. Just above the horizon, the optical path length (l) has the potential to be infinite in the line of site. The optical depth increases as the amount of intervening atmosphere decreases with elevation above the horizon, owing to generally less total ozone, water vapor, other LW-emitting gases. One component is also aerosols, which is assumed to be mostly dust from the SAL. The source of energy measured by the FLIR is the scattered terrestrial and atmospheric LW radiance, which in

this study, is over ocean. The side-looking FLIR signal response is a function of the radiance scattered and emitted by constituents in the atmosphere. In a simple model, spectral radiance (L_λ) at the camera sensor is determined by the following equation:

$$L_\lambda = \varepsilon_\lambda \tau_\lambda B(T) + (1 - \varepsilon_\lambda)\tau_\lambda B(Tatm) + (1 - \tau_\lambda)B(Tatm) \quad (25)$$

where, ε is the land surface emissivity, τ is the transmissivity, $B(T)$ is blackbody radiance at temperature T. $Tatm$ is the temperature of the atmosphere. The first term in this equation is the direct outgoing Earth surface radiance modified by land surface ε and the τ of the atmosphere. If the land surface is not measured directly, the first term can be considered negligible for measurements of atmosphere. The values of interest are measured above the horizon and are over ocean. The relatively colder ocean is expected to contribute far less LW radiance than the land surface. The second term is the reflected direct surface radiance. Seawater emissivity equals 1.0 and is low in spectral contrast; therefore the second term is also considered negligible. Although, the seawater spectra measured from ASTER was not flat in section 5.4, this was probably due to the effects of aerosols and water vapor. The radiance measured at the camera can thus be assumed to be a function of τ and atmospheric temperature. In the SAL, aerosols in the atmosphere are also assumed to absorb and emit radiance in the TIR wavelength region, therefore the first term in equation (25) can be used to represent the emitted radiance due to aerosols. The second term in (25) may or may not be a relatively low signal at low elevation angles. For simplicity here, it is assumed to be negligible. The resulting equation is:

$$L_\lambda = \varepsilon_\lambda \tau_\lambda B(T_{aerosols}) + (1 - \tau_\lambda)B(T_{atm}) \quad (26)$$

L_λ cannot be simply obtained as a function of elevation (z) above the horizon, and the geometry of the side-looking FLIR measurements poses a problem in obtaining L_λ vs. z. The measurement is integrated over the effective optical path length (l) at some viewing angle. l is a function of the camera look angle (or zenith angle θ), thickness (or height h) of the atmosphere, the transmittance (τ) and emissiviity (ε). An expression for the total atmospheric absorption (α) is:

$$\alpha = \gamma \sec\theta \int_0^\infty \varphi(z)dz = \gamma H \sec\theta \tag{27}$$

where γ is the atmospheric absorption at sea level, $\varphi(z)$ is the variation of atmospheric absorption with elevation above mean sea level (a.m.s.l.) and the integration H represents the effective optical path length (l) in the atmosphere [*Kislyakov* 1966]. The path length varies with sec θ because each angle integrates a varying thickness of atmosphere, and sec θ is not accurate for $\theta \geq$ 85°. Other methods exist for estimating a more accurate effective path length, for example, [*Young* 1974; *Young* 1994], where these functions vary with the model of atmospheric temperature, heterogeneity and density. Continuing, the example here adequately demonstrates the geometry and physics at work. Assuming that emission equals absorption, the measured average temperature T in the θ direction is described as [modified after *Kislyakov* 1966]:

$$\overline{T} = \frac{\int_0^\infty \varphi(z)B(T,z)\exp\left\{-\bar{\varepsilon}\sec\theta\int_0^\infty \varphi(z)dz\right\}dh}{\int_0^\infty \varphi(z)\exp\left\{-\bar{\varepsilon}\sec\theta\int_0^\infty \varphi(z)dz\right\}dh} \tag{28}$$

where, $B(T,z)$ is the blackbody radiance, and ε *bar* is the effective or average emissivity of absorbing (and therefore emitting) constituents. Because measurements are taken in the atmospheric window (the 8-12 μm wavelength region) and at an elevation z within the SAL, $\varphi(z)$ is assumed to be greatly affected by mineral dust, and to a lesser extent, ozone and water vapor that also have absorption features and emit into the aperture of the camera. The transmitted signal reaching the camera is also probably affected by the attenuated radiance that is scattered from the terrestrial surface (i.e., the second term in equation 25). It is difficult to assume these factors of molecular absorption (and therefore emission) are negligible, therefore correction is necessary for water vapor, ozone and other molecular absorption along the slanted, effective optical path that the FLIR camera is measuring. This problem can be solved using radiative transfer models.

5.4.4 Modeling Potential of SAL Aerosol Radiance

The first step of the theoretical approach described above is to first model clear sky atmospheric conditions that are affected by water vapor, ozone and other molecular absorption. A variety of radiative transfer codes exist, such as LOWTRAN [*Kneizys et al.* 1983]. A user friendly, publically available and widely used tool was selected, the Santa Barbara DISORT Atmospheric Radiative Transfer (SBDART) software tool [*Ricchiazzi et al*.1998]. SBDART can be used online or it can be downloaded. The downloaded version is without a cumbersome graphic interface, and operates at a command prompt in a Unix, Linux or Cygwin environment to compute plane-parallel radiative transfer in clear and cloudy conditions at TOA, BOA, ground surface or, in this case, within the Earth's atmosphere at a side-looking angle. A variety of customizable inputs can be used, including measured weather, temperature, water vapor and ozone from radiosonde and ozonosonde profiles. Longwave radiation fluxes can be modeled and calculated using viewing geometry variables that match those set up in the field at Tenerife as described above. Output can also be extracted representing TOA values according to custom satellite filter functions (i.e., ASTER, AIRS or MODIS). Using the tool to model clear sky radiance incident at the lens aperture, the measured values can be directly compared to modeled values. Assuming the model accounts for attenuation and transmission due to water vapor, ozone and molecular absorption correctly, the difference between measured and modeled data can be assumed to be due to airborne mineral dust. Supporting weather data available from the Izaña Atmospheric Observatory, ozone and water vapor data from AERONET and AIRS, and radiosonde data from the Guimar airport on the island of Tenerife enable accurate modeling of clear sky conditions. Radiosondes retrieve the necessary data for profiles of temperature, water vapor, winds and atmospheric pressure that serve as input to the SBDART radiative transfer model. The radiance due to aerosols is the difference between the clear and measured sky irradiances:

$$L_{aerosols} = L_{sky\text{-}measured} - L_{clear\text{-}sky} \tag{29}$$

A negative value indicates loss of loss of energy and a negative radiative forcing. Positive values, in contrast, indicate emitted radiance from particles (term 1 of equation 2) and/or

scattered terrestrial outgoing LW radiance (term 2 of equation 2) or both. For the SAL scenario, dust particles are already in a relatively warm air layer, and therefore are expected to absorb and emit energy from surrounding air. This contributes to a net zero radiative force between upward and downward emitted fluxes. This energy is emitted in all directions, and is also transmitted laterally, and hence is available for measurement by the FLIR camera. Dust particles attenuate the terrestrial upwelling LW radiance through scattering and absorption. Transmitted energy is lost to space, but can be detected by orbital sensors. Orbital sensors, however, integrate both the atmospheric and land surface radiance. This is why the side-looking or limb FLIR measurements are unique within the analysis of the SAL. The radiance incident at the aperture of the camera can be assumed to be a function of scattering and emission from atmospheric particles only. The effective emissivity of the atmosphere due to aerosols is:

$$\varepsilon = \frac{(1-\rho)(1-\tau)}{1-\rho\tau} \tag{30}$$

where $(1 - \rho)$ is due to scattered and $(1\text{-}\tau)$ is the emitted LW radiance measured by side-looking thermal IR. According to the FLIR ThermaCam S40 manual, this effective emissivity (ε) is correct for a semi-transparent material "where the resulting geometric series is summed." Assuming that scattering is less iimportant, which it may not be, the expression simplifies to $\varepsilon = (1 - \tau)$. The ability to use FLIR data to determine optical properties of atmospheric aerosols is relatively new and has not been thoroughly validated, nor is a theory completely made here because results will depend on model feedback. Likewise, to calculate spectral emissivity values, derive aerosol composition and generate accurate temperatures, multi-wavelength data best suited to solve the Planck function. The data here are broadband measurements, and therefore would generate broadband emissivity measurements. In this study, because the camera makes a broadband measurement, ε will always be an effective quantity, integrating emission, transmission and scattering values (equation 30). Combining the radiation measurements made here with aerosol volumes determined from AERONET, one can determine longwave radiative forcing efficiency ($\Delta F_{eff} = W/m^2/\tau$ or $\Delta F_{eff} = W/g^3$ dust), where τ in this case is AOD in the line of sight for FLIR measurements. Radiative forcing efficiency is also determined from AERONET data as well, but the technique suggested here uses side-looking FLIR data to make

these measurements are specifically made for emitted LW atmospheric radiation. Orbital measurements integrate land surface radiance, and this is directly avoided using the side-looking measurements. Only the LW radiance that is scattered by or emitted from the atmosphere is measured. AOD for the 8-12 μm wavelength region can be determined as:

$$AOD_{\lambda=8-12\,\mu m} = \frac{L_{aerosols}}{L_{clear-sky}} \tag{31}$$

Theoretically, this AOD is similar to a measure of the atmospheric effective emissivity of the dust if $L_{clear\text{-}sky} \approx$ blackbody radiance ($B(T)$).

Theoretically, these data could be used to back-calculate the vertical distribution of aerosols or the integrated TOA value, probably with the necessity to use the SBDART radiative transfer code to forward-model dusty conditions. In summary, the camera was set up to the best of available resources to measure the integrated radiance emitted within the depth of field that accounts for the entire atmospheric line of sight (LOS). Therefore, assuming the geometry of the camera setup is well constrained, the image data can be used to accurately map the distribution of radiance in the atmosphere. Using the SBDART to model clear-sky radiance, a number of aerosol properties and longwave radiative forcing values could be estimated from the side-looking FLIR data. In the next section, the trends in the raw data are examined.

5.4.5 Preliminary Results

As shown from the time-series analysis of orbital and AERONET data, July was marked by a cycle of dusty and non-dusty conditions. Data were collected every six hours from the same location from July 11 through August 3 coincident with MODIS and Terra overpasses. These data were collected from the same viewing geometry of the eastern sky from 0° N to 0°S. Dusty conditions were easily identified in the field from visual observations. The sky parallel and above 2390 m.a.s.l. was clear of clouds 90% of the time. To document clouds, haze and the visual observations of dust, an 8 megapixel camera was used to collect panoramic images in the same field of view as the FLIR data collection at every observation time. The hazy or dusty

conditions were evident in the FLIR observations where the visible and thermal IR images between clear conditions on July 13 and July 22 are compared (Figure 70). On July 13, an apparent horizon is clearly visible in both visible and FLIR images. On July 22, the horizon is obscured by dust and/or haze.

Figure 70. Upper images are for July 13. Lower image are for July 22. Left images are standard 35 mm camera images. Right images are from the FLIR camera. Coincident thermal imagery showing sky brightness temperature ranging from < 273 K (in black) in the upper atmosphere to > 300 K (white color) for the land surface in the foreground. Time is 12:00 GMT.

The vertical distribution of humidity and temperature of these days can be observed from the radiosonde profile data (Figure 71). A black horizontal line demarks the approximate elevation of the IZO observation point. The temperature inversion at the MBL and its effect on relative humidity is apparent on both days at ~900 m.a.s.l.. The inversion is much stronger on July 20. Surface temperatures are similar in the MBL, where higher day to day variability is experienced

at 2390 m.a.s.l. Relative humidity is significantly higher on the 22 at and above IZO, increasing from 22% to 65% at 4600 m.a.s.l. Actual water vapor density was not calculated here. The FLIR camera's band pass filter is theoretically within the atmospheric window, where some minor water, CO_2 and ozone absorption features exist (Figure 69). Therefore, the humidity levels experienced at the higher elevations could have affected the side-looking FLIR measurements. Consequently, the observation between these clear and dusty data suggests that radiative transfer is needed to accurately obtain radiant energy from aerosols. In Figure 72, the profiles of brightness temperature with increasing viewing angle are compared between July 13 (clear) and July 22 (dusty). The effect of dust (and/or possibly water vapor) increased the overall temperature throughout the vertical air column and reducted the slope of temperature with height. Difference in land surface temperature was responsible for part of the offset between the two profiles at the horizon. Atmospheric composition was responsible for the decrease in slope. Because these data were collected as a function of viewing angle, it was difficult to compare these data to the temperature and humidity profiles from the radiosonde. The FLIR measurements have not yet been atmospherically corrected either.

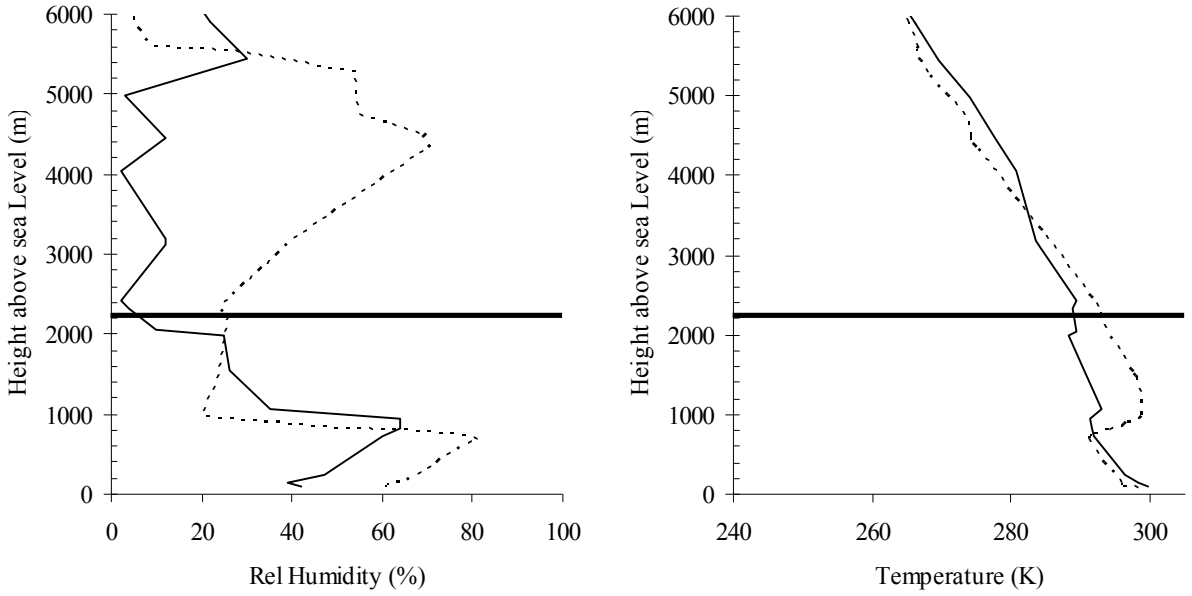

Figure 71. Vertical relative humidity and temperature profiles for July 13 (solid lines) and July 22 (dotted lines). The darker solid horizontal line is the elevation of IZO observations.

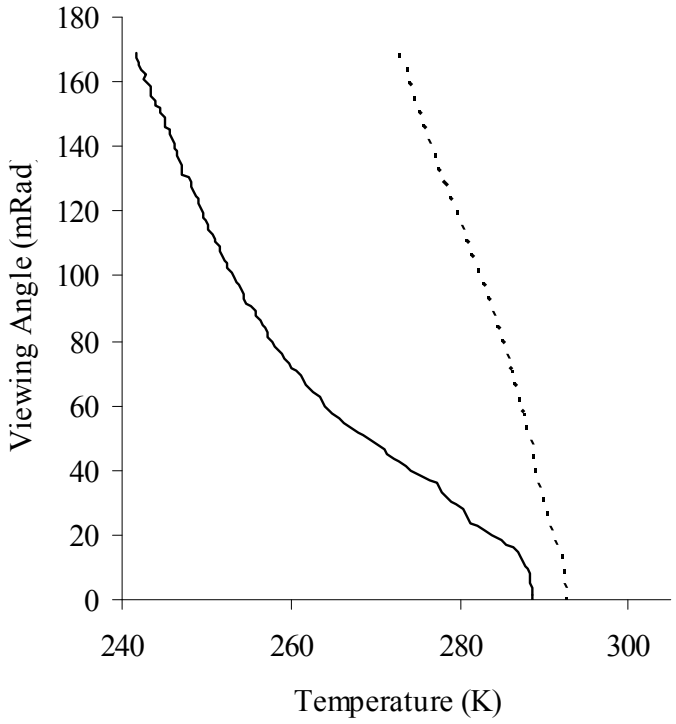

Figure 72. Profiles of brightness temperature extracted from FLIR data on July 13 (solid line) and July 22 (dotted line) as a function of viewing angle. An increase in viewing angle ≈ an increase in height.

The largest dust event had a noticeable impact on the FLIR measurements on the 12:00 observation time on July 20 compared to clear sky conditions on July 13. In Figure 73a, the panoramic of the FLIR TIR data are compared to the clear sky condition. The temperature range of each image is 240-320 K, where higher temperatures indicate higher OLW radiance. The warmest areas of the image are land surface temperatures from the hills below and the observation tower railings, satellite dish and other obstructions. In the clear image on July 13, where below the hills, the ocean surface shows as bright blue throughout the bottom half of the image. The colder, clearer sky is black. The dusty sky on July 20 has a higher OLW radiance. The OLW is affected by atmospheric aerosols emitting in the TIR wavelength region, absorbing and/or scattering the OLW radiance from the land surface into the aperture of the FLIR camera lens. A panoramic, as shown in these examples, was created for each observation time, and a significant amount of information can be extracted using just profiling tools in the ENVI image visualization software. Some of these data are presented below each image in Figure 73a and Figure 73b.

The graphs on the left are horizontal profiles across the atmosphere above the apparent horizon, which can be seen visually in the July 13 image but not for July 20. The average brightness temperature on July 20 at this elevation is higher at 283 K, where on July 13, the brightness temperature is 260 K. The north-south tilt in elevation of the horizontal profiles is an image error because of the tilt of the camera with respect to the horizon as it was rotated in the field of view. An important and interesting observation is imbedded in the noise in the horizon direction of the July 20 image, where this noise is not seen to the same degree for the July 13 image. The noise is due to adjacent images not mosaicking well because temperatures were slightly higher around each of the image's edges. It is possible that this is an effect of the dust or haze in the atmosphere, where the same "aura" or "halo" is seen in other images taken of scenes that lack dynamic range. For example, aiming the camera at a stone wall that is isothermal and homogenous in composition shows the instrument error in temperature across the scene. The noise variation is low and can be averaged out in the horizontal direction.

The most important data are extracted from the vertical direction; the July 13 and July 20 profiles are shown on the right in Figure 73. Again, July 20 temperature is high overall, but in this image, the slope of temperature is significantly affected. On the x-axis, a zenith angle of 90° indicates the start of the apparent horizon along the graph in the left direction. For the July 13

image, the “kink” in the profile indicates the ocean-atmosphere interface; it is slightly curved because of the effects of the MBL. As zenith angle decreases (the camera points upward), temperature decreases with decreasing slope. In the July 20 image, the temperature decreased no more than 23 K and the slope of the curve is convex compared to the concave shape of the July 13 temperature profile. Even though the primary focuses of these data are ultimately to derive the direct effects of aerosol LW radiative forcing, the potential for measuring indirect effects may also be possible. For example, clouds are present in different areas through the July 20 image, which is responsible in part for the horizontal “noise” described earlier. This variance may be useful data to measuring the radiative energy of clouds, as well as the interaction with dust in the SAL. For example, the difference in OLW for different types of clouds could be assessed with this tool and method of measurement.

(a) July 13 FLIR

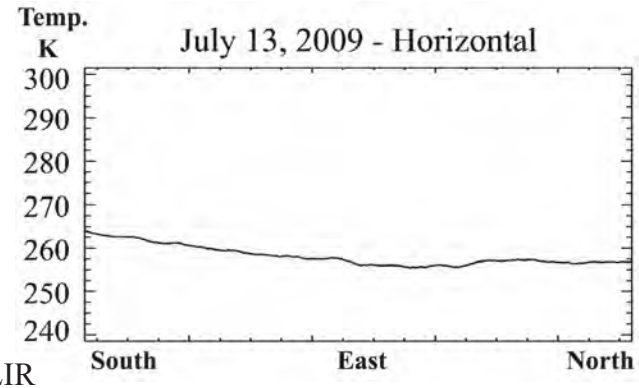

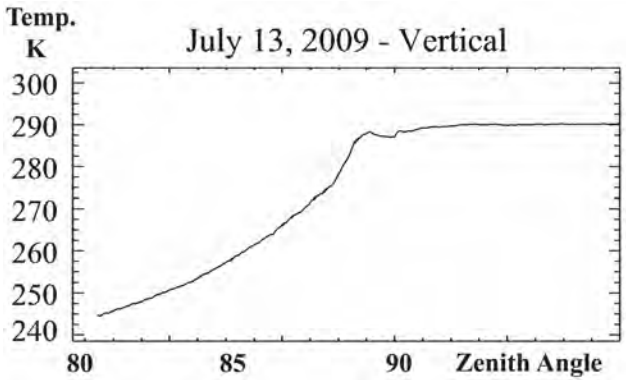

(b) July 20 FLIR

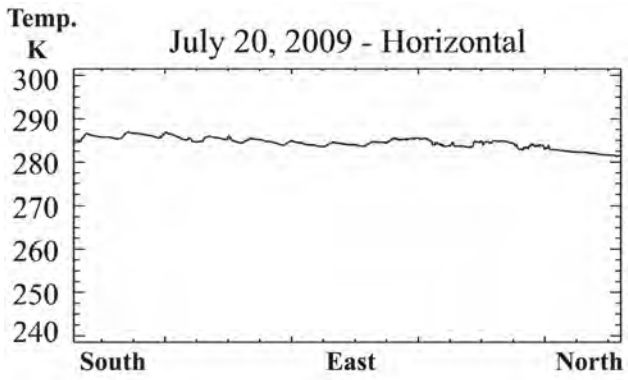

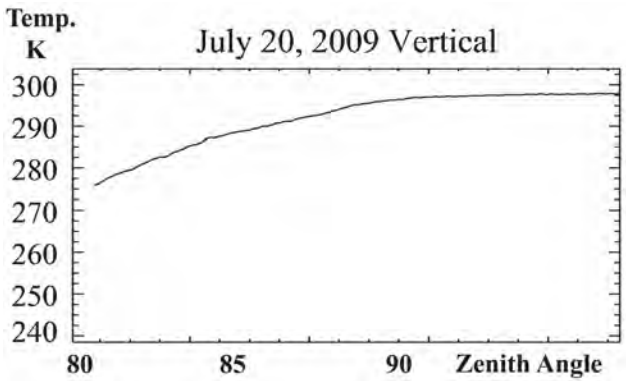

Figure 73. Examples of FLIR data on (a) July 13 and (b) July 20, 2009.

5.5 DISCUSSION AND CONCLUSIONS

IZO researchers described that typical strong SAL dust events deposit a red dust, where the dust events observed here appeared generally as a white color in the atmosphere, depositing a light brownish-yellow dust on surfaces. At the same time that the brownish-yellow dust was deposited on surfaced at the IZO, Sergio Rodriguez, an IZO researcher, had arrived on the island of Lanzarote and made a field observation of a thick layer of red dust deposited on surfaces there. This dust was collected and sent to the University of Pittsburgh for spectral analysis. The difference between simultaneous field observations at the two sites possibly suggests that the dust deposited at Lanzarote, because it did not reach the IZO, may be larger in particle size and also had a different composition because of the color. This hypothesis is based on the reasoning that larger particles settle out of suspension faster or are not lofted as high as smaller dust particles that reach the IZO. The different color of the particles suggested that particles deposited at Tenerife might be more iron rich, but because of particle size effects on spectra, this can only be confirmed by laboratory analysis. A second variation to the hypothesis could be made about the dust is that is is from two different source areas (and not necessarily varying in particle size). Yellowish particles may be from a source further downwind and have simply been suspended higher into the atmosphere. Lastly, a third hypothesis was proposed by Sergio Rodriquez that the extended residence time of dust in the atmosphere serve as locations for condensation of water vapor on dust particles, creating a "wet dust" that generates atmospheric haze. The compositional and particles size differences determined later by future chemical analysis from AEMET and spectral analysis of samples at the University of Pittsburgh may help to confirm one of these hypotheses.

According to discussion with local residents and IZO researchers, dust events during the month of July 2009 were not nearly the strongest dust events that have occurred at the IZO site. Consequently, the largest effects of aerosols on emitted longwave radiation were not measured by the FLIR field camera. However, enough data were collected from day and night times and over a sufficient length of time to develop a dataset showing variability in atmospheric dust (as well as other atmospheric conditions). These data will be ideal to further develop the method of modeling the emitted longwave radiant energy from atmospheric aerosols.

In this Chapter, quantitative approaches of measuring Saharan dust addressed aspects of the cycle of atmospheric dust and its radiative effects, mapping dust source composition, and directly measuring emitted longwave radiation from the dusty atmosphere. Moreover, a series of several different datasets that were simultaneously collected clearly demonstrates the ability to study dust at many scales in the life cycle of dust from source to becoming an atmospheric constituent. What has not yet been done is making the linkages between the different research objectives pursued in this Chapter. For example, the variability of mineral dust aerosols in the atmosphere and their effect on the Earth's radiation budget through time was examined. Data were simultaneously acquired from both orbital and ground-based sources at the IZO taking advantage of AERONET instrumentation and available satellites. Wind patterns affecting the transport of dust were viewed, and dust plumes could be tracked from source locations. Dust source composition was identified, and in one case, the spectral emissivity of the dust was related to atmospheric measurements using ASTER data. Otherwise, the Bodele dust source measurements did not appear to apply to the observations at the IZO because no dust plumes appeared to have traveled from this location. Relating dust source composition measurements to measurements of atmospheric dust composition is a challenge. Fifteen minute time-resolved SEVIRI data alone shows the complexity that occurs as dust storms mix before transporting dust to the Atlantic. It also appeared from these data that even though there are dust hot spots, there were also significant broad expanses of land in the Sahara that emitted dust, which was more difficult to pinpoint and estimate dust emission rates.

This Chapter did not relate composition of Saharan dust sources to the variability of LW radiative forcing. The composition of the dust aerosols were best understood by examining multiple, concurrent datasets. To determine the variability of emitted longwave radiative forcing, the FLIR data set must first be completed, relying on the modeling of clear sky irradiance to determine the effect of dust (modeled vs. measured data). Only five dust events occurred throughout the month of July, where the sources of these plumes could be constrained by analyzing the higher resolution SEVIRI data. ASTER TIR data and ground-based Forward Looking Infrared (FLIR) were employed to study the SAL using their capabilities to examine longwave radiation and dust composition simultaneously. ASTER data were effective in examining dust source composition and characteristics and determining the effect of aerosols on outgoing longwave radiative forcing in the atmosphere. FLIR data were used to measure

longwave radiative forcing, which was a new experimental approach for SAL dust studies. Development of the data collected at Tenerife should produce insightful results into climate studies and the understanding of Earth's radiant energy budget.

The potential results from this work could have a direct bearing on public health, air quality, disaster management, and ecological forecasting with respect to dust hazards. This work is the first documentation of the use of FLIR IR data for the detection and study of SAL aerosols. The method development should be applicable for other field studies of dust, for example, measuring dust emission rates at dust source locations in the field.

6.0 CONCLUDING REMARKS AND FUTURE DIRECTION

This dissertation documented the application of a significant variety of techniques in thermal infrared remote-sensing to study aeolian systems. These techniques included (a) radiometric normalization of thermal infrared data for mosaicking imagery of large aeolian systems in the Gran Desierto and the Sahara Desert, (b) the application of compositional mapping techniques [*Ramsey et al.* 1999] to derive sand and dust compositions of the mosaicked data results, and (c) quantification of aeolian dust source dynamics through the determination of an erosion potential parameter derived from satellite data at the White Sands dune field. Finally, some of these techniques, analysis of a variety of orbital data, ground measurements and modeling predictions were integrated to study and describe global Saharan dust emission during July 2009 (a month in the dusty season) at the island of Tenerife, Spain. Dust emissions were related to actual measurements of atmospheric dust in the Saharan Air Layer to dust source composition on the African continent. Because several geographic locations were studied, a central thesis with respect to a single aeolian system or study region is not possible. However, the application of these techniques for a single field site (if the data were available), would provide a highly comprehensive picture of an aeolian system. The Sahara Desert was the prime target for the synthesis of these types of tools and techniques, where chapter 5 addressed some of these opportunities by examining the cycle of dust in the atmosphere, mapping dust source composition using ASTER TIR data and developing a method of measuring the variability of emitted longwave atmospheric radiance to determine the radiative forcing of dust. No single data source or technique is adequate to address the issues of sand movement, dust emissions, and atmospheric properties, and that the sum of using multiple data sets and analysis techniques is greater than the impact of individual techniques/data sources. Data intercomparison and fusion is a key for understanding these complex systems.

How are the aeolian systems in the Sahara Desert changing through time? The radiometric normalization technique is not only a solution to studying a single large aeolian system by mosaicking image data together, it is also a tool for measuring land surface changes. The tool led to the ability to use surface composition mapping techniques [*Ramsey et al.* 1999] for the Gran Desierto sand sea as a whole at a high spatial resolution. These techniques were then applied to larger areas in the Sahara desert successfully. Combining ancillary data sets with the ASTER TIR data, it was possible to identify dust composition interacting with sand transport pathways, a key feature of aeolian system dynamics. The analysis of dust emission sources (as well as their composition) and sand transport showed that these interactions are important. Without the radiometric balancing tool, several of these activities would be difficult. Thermal infrared data vary with land surface temperature, which is important to radiative budget studies. Changes in emissivity, used to measure compositional change, can be used simultaneously to determine how change in surface composition affects land surface radiance. Because the radiometric balancing tool identifies areas of change between dates spectrally, changes in vegetation communities or mineral composition can be monitored. In the Sahara, where wind erosion is a constant force acting on the land, changes could be measured on the shorter time scales needed for satellite remote-sensing. Future work will take advantage of the temporal resolution of satellite data and use the radiometric normalization technique to map changes in dust source composition and sand transport pathways. These techniques have already been successful in studied dust sources in Soda Lake [*Katra and Lancaster* 2008] and sand deposits in the Coachella Valley [*Katra et al*. 2008].

The techniques developed at White Sands using thermal infrared data to derive thermal inertia, soil moisture and the wind threshold velocity is also highly applicable to studying dynamics or change in the Sahara Desert. The tool was developed using ASTER data, and the uniqueness of the study focused on the high spatial resolution of the data to derive different properties of dune and interdune areas. With the volume of data collected and continuing to be collected by ASTER (as of 2009), this technique should be appied in the Sahara for monitoring. Important areas were identified during mapping activities of sand transport pathway using ASTER [*Scheidt et al.* 2007], where these areas could be very important in controlling the frequency of dust emissions. In the analysis of SEVIRI data at 15 minute intervals, it was observed that dust emissions occurring in the month of July did not necessarily correlate well

with the locations of dust hotspots that were identified by TOMS AI data. This could suggest that dust source regions probably change geographically, which could have a significant impact if comparing models that are based on older dust source emission scenarios. As was previously mentioned, the parameters derived at White Sands can be generated using other thermal IR datasets where the temporal resolution exists. MODIS and SEVIRI are prime instruments for future thermal inertia and soil moisture modeling where spatial resolution is less important. In future work, sediment availability of Saharan dust sources can be mapped through time.

Analysis of aeolian systems from remote-sensing is a highly practical science, but as the compositional mapping work in the Gran Desierto demonstrated, ground truth of hundreds of sand samples was crucial to making good interpretations. For example, the identification of the microcline sources in the Sierra Pinacate region is unique, especially the trachyte deposits in the volcanic field. Are these really potassium feldspar sources and are they important to the composition of aeolian sands there? Could the spectral data be explained by other variables besides composition? The reality is that ASTER only resolves five points of an emissivity spectrum for a 90 m^2 area, and field work will be conducted to further validate source areas for the Sonoyta Dune area. Likewise, the correct design of satellite instruments can enable the measurement of wavelengths for which Earth surface materials have spectral absorption features. Modification proposed for the HysPIRI instrument would include a bandpass to better map feldspars [*Ramsey and Rose* 2009]. Ground truth in the Sahara desert proved to be a logistical impossibility between years 2004 and 2009 due to concerns of safety and the coordination needed to organize a field campaign in this remote and hazardous location. Study of the Sahara desert under these conditions and resources leaves the approach to remote-sensing only. This is a quandary considering that the Sahara contains a host of terrestrial analogues and are valuable to Martian aeolian studies. To this end, future work should continue to focus on the systems of the Sahara, and as satellite systems improve, these efforts form the basis for future research as soon as ground truth becomes more accessible.

Lastly, the thermography data generated from handheld thermal cameras is this study has considerable potential application to field studies of aeolian dynamics, land conservation in arid regions and climate. These FLIR data are important to linking ground based observations to orbital data sets, providing an intermediary remote-sensing instrument that is mobile. The FLIR data collected at Tenerife during July 2009 is a large and rich data set, providing tangible field

data for modeling studies of LW radiative forcing of the SAL. Weather data, radiosonde profiles, orbital data and AERONET inversion products give a complete data picture to support FLIR analysis. The outcome of the FLIR data set is a unique and a novel approach to studying aerosols, especially if clear sky modeling using SBDART proves successful. The technique brought direct measurements of the variation of emitted longwave radiance components under study, and has the potential to retrieve aerosol optical depth in the 8-12 μm atmospheric windows. The FLIR data set generated in this dissertation applies to global dust sources and the effects on longwave radiance as it pertains to climate. The data resolve some vertical distribution of dust in the atmosphere under dusty conditions. However, if the FLIR data are useful, other applications could be pursued on the ground at dust emission sources. For example: (a) quantification of dust emission rates at dust sources, such as at White Sands, NM, (b) examination of the thermal structure of dust devils and (c) rates of saltation with changing soil moisture conditions. Work continues on the FLIR dataset and in collaboration with IZO researchers and will result in the comparison of FLIR LW radiative forcing values with independent lab measurements of aerosols composition, size distribution and concentrations.

APPENDIX A

A.1 RADIOMETRIC NORMALIZATION CODE FOR ASTER TIR

The radiometric normalization used to balance and mosaic ASTER thermal infrared (TIR) satellite data was written in the Interactive Data Language (IDL). This code requires the used to first convert their ASTER data from DN to calibrated thermal radiance from the AST_09T standard data product. (More information on how to obtain ASTER data can be found at http://asterweb.jpl.nasa.gov/). The code will allow the user to include binary images to be used as masks to prevent the algorithm from using unwanted data. All files that are input should be ENVI standard files that have been north-oriented, where the code cannot process native HDF format. Native ASTER data have a rotation to the 2-D array of pixel values. Data that have not been rotated to true North will produce erroneous results. This code is version 1.0, a draft version not an "out-of-box" tool into and only operates and balances radiance. Other versions of the code have been created in order to balance the VNIR and SWIR products, and have an array of processing options for TIR, including emissivity and AST05 data. See annotations (preceded by ";" in IDL code lines) for further information.

A.2 RADIOMETRIC NORMALIZATION FOR ASTER TIR VERSION 1.0

```
; ********************************************************************
; ASTER RADIOMETRIC NORMALIZATION VERSION 1.0
; cross_track_aster v1.0, 08/30/2006
; ********************************************************************
; IDL code written by Stephen Paul Scheidt
; email (sscheidt77@gmail.com)
; ********************************************************************
; For this version, create an entry in the envi.men located
; in the IDL/ENVI menu folder.  For ENVI 4.3, this location
; was \rsi\idl63\products\envi43.  For example:
; 1 {Radiometric Normalization, TIR ONLY} {not used} {cross_track_aster}
; See ENVI help for more guidelines.
; ********************************************************************

; Code initialization.

    pro cross_track_aster, event
    compile_opt idl2
    envi, /restore_base_save_files
    envi_batch_init, log_file='batch.txt'

; A top level menu (not a widget) appears and asks the user to choose the
; TIR reference image, and then the file that needs to be normalized to the
; reference.

    fix_img=dialog_pickfile(/READ, TITLE='Choose the TIR Reference Radiance Image')
    adj_img=dialog_pickfile(/READ, GET_PATH=layer_path, TITLE='Choose the Radiance File to be
  Normalized')

    envi_open_file, fix_img, r_fid=fix_fid
    if (fix_fid eq -1) then begin
    envi_batch_exit
    return
    endif

    envi_file_query, fix_fid, dims=dims, ns=ns, nl=nl
    t_fid = [fix_fid,fix_fid,fix_fid,fix_fid,fix_fid]
    pos  = [0,1,2,3,4]
    exp = '(b1 ne 0) and (b2 ne 0) and (b3 ne 0) and (b4 ne 0) and (b5 ne 0)'

    envi_doit, 'math_doit', fid=t_fid, pos=pos, dims=dims, exp=exp, r_fid=msk1_fid, out_name=layer_path
  + file_basename(fix_img) + '-zeromsk'

    envi_open_file, adj_img, r_fid=adj_fid
    if (adj_fid eq -1) then begin
    envi_batch_exit
    return
    endif

    envi_file_query, adj_fid, dims=dims, ns=ns, nl=nl
    t_fid = [adj_fid,adj_fid,adj_fid,adj_fid,adj_fid]
    pos  = [0,1,2,3,4]
```

```
    exp = '(b1 ne 0) and (b2 ne 0) and (b3 ne 0) and (b4 ne 0) and (b5 ne 0)'

    envi_doit, 'math_doit', fid=t_fid, pos=pos, dims=dims, exp=exp, r_fid=msk2_fid, out_name=layer_path
+ file_basename(adj_img) + '-zeromsk'
```

; Next, the algorithm will determine the degree
; of correlation between pixels using from emissivity.
; Calculate emissivity from the radiance files that were chosen if the user selected emissivity.

```
    envi_file_query, fix_fid, dims=dims, ns=ns, nl=nl, nb=nb
    envi_doit, 'emittance_calc_doit', data_scale=1, dims=dims, fid=fix_fid, method=1, pos=[0,1,2,3,4],
emissivity_value=0.97, wl_scale=1, r_fid=e_fid, out_name=layer_path + file_basename(fix_img) + '-
e_temp'

    envi_doit, 'envi_mask_apply_doit', dims=dims, fid=e_fid, M_FID=msk1_fid, M_POS=0,
OUT_BNAME=Mask, POS=[0,1,2,3,4], VALUE=0, r_fid=emis1_fid, out_name=layer_path +
file_basename(fix_img) + '-emissivity'

    envi_file_mng, id=e_fid, /remove, /delete

    envi_file_query, adj_fid, dims=dims, ns=ns, nl=nl, nb=nb

    envi_doit, 'emittance_calc_doit', data_scale=1, dims=dims, fid=adj_fid, method=1, pos=[0,1,2,3,4],
emissivity_value=0.97, wl_scale=1, r_fid=e_fid, out_name=layer_path + file_basename(adj_img) + '-
e_temp'

    envi_doit, 'envi_mask_apply_doit', dims=dims, fid=e_fid, M_FID=msk2_fid, M_POS=0,
OUT_BNAME=Mask, POS=[0,1,2,3,4], VALUE=0, r_fid=emis2_fid, out_name=layer_path +
file_basename(adj_img) + '-emissivity'

    envi_file_mng, id=e_fid, /remove, /delete
```

; Set up the dimensions for the combined stack of the two emissivity files.

```
    envi_file_query, emis1_fid, $
    ns=emis1_ns, nl=emis1_nl, nb=emis1_nb
    envi_file_query, emis2_fid, $
    ns=emis2_ns, nl=emis2_nl, nb=emis2_nb

    nb = emis1_nb + emis2_nb
    fid = lonarr(nb)
    pos = lonarr(nb)
    dims = lonarr(5,nb)

    for i=0L,emis1_nb-1 do begin
    fid[i] = emis1_fid
    pos[i] = i
    dims[0,i] = [-1,0,emis1_ns-1,0,emis1_nl-1]
    endfor

    for i=emis1_nb,nb-1 do begin
    fid[i] = emis2_fid
    pos[i] = i-emis1_nb
    dims[0,i] = [-1,0,emis2_ns-1,0,emis2_nl-1]
    endfor
```

; Set projection, pixel size and the data type to floating point.

```
out_proj = envi_get_projection(fid=emis1_fid, pixel_size=out_ps)
out_dt = 4
```

; Call the layer stacking routine. Do not set the exclusive keyword allow for an
; inclusive result. Use cubic convolution for the interpolation method.

```
envi_doit, 'envi_layer_stacking_doit', fid=fid, pos=pos, dims=dims, out_dt=out_dt, interp=0,
out_ps=out_ps, out_proj=out_proj, r_fid=stack1_fid, out_name=layer_path + 'lrg_stack1'
```

; Determine the image overlap area and apply the mask. Delete the large stack image
; to save disk space.

```
envi_file_query, stack1_fid, dims=dims, ns=ns, nl=nl
z_fid = [stack1_fid,stack1_fid]
pos  = [0,5]
exp = 'b1 ne 0 AND b2 ne 0'

envi_doit, 'math_doit', fid=z_fid, pos=pos, dims=dims, exp=exp, r_fid=mskoverlap_fid,
out_name=layer_path + 'lrg_stack1_msk'

envi_doit, 'envi_mask_apply_doit', dims=dims, fid=stack1_fid, M_FID=mskoverlap_fid, M_POS=0,
POS=[0,1,2,3,4,5,6,7,8,9], VALUE=0, r_fid=stack2_fid, out_name= layer_path + 'lrg_stack2'

envi_file_mng, id=stack1_fid, /remove, /delete
```

; Create an ROI from the 'lrg_stack1_msk' file that contains the pixels that
; are overlapping between adj and fix images. From the ROI determine the
; spatial boundary area (new_dims) to subset the overapped area from lrg_stack2.
; Remove the ROI when finished because it takes up a lot of memory.

```
envi_file_query, mskoverlap_fid, dims=dims, ns=ns, nl=nl
data=envi_get_data(fid=mskoverlap_fid,dims=dims,pos=0)
ind = array_indices(data,where(data eq 1))
roi_id = envi_create_roi(ns=ns, nl=nl, name='overlap.roi')
xpts = reform(ind[0,*])
ypts = reform(ind[1,*])
envi_define_roi, roi_id, xpts=xpts, ypts=ypts, /point
envi_roi_compute_spatial_boundry, roi_id, new_dims
print, 'new dims are', new_dims
envi_delete_rois, roi_id
```

; Create the band layers for the temporal stack and the spectral correlation function.

```
envi_doit, 'cf_doit', dims=new_dims, fid=stack2_fid, pos=[0], out_dt=4, $
out_name=layer_path + 'A_' + file_basename(fix_img) + 'Band_10', r_fid=one_fid
envi_doit, 'cf_doit', dims=new_dims, fid=stack2_fid, pos=[1], out_dt=4, $
out_name=layer_path + 'A_' + file_basename(fix_img) + 'Band_11', r_fid=two_fid
envi_doit, 'cf_doit', dims=new_dims, fid=stack2_fid, pos=[2], out_dt=4, $
out_name=layer_path + 'A_' + file_basename(fix_img) + 'Band_12', r_fid=thr_fid
envi_doit, 'cf_doit', dims=new_dims, fid=stack2_fid, pos=[3], out_dt=4, $
out_name=layer_path + 'A_' + file_basename(fix_img) + 'Band_13', r_fid=four_fid
envi_doit, 'cf_doit', dims=new_dims, fid=stack2_fid, pos=[4], out_dt=4, $
out_name=layer_path + 'A_' + file_basename(fix_img) + 'Band_14', r_fid=five_fid
envi_doit, 'cf_doit', dims=new_dims, fid=stack2_fid, pos=[5], out_dt=4, $
```

```
out_name=layer_path + 'B_' + file_basename(adj_img) + 'Band_10', r_fid=six_fid
envi_doit, 'cf_doit', dims=new_dims, fid=stack2_fid, pos=[6], out_dt=4, $
out_name=layer_path + 'B_' + file_basename(adj_img) + 'Band_11', r_fid=sev_fid
envi_doit, 'cf_doit', dims=new_dims, fid=stack2_fid, pos=[7], out_dt=4, $
out_name=layer_path + 'B_' + file_basename(adj_img) + 'Band_12', r_fid=eight_fid
envi_doit, 'cf_doit', dims=new_dims, fid=stack2_fid, pos=[8], out_dt=4, $
out_name=layer_path + 'B_' + file_basename(adj_img) + 'Band_13', r_fid=nine_fid
envi_doit, 'cf_doit', dims=new_dims, fid=stack2_fid, pos=[9], out_dt=4, $
out_name=layer_path + 'B_' + file_basename(adj_img) + 'Band_14', r_fid=ten_fid

envi_file_mng, id=stack2_fid, /remove, /delete
```

; Ask the user if more masks will be used for the correlation mask.

```
base13 = widget_auto_base(title='Include an Additional Mask')
list13 = ['Use Masks','Proceed without Additional Masks']
wm13 = widget_menu(base13,list=list13,uvalue='menu13', /excl, /auto)
result13=auto_wid_mng(base13)
if(result13.accept eq -1) then return
print, 'Menu Selected',result13.menu13

if (result13.menu13 eq 0) then begin
add_msk1=dialog_pickfile(/READ, TITLE='Choose an Additional Mask for the Reference Image')
add_msk2=dialog_pickfile(/READ, TITLE='Add a mask to the Normalization Image')

envi_open_file, add_msk1, r_fid=wtr_msk1
if (wtr_msk1 eq -1) then begin
envi_batch_exit
return
endif

envi_open_file, add_msk2, r_fid=wtr_msk2
if (wtr_msk2 eq -1) then begin
envi_batch_exit
return
endif
```

; Set up the dimensions for the combined stack of the two radiance files.

```
envi_file_query, wtr_msk1, $
ns=wtr_msk1_ns, nl=wtr_msk1_nl, nb=wtr_msk1_nb
envi_file_query, wtr_msk2, $
ns=wtr_msk2_ns, nl=wtr_msk2_nl, nb=wtr_msk2_nb

nb = wtr_msk1_nb + wtr_msk2_nb
fid = lonarr(nb)
pos = lonarr(nb)
dims = lonarr(5,nb)

for i=0L,wtr_msk1_nb-1 do begin
fid[i] = wtr_msk1
pos[i] = i
dims[0,i] = [-1,0,wtr_msk1_ns-1,0,wtr_msk1_nl-1]
endfor

for i=wtr_msk1_nb,nb-1 do begin
```

```
    fid[i] = wtr_msk2
    pos[i] = i-wtr_msk1_nb
    dims[0,i] = [-1,0,wtr_msk2_ns-1,0,wtr_msk2_nl-1]
    endfor
```

; Call the layer stacking routine again. Do not set the exclusive keyword allow for an
; inclusive result. Use nearest neighbor for the interpolation method.

```
    envi_doit, 'envi_layer_stacking_doit', fid=fid, pos=pos, dims=dims, out_dt=out_dt,
out_name=layer_path + 'wtrmsk_stack1', interp=0, out_ps=out_ps, out_proj=out_proj, r_fid=stack3
```

; Determine the image overlap area and apply the mask. Delete the large stack image
; to save disk space.

```
    envi_file_query, stack3, dims=dims, ns=ns, nl=nl
    z_fid = [stack3,stack3]
    pos  = [0,1]
    exp = 'b1*b2'

    envi_doit, 'math_doit', fid=z_fid, pos=pos, dims=dims, exp=exp, r_fid=wtrmsk3, out_name=layer_path
+ 'wtrmsk_stack3'

    envi_file_mng, id=stack3, /remove, /delete
    envi_file_mng, id=wtr_msk1, /remove
    envi_file_mng, id=wtr_msk2, /remove
```

; Subset the mask to match the correlation coefficient files.

```
    envi_doit, 'cf_doit', dims=new_dims, fid=wtrmsk3, pos=[0], out_dt=4, r_fid=wtr_msk,
out_name=layer_path + 'A_' + file_basename(fix_img) + '-B_' + file_basename(adj_img) + '-wtr_msk'

    envi_file_mng, id=wtrmsk3, /remove, /delete

    endif
```

; Calculate the Pearson correlation coefficient image from the overlapping areas.

```
    envi_file_query, one_fid, ns=ns, nl=nl, dims=dims
    z_fid = [one_fid,two_fid,thr_fid,four_fid,five_fid,six_fid,sev_fid,eight_fid,nine_fid,ten_fid]
    pos  = [0,0,0,0,0,0,0,0,0,0]
    exp='((((5)*((b1*b6)+(b2*b7)+(b3*b8)+(b4*b9)+(b5*b10)))-
((b1+b2+b3+b4+b5)*(b6+b7+b8+b9+b10))))

    envi_doit, 'math_doit', fid=z_fid, pos=pos, dims=dims, exp=exp, r_fid=temp1_fid, out_name=layer_path
+ 'temp1'

    envi_file_query, one_fid, ns=ns, nl=nl, dims=dims
    z_fid = [one_fid,two_fid,thr_fid,four_fid,five_fid,six_fid,sev_fid,eight_fid,nine_fid,ten_fid]
    pos  = [0,0,0,0,0,0,0,0,0,0]
    exp='((((sqrt(((5)*((b1^2)+(b2^2)+(b3^2)+(b4^2)+(b5^2)))-
((b1+b2+b3+b4+b5)^2)))*(sqrt(((5)*((b6^2)+(b7^2)+(b8^2)+(b9^2)+(b10^2)))-
((b6+b7+b8+b9+b10)^2)))))'

    envi_doit, 'math_doit', fid=z_fid, pos=pos, dims=dims, exp=exp, r_fid=temp2_fid, out_name=layer_path
+ 'temp2'
```

```
    envi_file_query, one_fid, ns=s, nl=nl, dims=dims
    z_fid = [temp1_fid,temp2_fid]
    exp='(b1/b2)'

    envi_doit, 'math_doit', fid=z_fid, pos=pos, dims=dims, exp=exp, r_fid=corr_fid,  out_name=layer_path +
'A_' + file_basename(fix_img) + '-B_' + file_basename(adj_img) + '-em_corr'

    envi_file_mng, id=temp1_fid, /remove, /delete
    envi_file_mng, id=temp2_fid, /remove, /delete
```

; Create a widget for theuser to enter the correlation threshold.

```
    base8 = widget_auto_base(title='Enter Bandmath Equation for Correlation Threshold')
    ws8 = widget_string(base8, uvalue='str', /auto, default='b1 ge 0.99')
    result8 = auto_wid_mng(base8)
    if (result8.accept eq -1) then return
    print, 'Bandmath Equation for Correlation Threshold is:  ', result8.str
```

; Create the mask for the statistics calculations.

; Mask the correlation file with the additional mask first if masks are being added.

```
    if (result13.menu13 eq 0) then begin

    envi_file_query, corr_fid, dims=dims, ns=ns, nl=nl
    t_fid = [corr_fid,wtr_msk]
    pos  = [0,0]
    exp = 'b1*b2'

    envi_doit, 'math_doit', fid=t_fid, pos=pos, dims=dims, r_fid=mskcorr_fid, exp=exp,
out_name=layer_path + 'msk_temp'

    envi_file_query, mskcorr_fid, dims=dims, ns=ns, nl=nl
    t_fid = [mskcorr_fid]
    pos  = [0]
    exp = result8.str

    envi_doit, 'math_doit', fid=t_fid, pos=pos, dims=dims, r_fid=corrmsk_fid, exp=exp,
out_name=layer_path + 'A_' + file_basename(fix_img) + '-B_' + file_basename(adj_img) + '-rd_corr-msk'

    envi_file_mng, id=mskcorr_fid, /remove, /delete

    endif
```

; Proceed without additional masking if no additional masks were included by the user.

```
    if (result13.menu13 eq 1) then begin

    envi_file_query, corr_fid, dims=dims, ns=ns, nl=nl
    t_fid = [corr_fid]
    pos  = [0]
    exp = result8.str

    envi_doit, 'math_doit', fid=t_fid, pos=pos, dims=dims, r_fid=corrmsk_fid, exp=exp,
out_name=layer_path + 'A_' + file_basename(fix_img) + '-B_' + file_basename(adj_img) + '-rd_corr-msk'
```

```
endif
```

; Clean up the emissivity bands because they are no longer needed here. Proceeding forward with radiance
; mosaicing procedure.

```
envi_file_mng, id=one_fid, /remove, /delete
envi_file_mng, id=two_fid, /remove, /delete
envi_file_mng, id=thr_fid, /remove, /delete
envi_file_mng, id=four_fid, /remove, /delete
envi_file_mng, id=five_fid, /remove, /delete
envi_file_mng, id=six_fid, /remove, /delete
envi_file_mng, id=sev_fid, /remove, /delete
envi_file_mng, id=eight_fid, /remove, /delete
envi_file_mng, id=nine_fid, /remove, /delete
envi_file_mng, id=ten_fid, /remove, /delete
```

; Reset dims. Set up the dimensions for the combined stack of the two radiance files.

```
dims=0

envi_file_query, fix_fid, $
ns=fix_ns, nl=fix_nl, nb=fix_nb
envi_file_query, adj_fid, $
ns=adj_ns, nl=adj_nl, nb=adj_nb

nb = fix_nb + adj_nb
fid = lonarr(nb)
pos = lonarr(nb)
dims = lonarr(5,nb)

for i=0L,fix_nb-1 do begin
fid[i] = fix_fid
pos[i] = i
dims[0,i] = [-1,0,fix_ns-1,0,fix_nl-1]
endfor

for i=fix_nb,nb-1 do begin
fid[i] = adj_fid
pos[i] = i-fix_nb
dims[0,i] = [-1,0,adj_ns-1,0,adj_nl-1]
endfor
```

; Set projection, pixel size and the data type to floating point.

```
out_proj = envi_get_projection(fid=fix_fid, pixel_size=out_ps)
out_dt = 4
```

; Call the layer stacking routine. Do not set the exclusive keyword allow for an
; inclusive result. Use cubic convolution for the interpolation method.

```
envi_doit, 'envi_layer_stacking_doit', fid=fid, pos=pos, dims=dims, out_dt=out_dt, $
out_name=layer_path + 'lrg_stack1', interp=0, out_ps=out_ps, out_proj=out_proj, r_fid=stack1_fid
```

; Determine the image overlap area and apply the mask. Delete the large stack image
; to save disk space.

```
    envi_file_query, stack1_fid, dims=dims, ns=ns, nl=nl
    z_fid = [stack1_fid,stack1_fid]
    pos  = [0,5]
    exp = 'b1 ne 0 AND b2 ne 0'

    envi_doit, 'math_doit', fid=z_fid, pos=pos, dims=dims, exp=exp, r_fid=mskoverlap_fid,
  out_name=layer_path + 'lrg_stack1_msk'

    envi_doit, 'envi_mask_apply_doit', dims=dims, fid=stack1_fid, M_FID=mskoverlap_fid, M_POS=0,
  POS=[0,1,2,3,4,5,6,7,8,9], VALUE=0, r_fid=stack2_fid, out_name= layer_path + 'lrg_stack2'

    envi_file_mng, id=stack1_fid, /remove, /delete
```

; Create an ROI from the 'lrg_stack1_msk' that contains the pixels that
; are overlapping between adj and fix images. From the ROI determine the
; spatial boundary area (new_dims) to subset the overapped area from lrg_stack2.
; Remove the ROI when finished because it may take up a lot of memory.

```
    envi_file_query, mskoverlap_fid, dims=dims, ns=ns, nl=nl
    pos = [0]

    envi_doit, 'ROI_THRESH_DOIT', dims=dims, fid=mskoverlap_fid, MAX_THRESH=100,
  MIN_THRESH=0.00000001, /no_query, $
    pos=pos, roi_id=roi_id, roi_name='overlap.roi', roi_color=5

    envi_roi_compute_spatial_boundry, roi_id, new_dims
    print, 'The overlap dimensions are ', new_dims
    envi_delete_rois, roi_id
```

; Create the band layers for the temporal stack and the spectral correlation function.

```
    envi_doit, 'cf_doit', dims=new_dims, fid=stack2_fid, pos=[0], out_dt=4, $
    out_name=layer_path + 'A_' + file_basename(fix_img) + 'Band_10', r_fid=one_fid
    envi_doit, 'cf_doit', dims=new_dims, fid=stack2_fid, pos=[1], out_dt=4, $
    out_name=layer_path + 'A_' + file_basename(fix_img) + 'Band_11', r_fid=two_fid
    envi_doit, 'cf_doit', dims=new_dims, fid=stack2_fid, pos=[2], out_dt=4, $
    out_name=layer_path + 'A_' + file_basename(fix_img) + 'Band_12', r_fid=thr_fid
    envi_doit, 'cf_doit', dims=new_dims, fid=stack2_fid, pos=[3], out_dt=4, $
    out_name=layer_path + 'A_' + file_basename(fix_img) + 'Band_13', r_fid=four_fid
    envi_doit, 'cf_doit', dims=new_dims, fid=stack2_fid, pos=[4], out_dt=4, $
    out_name=layer_path + 'A_' + file_basename(fix_img) + 'Band_14', r_fid=five_fid
    envi_doit, 'cf_doit', dims=new_dims, fid=stack2_fid, pos=[5], out_dt=4, $
    out_name=layer_path + 'B_' + file_basename(adj_img) + 'Band_10', r_fid=six_fid
    envi_doit, 'cf_doit', dims=new_dims, fid=stack2_fid, pos=[6], out_dt=4, $
    out_name=layer_path + 'B_' + file_basename(adj_img) + 'Band_11', r_fid=sev_fid
    envi_doit, 'cf_doit', dims=new_dims, fid=stack2_fid, pos=[7], out_dt=4, $
    out_name=layer_path + 'B_' + file_basename(adj_img) + 'Band_12', r_fid=eight_fid
    envi_doit, 'cf_doit', dims=new_dims, fid=stack2_fid, pos=[8], out_dt=4, $
    out_name=layer_path + 'B_' + file_basename(adj_img) + 'Band_13', r_fid=nine_fid
    envi_doit, 'cf_doit', dims=new_dims, fid=stack2_fid, pos=[9], out_dt=4, $
    out_name=layer_path + 'B_' + file_basename(adj_img) + 'Band_14', r_fid=ten_fid

    envi_file_mng, id=mskoverlap_fid, /remove, /delete
    envi_file_mng, id=stack2_fid, /remove, /delete
```

; Combine the layers to perform the band-to-band eigendecomposition. Clean up old files.

```
   envi_file_query, corrmsk_fid, dims=dims, ns=ns, nl=nl
   envi_doit, 'cf_doit',
fid=[one_fid,two_fid,thr_fid,four_fid,five_fid,six_fid,sev_fid,eight_fid,nine_fid,ten_fid],out_dt=4, pos =
[0,0,0,0,0,0,0,0,0,0], r_fid=stat1_fid, dims=dims, $
   out_name=layer_path + 'A_' + file_basename(fix_img) + '-B_' + file_basename(adj_img) + '-re_overlap'

   envi_file_mng, id=one_fid, /remove, /delete
   envi_file_mng, id=two_fid, /remove, /delete
   envi_file_mng, id=thr_fid, /remove, /delete
   envi_file_mng, id=four_fid, /remove, /delete
   envi_file_mng, id=five_fid, /remove, /delete
   envi_file_mng, id=six_fid, /remove, /delete
   envi_file_mng, id=sev_fid, /remove, /delete
   envi_file_mng, id=eight_fid, /remove, /delete
   envi_file_mng, id=nine_fid, /remove, /delete
   envi_file_mng, id=ten_fid, /remove, /delete
```

; Calculate Statistics. B_Band_10 -> *B_Band_10.

```
   ENVI_DOIT, 'ENVI_STATS_DOIT', COMP_FLAG=4, fid=stat1_fid, cov=cov10, dims=dims,
evec=evec10, /interrupt, m_fid=corrmsk_fid,   m_pos=[0], mean=mean10, pos=[0,5], PREC=[16,0],
REPORT_FLAG=1 AND 4, REP_NAME=stats_10
```

; Calculate Statistics. B_Band_11 -> *B_Band_11.

```
   ENVI_DOIT, 'ENVI_STATS_DOIT', COMP_FLAG=4, fid=stat1_fid, cov=cov11, dims=dims,
evec=evec11, /interrupt, m_fid=corrmsk_fid, m_pos=[0], mean=mean11, pos=[1,6], PREC=[16,0],
REPORT_FLAG=1 AND 4, REP_NAME=stats_11
```

; Calculate Statistics. B_Band_12 -> *B_Band_12.

```
   ENVI_DOIT, 'ENVI_STATS_DOIT', COMP_FLAG=4, fid=stat1_fid, cov=cov12, dims=dims,
evec=evec12, /interrupt, m_fid=corrmsk_fid, m_pos=[0], mean=mean12, pos=[2,7], PREC=[16,0],
REPORT_FLAG=1 AND 4, REP_NAME=stats_12
```

; Calculate Statistics. B_Band_13 -> *B_Band_13.

```
   ENVI_DOIT, 'ENVI_STATS_DOIT', COMP_FLAG=4, fid=stat1_fid, cov=cov13, dims=dims,
evec=evec13, /interrupt, m_fid=corrmsk_fid, m_pos=[0], mean=mean13, pos=[3,8], PREC=[16,0],
REPORT_FLAG=1 AND 4, REP_NAME=stats_13
```

; Calculate Statistics. B_Band_14 -> *B_Band_14.

```
   ENVI_DOIT, 'ENVI_STATS_DOIT', COMP_FLAG=4, fid=stat1_fid, cov=cov14, dims=dims,
evec=evec14, /interrupt, m_fid=corrmsk_fid, m_pos=[0], mean=mean14, pos=[4,9], PREC=[16,0],
REPORT_FLAG=1 AND 4, REP_NAME=stats_14
```

; Calculate gain and offsets.

```
   gain10=evec10[0]/evec10[1]
   gain11=evec11[0]/evec11[1]
   gain12=evec12[0]/evec12[1]
   gain13=evec13[0]/evec13[1]
   gain14=evec14[0]/evec14[1]
   offset10=mean10[0]-gain10*mean10[1]
```

```
    offset11=mean11[0]-gain11*mean11[1]
    offset12=mean12[0]-gain12*mean12[1]
    offset13=mean13[0]-gain13*mean13[1]
    offset14=mean14[0]-gain14*mean14[1]
    print, gain10, offset10
    print, gain11, offset11
    print, gain12, offset12
    print, gain13, offset13
    print, gain14, offset14
```

; Clean up files.

```
    envi_file_mng, id=corr_fid, /remove
    envi_file_mng, id=corrmsk_fid, /remove
    envi_file_mng, id=stat1_fid, /remove
```

; Set number format.

```
    precision16format= '(D24.16)'
```

; Create the balancing equations and save them as functions for later reference.

; Define and apply the balancing equation to band 10.

```
    envi_file_query, adj_fid, dims=dims, ns=ns, nl=nl, nb=nb
    adj10_fid = [adj_fid]
    pos  = [0]
    exp=string(gain10, FORMAT=precision16format)+'*b10+('+string(offset10,
  format=precision16format)+')'
    envi_doit, 'math_doit', fid=adj10_fid, pos=pos, dims=dims, exp=exp, r_fid=adjd10_fid, $
    out_name=layer_path + 'B_' + file_basename(adj_img) + 'Band_10'

    bm_tir10 = layer_path + 'B_' + file_basename(adj_img) + '-erd_bmb10.pro'
    openw,10,bm_tir10
    writeu,10,'FUNCTION bm_tir10, b10'
    writeu,10,string(13b)
    writeu,10,'tirb10 = '
    writeu,10,exp
    writeu,10,string(13b)
    writeu,10,'RETURN, tirb10'
    writeu,10,string(13b)
    writeu,10,'END'
    close,10
    print, 'Normalization Equation for Band 10: ', exp
```

; Define and apply the balancing equation to band 11.

```
    envi_file_query, adj_fid, dims=dims, ns=ns, nl=nl, nb=nb
    adj11_fid = [adj_fid]
    pos  = [1]
    exp=string(gain11, FORMAT=precision16format)+'*b11+('+string(offset11,
  format=precision16format)+')'
    envi_doit, 'math_doit', fid=adj11_fid, pos=pos, dims=dims, exp=exp, r_fid=adjd11_fid, $
    out_name=layer_path + 'B_' + file_basename(adj_img) + 'Band_11'

    bm_tir11 = layer_path + 'B_' + file_basename(adj_img) + '-erd_bmb11.pro'
```

```
    openw,11,bm_tir11
    writeu,11,'FUNCTION bm_tir11, b11'
    writeu,11,string(13b)
    writeu,11,'tirb11 = '
    writeu,11,exp
    writeu,11,string(13b)
    writeu,11,'RETURN, tirb11'
    writeu,11,string(13b)
    writeu,11,'END'
    close,11
    print, 'Normalization Equation for Band 11: ', exp
```

; Define and apply the balancing equation to band 12.

```
    envi_file_query, adj_fid, dims=dims, ns=ns, nl=nl, nb=nb
    adj12_fid = [adj_fid]
    pos  = [2]
    exp=string(gain12, FORMAT=precision16format)+'*b12+('+string(offset12,
  format=precision16format)+')'
    envi_doit, 'math_doit', fid=adj12_fid, pos=pos, dims=dims, exp=exp, r_fid=adjd12_fid, $
    out_name=layer_path + 'B_' + file_basename(adj_img) + 'Band_12'

    bm_tir12 = layer_path + 'B_' + file_basename(adj_img) + '-erd_bmb12.pro'
    openw,12,bm_tir12
    writeu,12,'FUNCTION bm_tir12, b12'
    writeu,12,string(13b)
    writeu,12,'tirb12 = '
    writeu,12,exp
    writeu,12,string(13b)
    writeu,12,'RETURN, tirb12'
    writeu,12,string(13b)
    writeu,12,'END'
    close,12
    print, 'Normalization Equation for Band 12: ', exp
```

; Define and apply the balancing equation to band 13.

```
    envi_file_query, adj_fid, dims=dims, ns=ns, nl=nl, nb=nb
    adj13_fid = [adj_fid]
    pos  = [3]
    exp=string(gain13, FORMAT=precision16format)+'*b13+('+string(offset13,
  format=precision16format)+')'
    envi_doit, 'math_doit', fid=adj13_fid, pos=pos, dims=dims, exp=exp, r_fid=adjd13_fid, $
    out_name=layer_path + 'B_' + file_basename(adj_img) + 'Band_13'

    bm_tir13 = layer_path + 'B_' + file_basename(adj_img) + '-erd_bmb13.pro'
    openw,13,bm_tir13
    writeu,13,'FUNCTION bm_tir13, b13'
    writeu,13,string(13b)
    writeu,13,'tirb13 = '
    writeu,13,exp
    writeu,13,string(13b)
    writeu,13,'RETURN, tirb13'
    writeu,13,string(13b)
    writeu,13,'END'
    close,13
```

```
    print, 'Normalization Equation for Band 13: ', exp
```

; Define and apply the balancing equation to band 14.

```
    envi_file_query, adj_fid, dims=dims, ns=ns, nl=nl, nb=nb
    adj14_fid = [adj_fid]
    pos  = [4]
    exp=string(gain14, FORMAT=precision16format)+'*b14+('+string(offset14,
format=precision16format)+')'
    envi_doit, 'math_doit', fid=adj14_fid, pos=pos, dims=dims, exp=exp, r_fid=adjd14_fid, $
    out_name=layer_path + 'B_' + file_basename(adj_img) + 'Band_14'

    bm_tir14 = layer_path + 'B_' + file_basename(adj_img) + '-erd_bmb14.pro'
    openw,14,bm_tir14
    writeu,14,'FUNCTION bm_tir14, b14'
    writeu,14,string(13b)
    writeu,14,'tirb14 = '
    writeu,14,exp
    writeu,14,string(13b)
    writeu,14,'RETURN, tirb14'
    writeu,14,string(13b)
    writeu,14,'END'
    close,14
    print, 'Normalization Equation for Band 14: ', exp
```

; Recombine the scaled radiance files. Clean up layers.

```
    fid_array = [adjd10_fid,adjd11_fid,adjd12_fid,adjd13_fid,adjd14_fid]

    envi_doit, 'cf_doit', fid=fid_array, pos=[0,0,0,0,0], dims=dims, wavelength_unit=0, r_fid=rn_fid, $
    out_name=layer_path + file_basename(adj_img) + '-rd_temp'

    envi_file_mng, id=adjd10_fid, /remove, /delete
    envi_file_mng, id=adjd11_fid, /remove, /delete
    envi_file_mng, id=adjd12_fid, /remove, /delete
    envi_file_mng, id=adjd13_fid, /remove, /delete
    envi_file_mng, id=adjd14_fid, /remove, /delete
```

; Apply the mask to the balanced file.

```
    envi_doit, 'envi_mask_apply_doit', dims=dims, fid=rn_fid, M_FID=msk2_fid, M_POS=0,
OUT_BNAME=Mask,     POS=[0,1,2,3,4], VALUE=0, r_fid=rn2_fid, out_name= layer_path +
file_basename(adj_img) + '-em_norm'

    envi_file_query, adj_fid, file_type=file_type, dims=dims, ns=ns, nl=nl, nb=nb
    map_info=envi_get_map_info(fid=adj_fid)
    ast_bnames= ['Mos. Normalized ASTER TIR Band 10','Mos. Normalized ASTER TIR Band 11','Mos.
Normalized ASTER TIR Band 12','Mos. Normalized ASTER TIR Band 13','Mos. Normalized ASTER TIR
Band 14']

WL=[8.2910,8.6340,9.0750,10.6570,11.3180]

    envi_setup_head, bnames=ast_bnames, data_ignore_value=0, data_type=4, file_type=file_type, ns=ns,
nl=nl,     nb=nb, interleave=0, WL=WL, wavelength_unit=0, r_fid=out_fid, /WRITE, map_info=map_info,
fname = layer_path + file_basename(adj_img) + '-em_norm', descrip = ['Normalized Thermal Radiance
Using Bi-temporal Emissivity Statistics']
```

; Clean up and open the resulting normalized radiance file.

```
envi_file_mng, id=rn_fid, /remove, /delete
envi_file_mng, id=rn2_fid, /remove
envi_file_mng, id=msk1_fid, /remove
envi_file_mng, id=msk2_fid, /remove
fname = layer_path + file_basename(adj_img) + '-em_norm'
envi_open_file, fname, r_fid=norm_fid
envi_file_mng, id=adj_fid, /remove

end
```

APPENDIX B

B.1 DERIVATION OF THE WIND THRESHOLD VELOCITY RATIO FROM APPARENT THERMAL INERTIA

Apparent thermal inertia was calculated using the following wrote written in the Interactive Data Language (IDL). This reproduces the calculation of thermal inertia according to *Xu and Cracknell* [1995], modified here to adjust for the day time maximum temperature according to *Cai et al.* [2005]. The input data are ENVI standard files that must have the same pixel dimensions, geographic coverage, and be accurately coregistered. The input data files are: day time temperature, night time temperature, broadband albedo calculated according to *Liang* [2000] and a 2D array of latitude values, where each pixel value is equal to the latitude in decimal degrees. The output of the algorithm is thermal inertia, whereby bandmath equations (not shown here) are used to calculate soil moisture according a empirical relationship [see *Ma and Xu* [1990]; from soil moisture to the WTR parameterization given by *Fécan et al.* [1999].

B.2 THERMAL INERTIA CALCULATION VERSION 1.0

```
; IDL Code for Thermal Inertia Calculation
; ************************************************************************
; THERMAL INERTIA CALCULATION VERSION 1.0
; ati_calc, v1.0, 11/12/2008
; ************************************************************************
; IDL code written by Stephen Paul Scheidt
; email (sscheidt77@gmail.com)
; ************************************************************************

; Code initialization.

        pro ati_calc, event
        compile_opt idl2
        envi, /restore_base_save_files
        envi_batch_init, log_file='ati_batch.txt'

; Create a widget to start with MODIS data or ASTER data.

        base1 = widget_auto_base(title='Instrument')
        list1 = ['ASTER','MODIS']
        wm1 = widget_menu(base1,list=list1,uvalue='menu1', /excl, /auto)
        result1=auto_wid_mng(base1)
        if(result1.accept eq -1) then return

; For ASTER data:
; Select the image data for processing.  These files include the latitude,
; temperature (day and night), and albedo images. These files must be premade
; by the user for this version of the code.  Each image file must have the
; same dimensions, pixel size and be accurately coregistered. Temperature images
; are created by using the emissivity normalization and extracting the temperature
; images for day and night, no more than 36 hours apart in this study. Albedo data
; are calculated using the equations of Liang 2000.  Latitude is a separate data
; plane extracted from MODIS data, whereas for ASTER data, this data has to be
; created so that each pixel value = latitude of pixel.

        if(result1.menu1 eq 0) then begin

        night_img=dialog_pickfile(/READ, GET_PATH=layer_path, TITLE='Choose the nighttime temperature
      image')
        day_img=dialog_pickfile(/READ, GET_PATH=layer_path, TITLE='Choose the daytime temperature
      image')
        lat_img=dialog_pickfile(/READ, TITLE='Choose the latitude image')
        alb_img=dialog_pickfile(/READ, TITLE='Choose the day overpass albedo image')

; Enter parameters for the ATI processing.

        TLB = WIDGET_AUTO_BASE(title='Enter Parameters for ATI')

        row_base1 = WIDGET_BASE(TLB, /row)

        p1 = WIDGET_PARAM(row_base1, /auto_manage, dt=4, default='1367', $
```

```
field=2, prompt='Enter the solar constant in watts/sq meter', uvalue='p1')

row_base2 = WIDGET_BASE(TLB, /row)

p2 = WIDGET_PARAM(row_base2, /auto_manage, dt=4, default='365', $
field=2, prompt='Enter the calendar DAY of daytime overpass', uvalue='p2')

row_base3 = widget_base(TLB, /row)

p3 = WIDGET_PARAM(row_base3, /auto_manage, dt=4, default='11.0', $
field=2, prompt='Enter the TIME of daytime overpass (units=hours)', uvalue='p3')

row_base4 = widget_base(TLB, /row)

p4 = WIDGET_PARAM(row_base4, /auto_manage, dt=4, default='22.0', $
field=2, prompt='Enter the TIME of the nighttime overpass (units=hours)', uvalue='p4')

row_base5 = widget_base(TLB, /row)

p5 = WIDGET_PARAM(row_base5, /auto_manage, dt=4, default='14.0', $
field=2, prompt='Enter the TIME of maximum daily temperature (units=hours)', uvalue='p5')

row_base6 = widget_base(TLB, /row)

p6 = WIDGET_PARAM(row_base6, /auto_manage, dt=4, default='0.75', $
field=2, prompt='Enter the average atmospheric transmissivity', uvalue='p6')

result=AUTO_WID_MNG(TLB)

print, result.p1
print, result.p2
print, result.p3
print, result.p4
print, result.p5
print, result.p6
```

; Open files.

```
envi_open_file, lat_img, r_fid=lat_fid
if (lat_fid eq -1) then begin
envi_batch_exit
return
endif

envi_open_file, alb_img, r_fid=alb_fid
if (alb_fid eq -1) then begin
envi_batch_exit
return
endif

envi_open_file, night_img, r_fid=night_fid
if (night_fid eq -1) then begin
envi_batch_exit
return
endif
```

```
envi_open_file, day_img, r_fid=day_fid
if (day_fid eq -1) then begin
envi_batch_exit
return
endif
```

; Calculate ATI value.

```
envi_file_query, day_fid, dims=dims, ns=ns, nl=nl
t_fid = [alb_fid,day_fid,night_fid]
pos  = [0,0,0]
exp = 'float((1-b1)/(b2-b3))'

envi_doit, 'math_doit', fid=t_fid, pos=pos, dims=dims, exp=exp, r_fid=ati_fid, $
out_name=layer_path + 'ati'
```

; Calculate T1-T2.

```
envi_file_query, day_fid, dims=dims, ns=ns, nl=nl
t_fid = [day_fid,night_fid]
pos  = [0,0]
exp = 'float(b1-b2)'

envi_doit, 'math_doit', fid=t_fid, pos=pos, dims=dims, exp=exp, r_fid=t1t2_fid, $
out_name=layer_path + 'T1-T2'
```

; Subset the latitude file for the area needed.
; Set up the dimensions for the combined stack of the two files.
; Set projection, pixel size and the data type to floating point.

```
envi_file_query, ati_fid, $
ns=ati_ns, nl=ati_nl, nb=ati_nb
envi_file_query, lat_fid, $
ns=lat_ns, nl=lat_nl, nb=lat_nb

nb = ati_nb + lat_nb
fid = lonarr(nb)
pos = lonarr(nb)
dims = lonarr(5,nb)

for i=0L,ati_nb-1 do begin
fid[i] = ati_fid
pos[i] = i
dims[0,i] = [-1,0,ati_ns-1,0,ati_nl-1]
endfor

for i=ati_nb,nb-1 do begin
fid[i] = lat_fid
pos[i] = i-ati_nb
dims[0,i] = [-1,0,lat_ns-1,0,lat_nl-1]
endfor

out_proj = envi_get_projection(fid=ati_fid, pixel_size=out_ps)
out_dt = 4
```

; Call the layer stacking routine. Set the exclusive keyword to subset the latitude values

```
; Use cubic convolution for the interpolation method.

    envi_doit, 'envi_layer_stacking_doit', fid=fid, pos=pos, /exclusive, dims=dims, out_dt=out_dt, interp=0,
$
    out_ps=out_ps, r_fid=stack1_fid, out_proj=out_proj, out_name=layer_path + 'lat_pre_subset'

    envi_file_query, stack1_fid, ns=ns, nl=nl, nb=nb, dims=dims

    envi_doit, 'cf_doit', dims=dims, out_dt=out_dt, fid=stack1_fid, out_bname='Latitude', $
    pos=[1], r_fid=lat2_fid, out_name=layer_path + 'lat_temp'

    envi_file_mng, id=stack1_fid, /remove, /delete


; Determine the equation for the solar declination.  Call a widget, enter the default bandmath
; equation.  User must enter the Julian calendar day in place of the DAY text.
; result.p1 -solar constant
; result.p2 -calender day
; result.p3 -day time
; result.p4 -night time
; result.p5 -maximum daily temp

    declination = double((-23.45)*(cos(0.0174532925*((360.0/365.0)*(result.p2 + 10.0)))))
    print, declination
    dec1 = double(declination)
    dec2 = (dec1 * 0.0174532925)
    dec3 = string(dec2)
    print, dec3

    pi = double(3.14159265358979323846264338327 95)

; Convert latitude to radian value.

    envi_file_query, lat2_fid, dims=dims, ns=ns, nl=nl
    t_fid = [lat2_fid]
    pos  = [0]
    exp = 'b1 * 0.0174532925'

    envi_doit, 'math_doit', fid=t_fid, pos=pos, dims=dims, r_fid=lat3_fid, exp=exp, $
    out_name=layer_path + 'latitude_subset'

    envi_file_mng, id=lat2_fid, /remove, /delete

; Calculate psi.

    envi_file_query, lat3_fid, dims=dims, ns=ns, nl=nl
    t_fid = [lat3_fid]
    pos = [0]
    exp = 'float(acos((tan('+dec3+'))*(tan(b1))))'

    envi_doit, 'math_doit', fid=t_fid, pos=pos, dims=dims, r_fid=psi_fid, exp=exp, $
    out_name=layer_path + 'psi'

; Calculate first Fourier-Series Cofficient.

  str_pi = string(pi)
```

```
   envi_file_query, psi_fid, dims=dims, ns=ns, nl=nl
   t_fid =[lat3_fid,psi_fid]
   pos = [0,0]
   exp=
'(float((2/'+str_pi+')*(sin('+dec3+'))*(sin(b1)))+((1/(2*'+str_pi+'))*(cos('+dec3+'))*(cos(b1))*((sin(2*b2))+
(2*(b2)))))'
   print, exp
   envi_doit, 'math_doit', fid=t_fid, pos=pos, dims=dims, r_fid=A1_fid, exp=exp, out_name=layer_path +
'Fourier1'
```

; Calculate second Fourier-Series Cofficient.

```
   envi_file_query, psi_fid, dims=dims, ns=ns, nl=nl
   t_fid =[lat3_fid,psi_fid]
   pos = [0,0]
   exp=
'float((((2*sin('+dec3+')*sin(b1))/(2*'+str_pi+'))*sin(2*b2))+((2*cos('+dec3+')*cos(b1))/(3*'+str_pi+'))*((2
*sin(2*b2)*cos(b2))-(cos(2*b2)*sin(b2))))'
   print, exp
   envi_doit, 'math_doit', fid=t_fid, pos=pos, dims=dims, r_fid=A2_fid, exp=exp, out_name=layer_path +
'Fourier2'
```

; Calculate time variables

```
   T = 24.0
   print, T

   w_hr = (2*pi)/T
   print, w_hr

   w_s = w_hr/3600
   print, w_s

   sqrt_w = sqrt(w_s)
   print, sqrt_w

   w_tmax = result.p5 * w_hr
   print, w_tmax

   b = (tan(w_tmax))/(1-(tan(w_tmax)))
   print, b

   del1 = atan(b/(1+b))
   print, del1

   del2 = atan((b*(sqrt(2)))/(1+(b*(sqrt(2)))))
   print, del2

   wt1 = (result.p3 * w_hr)
   print, wt1

   wt2 = (result.p4 * w_hr)
   print, wt2

   A1_t = -2*(SIN(((wt2 - del1)+(wt1 - del1))/2))*(SIN(((wt2 - del1)-(wt1 - del1))/2))
```

```
print, A1_t

A1_d = sqrt(1+(1/b)+(1/(2*(b^2))))
print, A1_d

A2_t = -2*(SIN(((wt2 - del2)+(wt1- del2))/2))*(SIN(((wt2 - del2)-(wt1- del2))/2))
print, A2_t

A2_d = sqrt(2+((sqrt(2))/b)+(1/(2*(b^2))))
print, A2_d

N1 = A1_t/A1_d
print, N1
N1a = string(N1)

N2 = A2_t/A2_d
print, N2
N2a = string(N2)
```

; Combine and scale Fourier series with time variables.

```
envi_file_query, A1_fid, dims=dims, ns=ns, nl=nl
t_fid =[A1_fid,A2_fid]
pos = [0,0]
exp = 'float((b1*'+N1a+')+(b2*'+N2a+'))'
print, exp
envi_doit, 'math_doit', fid=t_fid, pos=pos, dims=dims, r_fid=NC_fid, exp=exp, out_name=layer_path +
'NC'
```

; Calculate P (Xue and Cracknell 1995; Cai et al. 2005).
; Average atmospheric transmissivity Ct = 0.75.

```
Ct = result.p6
So = result.p1
term1 = float((Ct*So)/(sqrt_w))
print, term1
term2 = string(term1)

envi_file_query, NC_fid, dims=dims, ns=ns, nl=nl
t_fid =[ati_fid,NC_fid]
pos = [0,0]
exp = 'float('+term2+'*b1*b2)'
print, exp
envi_doit, 'math_doit', fid=t_fid, pos=pos, dims=dims, r_fid=P_fid, exp=exp, out_name=layer_path + 'P'
```

; Calculate P using Tmax and Tmin. The following are calculations
; for parts of the larger equation for P.

; adj_wt1, adj_wt2

```
adj_wt1 = (14.0 - result.p3) * w_hr
adj_wt2 = (result.p4 - 14.0) * w_hr
wtmin = (12) * w_hr

print, adj_wt1
print, adj_wt2
```

```
print, wtmin
```

; cos(wt1)-cos(wt2)

```
time_d = -2*(SIN((adj_wt1+adj_wt2)/2))*(SIN((adj_wt1-adj_wt2)/2))
print, time_d
```

; cos(wtmax)-cos(wt1)

```
max_n = -2*(SIN((0+adj_wt1)/2))*(SIN((0-adj_wt1)/2))
print, max_n
```

; cos(wtmin)-cos(wt2)

```
min_n = -2*(SIN((wtmin+adj_wt2)/2))*(SIN((wtmin-adj_wt2)/2))
print, min_n
```

; Calculate time scaling factors to estimate tmax and tmin.

```
tmax_adj = max_n/time_d
print, tmax_adj
tmax_adj2 = string(tmax_adj)

tmin_adj = min_n/time_d
print, tmin_adj
tmin_adj2 = string(tmin_adj)
```

; Calculate deltaT from Tmax and Tmin.

```
envi_file_query, day_fid, dims=dims, ns=ns, nl=nl
t_fid = [day_fid,t1t2_fid]
pos  = [0,0]
exp = 'float((b1)+(b2*('+tmax_adj2+')))'

envi_doit, 'math_doit', fid=t_fid, pos=pos, dims=dims, exp=exp, r_fid=Tmax_fid, $
out_name=layer_path + 'Tmax'

envi_file_query, night_fid, dims=dims, ns=ns, nl=nl
t_fid = [night_fid,t1t2_fid]
pos  = [0,0]
exp = 'float((b1)+(b2*('+tmin_adj2+')))'

envi_doit, 'math_doit', fid=t_fid, pos=pos, dims=dims, exp=exp, r_fid=Tmin_fid, $
out_name=layer_path + 'Tmin'

envi_file_query, Tmax_fid, dims=dims, ns=ns, nl=nl
t_fid = [Tmax_fid,tmin_fid]
pos  = [0,0]
exp = 'float(b1-b2)'

envi_doit, 'math_doit', fid=t_fid, pos=pos, dims=dims, exp=exp, r_fid=deltaT_fid, $
out_name=layer_path + 'deltaT'
```

; Calculate ATI value again with new deltaT.

```
envi_file_query, deltaT_fid, dims=dims, ns=ns, nl=nl
```

```
   t_fid = [alb_fid,deltaT_fid]
   pos  = [0,0,0]
   exp = 'float((1-b1)/(b2))'

   envi_doit, 'math_doit', fid=t_fid, pos=pos, dims=dims, exp=exp, r_fid=ati2_fid, $
   out_name=layer_path + 'ati-adjusted'

   ; Calculate new P values using the new ATI value.

   envi_file_query, NC_fid, dims=dims, ns=ns, nl=nl
   t_fid =[ati2_fid,NC_fid]
   pos = [0,0]
   exp = 'float('+term2+'*b1*b2)'
   print, exp
   envi_doit, 'math_doit', fid=t_fid, pos=pos, dims=dims, r_fid=P2_fid, exp=exp, out_name=layer_path +
'P-adjusted'

   endif
   end
```

BIBLIOGRAPHY

Abrams, M. (2000), The Advanced Spaceborne Thermal Emission And Reflectance Radiometer (ASTER): Data products for the high spatial resolution imager on NASA's Terra platform, Int. J. Remote Sens., 21(5), 847–859, doi:10.1080/014311600210326.

Acker, J.G. and G. Leptoukh (2007), Online Analysis Enhances Use of NASA Earth Science Data, Eos, Trans. AGU, 88, 2, 14-17.

Allan, R.P., M.A. Ringer, J.A. Pamment, and A. Slingo (2004), Simulation of the Earth's radiation budget by the European Centre for Medium-Range Weather Forecasts 40-year reanalysis (ERA40), J. Geophys. Res., 109, D18107.

Alley, R.E. (1996), Algorithm theoretical basis document for decorrelation stretch, version 2.2. JPL Publication ATBD-AST-06, 19 p.

Allmendinger, R.J. (1972), Hydrologic control over the origin of gypsum at Lake Lucero, White Sands National Monument, New Mexico, M.S. thesis, 182 pp., New Mexico Institute of Mining and Technology, Socorro, New Mexico.

Allmendinger, R.J., and F.B. Titus (1973), Regional hydrology and evaporative discharge as a present-day source of gypsum at White Sands National Monument, New Mexico, New Mexico Bureau Mines and Mineral Resources Open-File Report OF-55, 53 pp., Socorro, New Mexico.

Alpert P., P. Kishcha, A. Shtivelman, S.O. Krichak, and J.H. Joseph (2005), Vertical distribution of Saharan dust based on 2.4 year model predictions, Atmospheric Research 70, 2, p. 109-130.

Aumann, H. H., M.T. Chahine, C. Gautier, M.D. Goldberg, E. Kalnay, L.M. McMillin, H. Revercomb, P.W. Rosenkranz, W.L. Smith, D.H. Staelin, L.L. Strow and J. Susskind (2003), AIRS/AMSU/HSB on the Aqua mission: Design, science objectives, data products and processing systems, IEEE Trans. Geosci. Rem. Sens., 41, 2, 253–264.

Ballantine, J.C., G.S. Okin, D.E. Prentiss and D.A. Roberts (2005), Mapping North Africa landforms using continental scale unmixing of MODIS imagery. Remote Sensing of Environment, 97, 470 – 483.

Bandfield, J. L., V.E. Hamilton and P.R. Christensen (2000), A global view of Martian surface compositions from MGS-TES. Science, 287(5458), 1626–1630.

Bandfield, J.L., K.S. Edgett and P.R Christensen (2002), Spectroscopic study of the Moses Lake dune field, Washington: Determination of compositional distributions and source lithologies, J. Geophys. Res.107, E11, 5092, doi:10.1029/2000JE001469.

Bandfield, J.L., P.R. Christensen and M.D. Smith (2000), Spectral data set factor analysis and end-member recovery: Application to analysis of Martian atmospheric particles, J. Geophys. Res.105, E4, 9573-9587.

Basart, S. C. Perez, E. Cuevas and J.M. Baldasano (2009), Verification of a SDS forecast model for North Africa, Europe and Middle East with AERONET data, ESA/WMO Expert Consultation Meeting For Development of Satellite Products Relevant to the WMO SDS-WAS Barcelona, Spain, September 8-9.

Bellouin, N., O. Boucher, J. Haywood, and M.S. Reddy (2005), Global estimate of aerosol direct radiative forcing from satellite measurements, Nature, 438, 1138 – 1141, doi:10.1038/nature04348.

Beveridge, C.A., G. Kocurek, R. Ewing, R., N. Lancaster, P. Morthekai, A.K. Singhvi and S.A. Mahan (2006), Development of spatially diverse and complex dune-field patterns: Gran Desierto Dune Field, Sonora, Mexico, Sedimentology, 53(6), 1391-1409.

Bindlish, R., T.J. Jackson, A.J. Gasiewski, M. Klein, and E. Njoku (2006), Soil moisture mapping and AMSR-E validation using the PSR in SMEX02, Remote Sens. Environ., 103(2), 127-139, doi:10.1016/j.rse.2005.02.003.

Bindlish, R., T.J. Jackson, E.Wood, H. Gao, P. Starks, D. Bosch, and V. Lakshmi (2003), Soil moisture estimates from TRMM Microwave Imager observations over the Southern United States, Rem. Sens. Environ., 85, 507-515, doi:10.1016/S0034-4257(03)00052-X.

Blount, G. (1988), Regional Aeolian Dynamics from remote sensing: Origin of the Gran Desierto, Sonora, Mexico. Dissertation, Arizona State University, 226p.

Blount, G. and N. Lancaster (1990), Development of the Gran Desierto sand sea, northwestern Mexico, Geology, 18, 724-728.

Blount, G., M.O. Smith, J.B. Adams, R. Greeley, and P.R. Christensen (1990), Regional aeolian dynamics and sand mixing in the Gran Desierto: evidence from Landsat Thematic Mapper images. J. Geophys. Res., 95, 15463-15482.

Byrnes, J.M., Ramsey, M.S., King, P.L., and R. J. Lee (2007), Thermal infrared reflectance and emission spectroscopy of quartzofeldspathic glasses, Geophys. Res. Let., 34, L01306, doi:10.1029/ 2006GL027893.

Cai, G. J. Wu, Y. Xue, Y. Hu, J. Guo, and J. Tang (2005), Soil moisture retrieval from MODIS data in northern china plain using thermal inertia model (SoA-TI), Geoscience and Remote Sensing Symposium, 2005, IGARSS '05, Proceedings, 2005 IEEE International, vol. 6, 25-29 July 2005, 4501-4504.

Cai, G., J. Wu, Y. Xue, W. Wan, and X. Huang (2007b), Oil spill detection from thermal anomaly using ASTER data in Yinggehai of Hainan, China, Geoscience and Remote Sensing Symposium, 2007, IGARSS 2007, IEEE International, 23-28 July 2007, 898-900.

Cai, G., Y. Cue, Y. Hu, Y. Wang, J. Guo, Y. Luo, C. Wu, S. Zhong, and S. Qi (2007a), Soil moisture retrieval from MODIS data in Northern China Plain using thermal inertia model, Int. J. Remote Sens, 28(16), 3567-3581, doi:10.1080/01431160601034886.

Carn, S., L. Strow, S. DeSouza-Machado, Y. Edmonds, and S. Hannon (2005), Quantifying tropospheric volcanic eruptions with AIRS : the 2002 eruption of Mt. Etna (Italy), GRL, 32, L02,301.

Canty, M.J., A.A. Nielsen, and M. Schmidt, (2004), Automatic radiometric normalization of multitemporal satellite imagery. Rem. Sens. Environ., 91(3-4), 441-451.

Chepil, W.S. (1956), Influence of moisture on erodibility of soil by wind, Proc. Soil Sci. Soc. Am., 20, 288-292.

Christensen, P. R., J. L. Bandfield, M. D. Smith, V. E. Hamilton, and R. N. Clark (2000), Identification of a basaltic component on the Martian surface from Thermal Emission Spectrometer data, J. Geophys. Res., 105, 9609–9621.

Christensen, P.R., B.M. Jakosky, H.H. Kieffer, M.C. Malin, H.Y. McSween, Jr., K. Nealson, G.L. Mehall, S.H. Silverman, S. Ferry, M. Caplinger, and M. Ravine (2004), The Thermal Emission Imaging System (THEMIS) for the Mars 2001 Odyssey Mission, Space Science Reviews, 110, 85-130.

Christensen, P.R., J.L. Bandfield, V.E. Hamilton, S.W. Ruff, G.L. Mehall, N. Gorelick, K. Bender, K. Murray, H.H. Kieffer, and N.T. Titus, (2001), Mars Global Surveyor Thermal Emission Spectrometer experiment: Investigation description and surface science results, J. Geophys. Res., 106(E10), 23,823– 23,871.

Christopher, S.A. and T. Jones, T. (2008), Dust radiative effects over global oceans, IEEE Trans. Geosci. Rem. Sens., 5, 1, 4pp.

Christopher, S.A. and T. Jones (2007), Satellite-based assessment of cloud-free net radiative effect of dust aerosols over the Atlantic Ocean, Geophys. Res. Lett., 34, L02810, doi:10.2006GL027783.

Clark, R.N., T.V.V. King, M. Klejwa, and G.A Swayze, (1990), High spectral resolution reflectance spectroscopy of minerals, J. Geophys. Res., 95(B8), 12653 – 12680.

Colleta, B., and L. Ortlieb (1984), Deformations of middle and late Pleistocene deltaic deposits at the mouth of the Rio Colorado, northwestern Gulf of California. In Malpica-Cruz, V. et al. (Eds.), Neotectonics and sea level variations in the Gulf of California area: A symposium. University Nacional Autónoma de México, Instituto de Geologia, pp. 31-53.

Coolbaugh, M.F., C. Kratt, A. Fallacaro, W.M. Calvin, and J.V. Taranik (2007), Detection of geothermal anomalies using Advanced Spaceborne Thermal Emission and Reflection Radiometer (ASTER) thermal infrared images at Bradys Hot Springs, Nevada, USA, Remote Sens. Environ., 106(3), 350-359, doi:10.1016/j.rse.2006.09.001.

Cooper, C.D. and J.F. Mustard (1999), Effects of very fine particle size on reflectance spectra of smectite and palagonitic soil, Icarus, 142, 2, 557-570.

Cornelis, W.M., and D. Gabriels (2003), The effect of surface moisture on the entrainment of dune sand by wind: an evaluation of selected models, Sedimentology, 50(4), 771-790, doi:1046/j.1365-3091.2003.00577.x.

Crabaugh, M.M. (1994), Controls on accumulation in modern and ancient wet eolian systems, PhD dissertation, 135 pp., University of Texas, Austin, Texas.

Cracknell, A.P. and Y. Xue (1996), Thermal inertia determination from space-a tutorial review, Int. J. Remote Sens., 17(3), 431-461, doi:10.1080/01431169608949020.

Crowley, J.K., S.J. Hook (1996), Mapping playa evaporite minerals and associated sediments in Death Valley, California, with multispectral thermal infrared images. J. Geophys. Res., 101(B1), 643 – 660.

Davis, J.C. (1986), Statistics and Data Analysis in Geology, John Wiley and Sons, New York.

Derickson, D., G. Kocurek, R.C. Ewing, and C. Bristow (2007), Origin of a complex and spatially diverse dune-field pattern, Algodones, southeastern California, Geomorphology, 99, 186-204, doi: DOI: 10.1016/j.geomorph.2007.10.016.

De Souza-Machado, S.G., L. L. Strow, H. Motteler, and S. Hannon (2006), Infrared dust spectral signatures from AIRS, GRL, 33, doi:10.1029/2005GL024,364, 2006.

De Souza-Machado, S.G., B Imbiriba, K. McCann, L.L. Strow, S.E. Hannon, R. Hoff, and H.E. Motteler (submitted), Geophys. Res. Lett., http://asl.umbc.edu/~imbiriba /paper8.pdf.

Du, Y., J. Cihlar, J. Beaubien, and R. Latifovic, (2001), Radiometric normalization, Compositing, and quality control for satellite high resolution image mosaics over large areas. Transactions on Geoscience and Remote Sensing, 39, 3, 623 – 634.

Du, Y., P.M. Teillet, and J. Cihlar (2002), Radiometric normalization of multitemporal high-resolution satellite images with quality control for land cover change detection. Rem. Sens. Environ., 82, 123 – 134.

Dubovik, O. and M. D. King (2000), A flexible inversion algorithm for retrieval of aerosol optical properties from Sun and sky radiance measurements, J. Geophys. Res., 105, 20,673-20,696.

Dubovik, O., A. Sinyuk, T. Lapyonok, B. N. Holben, M. Mishchenko, P. Yang, T. F. Eck, H. Volten, O. Munoz, B. Veihelmann, van der Zander, M Sorokin, and I. Slut-sker (2006), Application of light scattering by spheroids for accounting for particle non-sphericity in remote sensing of desert dust, J. Geophys. 111, D11208, doi:10.1029/2005JD006619.

Dubovik, O., A. Smirnov, B.N. Holben, M.D. King, Y. J. Kaufman, T.F. Eck and I. Slutsker (2000), Accuracy assessment of aerosol optical properties retrieval from AERONET sun and sky radiance measurements, J. Geophys. Res ,105, 9791-9806.

Dubuisson, P., J.C. Buriez and Y. Fouquart (1996), High Spectral Resolution Solar Radiative Transfer in Absorbing and Scattering media, application to the satellite simulation, J. Quant. Spectros. Radiat. Transfer, Vol. 55, No 1, pp. 103-126.

Dunion, J. P. and C.S. Velden (2004), The impact of the Saharan Air Layer on Atlantic tropical cyclone activity, Bull. Am. Meteorol. Soc., 85, 353–365.

Drake, N. and C. Bristow (2006), Shorelines in the Sahara: geomorphological evidence enhanced monsoon from paleolake Megachad, The Holocene, 16, 6, 901-911.

Edgett, K. S., M.S. Ramsey, and P.R. Christensen (1995), Aeolian erosion, transport, and deposition of volcaniclastic sands among the Shifting Sand Dunes, Christmas Lake, Oregon: TIMS image analysis, in Realmuto, V. J., ed., Summaries, Fifth Annual Airborne Earth Science Workshop, Volume 2: Pasadena, California, Jet Propulsion Laboratory Publication 95–1, p. 13–16.

Entekhabi, D., T.J. Jackson, E. Njoku, P. O'Neill, and J. Entin (2008), Soil Moisture Active/Passive (SMAP) Mission concept, Proc. SPIE, 7085, 70850H, doi:10.1117/12.795910.

Engelstaedter, S. and R. Washington (2007), Temporal controls on global dust emissions: The role of surface gustiness, Geophys.l Res. Lett., 34, L15805, doi:10.1029/2007 GL029971.

Engelstaedter, S., I. Tegen, and R. Washington, (2006), North Africa dust emissions and transport, Earth-Science Reviews, 79, p. 74 – 100.

Ewing, R.C., B.J. McElroy, and B.J. Andrews (2007), Point pattern analysis of Star-Dune Fields, Eos Trans. AGU, 88(52): Fall Meet. Suppl., Abstract NG41C-0673.

Ewing, R.C., G. Kocurek, and L.W. Lake (2006), Pattern analysis of dune-field parameters. Earth Surface Processes and Landforms, 31, 9, 1176 – 1191.

Fan, Y., C.J. Duffy, and D.S. Oliver (1997), Density-driven groundwater flow in closed desert basins; field investigations and numerical experiments, J. of Hydrol., 196(1-4), 139-184, doi:10.1016/S0022-1694(96)03292-1.

Fécan, F., B. Marticorena, and G. Bergametti (1999), Parameterization of the increase of the aeolian erosion threshold wind friction velocity due to soil moisture for arid and semi arid areas, Ann. Geophys., 17(1), 149-157, 10.1007/s00585-999-0149-7.

Feely, K. C., and P. R. Christensen (1999), Quantitative compositional analysis using thermal emission spectroscopy: Application to igneous and metamorphic rocks, J. Geophys. Res., 104(E10), 24,195– 24,210.

Fouquart, Y., B. Bonnel, G. Brogniez, J.C. Buriez, L. Smith, and J.J. Morcrette (1987), Observations of Saharan aerosols: Results of ECLATS field experiment: Part II: Broadband radiative characteristics of aerosols and vertical flux divergence, J. Clim. Appl. Meterorol., 26, 38-52.

Fryberger, S.G. (2003), Geological overview of White Sands National Monument, web page www.nps.gov/whsa/Geology of White Sands/GeoHome.html.

Fujisada, H., F. Sakuma, A. Ona, A. and M. Kudoh (1998), Design and pre-flight performance of ASTER instrument protoflight model, IEEE Transactions on Geoscience and Remote Sensing, 36(4), 1152 – 1160.

Furby, S.L., & Campbell, N.A. (2001), Calibrating images from different dates to 'like-value' digital counts, Rem. Sens. Environ., 77, 186 – 196.

Gillespie, A. R. (1992), Spectral mixture analysis of multispectral thermal infrared images, Remote Sens. Environ., 42, 137– 145.

Gillespie, A., S. Rokugawa, T. Matsunaga, J.S. Cothern, S.J. Hook and A.B. Kahle (1998), A temperature and emissivity separation algorithm for Advanced Spaceborne Thermal Emission and Reflection Radiometer (ASTER) images, IEEE Trans. Geo. Rem. Sci., 36, 113-1126.

Gillespie, A.R. (1992), Enhancement of multispectral thermal infrared images: decorrelation contrast stretching, Rem. Sens. Environ., 42, 147-155.

Gillespie, A.R. and A.B. Kahle (1977), Construction and interpretation of a digital thermal inertia image, Photogramm. Eng. Rem. S., 43(8), 983-1000.

Gillette, D.A. (1999), A qualitative geophysical explanation for “hot spot” dust emitting source regions: Contributions to Atmospheric Physics, 72, p. 67-77.

Greeley, R., and J.D. Iversen (1985), Wind as a Geologic Process: On Earth, Mars, Venus and Titan, 348 pp., Cambridge University Press, Cambridge.

Gu, Y., W.I. Rose, and G.J.S. Bluth (2003), Retrieval of mass and sizes of particles in sandstorms using two MODIS IR bands: A case study of April 7, 2001 sandstorm in China, Geophys. Res. Lett., 30, 15, 1805, doi:10.1029/2003GL017405.

Gupta, P., F. Patadia, and S.A. Christopher (2008), Multisensor data product fusion for aerosol research, IEEE Trans. Geosci. Rem. Sens., 46, 5, 1407-1415.

Gustafson, W. T., A. R. Gillespie, and G. J. Yamada (2006), Revisions to the ASTER temperature/emissivity separation algorithm, paper presented at 2nd International Symposium on Recent Advances in Quantitative Remote Sensing, Global Change Unit, Univ. of Valencia, Torrent, Spain.

Gutmann, J.T. and M.F. Sheridan (1978), Geology of the Pinacate volcanic field, Ariz. Bur. Geol. Min. Technol., Spec. Pap., 2, 47-59.

Hamilton, E. (1999), Particle size effects in particulate rock samples – Implications for thermal emission spectrometer (TES) data analysis in high albedo regions of Mars, The Fifth International Conference on Mars, July 19-24, 1999, Pasadena, CA, abstract no. 6159.

Hamilton, V. E., and P. R. Christensen (2000), Determining the modal mineralogy of mafic and ultramafic igneous rocks using thermal emission spectroscopy, J. Geophys. Res., 105(E4), 9717– 9733.

Hamilton, V. E., M. B. Wyatt, H. Y. McSween Jr., and P. R. Christensen (2001), Analysis of terrestrial and Martian volcanic compositions using thermal emission spectroscopy: 2. Application to Martian surface spectra from the Mars Global Surveyor Thermal Emission Spectrometer, J. Geophys. Res., 106(7), 14,733– 14,746.

Hamilton, V. E., M. M. Osterloo, and B. S. McGrane (2007), THEMIS decorrelation stretched infrared mosaics for compositional evaluation of candidate 2009 Mars Science Laboratory landing sites, Lunar Planet. Sci., XXXVIII.

Hamilton, V. E., P. R. Christensen, and H. Y. McSween (1997), Determination of Martian meteorite lithologies and mineralogies using vibrational spectroscopy, J. Geophys. Res., 102(E11), 25,593– 25,603.

Hao, X. and J.J. Qu (2007), Saharan dust storm detection using moderate resolution imaging spectroradiometer thermal infrared bands, Journal of Applied Remote Sensing, 1, 013510 (April 24, 2007), doi: 10.1117/1.2740039.

Hapke, B. (1981), Bidirectional reflectance spectroscopy, 1, Theory: J. Geophys. Res., 86, p. 3039–3054.

Haywood, J. M. and O. Boucher (2000), Estimates of the direct and indirect radiative forcing due to tropospheric aerosols: A review, Rev. Geophys., 38, 513–543.

Haywood, J.M., P.N. Francis, M.D. Glew, and J.P. Taylor (2001), Optical properties and direct radiative effect of Saharan dust; a case study of two Saharan dust outbreaks using aircraft data, J. Geophys. Res. Atmos., 106, 18,417 – 18,430.

Haywood, J.M., R.P. Allan,I. Culverwell, T. Slingo, S. Milton, J. Edwards, and N. Clerbaux (2005), Can desert dust explain the outgoing longwave radiation anomaly over the Sahara during July 2003?, J. Geophys. Res., 110, D05105, 14 p.

Herman, J.R., P.K. Bhartia, O. Torres, C. Hsu, C. Sefton, and E. Celarier (1977), Global distribution of UV-absorbing aerosols from Nimbus-7/TOMS data, J. Geophys. Res., 102, p. 16,911 – 16,922

Hewson, R.D., T.J. Cudahy, and J.F. Huntington, (2001), Geologic and alteration mapping at Mt. Fitton, South Australia, using ASTER satellite-borne data. In IEEE, IGARSS 2001: scanning the present and resolving the future, Proceedings IEEE 2001 International Geoscience and Remote Sensing Symposium, Sydney, Australia, 9 –13 July 2001, II, (pp. 724 – 726). New York: The Institute of Electrical and Electronics Engineers Inc.

Hewson, R.D., T.J. Cudahy, S. Mizuhiko, K. Ueda, and A.J. Mauger (2005), Seamless geological map generation using ASTER in the Broken Hill-Curnamona province of Australia. Rem. Sens. Environ., 99, p. 159 – 172.

Holben, B. N., T. F. Eck, I. Slutsker, et al., 1998: AERONET—A federated instrument network and data archive for aerosol characterization. Remote Sens. Environ., 66, 1-16.

Hook, S. J., K. E. Karlstrom, C. F. Miller, and K. J. W. McCaffrey (1994), Mapping the Piute Mountains, California, with thermal infrared multispectral scanner (TIMS) images, J. Geophys. Res., 99(B8), 15,605 – 15,622.

Hotta, S., S. Kubota, S. Katori, and K. Horikawa (1984), Sand Transport by wind on a wet sand surface, in Coastal Engineering - Nineteenth Coastal Engineering Conference: Proceedings of the International Conference, Sept. 3-7, 1984, Houston, TX, edited by B.L. Edge, pp. 1265-1281, ASCE, New York.

Huang, J., H. van den Dool, and K.P. Georgarakos (1996), Analysis of Model-Calculated Soil Moisture over the United States (1931–1993) and Applications to Long-Range Temperature Forecasts, J. Climate, 9(6), 1350–1362.

Huang, M.-F., J. Yu, S. Hu, and M. Jing (2006), Study on Evapotranspiration Estimation of Small Drainage based on ASTER Data, Geoscience and Remote Sensing Symposium, IGARSS 2006, IEEE International Conference on, July 31 - Aug. 4, 3696-3699.

Hudson, P.K., M.A. Young, P.D. Kleiber, and V.H. Grassian (2008), Coupled infrared extinction spectra and size distribution measurements for several non-clay components of mineral dust aerosols (quartz, calcite and dolomite), Atmospheric Environment, 42, 24, 5991-5999.

Hulley, G. and S.J. Hook (2009), The North American ASTER Land Surface Emissivity Database (NAALSED) Version 2.0, Rem. Sens. Environ., 113, 1967-1975.

Hulley, G. C., S. J. Hook, and A. M. Baldridge (2008), ASTER Land Surface Emissivity Database of California and Nevada, Geophys. Res. Lett., 35, L13401, doi:10.1029/2008GL034507.

Ivis, R.L. (1959), Shell dunes of the Sonoran shore, Am. J. Sci., 257, 449-457.

Iwasaki, A. and H. Fujisada (2005a), ASTER geometric performance, IEEE T. Geosci. Remote, 43(12), 2707-2714, doi:10.1109/TGRS.2005.849055.

Iwasaki, A., and H. Tonooka (2005b), Validation of a crosstalk correction algorithm for ASTER/SWIR, IEEE T. Geosci. Remote, 43(12), 2747- 2751, doi:10.1109/TGRS.2005.855066.

Iwasaki, A., H. Fujisada, H. Akao, O. Shindou, and S. Akagi (2002), Enhancement of Spectral Separation Performance for ASTER/SWIR, Proc. SPIE, 4486, 42-50, doi:10.1117/12.455140.

Jackson, T.J. (1993), Measuring surface soil moisture using passive microwave remote sensing, Hydrol. Process, 7, 139-152.

Jackson, T.J. (1997), Soil moisture estimation using SSM/I satellite data a over grassland region, Water Resour. Res., 33, 1475-1484.

Jacob, F., F. Petitcolin, T. Schmugge, E. Vermote, A. French, and K. Ogawa (2004), Comparison of land surface emissivity and radiometric temperature derived from MODIS and ASTER sensors, Remote Sens. Environ., 90(2), 137-152, doi:10.1016/j.rse.2003.11.015.

Johnson, P.E., M.O. Smith, and J.B. Adams (1992), Simple algorithms for remote determination of mineral abundances and particle sizes from reflectance spectra. J. Geophys. Res., 97, 2649 – 2657.

Kahle, A. B., and R.E. Alley (1992), Separation of temperature and emittance in remotely sensed radiance measurements, Remote Sens. Environ., 42(2), 107−111.

Kahle, A.B. (1977), A simple thermal model of the Earth's surface for geologic mapping by remote sensing, J. Geophys. Res., 82, 1673-1680.

Kahle, A.B. (1987), Surface emittance, temperature, and thermal inertia derived from Thermal Infrared Multispectral Scanner (TIMS) data for Death Valley, California, Geophysics, 52, 858-874.

Kahle, A.B., A.R. Gillespie, and A.F.H. Goetz (1976), Thermal inertia imaging: a new geologic mapping tool, Geophys. Res. Lett., 3(1), 26-28.

Karyampudi, V. M. and H.F. Pierce (2002), Synoptic-Scale Influence of the Saharan Air Layer on Tropical Cyclogenesis over the Eastern Atlantic, Monthly Weather Review, 130, 12, 3,100-3,128.

Kasper-Zubillaga, J. J. and A. Carranza-Edwards (2005), Grain size discrimination between sands of desert and coastal dunes from northwestern Mexico, Rev. Mex. Cienc. Geo., l.–390.

Kasper-Zubillaga, J. J., B. Acevedo-Vargas, O. Morton Bermea, and G. Ortiz-Zamora (2008), Rare earth elements of the Altar Desert dune and coastal sands, Northwestern Mexico, Chemie Der Erde Geochemistry, 68: 45–59.

Kasper-Zubillaga, J.J., H. Zolezzi-Ruíz, A. Carranza-Edwards, P. Girón-García, G. Ortiz-Zamora, and M. Palma (2007), Sedimentological, modal analysis and geochemical studies of desert and coastal dunes, Altar Desert, NW Mexico, Earth. Surf. Process. Landforms, 32, 489-508.

Katra, I. and N. Lancaster (2008), Surface-sediment dynamics in a dust source from spaceborne multispectral thermal infrared data, Remote Sens. Environ., 112(7), 3212-3221, doi:10.1016/j.rse.2008.03.016.

Katra, I., S. Scheidt, and N. Lancaster (2008), Changes in active eolian sand at northern Coachella Valley, California, Geomorphology, 105(3-4), 277-290, doi:10.1016/j.geomorph.2008.10.004.

Kaufman, Y.J., I. Koren, L.A. Remer, D. Tanre, P. Ginoux, P., and S. Fan (2005), Dust transport and deposition observed from the Terra-Moderate Resolution Imaging Spectroradiometer (MODIS) spacecraft over the Atlantic Ocean, J. Geophys. Res., 110, D10S12, doi:10.1029/2003JD004436.

Kaufman, Y. J., D. Tanre´, L. A. Remer, E. F. Vermote, A. Chu, and B. N. Holben (1997), Operational remote sensing of tropospheric aerosol over land from EOS moderate-resolution imaging spectroradiometer, J. Geophys. Res., 102, 17,051– 17,067.

Kellogg, C.A., D.W. Griffin, V.H. Garrison and E.A. Shinn (2005), Dust in the wind; intercontinental transport of desert dust in the atmosphere and its implications for human and ecosystem health, Abstr. with Progs., Geol. Soc. Amer., 36, pp. 25.

Kendall, M. and A. Stuart (1979), The advanced theory of statistics, 4th ed., vol. 2. London: Charles Griffen.

Kerr, P. F., and A.M. Langer (1965), Mineralogical features of Mojave Desert playa crusts, in Geology, mineralogy, and hydrology of U.S. playas, edited by J. T. Neal, 176 pp., Office of Aerospace Research, U.S. Air Force, AFCRL-65-266.

King, M.D., Y.J. Kaufman, W.P. Menzel, and D. Tanré (1992), Remote sensing of cloud, aerosol, and water vapor properties from the moderate resolution imaging spectrometer (MODIS), IEEE Trans. Geosci. Sens., 3, 1, 2-27.

King, M.D., W.P. Menzel, Y.J. Kaufman, D. Tanré, B. Gao, S. Platnick, S.A. Ackerman, L.A. Remer, R. Pincus and P.A. Hubanks, IEEE Trans. Geosci. Sens., 41, 2, 422-458.

Kirkland, L. E., K. C. Herr and J. W. Salisbury (2001), Thermal Infrared Spectral Band Detection Limits for Unidentified Surface Materials, Appl. Opt. 40, 4852-4862.

Kirkland, L., K. Herr, E. Keim, P. Adams, J. Salisbury, J. Hackwell and A. Treiman (2002), First use of an airborne thermal infrared hyperspectral scanner for compositional mapping, Rem. Sens. Environ., 80, 447-459.

Kneizys, F.X., E.P. Shettle, W.O. Gallery, J.H. Chetwynd, Jr., L.W. Abreu, J.E.A. Selby, R.W. Fenn and R.A. McClatchey (1983), Atmospheric Transmittence/Radiance: Computer Code LOWTRAN 6, Air Force Geophysics Laboratory AFGL-TR-83-0187.

Kislyakov, A.G. (1966), Effective path length and mean temperature of the atmosphere, Izvestiya VUZ. Radiofizika, 9, 3, 451-461.

Knippertz, P., A. Ansmann, D. Althausen, D. Müller, M. Tesche, E. Bierwirth, T. Dinter, T. Müller, W. V.Hoyningen-Huene, K. Schepanski, M. Wendisch, B. Heinold, K. Kandler, A. Petzold, L. Schütz and I. Tegen (2009), Dust mobilization and transport in the northern Sahara during SAMUM 2006 – a meteorological overview, Tellus, 61B, 12-31.

Kocurek, G. and K.G. Havholm (1994), Eolian sequence stratigraphy - a conceptual framework, in Siliclastic Sequence Stratigraphy (American Association Petroleum Geologists Memoir 58), edited by P. Weimer, and H.W. Posamentier, p.393-409, Tulsa, Oklahoma.

Kocurek, G. and N. Lancaster (1999), Aeolian system sediment state: theory and Mojave Desert Kelso dune field example, Sedimentology, 46(3), 505–515, doi:10.1046/j.1365-3091.1999.00227.x.

Kocurek, G., M. Carr, R. Ewing, K.G. Havholm, Y.C. Nagar and A.K. Singhvi, (2007), White Sands Dune Field, New Mexico: Age, dune dynamics and recent accumulations, Sediment. Geol., 197(3-4), 313-331, doi:10.1016/j.sedgeo.2006.10.006.

Kotchenova, S., E. Vermote, R. Matarrese, and F. Klemm (2006), Validation of a vector version of the 6S radiative transfer code for atmospheric correction of satellite data. Part I: Path radiance, Appl. Optics, 45(26), p. 6762-6774, doi:10.1364/AO.45.006762.

Lancaster, N. (1989), The dynamics of star dunes: an example from the Gran Desierto, Mexico. Sedimentology, 36, 273–289.

Lancaster, N. (1992), Relations between dune generations in the Gran Desierto of Mexico. Sedimentology, 39, 631–644.

Lancaster, N. (1993), Origins and sedimentary features of supersurfaces in the northwestern Gran Desierto sand sea In: Eolian Sediments: Ancient and Modern (Eds K. Pye and N. Lancaster), Int. Assoc. Sedimentol. Spec. Publ., 16, 71–83.

Lancaster, N. (1995), Origin of the Gran Desierto Sand Sea, Sonora, Mexico: evidence from dune morphology and sedimentology, In: Desert Aeolian Processes (Ed. V.P. Tchakerian), pp. 11–35. Chapman & Hall, London.

Lancaster, N., R. Greeley, and P.R. Christensen (1987), Dunes of the Gran Desierto sand sea, Sonora, Mexico, Earth Surface Processes and Landforms, 12, 277 – 288.

Langford, R.P. (2003), The Holocene history of the White Sands dune field and influences on eolian deflation and playa lakes. Quatern. Int., 104(1), 31–39, doi:10.1016/S1040-6182(02)00133-7.

Langford, R.P., J.M. Rose and D.E. White (2009), Groundwater salinity as a control on development of eolian landscape: An example from the White Sands of New Mexico, Geomorphology, 105, 39-49.

Law, D.B. (1988), IR sky radiance distributions in the marine boundary layer, SPIE 88 Technical Symposium, Southeast on Optics, Electro-Optics, & Sensors-Wave Propagation and Scattering In Varied Media, Orlando, FL, 04/04/88. Published in Proceedings, 5-7 April 1988.

Levy, R. C., L. A. Remer, D. Tanre´, Y. J. Kaufman, C. Ichoku, B. N. Holben, J. Livingston, P. Russell, and H. Maring (2003), Evaluation of the Moderate-Resolution Imaging Spectroradiometer (MODIS) retrievals of dust aerosol over the ocean during PRIDE, J. Geophys. Res., 108, doi:10.1029/2002JD002460.

Liang, S. (2000), Narrowband to broadband conversions of land surface albedo I Algorithms, Remote Sens. Environ., 76(2), 213-238.

Liu, Y., Y. Yamaguchi, and C. Ke (2007), Reducing the discrepancy between ASTER and MODIS land surface temperature products, Sensors, 7(12), 3043-3057, doi:10.3390/s7123043.

Lohman, U. and J. Feichter (2005), Global indirect aerosol effects: a review, Atmos. Chem. Phys., 5, 715-737.

Luo, C., N.M. Mahowald and J. del Corral (2003), Sensitivity study of meteorological parameters on mineral aerosol mobilization, transport, and distribution, J. Geophys. Res., D15, p. 4447.

Lynch, D.J. and J.T. Gutmann, (1990), Volcanic structure and alkaline rocks in the Pinacate volcanic field of Sonora, Mexico. In: Geologic Excursions Through the Sonoran Desert Region, Arizona and Sonora (Eds G.E. Gehrels and J.E. Spencer), Arizona Geol. Surv. Spec. Pap., 7, 309–322.

Ma, A.N. and Y. Xue (1990), A study of remote sensing information model of soil moisture, in Proceedings of the 11th Asian Conference on Remote Sensing, 15-21, November, 1990, 1, pp. P-11-1-P-11-5, International Academic Publishers, Beijing.

Malim, K.A., H.Y. McSween Jr., V.E. Hamilton, J.M. Moersch and P.R. Christensen (2004), Accuracy of plagioclase compositions from laboratory and Mars spacecraft thermal emission spectra, J. Geophys. Res., 109, E04001, doi:10.1029/2003JE002097.

Martinez-Alonso, S., B.M. Jakosky, M.T. Mellon and N.E. Putzig (2005), A volcanic interpretation of Gusev Crater surface materials from thermophysical, spectral and morphological evidence, J. Geophys. Res., 110, E01003, doi:10.1029/2004JE002327, 20.

May, L.A. (1973), Geological reconnaissance of the Gran Desierto region, northwestern Sonora, Mexico, J. Arid Acad. Sci, 8, 158-169.

McAtee, B.K., A.J. Prata,and M.J.Lynch, (2003), The angular behavior of emitted thermal infrared radiation (8-12 μm) at semiarid site, Journal of Meteorology, 42(8), 1060-1071.

McKee, E.D. (1966), Structures of dunes at White Sands National Monument, New Mexico (and a comparison with structures of dunes from other selected areas), Sedimentology, 7, 1–69.

McKenna-Neuman, C. and W.G. Nickling (1989), A theoretical and wind tunnel investigation of the effect of capillarity water on the entrainment of sediment by wind, Can. J. Soil Sci., 69, 79-96.

MDA Federal (2004), Landsat GeoCover ETM+ 2000 Edition Mosaics Tile N-03-05.ETM-EarthSat-MrSID, 1.0, USGS, Sioux Falls, South Dakota.

Meloni, D., A. Di Sarra, T. Di Iorio, and G. Fiocco (2004), Direct radiative transfer of Saharan dust in the Mediterranean from measurements at Lempedusa and MISR space-borne observations, J. Geophys. Res. - Atmos., 109, 15 pp.

Merriam, R. and O.L. Brandy (1969), Source of upper Cenozoic sediments in the Colorado River delta region, J. Sediment. Petrol., 35, 911-916.

Middleton, N.J., A.S. Goudie, and G.L. Wells (1986), The frequency and source areas of dust storms, in Nickling, W.G., ed., Aeolian Geomorphology: Boston, London, Sydney, Allen and Unwin, p. 237 – 259.

Miller, R.L., R.V. Cakmur, J. Perlwitz, I.V. Geogdzhayev, P. Ginoux, D. Koch, K.E. Kohfeld, C. Prigent, R. Ruedy, G.A. Schmidt, and I. Tegen (2006), Mineral dust aerosols in the NASA Goddard Institute for Space Sciences ModelE atmospheric general circulation model, J. Geophys. Res., 111, D06208, doi:10.1029/2005JD005796.

Miller, S.D. (2003), A consolidated technique for enhancing desert dust storms with MODIS, Geophys. Res. Lett., 30, 20, 2071, doi:10.1029/2003GL018279.Miller, S. (2004), Toward NPOESS and GOES-R: Some Advanced MODIS Applications, 14th International Terscan Conference, Nanjing, China, June 6, 2004.

Miller, R. and I. Tegen (1998), Climate response to mineral dust aerosols, Journal of Climate, 11, 3247-3267.

Miura, T., H. Yoshioka, K. Fujiwara, and H. Yamamoto (2008), Inter-comparison of ASTER and MODIS surface reflectance and vegetation index products for synergistic applications to natural resource monitoring, Sensors, 8(4), 2480-2499, doi:10.3390/s8042480.

Moulin, C., H.R. Gordon, V.F. Banzon, and R.H. Evans (2001), Assessment of Saharan dust absorption in the visible from SeaWiFS imagery, J. Geophys. Res., 106, 18,239 – 18,249.

Muhs, D.R., R.L. Reynolds, J. Been and G. Skipp (2003), Eolian sand transport pathways in the southwestern United States: importance of the Colorado River and local sources. Quaternary International, 104, 3 – 18.

Muhs, D.R. (2004), Mineralogical maturity in dunefields of North America, Africa and Austalia, Geomorphology, 59, 1-4, 247-269.

Mustard, J.F. and J.E. Hays (1997), Effects of hyperfine particles on reflectance spectra from 0.3 to 25 um, Icarus, 125, 1, 145-163.

Mustard, J.F. and C.M. Pieters (1988), Predicting mineral abundances from reflectance spectra, abs., Lunar Planet. Sci. Conf., XIX, 825-826.

Nasipuri, P., T.J. Majumdar, and D.S. Mitra (2006), Study of high-resolution thermal inertia over western India oil fields using ASTER data, Acta Astronaut., 58(5), 270-278, doi:10.1016/j.actaastro.2005.11.002.

Nicholson, S.E., C.J. Tucker, and M.B. Ba (1998), Desertification, drought and surface vegetation: An example from the West African Sahel. Bulletin of the American Meteorological Society, 79, 815 – 829.

Nickling, W.G. and C. McKenna-Neuman (1994), Aeolian Sediment Transport, in Geomorphology of Desert Environments, edited by A.J. Parsons and A.D. Abrahams, pp. 517-556, Springer, London.

Nickling, W.G., G.H. McTainsh, and J.F. Leys (1998). Dust emissions from the Channel Country of western Queensland, Australia. In Livingston, I. (Ed.), Aeolian Geomorphology, Papers from the 4th International Conference on Aeolian Research, 1 – 17.

Nickovich, S., A. Papdopoulos, O. Kakaliagou, and G. Kallos (2001), Model for prediction of desert dust cycles in the atmosphere, J. Geophys. Res., 106(D16), 18103-18130, doi:10.1029/2000JD900794.

Nielsen, A.A., K. Conradsen, and J.J. Simpson (1998), Multivariate alteration detection (MAD) and MAF postprocessing in multispectral, bitemporal image data: New approaches to change detection studies. Rem. Sens. Environ., 64, 1 – 19.

Njoku, E.G., Jackson, T.J., Lakshmi, V., Chan, T.K., and S.V. Nghiem (2003), Soil moisture retrieval from AMSR-E, IEEE T. Geosci. Remote, 41(2), 215-229, doi:10.1109/TGRS.2002.808243.

Nourse, J.A., W.R. Premo, A. Iriondo and E.R. Stahl (2005), Contrasting Proterozoic basement complexes near the truncated margin of Laurentia, northwestern Sonora-Arizona international border region, GSA Special Papers, 393, 123-182, doi: 10.1130/0-8137-2393-0.123

Ogawa, K., T. Schmugge, F. Jacob, A. French, (2002), Estimation of land surface window emissivity from multi-spectral thermal infrared remote sensing—A case study in part of the Sahara Desert. Agronomie, 22, 595−696.

Ogawa, K. and T. Schmugge (2004), Mapping surface broadband emissivity of the Sahara Desert using ASTER and MODIS data, Earth Interactions, 8, Paper No. 7, 1-14.

Ortega-Gutiérrez F, L.M. Mitre-Salazar, J. Roldán-Quintana, J. Aranda-Gómez, D. Morán-Zenteno, A. Nieto-Samaniego (1992), Carta Geológica de la República Mexicana [Geologic Chart of the Mexican Republic] 1:2 000.000. Instituto de Geología, Universidad Nacional Autónoma de México: Mexico.

Paisley, E.C.I., N. Lancaster, LR. Gaddis, and R. Greeley, (1991), Discrimination of active and inactive sand from remote sensing: Kelso Dunes, Mojave Desert, California. Rem. Sense Environ., 37, 153 – 166.

Paolini, L., F. Grings, J.A. Sobrino, J.C. Jimenez Munoz, and H. Karszenbaum (2006), Radiometric correction effects in Landsat multi-date/multi-sensor change detection studies, International Journal of Remote Sensing, 27, 4, 685 – 704.

Parkinson, C.L. (2003), Aqua: An Earth-Observing Satellite Mission to Examine Water and Other Climate Variables, IEEE Trans. Geosci. Rem. Sens., 41, 2, 173-183.

Pease, P.P., G.D. Bierly, V.P. Tchakerain, and N.W. Tindale (1999), Mineralogical characterization and transport pathways of dune sand using Landsat TM data, Wahiba Sand Sea, in the Central Taklimakan sand sea. Sedimentary Geology, 161, 1 – 14.

Peŕez, C., S. Nickovic, G. Pejanovic, J.M. Baldasano and E. Ōzsoy (2006b), Interactive dust-radiation modeling: A step to improve weather forecasts, J. Geophys. Res.111,D16206, doi:10.1029/2005JD006717.

Peŕez, C., S. Nickovic, J.M. Baldasano, M. Sicard, F. Rocadenbosch and V.E. Cachorro (2006a), A long Saharan dust event over the west Mediterranean: Lidar, Sun photometer observations, and regional dust modeling, J. Geophys. Res.111, D15214, doi:10.1029/2005JD006579.

Pierangelo, C., A. Chedin, S. Heilliette, N. Jacquinet-Husson, and R. Armante (2004), Dust altitude and infrared optical depth from AIRS, Atmos. Chem. Phys., 4, 1813-1822.

Pieri, D.C., and M.J. Abrams (2004), ASTER watches the world's volcanoes: a new paradigm for volcanological observations from orbit, J. Volcanol. Geotherm. Res., 135(1-2), 13–28, doi:10.1016/j.jvolgeores.2003.12.018.

Pratt, D.A., and C.D. Ellyett (1979), The thermal inertia approach to mapping soil moisture and geology, Remote Sens. Environ., 8(2), 151-168, doi:10.1016/0034-4257(79)90014-2.

Price, J.C. (1977), Thermal inertia mapping: a new view of Earth, J. Geophys. Res., 82(C18), 2582-2590, doi: 10.1029/JC082i018p02582.

Price, J.C. (1980), The potential of remotely sensed thermal infrared data to infer surface soil moisture and evapotranspiration, Water Resour. Res., 16(4), 787-795.

Price, J.C. (1985), On the analysis of thermal infrared imagery: the limited utility of apparent thermal inertia, Remote Sens. Environ., 18(1), 59-73, doi:10.1016/0034-4257(85)90038-0.

Prospero, J.M., P. Ginoux, and O. Torres (2002), Environmental characterization of global sources of atmospheric soil dust identified with the Nimbus 7 Total Ozone Mapping Spectrometer (TOMS) Absorbing Aerosol Product. Review of Geophysics, 40, 1, 1002.

Ramsey, M.S. and S. Rose, (2009), The complex effects of subpixel compositional, thermal and textural heterogeneities on spaceborne TIR data, 2nd HyspIRI Science Workshop, Pasadena, CA.

Ramsey, M.S. (2002), Closing the terrestrial-planetary remote sensing loop: Spectral, spatial and physical proxies, American Geophysical Union Fall Meeting (abs. P62B-12).

Ramsey, M.S. (2002), Ejecta distribution patterns at Meteor Crater, Arizona: On the applicability of lithologic end-member deconvolution for spaceborne thermal infrared data of Earth and Mars, J. Geophys. Res., 107(E8), doi:10.1029/2001JE001827.

Ramsey, M.S. and P.R. Christensen (1998), Mineral abundance determination: Quantitative deconvolution of thermal emission spectra, J. Geophys. Res., 103, 577-596.

Ramsey, M.S., and P.R. Christensen (1998), Mineral abundance determination: Quantitative deconvolution of thermal emission spectra. J. Geophys. Res., 103, 577-596.

Ramsey, M.S., P.R. Christensen, N. Lancaster, and D.A. Howard (1999), Identification of sand sources and transport pathways at the Kelso Dunes, California using thermal infrared remote sensing, Geological Society of America Bulletin, 111, 646-662.

Realmuto, V. (1990), Separating the effects of temperature and emissivity: Emissivity spectrum normalization, In Abbott, E.A., (Ed.), Proceedings, Second Annual Airborne Earth Science Workshop, Volume 2: Jet Propulsion Laboratory Publication 90-55, 31 – 35.

Reheis, M.C. (2006), A 16-year record of eolian dust in Southern Nevada and California, USA: Controls on dust generation and accumulation, J. Arid Environ., 67(3), 487-520, doi:10.1016/j.jaridenv.2006.03.006.

Remer, L. A., et al (2002)., Validation of MODIS aerosol retrieval over ocean, Geophys. Res. Lett., 29(12), 8008, doi:10.1029/2001GL013204.

Reynolds, R.L., J.C. Yount, M. Reheis, H Goldstein, P. Jr. Chavez, R. Fulton, J. Whitney, C. Fuller, and R.M. Forester (2007), Dust emission from wet and dry playas in the Mojave Desert, USA, Earth. Surf. Process. Land., 32(12), 1811-1827, doi:: 10.1002/esp.1515.

Ricchiazzi, P., S. Yang, C. Gautier, and D. Sowle (1998), SBDART: A research and teaching software tool for plane-parallel radiative transfer in the Earth's atmosphere, Bulletin of the American Meteorology Society, 79(10):2101-2114.

Richards, J.A. (1999), Remote Sensing Digital Image Analysis: An Introduction, Springer-Verlag, Berlin, Germany, p. 240.

Rooney, C.B. and A. Basu, (1994), Provenance analysis of muddy sandstones, J. Sed. Res.,A64, 2–7.

Rosen, M. R. (1994), The importance of groundwater in playas: a review of playa classifications and the sedimentology and hydrology of playas, in Paleoclimate and Basin Evolution of Playa Systems, edited by Rosen, M.R., p. 1-18, Geological Society of America Special Paper 289, Boulder, CO.

Rowan, L.C. and J.C. Mars (2003), Lithologic mapping in the Mountain Pass, California area using Advanced Spaceborne Thermal Emission and Reflection Radiometer (ASTER) data, Rem, Sens. Environ., 84, 350 – 366.

Rowan, L.C., J.C. Mars, and C. J. Simpson (2005), Lithologic mapping of the Mordor, NT, Australia ultramafic complex by using the Advanced Spaceborne Thermal Emission and Reflection Radiometer (ASTER). Remote Sens. Environ., 99, 105 – 126.

Ruff, S. W. (1998), Quantitative thermal emission spectroscopy applied to granitoid petrology, Ph.D. dissertation, Ariz. State Univ., Tempe.

Ruff, S., P.R. Christensen, P.W. Barbera and D.L. Anderson, (1997), Quantitative thermal emission spectroscopy of minerals: A laboratory technique for measurement and calibration: J. Geophys. Res., 102, p. 14899–14913.

Sabins, F.F. (1997), Remote sensing principles and interpretation, W.H. Freeman & Co., NY.

Sabol, D.E., A.R. Gillespie, E. McDonald, and I. Danillina (2006), Differential thermal inertia of geological surfaces, submitted 2nd Annual International Symposium of Recent Advances in Quantitative Remote Sensing, Torrent, Spain, 6pp, 25-29 July 2006.

Saleh, A., and D.W. Fyrear (1995), Threshold wind velocities of wet soils as affected by windblown sand, Soil Sci., 160(4), 304-309.

Salisbury, J.W., and D.M. D'Aria, (1992), Emissivity of terrestrial materials in the 8-14 μm atmospheric window, Rem. Sens. Environ., 42, 83 – 106.

Schaaf, C.B., F. Gao, A.H. Strahler, W. Lucht, X. Li, T. Tsang, N.C. Strugnell, X. Zhang, Y. Jin, J.-P. Muller, P. Lewis, M. Barnsley, P. Hobson, M. Disney, G. Roberts, M. Dunderdale, C. Doll, R.P. d'Entremont, B. Hu, S. Liang, J.L. Privette, and D. Roy (2002), First operational BRDF, albedo nadir reflectance products from MODIS, Remote Sens. Environ., 83(1-2), 135-146, doi:10.1016/S0034-4257(02)00091-3.

Schädlich, S., F.M. Göttsche, and F.-S. Olesen (2001), Influence of land surface parameters and atmosphere on METEOSAT brightness temperatures and generation of land surface temperature maps by temporally and spatially interpolation atmospheric correction, Remote Sens. Environ., 75(1), 39-46, doi:10.1016/S0034-4257(00)00154-1.

Scheidt, S.P., M.S. Ramsey and N. Lancaster (2008), Radiometric normalization and image mosaic generation of ASTER thermal infrared data: An application to extensive sand sheets and dune fields, Rem. Sens. Environ., 112, 920-933.

Scheidt, S.P., M.S. Ramsey, and N. Lancaster, (2007), Integration of ASTER TIR data and the Google Earth application to examine the relationships between sand transport pathways and dust emission hotspots, Eos Trans. AGU, 88(52): Fall Meet. Suppl., Abstract NG41C-0667.

Scheidt, S.P., M.S. Ramsey, and N. Lancaster (2006), Fusion of multitemporal/multispectral satellite data for the Gran Desierto: Implications for long distance sand transport. In Nickling, W.G., Turner, S., Gillies, J.A., & Puddister, M. Sixth International Conference on Aeolian Research, July 24 – 26, 2006, University of Guelph, Ontario, Canada, Program and Abstracts, (p. 86).

Scheidt, S.P., M.S., Ramsey, and N. Lancaster (2008b), Thermal remote sensing of sand transport systems, in Planetary Dunes Workshop: A Record of Climate Change, Lun. Planetary Instit. No. 1403, p. 62.

Shao, Y. (2001), Physics and modeling of wind erosion: Dordrecht, Kluwer Academic Publishers, 408 p.

Shao, Y., M.R. Raupach, and J.F. Leys (1996), A model for predicting aeolian sand drift and dust entrainment on scales from paddock to region. Aust. J. Soil Res., 34, 309–342.

Shao, Y., M.R. Raupach, and P.A. Findlater (1993), Effect of saltation bombardment on the entrainment of dust and wind, J Geophys. Res., 98(D7), 12719-12736.

Shao, Y., M.R. Raupach, and P.A. Findlater (1993), Effect of saltation bombardment on the entrainment of dust by wind, J. Geophys. Res., 98, 12,719-12,726.

Shapiro, L.S. and M. Brady (1995), Rejecting outliers and estimating errors in an orthogonal-regression framework, Philosophical Transactions: Physical Sciences and Engineering, 350(1694), 407-439.

Sherman, D.J. (1990), Evaluation of aeolian sediment sand transport equations using intertidal-zone measurements, Saunton Sands, England, Sedimentology, 37(2), 385-392.

Shipman, H. and J.B. Adams, (1987), Detectability of minerals on desert alluvial fans using reflectance spectra: J. Geophys. Res., 92, p. 10391–10402.

Sokolik, H., D.M. Winkler, G. Bergametti, D.A. Gillette, G. Carmichael, Y.J. Kaufman, L. Gomes, L. Schuetz and J.E. Penner (2001), Introduction to special section: Outstanding problems in quantifying the radiative impacts of mineral dust, J. Geophys. Res., 106, 18,015-18,028.

Strow, L., S. Hannon, S. DeSouza-Machado, D. Tobin, and H. Motteler, (2003), An overview of the AIRS radiative transfer model, IEEE Trans. Geosci. Rem. Sens., 41, 303–313

Sun, D., K.M. Lau and K. Menas (2008), Contrasting the 2007 and 2005 hurricane seasons: Evidence of possible impacts of Saharan dry air and dust on tropical cyclone activity in the Atlantic basin, Geophysical Research Letters 35, L15405.

Svoboda, M., D. LeComte, M. Hayes, R. Heim, K. Gleason, J. Angel, B. Rippey, R. Tinker, M. Palecki, D. Stooksbury, D. Miskus, and S. Stephens (2002), The drought monitor, Bull. Am. Meteorol. Soc., 83(8), 1181–1190, doi: 10.1175/1520-0477(2002)083<1181:TDM>2.3.CO;2.

Tanamachi, R.L., H.B. Bluestein, S.S. Moore, and R.P. Madding, (2006), Thermal imagery of cloud base in tornadic supercells, Journal of Atmsopheric and Oceanic Tehnology, 23, 11, 1445-1461.

Tanré, D., Haywood, J., Pelon, J., Leon, J.F., Chatenet, B., Formenti, P., Francis, P., Goloub, P., Highwood, E.J., and Myhre, G. (2003), Measurement and modeling of the Saharan dust radiative impact: Overview of the Saharan Dust Experiment (SHADE), J. Geophys. Res., 108, D18, 8574, doi:10.1029/2002JD003273.

Tanre´, D., Y. J. Kaufman, M. Herman, and S. Mattoo (1997), Remote sensing of aerosol properties over oceans using the MODIS/EOS spectral radiances., J. Geophys. Res., 102, 16,971– 16,988.

Thome, K., F. Palluconi, T. Takashima, and K. Masuda (1998), Atmospheric correction of ASTER. IEEE T. Geosci. Remote, 36(4), 1199−1211.

Thomson, J. L., and J.W. Salisbury (1993), The mid-infrared reflectance of mineral mixtures (7–14 mm): Rem. Sens. Environ., 45, p. 1–13.

Tonooka, H., and A. Iwasaki (2003), Improvement of ASTER/SWIR Crosstalk Correction, Proc. SPIE, 5234(168), 168-179, doi:10.1117/12.511811.

Twomey, S. (1974), Pollution and the planetary albedo, Atmsopheric Environment, 8, 1251-1256.

USGS (2002), WA/ID National Map Pilot–Digital Orthophoto Quadrangles (DOQ), United States Geological Survey, http://online.wr.usgs.gov/ngpo/doq/MD-DOQs.html.

Van den Bergh, F., A. van Wyk, B.J. van Wyk, and G. Udahemuka (2007), A comparison of data-driven and model-driven approaches to brightness temperature diurnal cycle interpolation, SAIEE Africa Research Journal, 98(3), 81-86.

Van den Dool, H., J. Huang, and Y. Fan (2006), Performance and analysis of the constructed analogue method applied to U.S. soil moisture over 1981-2001, J. Geophys. Res., 108(D16), doi:10.1029/2002JD003114.

Van der Meer, F.D., A. Stein, and B. Gorte (1999), Spatial Statistics for Remote Sensing. Boston: Kluwer Academic Publishers, pp. 16-17.

Vermote, E. F. and N.Z. El-Saleous (2006), Operational atmospheric correction of MODIS visible to middle infrared land surface data in the case of an infinite Lambertian target, in Earth Science Satellite Remote Sensing, Vol.I: Science and Instruments, edited by J.J. Qu, M. Kafatos, R.E. Murphy, V.V. Salomonson, and W. Gao, pp. 123 – 153, Tsinghua University Press, Beijing and Springer-Varlag GmbH, Berlin, Heidelberg.

Vincent, R.K., and F. Thomson, (1972), Spectral compositional imaging of silicate rocks. J. Geophys. Res., 77(14), 2465-2472.

Volz, F.E. (1973), Infrared optical constants of ammonium sulphate, Sahara dust, volcanic pumice and flyash, Appl. Opt., 12, 564-567.

Wang, C.Y., S.H. Qi, and Z. Niu (2004), Evaluating soil moisture status in China using the temperature-vegetation dryness index (TVDI), Can. J. of Remote Sens., 30(5), 671-679.

Washington, R., M.C. Todd, S. Engelstaedter, S. Mbainayel, and F. Mitchell (2006), Dust and the low-level circulation over the Bodele Depression, Chad: observations from BoDEx 2005. J. Geophys. Res., 111, D3, D03201

Watkins, T. (2003), Geologic history of Proterozoic basement in the area of Desierto de Altar, Sonora, Mexico, near Sierra Los Ojos; with possible relations to the Rodinia supercontinent [senior thesis]: California State Polytechnic University, Pomona, California, 42 p.

Watson, K., L.C. Rowen, and T.W. Offield (1971), Application of thermal modeling in the geologic interpretation of IR images, Remote Sens. Environ., 3, 2017-2041.

Wenrich, M.L. and P.R. Christensen (1996), Optical constants of minerals derived from emission spectroscopy: application to quartz, J. Geophys. Res., 101, B7, 15921 – 15931.

White, K., J. Walden, N. Drake, F. Echardt, and J. Settle (1997), Mapping the iron oxide content of dune sands, Namib Sand Sea, Namibia, using Landsat Thematic Mapper data. Rem. Sens. Environ., 62, 30 – 39.

Wilber, A.C., D.P. Kratz, and S.K. Gupta (1999), Surface emissivity maps for use in satellite retrivals of longwave radiation, NASA/TP-1999-209362, 30 p.

Wolfe, R.E., M. Nishihama, A.J. Fleig, J.A. Kuyper, D.P. Roy, J.C. Storey, and F.S. Patt (2002), Achieving sub-pixel Geolocation accuracy in support of MODIS land science, Remote Sens. Environ., 83(1-2), 31-49, doi:10.1016/S0034-4257(02)00085-8.

Wolff, M.J., M.D. Smith, R.T. Clancy, N. Spanovich, B.A. Whitney, M.T. Lemmon, J.L. Bandfield, D. Banfield, A. Ghosh, G. Landis, P.R. Christensen, J.F. Bell, S.W. Squyres (2006), Constraints on dust aerosols from the Mars Exploration Rovers using MGS overflights and Mini-TES, J. Geophys. Res., 111, E12S17, doi: 10.1029/2006JE002786.

Wood, C.A. (1974), Reconnaissance geophysics and geology of the Pinacate craters, Sonora, Mexico, Bull. Volcanol., 38, 149-172.

Wright, S.P. and Ramsey, M.S. (2006), Thermal infrared data analyses of Meteor Crater, Arizona: Implications for Mars spaceborne data from the Thermal Emission Imaging System, J. Geophys. Res., 111(E8), doi:10.1029/2005JE002472.

Wyatt, M. B. and H. Y. McSween Jr. (2002), Spectral evidence for weathered basalt as an alternative to andesite in the northern lowlands of Mars, Nature, 417, 263–266.

Xie, J. and X. Xie (2008), Long-term trend in aerosol optical depth from 1980 to 2001 in north China, Particuology, 6, 2, 106-111.

Xue, Y. and A.P. Cracknell (1995), Advanced thermal inertia modeling, Int. J. Remote Sens., 16(3), 431-446, doi:10.1080/01431169508954411.

Xue, Y., and A.P. Cracknell (1992), Thermal inertia mapping: from research to operation, in Proceedings of the 18th Annual Conference of the Remote Sensing Society held in University of Dundee on 15-17 September 1992, edited by A.P. Cracknell and R.A. Vaughan, pp. 471-480, Nottingham: Remote Sensing Society.

Yamaguchi, Y., A. Kahle, H. Tsu, T. Kawakami, and M. Pniel (1998), Overview of the Advanced Spaceborne Thermal Emission and Reflectance Radiometer (ASTER). IEEE Trans. Geosci. Remote Sens. 36, 1062– 1071.

Young, A. T. (1974), Atmospheric Extinction. Ch. 3.1 in Methods of Experimental Physics, Vol. 12 Astrophysics, Part A: Optical and Infrared. ed. N. Carleton. New York: Academic Press. ISBN 0-12-474912-1

Young, A. T. (1994.), Air mass and refraction. Applied Optics. 33:1108–1110.

Yoshioka, M., N.M. Mahowald, A.J. Conley, W.D. Collins, D. W. Fillmore, C.S. Zender, and D.B. Coleman (2007), Impact of Desert Dust Radiative Forcing on Sahel Precipitation: Relative importance of dust compared to sea surface temperature variations, vegetation changes and greenhouse gas warming, J. Clim., 20, 8, 1445-1467.

Yoshioka, M., N. Mahowald, J. Dufresne, and C. Luo (2005), Simulation of absorbing aerosol indices for African dust, J. Geophys. Res., 110, D18, 22 p.

Zender, C.S., H. Bian, and D. Newman (2003), Mineral dust entrainment and deposition (DEAD) model: Description and 1990s dust climatology, J. Geophys. Res., 108, No. D14, 4416, doi:10.1029/2002JD002775.

Zhang, J. and S.A. Christopher, (2003), Longwave radiative forcing of Saharan dust aerosols estimated from MODIS, MISR, and CERES observations on Terra, Geophys. Res., Let., 30, 4 pp.

Zhang, R.H., X.M. Sun, and Z.L. Zhu (2002), Remote sensing information model in surface evaporation from differential thermal inertia and it's validation in Gansu Province, Sci. China Ser. D., 32, 1041-1050.

Zhenhua, L. and Z. Yingshi (2006), Research on the method for retrieving soil moisture using thermal inertia model, Sci. China Ser. D., 49, 539-545.

Zhou, L., R.E. Dickinson, K. Ogawa, Y. Tian, M. Jin, T. Schmugge, and E. Tsvetsinskaya (2003), Relations between albedos and emissivities from MODIS and ASTER data over North African Desert, Geophys. Res. Lett., 30, 2026, doi:10.1029/2003GL018069.

Zimbelman, J.R., S.H. Williams, and V.P. Tchakerian (1995), Sand transport paths in the Mojave Desert, southwestern United States. In Tchakerian, V.P. (Ed.), (p. 101-129). Desert Aeolian Processes. Chapman and Hall, London.